Charles University in Prague

Faculty of Science

Ph.D. study program: Modelling of Chemical Properties of Nano- and Biostructures

M.Sc. Ho Viet Thang

Theoretical Investigation of Properties of 3D and 2D Zeolites

Dissertation

Supervisor:

prof. RNDr. Petr Nachtigall, Ph.D.

Prague, 2016

Univerzite Karlova v Praze

Přírodovědecká fakulta

Doktorský studijní program: Modelování chemických vlastností nano- a biostruktur

M.Sc. Ho Viet Thang

Teoretické studium vlastností 3D a 2D zeolitů

Disertační práce

Školitel:

prof. RNDr. Petr Nachtigall, Ph.D.

Praha, 2016

Declaration of Authorship

I, Ho Viet Thang, declare that this dissertation titled, “Theoretical Investigation of Properties of 3D and 2D Zeolites” and the work presented in it are my own. All the literature is properly cited, and I have not been yet awarded any other academic degree or diploma for this thesis or its substantial part.

Signed: _____

Date: _____

Acknowledgments

This thesis would not have been possible without the precious support of my supervisor, colleagues, family and friends. I would like to express my grateful acknowledgement to all of you.

First of all, I would like to express my sincere gratitude to my advisor Prof. Petr Nachtigall for his patience, support, helpful advices, motivation, and immense knowledge of my PhD study. His guidance helped me in all the time of research and revising of this thesis. I could not have imagined having a better advisor and mentor for my PhD study.

Besides my advisor, I would like to thank the rest of my thesis committee members for their insightful comments and the hard questions which encouraged me to widen my research from various perspectives.

My sincere thanks also go to Dr. Miroslav Rubeš, Dr. Lukáš Grajciar, Mgr. Miroslav Položij, and staff of Department of Physical and Macromacular chemistry, Falculty of Sciences, Charles University in Prague for kindly helping and supporting me.

I would like to acknowledge STARS program, Czech Science Foundation under the project P106/12/G015, European Union Seventh Framework Programme No. 604307 and Charles University Grant Agency (GAUK) No. 562214 B.-CH for financial support of my PhD study.

Last but not least, I would like to thank my family, my friends for supporting me spiritually throughout writing this thesis and my life in general.

Prague, August 8, 2016

Abstract

Zeolites have been widely used in many different fields including catalysis, adsorption and separation, ion exchange, or gas storage. Conventional zeolites have three-dimensional (3D) structures with microporous channel system; typical pore sizes are well below 1 nanometer, therefore, diffusion limitation plays important role in many process and bulkier reactants (or products) cannot enter (or leave) the zeolite channel system. Two-dimensional (2D) zeolites prepared in last years can lift all diffusion limitation and they thus offer a very attractive alternative to conventional 3D zeolites. 2D zeolites attracted considerable attention on the experimental side; however, understanding of 2D zeolites based on computational investigation or on a combination of experimental and computational investigation is limited. A motivation for the computational work presented here is to improve our understanding of properties of 2D zeolites based on computational investigation.

The originality of the research presented herein is in the strategy: we carried out systematic investigation of properties of corresponding 2D and 3D zeolites and we focus on the identification of similarities and differences. The most important zeolite properties, *i.e.*, presence of Brønsted and Lewis acid sites, are investigated. A number of different characteristics of acid sites are considered, focusing on those that can be also obtained experimentally. Our computational results are compared with experimental results available in literature and with those newly obtained by collaborating experimental research groups. Several zeolite topologies are investigated, including, UTL, MFI, MWW, and FAU; properties of traditional 3D zeolite as well as of corresponding 2D one are considered in all cases.

The results obtained were found to be in a good agreement with available experimental data. This agreement entitles us to outline a general connection between the properties of 3D and 2D zeolites. Two-dimensional zeolites with relatively thick layers (above 2 nm) and low concentration of surface silanol have almost identical properties as their corresponding 3D counterpart (MWW). Two-dimensional zeolites with thick layers and high concentration of surface silanols show rather different properties for the same crystallographic sites in 3D and 2D materials; however, averaged properties remain similar. Two-dimensional zeolites with thin layers (1 nm) appear to be less acidic than

corresponding 3D zeolites. In summary, our results indicate that neither Brønsted nor Lewis acidity is significantly influenced by the transition from 3D to 2D zeolites.

Abstrakt

Zeolity jsou široce využívány v řadě oblastí včetně katalýzy, adsorpcí a separací, iontových výměn a ukládání plynů. Běžné zeolity mají trojrozměrnou (3D) strukturu obsahující systém mikroporézních kanálů. Typická velikost těchto kanálů je pod 1 nm, v důsledku čehož je řada procesů limitována rychlostí difúze a větší reaktanty (produkty) nemohou vůbec vstoupit (opustit) do kanálového systému. Dvojrozměrné (2D) zeolity připravené v posledních letech mohou zmírnit nebo zcela eliminovat problémy spojené s difúzí a představují velmi zajímavou alternativu k běžným 3D zeolitům. 2D zeolity byly intenzivně zkoumány v posledních letech zejména experimentálně, zatímco porozumění jejich vlastností na základě teoretických výpočtů či na základě kombinace experimentu a teorie je zatím značně omezené. Práce zde předkládaná je motivována snahou vyjasnit vlastnosti 2D zeolitů na základě výpočetní studie.

Originalita našeho výzkumu je ve zvolené strategii – na základě systematického výzkumu vlastností 2D a korespondujících 3D zeolitů chceme nalézt a pochopit podobnosti a rozdílnosti mezi 3D a 2D zeolity. Soustředíme zejména na studium nejvýznamnějších vlastností zeolitů, tedy na popis Brønstedovské a Lewisovské kyselosti. Zabýváme se studiem různých charakteristik kyselých center v zeolitech a zejména takových charakteristik, které jsou experimentálně dostupné a mohou být porovnávány s experimentálními daty. Naše teoretické výsledky jsou srovnávány nejen s experimentálními daty dostupnými v literatuře, ale také s nově získávanými daty ve spolupracujících experimentálních laboratoří. V práci se zabýváme zeolity s různou strukturou (UTL, MFI, MWW a FAU), vždy studujeme stejné vlastnosti v běžném 3D zeolitu a v jeho 2D analogu.

Výsledky získané teoreticky jsou v dobré shodě s dostupnými experimentálními daty. Tato shoda nás opravňuje k formulaci obecných vztahů mezi vlastnostmi 3D a 2D zeolitů. Dvojrozměrné zeolity s relativně silnými deskami (silnějšími než 2 nm) a nízkou koncentrací povrchových silanolů mají prakticky totožné vlastnosti jako jejich 3D analog (například zeolity s MWW topologií). Dvojrozměrné zeolity se silnými deskami a vysokou koncentrací povrchových silanolů mají rozdílné vlastnosti pro jednotlivá krystalografická kyselá centra ve 3D a 2D materiálech, ale zprůměrované vlastnosti jsou velmi podobné. A dvojrozměrné zeolity s tenkými deskami (okolo 1 nm) mají o něco

slabší kyselá centra než korespondující 3D zeolit. Získané výsledky indikují, že ani Brønstedovská ani Lewisovská kyselá centra nejsou významně ovlivněna přechodem od 3D ke 2D zeolitům.

Contents

List of Figures

List of Tables

Abbreviations

DFT	**D**ensity Functional Theory
LDA	**L**ocal **D**ensity **A**pproximation
GGA	**G**eneralized **G**radient **A**pproximation
vdW	**v**an **d**er **W**aals
DFT-D	**D**ensity **F**unctional **T**heory with empirical **D**ispersion
DFT/CC	**D**ensity **F**unctional **T**heory corrected for **C**ouple **C**luster accuracy
vdW-DF	**v**an **d**er **W**aals **D**ensity **F**unctional **T**heory
CCSD(T)	**C**oupled **C**lusters with **S**ingles, **D**oubles and perturbative **T**riples
PBE	**P**erdew-**B**urke-**E**rnzerhof
IZA	**I**nternational **Z**eolite **A**ssociation
UTL	Three-letter code of zeolite according to IZA
OKO	Three-letter code of zeolite according to IZA
PCR	Three-letter code of zeolite according to IZA
MFI	Three-letter code of zeolite according to IZA
FAU	Three-letter code of zeolite according to IZA
MWW	Three-letter code of zeolite according to IZA
IPC-n	Materials prepared at the Institute of Physical Chemistry (Prague)
ZSM-5	Zeolite with MFI topology
BA	Brønsted acidity
LA	Lewis acidity

Chapter 1

Introduction

Microporous aluminosilicate materials, zeolites, have been widely used in many different fields, such as catalysis, adsorption and separation, ion exchange, or gas storage due to their high acidity, high surface area, high thermal stability, and environmentally friendly properties. In particular, they were established as an important industrial catalyst for important processes, such as hydrocarbon cracking, olefin oligomerization, methanol to olefin conversion, and fine chemical synthesis [1-5]. Conventional zeolites have three-dimensional (3D) structures with microporous channel system; typical pore sizes are well below 1 nanometer, therefore, diffusion limitation plays important role in many process and often only the fraction of active sites (closer to external surface) are really utilized. In addition, bulkier reactants (or products) cannot enter (or leave) the zeolite channel system.

In order to overcome limitations connected with the small size of zeolite micropores in conventional 3D zeolites, ordered mesoporous molecular sieves have been synthesized and explored for catalytic applications [6, 7]. Unfortunately, these materials containing amorphous walls do not have sufficient acid strength and activity. This facts triggered an intense research towards synthesis of new zeolite materials that possess both microporosity and mesoporosity. Hierarchical zeolites are materials that can be viewed as conventional zeolites with additional mesoporosity; crystalline structure of channel walls is preserved and thus, unique properties of zeolites, strong acidity in particular, are preserved. A very appealing way for preparation of hierarchical zeolites is the synthesis of two-dimensional (2D) zeolites and their subsequent pillaring providing mesoporous channels between individual zeolite layers [8-10].

2D zeolites attracted considerable attention in recent years, in particular on the experimental side; a number of experimental studies addressing experimental characterization of 2D zeolites as well as their catalytic and adsorption properties

increases every year [11-19]. However, understanding of 2D zeolites based on computational investigation or on a combination of experimental and computational investigation is limping. And this was a motivation for the computational work presented herein – the main goal of this thesis is to improve our understanding of properties of 2D zeolites based on computation investigation. While this thesis is purely computational work, the selection of systems as well as properties of 2D zeolites to be investigated was motivated by available experimental data. The originality of our research is in the strategy: we investigate the properties of 2D zeolite and corresponding 3D zeolite in parallel and we compare the results and discuss the differences and similarities. The focus is on the investigation of the most important zeolite properties, *i.e.*, catalysis; both Brønsted and Lewis acid sites are investigated. Number of different characteristics of acid sites are investigated, focusing on those that can be also obtained experimentally. The IR spectra corresponding to acid sites directly and to probe molecules adsorbed on acid sites are investigated. Most of the work presented herein is based on the CO probe molecule that is considered as one of the most suitable and that is applicable to almost any zeolite. In addition, NMR characteristics of Brønsted acid sites probes are also investigated and catalytic activity of Lewis acid sites is also investigated towards the end of this thesis.

Following 3D and 2D materials were investigated: UTL zeolite and corresponding IPC-1P layered zeolite, MCM-22 zeolite and MCM-22P layered zeolite (both with MWW topology), conventional 3D MFI and recently synthesized 2D MFI, and finally conventional FAU zeolite and hierarchical FAU represented by a model of 2D FAU. All calculations were performed at the density functional theory (DFT) level and we investigated both Brønsted and Lewis acid sites in these materials. The main focus of this work is on understanding of acid-base properties of these 2D zeolites and on the structural factors behind the similarity and difference from corresponding 3D materials. It must be noted that our computational results are compared with available experimental data from literature but also with newly acquired system characteristics obtained in parallel experimental investigation in several collaborating laboratories around the world (including Prof. Jiří Čejka at the IPC Academy of Science, Czech Republic, Prof. Roman Bulánek at University of Pardubice, Czech Republic, Prof. Carlos Otero at University of the Balearic Islands, Spain, Prof. Ryng Ryoo at KAIST, Republic of Korea, and Prof.

Javier Pérez-Ramírez at ETH Zurich, Switzerland). The work reported in this thesis has resulted so far in five papers in respected international journals, such as Phys. Chem. Chem. Phys. or J. Phys. Chem C; these papers are part of this thesis and they are given at Attachments. Several other papers based on the data reported in the thesis are under preparation.

This thesis is organized as follows: a general background of zeolite science, including some computational aspects, are given in Section 2. The models of 3D and 2D zeolites with different frameworks explored in the thesis (UTL, MWW, MFI and FAU) are provided in Section 3. Section 4 presents the methods which were applied in this work: DFT, dispersion corrections (vdW-DF, DFT-D, DFT/CC) and $\omega B97X$ correlation. Results and Discussion are presented in Section 5 that is the most comprehensive part of the thesis and is divided into several subsections: (i) Lewis acidity of 3D and 2D zeolite, (ii) Brønsted acidity of 3D and 2D zeolites and (iii) catalytic activities of hierarchical USY zeolites. Finally, Conclusions are drawn in Section 6.

Chapter 2

General background

It is the goal of this chapter to provide the reader with general background necessary for understanding of following chapters. Zeolites and in particular hierarchical zeolites are introduced first followed by the discussion of two-dimensional zeolites. The framework of zeolites discussed in following chapters are introduced next. We than introduce the concept of Brønsted and Lewis acidity in zeolites and the basics of experimental techniques typically used for their characterization and implications for computational investigation.

2.1. Zeolites

Zeolites are crystalline microporous aluminosilicates with three dimensional networks containing cavities and channel systems. Zeolite materials are based on the primary building unit – TO_4 tetrahedron – where T is a tetrahedrally coordinated cation (*e.g.*, Si^{4+}, Al^{3+}). The connection of primary building units via oxygen atoms forms the secondary building units (SBU) of n-ring structures, where n is the number of T atoms. Typically, n is 4, 6, 8, 12 as shown in Figure 1; these SBU's frequently occur in zeolite structures [20]. The linkages of SBU in regular arrays create pores and cavities that are characteristic for a particular zeolite topology. Up to now, more than 230 different zeolite frameworks have been synthesized and recognized by Internationl Zeolite Association and they received a unique three-letter code [20]. Examples of zeolite framework structures are shown in Figure 2 for UTL and MFI.

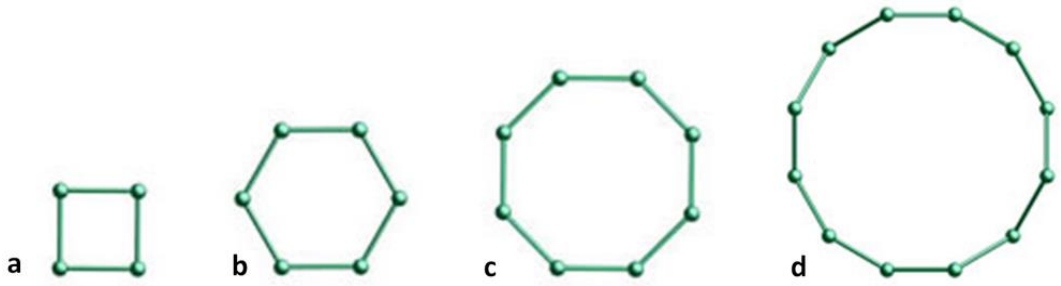

FIGURE 1. Examples of secondary building units of zeolite, shown for a) 4-ring, b) 6-ring, c) 8-ring, and d) 12-ring.

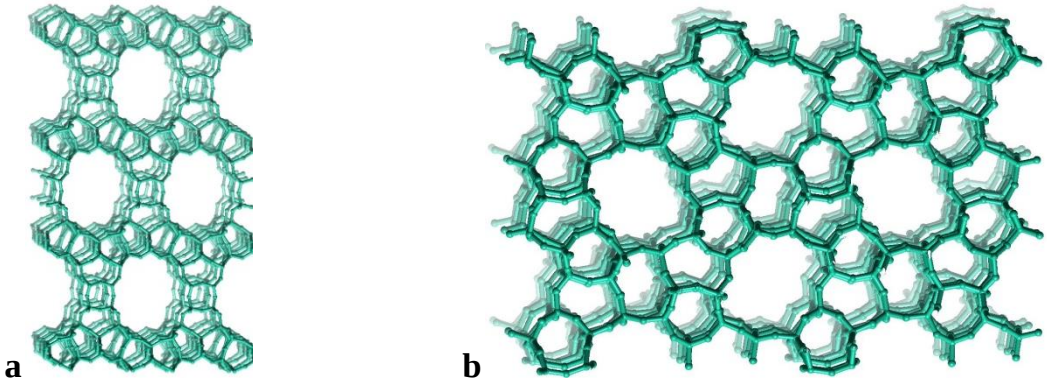

FIGURE 2. Framework structure of a) UTL and b) MFI zeolites, viewed along main channel systems.

Since zeolite frameworks expand in three dimensions they are in general considered to be three dimensional (3D) materials. While 3D zeolite materials have many advantages for catalytic and other applications, there is one disadvantage related to the fact that zeolites are 3D crystalline materials with microporosity: the size of the microporous channel (typically < 1nm) generate some diffusion limitations for small molecules and it does not allow bulkier molecules to even enter the channel system. In recent years, promising lamellar zeolite materials have been successful synthesized by various methods including direct synthesis and post-synthetic treatments to overcome this obstacle. These new materials are viewed as 2D materials because they can be obtained with very thin framework thickness (1-3 nm) in one dimension. For example, IPC-1P layered material was obtained by hydrolysis of UTL containing Ge-rich double four-memberd ring units [8]; the monolayers with MWW topology, a material denoted as

MCM-22P, were synthesized directly in aqueous media [21, 22], and MFI nanosheets were obtained by a synthesis route using special structure directing surfactants [10, 23].

2.1.1. Zeolites of IPC-1P family

It has been shown recently that UTL zeolite can be converted into layered two-dimensional (2D) material IPC-1P by selective hydrolysis [8] and this 2D material can be further converted into new zeolites IPC-2 and IPC-4 (having OKO and PCR topology, respectively) via ADOR mechanism [24-26]. The OKO zeolite was originally prepared via inverse sigma transformation [27]; OKO and IPC-2 have the same framework connectivity but differ in the symmetry. These four materials (IPC-1P, UTL, OKO, and PCR) thus constitute a unique set of adsorbents with the same dense 2D layers separated by different interlayer distances defined by different interlayer linkers. Consequently, these materials have different channel systems parallel to the same 2D layer (Figure 3). We denote these zeolites "IPC-1P family" since they all can be formally obtained from IPC-1P 2D precursor.

The UTL zeolite has a monoclinic unit cell with C2/m space group ($T_{64}Ge_{12}O_{152}$ where T is either Si or Al atom) in which 12 Ge and 4 Si atoms are located in the double-four ring (D4R) units [28]. The UTL structure contains a two-dimensional channel system with main channel along the *c* vector defined by a 14-ring (9.5 × 7.1 Å) and a perpendicular channel along *b* vector defined by a 12-ring (8.5 × 5.5 Å).

The OKO (IPC-2) zeolite has a monoclinic unit cell with C12/m1 space group ($T_{68}O_{136}$ where T is either Si or Al atom) in which there are eleven non-equivalent T sites and twenty-one non-equivalent framework oxygen atoms [20]. The OKO structure contains a two-dimensional channel system with the main channel along *c* vector defined by a 12-ring (5.6 x 7.0 Å) and a perpendicular channel along *b* vector defined by a 10-ring (4.7 x 6.1 Å).

The PCR (IPC-4) zeolite has a monoclinic unit cell with C1m1 space group ($T_{60}O_{120}$ where T is either Si or Al atom) in which there are ten non-equivalent T sites and eighteen non-equivalent framework oxygen atoms [20]. The PCR structure contains a two-dimensional channel system with the main channel along *c* vector defined by a 10-ring (5.1 x 6.1 Å) and a perpendicular channel along *b* vector defined a 8-ring (3.5 x 4.7 Å).

The pillared structures containing 2D IPC-1P layers and mesopores can be obtained by swelling of IPC-1P with suitable organic surfactants followed by intercalation with silica species and calcination. This material is denoted IPC-1PI. Therefore, the computational results obtained for IPC-1P layer can be compared to experimental data obtained for IPC-1PI zeolite.

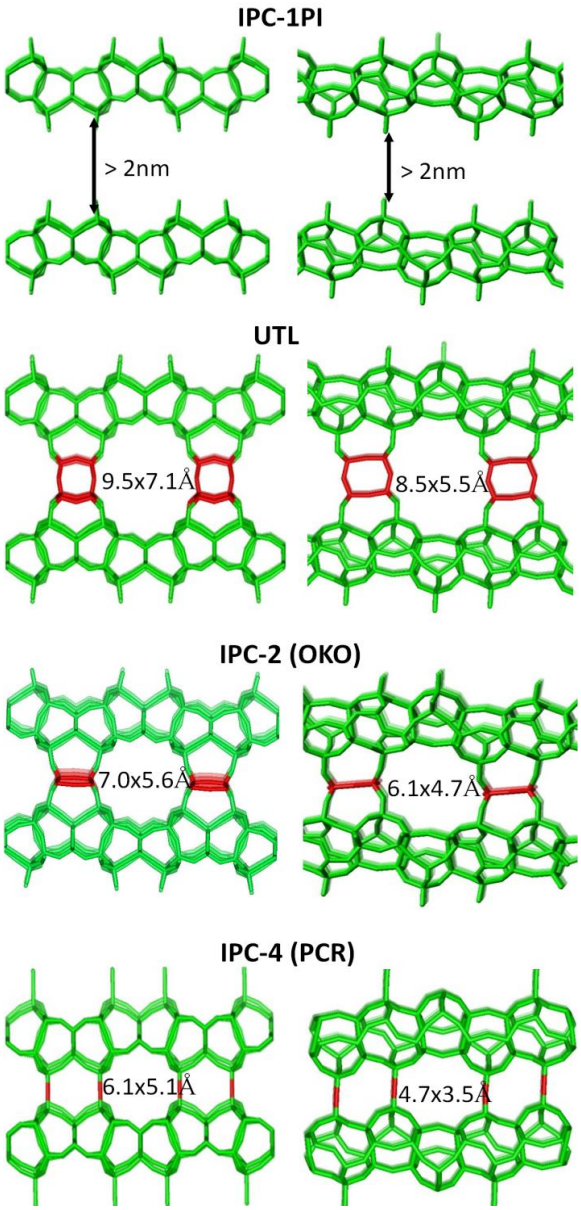

FIGURE 3. Structures of IPC-1PI, UTL, OKO and PCR consist of the same dense 2D layers (in green color) but different linkers (in red color) leading to the different pore sizes; shown along the main (left side) and perpendicular channels (right side).

2.1.2. 3D and 2D zeolites with MWW topology

The MCM-22 zeolite (MWW topology) has a hexagonal unit cell and P6/mmm space group ($T_{72}O_{144}$, where T is either a Si or Al atom), in which there are eight non-equivalent T sites and thirteen non-equivalent framework oxygen atoms [20]. The MCM-22 zeolite contains two independent channel systems: the two-dimensional sinusoidal 10-membered ring channels (4.1 x 5.1 Å) and the 12-membered ring cages (7.1 × 7.1 × 18.2 Å) interconnected via 10-membered ring windows (4.0 x 5.5Å) [20]. The three dimensional MCM-22 zeolite can be obtained from layered MCM-22 precursor MCM-22P, by direct condensation of individual MCM-22P (Figure 4); individual layers are stucked on top of each other upon the synthesis. Swelling of MCM-22P material with large organic surfactants followed by intercalation by silica species and calcination leads to the formation of interlayer inorganic pillars and mesopores; thus formed pillared material is denoted MCM-36 [23, 29]. Therefore, the results obtained computationally for MCM-22P layer can be compared to experimental data obtained using MCM-36 zeolite.

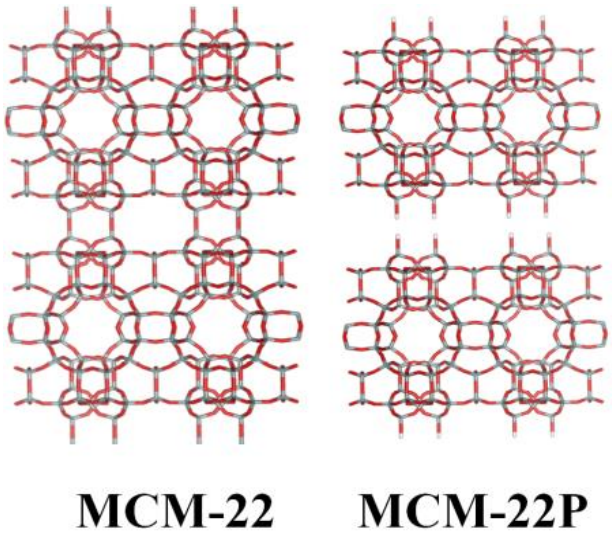

FIGURE 4. Structure of MCM-22 (left) and MCM-22P (right), The H, O and Si atoms are depicted in white, red, and gray color, respectively.

2.1.3. 3D and 2D zeolites with MFI topology

The ZSM-5 (MFI framework) has an orthorhombic unit cell, Pnma space group ($T_{96}O_{192}$ where T is either a Si or an Al atom), in which there are twelve non-equivalent T sites

and twenty-six non-equivalent framework oxygen atoms [20]. 3D-ZSM-5 consists of two types of 10-membered ring channels: straight channels (5.3 x 5.6 Å) oriented along the *b* vector and zigzag channels (5.1 x 5.5 Å) oriented along the *a* vector. The 2D-ZSM-5 zeolite was obtained via a synthesis route using zeolite structure directing surfactants [10, 23]. The pillared ZSM-5 nanosheets were created through coherent assembly of the zeolite layers and surfactants with long hydrocarbon chains [10]. The silica pillars retain the interlayer spaces of the lamellar MFI after calcination to remove surfactants. The structure of 3D-ZSM-5 and 2D-ZSM-5 are shown in Figure 5.

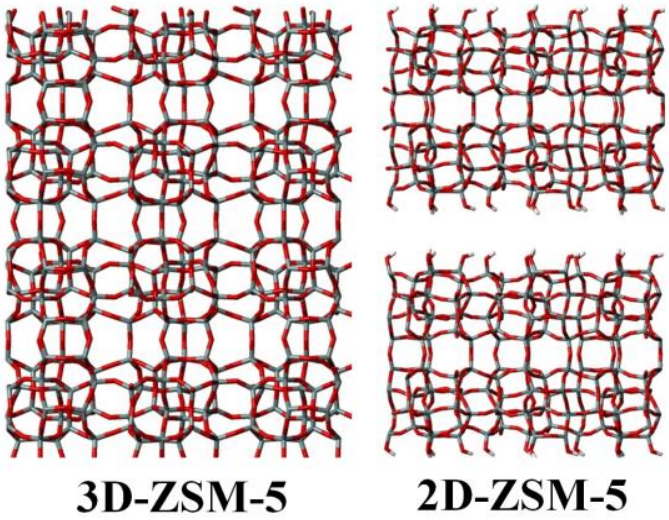

FIGURE 5. Structure of 3D-ZSM-5 (left) and 2D-ZSM-5 (right). The H, O and Si atoms are depicted in white, red, and gray color, respectively.

2.1.4. FAU zeolite and FAU layered material

The FAU structure has a cubic unit cell, Fd-3m space group ($T_{192}O_{384}$ where T is either a Si or an Al atom), in which all the T sites are equivalent and there are four non-equivalent framework oxygen atoms [20]. This material has three dimensional pore systems consisting of sodalite cages connected through hexagonal prisms or double six-ring (D6R). This results in 12-membered ring pores with a diameter of 7.4 Å and the large cavity with diameter of 12 Å surrounded by 10 sodalite cages (Figure 6a). The hierarchical FAU zeolites are obtained by different methods, such as a desilication by post synthesis treatments using alkaline [30], by the use of organosilan templates [31, 32] or inorganic salts [33] during zeolite synthesis. The surface of mesopore wall of

hierarchical FAU materials can be terminated by D6R or S6R [34] and example is shown in Figure 6b. Therefore, the hierarchical FAU can be represented by a layer-like material.

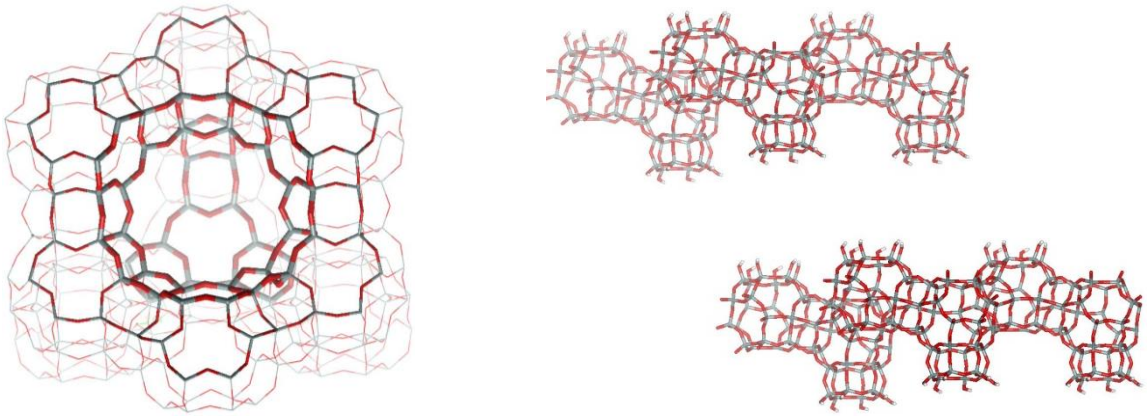

a **b**

FIGURE 6. Structure of FAU zeolite (a) and layered FAU zeolite terminated with D6R-S6R (b). The H, O and Si atoms are depicted in white, red, and gray color, respectively.

2.2. Brønsted and Lewis acidity in zeolites

The zeolite lattice consists of a three dimensional network of tetrahedra connecting four valent or three valent cations such as Si or Al, each having four oxygen atoms as neighbors, and each oxygen atom has two cations as the nearest neighbors. When all lattice cations are Si, the zeolite framework has no charge. However, when silicon is replaced by metal atom with lower valency (typically aluminum) negatively charged framework is formed. The negative charge in the zeolite framework is compensated by extra-framework cations in the vicinity of Al sites. The Brønsted acidic sites (Figure 7a) are created when a charge-compensating proton binds to one of four framework oxygen atoms bridging aluminum with adjacent silicons. Lewis acidic sites (Figure 7b) are generated when extra-framework metal cations such as Na^+ or Li^+ balance the negative charge of zeolite framework. In contrast to Brønsted acidic sites, Lewis acidic sites are stabilized by the coordination with 2, 3, or 4 framework oxygen atoms.

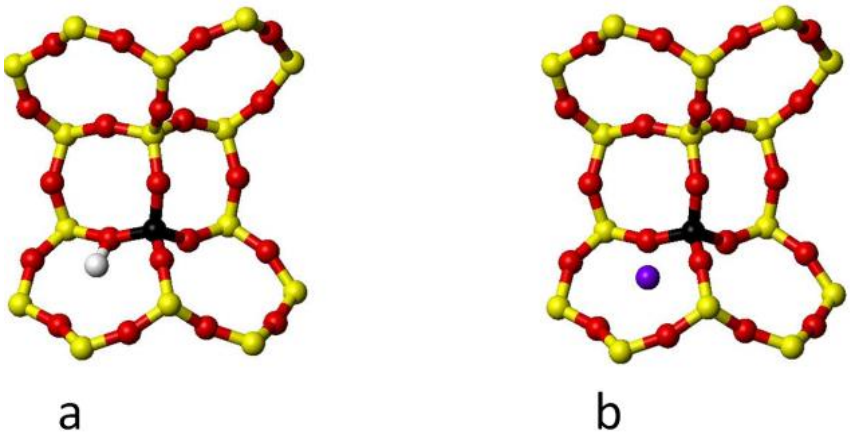

FIGURE 7. A Brønsted acidic site (a) and a Lewis acidic site (b). The atoms are depicted with following colors: Si (yellow), O (red), H (white) and extra-framework cation (purple).

2.3. Characterization of acid sites in zeolites – adsorption of probe molecules

Among methods for characterization of the acidity (either Brønsted or Lewis) of zeolites, the IR spectroscopy of adsorbed probe molecules is the most important one. Therefore, the selection of suitable probe molecules plays an important role in an accurate evaluation of acid-base properties in zeolite materials. The ideal probe molecule must fulfill certain criteria such as: a selective interaction with acid sites, a high specificity to discriminate between sites having small differences in acid strength, and the molecular size should be as small as possible to access the sites in narrow pores.

Many probe molecules ranging from strong base (NH_3, pyridine) to weak base (CH_4, N_2, CO) have been used but small and weakly interacting probe molecules, such as N_2 and CO [35-38], have been mostly used for probing acid properties of zeolites because they suit above mentioned criteria. Furthermore, their vibrational dynamics is relatively simple and adsorption induced frequency shifts can be evaluated easily. In addition, it is important to select such probe molecules for which accurate quantum chemical calculations can be carried out and provide complementary information (electronic structure details, binding energies and vibrational frequencies). Therefore, we have used predominantly CO as probe molecule for investigating acid properties of zeolite materials.

In addition to IR characterization, also NMR investigation of probe molecules adsorbed on acid sites are used; in particular, ^{31}P NMR of trimethylphosphine oxide

(TMPO) has been widely used in experimental characterization [39-41]. Compare to other NMR probes, such as acetone, pyridine or trialkyphosphine, the trialkylphosphine oxide probe molecules show higher sensitivity, wider range of chemical shifts and its dynamic diameter (ca. 0.55 nm) is suitable for small pores of many zeolites. Thus, the TMPO was used as a probe molecule to evaluate acidity in 3D and 2D zeolites in the present work.

2.4. Vibrational dynamics of adsorbed probe molecules

A harmonic vibration is an idealized expression which obeys Hooke's Law. It assumes that the magnitude of the restoring force for a system displaced from equilibrium is proportional to the displacement with the potential energy *V* as

$$V(x) = \frac{1}{2}kx^2 \quad , \qquad (1)$$

where k is the force constant and x is the displacement.

The potential energy within harmonic approximation has parabolic shape as shown in Figure 8 (green color).

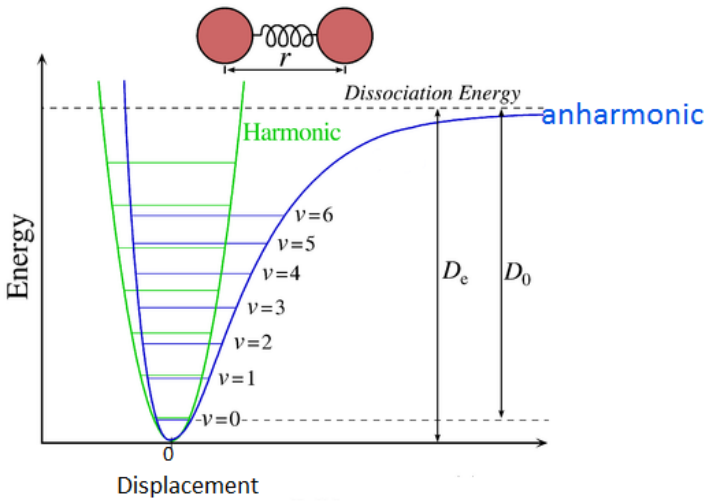

FIGURE 8. Harmonic vibration potential (green curve) and anharmonic vibration potential (blue curve).

Obviously, this idealized vibration fails to describe vibrational dynamics properly because the approximation of the potential energy by a parabola does not allow

molecules to dissociate. At the higher vibrational levels the atomic motion extends to the region of potential energy curve where the harmonic approximation fails and additional terms are required in potential V (Equation 2). Therefore, the vibrational dynamics description must go beyond harmonic approximation (Figure 8). Within the anharmonic description the potential V can be written as

$$V(x) = \frac{1}{2}kx^2 + \frac{\gamma_3^3}{6}x^3 + \frac{\gamma_4^4}{24}x^4 + higher\ terms, \qquad (2)$$

where γ_3 and γ_4 are anharmonic constants. The difference between adjacent vibrational energy level decreases with increasing vibrational level.

Chapter 3

Zeolite models

Early computational studies used small cluster models consisting of just a few atoms to represent the zeolite. The dangling bonds on the edges of the cluster model were terminated with hydrogen atoms. However, small cluster models could not possibly mimic a complex environment of active sites inside the microporous channels in zeolites. With rapid development of computational resources and rapid development of computational software (DFT in particular) in past 30 years it is now possible to use models containing hundreds of atoms. Instead of using large cluster models (they are also occasionally used) calculations can be performed with fully periodic models (employing periodic boundary conditions and utilizing the regular crystal structure of zeolites). All the calculations of zeolite properties reported herein were obtained with periodic models. Small cluster models were only used for testing the reliability and accuracy of methods employed (see below).

Periodic models of 3D zeolites are simply defined by the periodicity of the zeolite unit cell; periodic models of 2D zeolite layers also employ periodic boundary conditions in all three directions – unit cell vectors along the layer is defined by the crystal periodicity while periodicity along the surface normal is defined by the layer sickness and vacuum (typically 1-2 nm) separating periodic images of individual layers to minimize their spurious interactions (a supercell approximation). Models of 3D and 2D zeolites (those introduced in Section 2) were constructed and used for calculations. Technical details for individual zeolites are presented below.

3.1. Zeolites of IPC-1P family

The numbering scheme of framework atoms in UTL, OKO, and PCR structures is defined at the IZA database [20]; the use of three numbering schemes would make it complicated for a reader to follow the comparison of results for individual structure

types. In fact, all three UTL, OKO, and PCR framework types are based on the same dense 2D layers (a material denoted IPC-1P) [8] and they differ only by a linker inter-connecting these 2D layers into 3D zeolites (O atom, S4R, and D4R for PCR, OKO, and UTL, respectively). Therefore, for comparison of all 3 framework types the UTL numbering scheme is adopted (Figure. 9) and the mapping with the IZA numbering is shown in Table 1. The same numbering is used also for IPC-1P layered material. To prevent the confusion with the IZA numbering the T-sites are denoted as T'-sites throughout this section.

The notation of Li^+ cation positions for all structures is shown in Figure 9. Li^+ positions located on the surface of the channel wall (type I sites) can be classified as Mx and Px, where M is the main (larger) channel and P is the perpendicular (smaller) channel, x is the size of the ring on the channel wall that hosts the extra-framework cation and I2 stands for type II sites on the intersection (similar notation has been introduced previously for other high-silica zeolites [42, 43])

The unit cell of UTL (a= 29.8004 Å, b=13.9926 Å, c=12.3926 Å, and $\alpha=\gamma=90^o$, $\beta=105.1850^o$) were taken from zeolite structure database [20], the unit cell of IPC-1P is the same as for UTL along b and c vectors but the dimension along the a vector was adjusted to 29.8000 Å to introduce vacuum between layers and to avoid inter-layer interactions. Unit cell parameters previously determined for IPC-2 (OKO) (a= 12.5162 Å, b=13.8880 Å, c=13.9682 Å, and $\alpha= 118.7520^0$, $\beta=90.1740^o$, $\gamma=107.087^o$) and IPC-4 (PCR) (a= 20.3599 Å, b=14.1746 Å, c=12.4572 Å, and $\alpha=\gamma=90^o$, $\beta=114.0905^o$) were adopted [24].

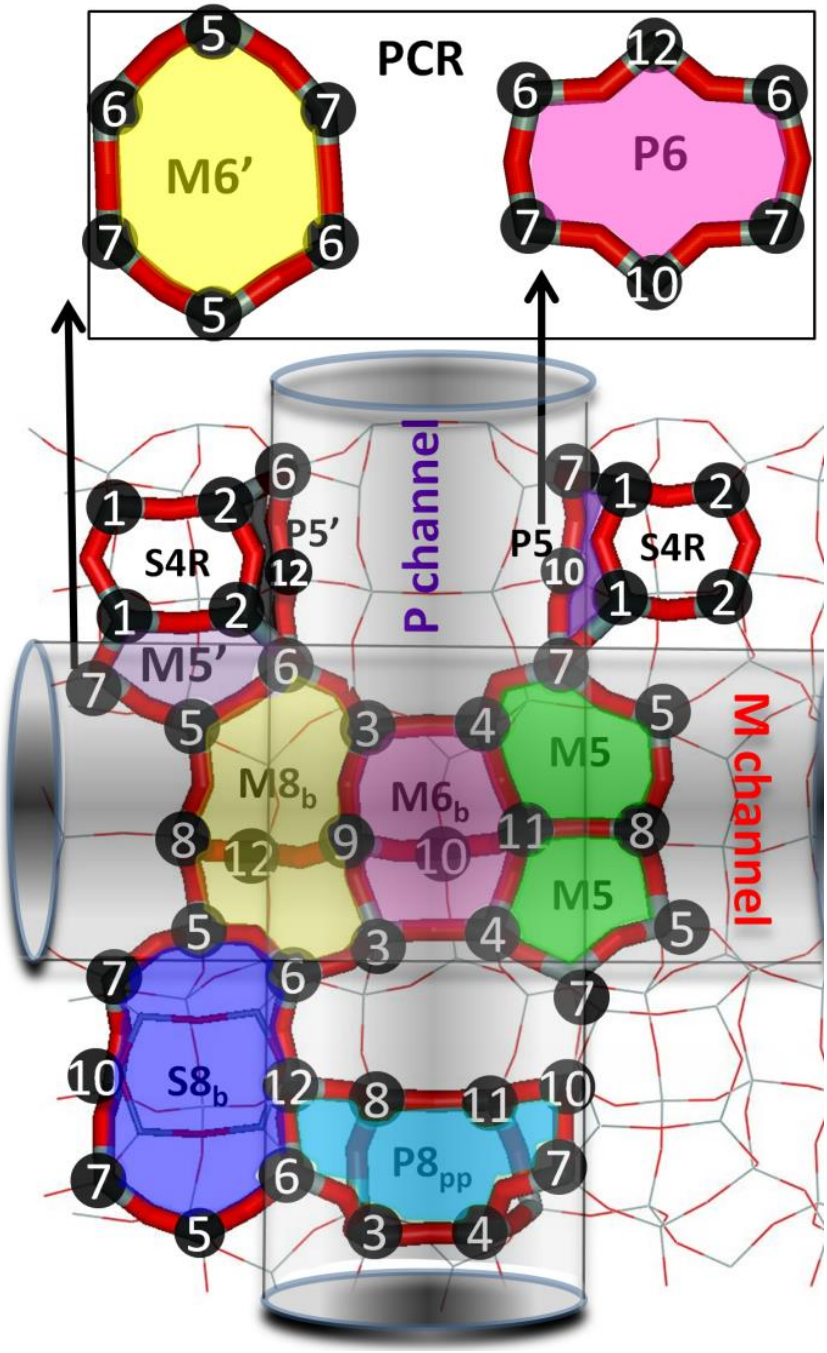

FIGURE 9. Notation used for extra-framework Li^+ cation sites in IPC-1P, UTL, OKO and PCR. Sites in the main and perpendicular channels are denoted as Mx and Px, respectively, where x stands for the size of the ring on the channel wall where the Li^+ cation is located. A new surface site in IPC-1P formed upon the removal of D4R is denoted S8b. Two sites in PCR at the location of P5 and M5 in UTL are denoted M6 and P6 (depicted in the inset). The numbering scheme of T' atoms based on the UTL numbering is also shown.

TABLE 1. The numbering of T sites in IPC-1P, UTL, OKO and PCR was taken from IZA database. The common numbering of the T' sites are chosen following numbering of UTL structure.

Common denotation	IPC-1P	UTL	IPC-2 (OKO)	IPC-4 (PCR)
T1'		T1		
T2'		T2	T6	
T3'	T3	T3	T1	T1
T4'	T4	T4	T2	T3
T5'	T5	T5	T3	T4
T6'	T6	T6	T4	T5
T7'	T7	T7	T5	T2
T8'	T8	T8	T7	T6
T9'	T9	T9	T8	T7
T10'	T10	T10	T9	T8
T11'	T11	T11	T10	T9
T12'	T12	T12	T11	T10

3.2. Materials with MWW topology

The MCM-22 structure and the atom numbering scheme (following the Database of Zeolite Structures) [20] are shown in Figure 10. The channel system including two 10-membered rings (MR) (10-MR sinusoidal and 10-MR crossing windows), as well as the 12-MR supercage and Li^+ cation positions are also shown. The unit cell parameters of MCM-22 were taken from Ref. [20] (a=b=14.39 Å, c=25.20 Å, and α=γ=90^o, β=120^o) and they remain the same for MCM-22P, except for the c direction which was adjusted to 55 Å to avoid inter-layer interactions.

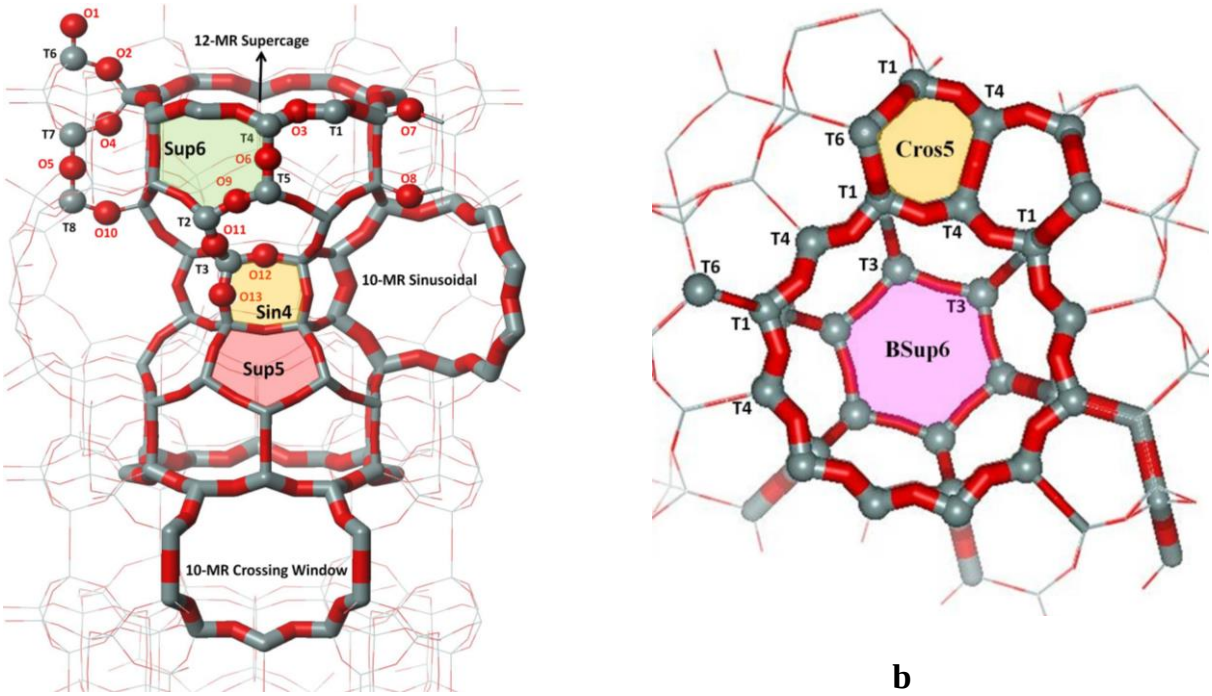

FIGURE 10. Structure of MCM-22 framework, numbering scheme and extra-framework cation positions; view along the *a* (or *b*) direction (a) and view along the *c* direction (b). O and Si atoms are depicted in red and gray color, respectively.

3.3. 3D and 2D zeolites with MFI topology

The MFI structure with numbering scheme taken from the Database of Zeolite Structure [20] and its channel system is shown in Figure 11. The 2D ZSM-5 structure was obtained from 3D ZSM-5 zeolite (Database of Zeolite Structure) by cutting along the *ac* plane at the middle of the zigzag channel, where the density of T-O-T bond is the lowest. That results in the slab thickness of approximately 21 Å. This structure also retains channels connecting upper and lower surfaces (unlike IPC-1P and MCM-22P). External surfaces were saturated by silanol groups. The unit cell parameters of 3D ZSM-5 (a=20.090 Å, b=19.738 Å, c=13.142 Å, and $\alpha=\gamma=\beta=90^{o}$) were taken from Ref. [20]. The calculations on 2D ZSM-5 were performed with the fixed the *a* and *c* lactic vectors (using values from 3D ZSM-5) and fixed *b* vector adjusted to 32 Å to avoid the interaction between layers.

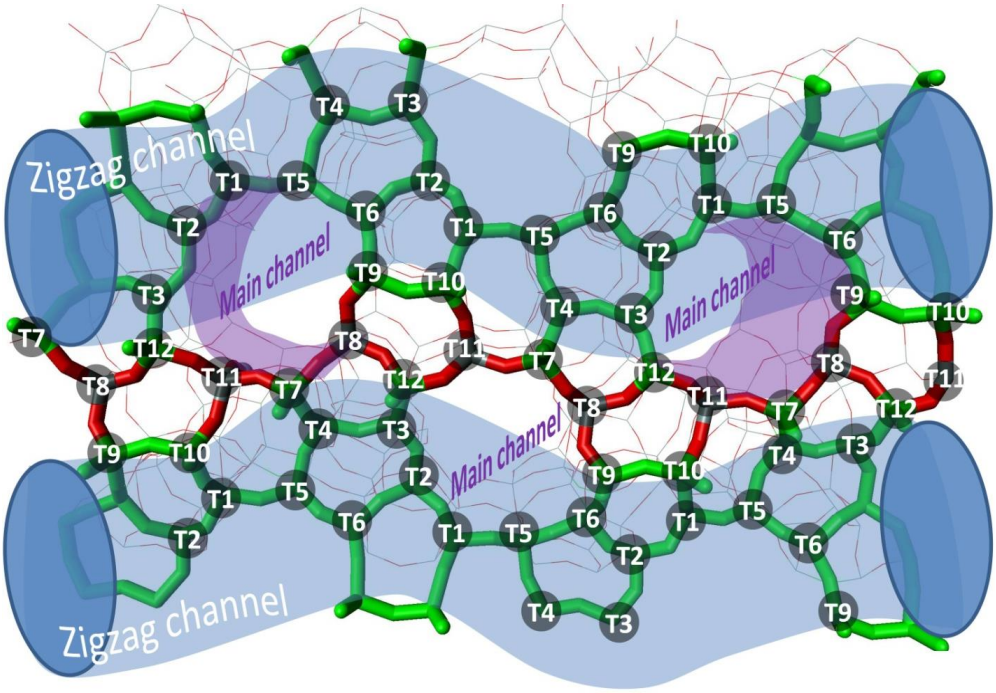

FIGURE 11. Numbering scheme and channel systems of MFI zeolite

3.4. FAU zeolite and layered FAU material

The FAU zeolite was represented by a reduced unit cell with the composition $Si_{35}Al_{13}Na_{13}O_{96}$ (Si/Al=2.69:1) and cell parameters α=β=γ=60 degree and a=b=c=17.37 Å. The structure with six different positions of extra-framework cations in faujasite is shown in Figure 12.

A periodic slab model consisting of layers of FAU zeolite was terminated with either D6R or S6R structural units (Figure 13). A vacuum of about 10 Å was introduced to avoid inter-layer interactions; resulting model ($Si_{60}O_{126}H_{11}Na$ composition) have following unit cell parameters: $a = c = 17.372$ Å, $b = 35.000$ Å, $\alpha = \beta = \gamma = 60.00°$).

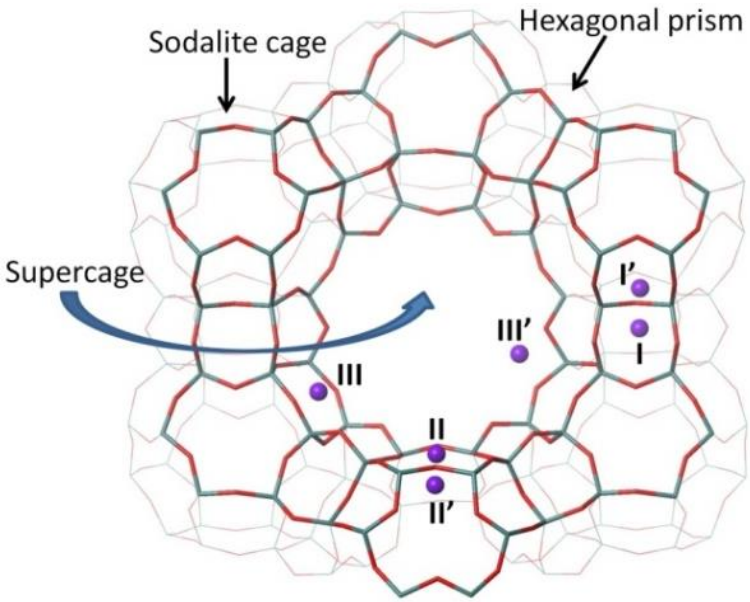

FIGURE 12. The structure of faujasite (FAU); extra framework cation sites (depicted as purple balls) sites are labeled with Roman numerals. O and Si atoms are depicted in red, and gray color, respectively.

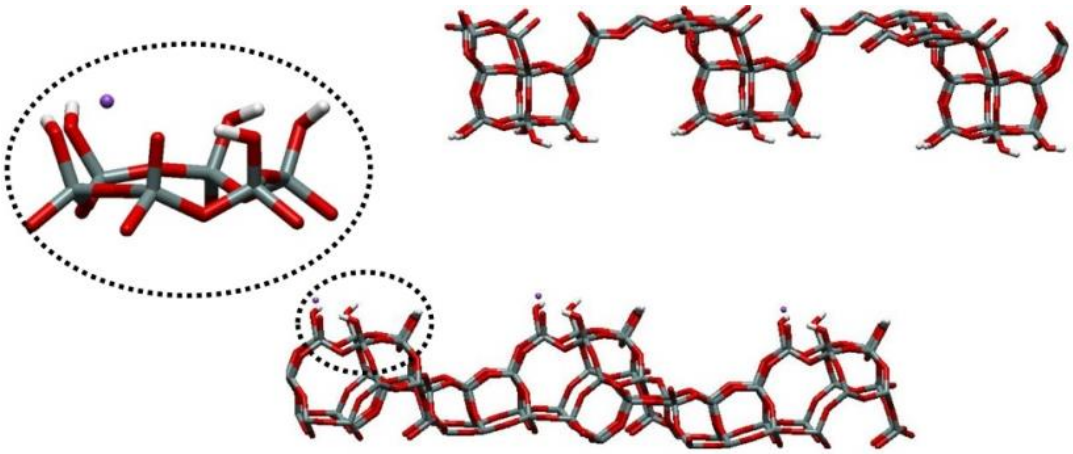

FIGURE 13. Model of a layered FAU zeolite terminated with D6R-S6R structural units exchanged with Na^+ cations. Si, O, H, and Na atoms are depicted in gray, red, white, and purple, respectively.

Chapter 4

Methods

The most of the calculations were performed at the density functional theory (DFT) level accounting for the dispersion energies using various approaches, including non-local DFT (vdW-DF2) [44, 45], DFT with empirical dispersion corrections (DFT-D2, DFT-D3) [46, 47], and DFT corrected based on the coupled cluster reference calculations (DFT/CC) [48-50].

4.1. DFT methods

Compared to the wave function based methods such as Hartree Fock (HF), Configuration Interaction (CI), Møller-Plesset PerturbationTheory up to nth order (MPn) and Coupled Cluster (CC) which are based on a many-electron wave function depending on 4N variables, DFT methods are based on electron density ρ depending on three (or six, in case of spin-polarized densities) spatial variables:

$$\rho(\vec{r}) = N \int \dots \int |\Psi(\vec{x}_1, \vec{x}_2, \dots, \vec{x}_N)|^2 \, ds_1 d\vec{x}_2 \dots d\vec{x}_N \,, \qquad (3)$$

where N is a number of electrons and Ψ is the wave function of the system containing N electrons in which each electron has spin s_i and spatial position r_i. The density functional theory is based on two theorems of Hohenberg and Kohn [51] and a computational implementation subsequently proposed by Kohn and Sham [52]. The first theorem shows that the ground-state electron properties such as wave function, energy, etc. are uniquely determined by the electron density and the second theorem shows that the electron density obeys the variational principle. The functional can be written within the Born-Oppenheimer approximation as follows:

$$E[\rho(\vec{r})] = T_{ni}[\rho(\vec{r})] + V_{ne}[\rho(\vec{r})] + V_{ee}[\rho(\vec{r})] + \Delta T[\rho(\vec{r})] + \Delta V_{ee}[\rho(\vec{r})] \,, \qquad (4)$$

where $T_{ni}[\rho(\vec{r})]$ is the kinetic energy of the non-interacting electrons, $V_{ne}[\rho(\vec{r})]$ is the nuclear-electron interaction, $V_{ee}[\rho(\vec{r})]$ is the electron-electron repulsion, $\Delta T[\rho(\vec{r})]$ is the correction to the kinetic energy deriving from the interacting nature of the electrons, and

$\Delta V_{ee}[\rho(\vec{r})]$ is the non-classical corrections to the electron-electron repulsion energy. While the first three terms in Eq.4 can be calculated exactly, the exact form of last two terms, also referred as exchange correlation functional $E_{xc}[\rho(\vec{r})]$, is not known. $E_{xc}[\rho(\vec{r})]$ contains a correction to kinetic energy deriving from interacting nature of electrons in real system and all non-classical correction of electron-electron interaction, including self-interaction correction, exchange and correlation. The accuracy of solution of Eq. 4 strongly depends on the form of a particular exchange correlation functional. The exact form of the exchange-correlation functional is not known and we have to rely just on the approximate formula. The most widely used is a local density approximation (LDA) where the functional depends only on the density:

$$E_{xc}[\rho(\vec{r})] = \int \varepsilon_{xc}[\rho(\vec{r})]\, d\vec{r} \ , \qquad (5)$$

where $\varepsilon_{xc}[\rho(\vec{r})]$ is the exchange-correlation energy per particle. However, the exchange-correlation energy per particle $\varepsilon_{xc}[\rho(\vec{r})]$ should depend on spin densities in the whole space and not only on the value at the integration point r. A simple way to improve the exchange correlation functional is to make it dependent not only on the local value of the density but also on the gradient of the density at the coordinate where the functional is evaluated leading to the generalized gradient approximation (GGA).

$$E_{xc}[\rho(\vec{r})] = \int \varepsilon_{xc}[\rho(\vec{r}), \nabla\rho(\vec{r})]\, d\vec{r}\,, \qquad (6)$$

Several approaches have been made to find expressions for the exchange correlation functional, for example Becke-Lee-Yang-Parr (B-LYP) [53, 54], Perdew-Wang (PWGGA) [55], Perdew 86 (P86) [56], Perdew-Burke-Ernzerhof (PBE) [57]. In this work, the GGA exchange-correlation functional of Perdew-Burke-Ernzerhof (PBE) [57] have been applied because it is widely used in solid state calculations and provide reliable results [36, 44, 48, 58-60].

However, neither local LDA nor semi-local GGA functionals can describe correctly non-local dispersion interactions. Therefore, the dispersion correction methods have been introduced to account in some way for dispersion interactions. Various methods currently in use for accounting dispersion interactions at the DFT level can be classified into three groups: (i) method explicitly considering interactions between electron densities at different regions – these include non-local vdW functionals (e.g., vdW-DF) [61], (ii) corrections based on atom-electron effective potentials, *e.g.*, dispersion-corrected atom-centered potentials (DCACP) or localized atomic potentials (DFT-LAP) [62], (iii) atom-

atom dispersion corrections (*e.g.*, DFT-D [63, 64] or DFT/CC [65]). The currently most popular methods are vdW DFT (vdW-DF) functionals and semiempirical atom-atom dispersion correction methods (DFT-D) and DFT/CC because they produce results in reasonably good agreement with experiment.

4.2. Non-local vdW functionals

Non-local functionals are based on explicitly interacting electron densities; therefore, this is non-empirical way to calculate the dispersion energy for arbitrary systems. In this method, the total exchange-correlation energy of a system has the following form

$$E_{xc} = E_x^{LDA/GGA} + E_c^{LDA/GGA} + E_c^{NL}\ , \qquad (7)$$

where standard exchange and correlation terms of local density approximation (LDA) and generalized gradient approximation (GGA) are calculated for short-ranged parts and E_c^{NL} represents the nonlocal term describing the dispersion energy with the form

$$E_c^{NL} = \frac{1}{2}\iint \rho\,(r)\,\Phi(r,r')\rho(r')drdr'\,. \qquad (8)$$

The different variants of vdW-DF differ in the choice of the nonlocal correlation kernel $\Phi(r,r')$ and it is based on local approximations to the dipole polarizability at frequency ω [i.e., α(r, ω)], which when integrated, yields the total polarizability α

$$\alpha(\omega) = \int \alpha(r,\omega)dr\ . \qquad (9)$$

4.3. Atom-atom dispersion corrections (DFT-D)

DFT-D type corrections are based on an atom-atom pairwise representation of (empirical) dispersion contributions with the general form

$$E_{disp}^{DFT-D} = -\sum_{AB}\sum_{n=6,8,10,\ldots} s_n \frac{C_n^{AB}}{R_{AB}^n} f_{damp}(R_{AB}), \qquad (10)$$

where the sum is over all atom pairs in the system, C_n^{AB} is the averaged (isotropic) nth-order dispersion coefficient (orders n = 6, 8, 10, . . .) for an atom pair AB, R_{AB} is internuclear distance, s_n is global scaling factors and it is used to adjust the correction to the repulsive behavior of the chosen density functional, and $f_{damp}(R_{AB})$ is damping function which is used to avoid double-counting effect of correlation at short and intermediate distances. The typical form of $f_{damp}(R_{AB})$ is

$$f_{damp}(R_{AB}) = \frac{1}{1+6(\frac{R_{AB}}{s_{r,n}R_0^{AB}})^{-\gamma}} \ , \qquad (11)$$

where R_0^{AB} is a cutoff radius for an atom pair AB, $s_{r,n}$ is global scaling factor, and γ is a global constant that determines the steepness of the functions for small R.

4.4. DFT/CC method

This method uses atom-centered pairwise corrections to account for the errors in the DFT interaction energies from the difference between the interaction energies of reference systems calculated using a high level coupled cluster method (CCSD(T)) and low level DFT

$$\Delta E = E_{CCSD(T)} - E_{DFT} \ , \qquad (12)$$

and the correction to the DFT interaction energy is expressed in terms of atom-atom correction functions

$$\Delta E = \sum_i \sum_j \varepsilon_{ij}(R_{ij}) \ , \qquad (13)$$

where R_{ij} is the distance between atoms i and j. There is no assumption about the functional form of ε_{ij}; instead the reciprocal-power reproducing kernel Hilbert space interpolation is used [50].

4.5. Calculations details

Calculations for all zeolites were carried out in parallel for 2D and 3D structures. Aluminum was placed subsequently to each of symmetry non-equivalent framework T positions (replacing Si) and a minimum energy structure of charge-compensating cations (Li^+ for Lewis acid sites and H^+ for Brønsted acid sites) was searched. For the energetically most stable Lewis and Brønsted sites found for each Al position the CO or TMPO adsorption complexes were further investigated.

For CO adsorption complexes, the CO frequencies were calculated with ω_{CO}/r_{CO} correlation methods [66]. While the CO stretching frequency calculated at the DFT level (within the harmonic approximation) cannot give the results which are comparable with experimental spectra, the ω_{CO}/r_{CO} method produces the CO frequency with very high accuracy. In this method, CO bond lengths (r_{CO}) obtained at the DFT level is correlated with the CO stretching frequencies calculated at the coupled cluster level with near

spectroscopic accuracy at different environments [29]. Based on ω_{CO}/r_{CO} scaling method, the CO stretching frequencies are computed from equation below:

$$\nu_{CO}[cm^{-1}] = ar_{CO}[\mathring{A}] + b + \Delta\nu + \Delta\omega\,, \qquad (14)$$

where a, b were obtained from a linear interpolation between CCSD(T) frequencies and DFT geometry obtained for a set of reference molecules: M^+CO, $H_2O\ldots M^+CO$, $(H_2O)_2\ldots M^+CO$, $F^{-1}\ldots M^+CO$, $(F^{-1})_2\ldots M^+CO$ (M^+ is a particular cation). $\Delta\nu$ is the anhamonicity correction and it was assumed to be equal to -29 cm^{-1} [29]; 1-T ($Al(OH)_4M^+{-}CO$) model was used for $\Delta\omega$ correction.

The same strategy described for a CO frequency was used to calculate vibrational frequencies of Brønsted OH groups before and after CO adsorption. However, the anharmonicity of the Brønsted OH is not assumed to be constant. The OH vibrational frequencies are calculated as [67]

$$\nu_{OH}[cm^{-1}] = ar_{OH}[\mathring{A}] + b + \Delta\nu\,, \qquad (15)$$

where $\Delta\nu$ = -50 cm^{-1} is correction for errors of coupled cluster method. Anharmonicity was evaluated using numerical integration for one-dimensional grid.

For TMPO adsorption complexes, The ^{31}P NMR chemical shift parameters were calculated using the gauge including atomic orbital (GIAO) [68] approach and referenced to that of physisorbed TMPO of 37 ppm. These calculations were carried out with 2T cluster model ($(OH)_3Al\text{-}OH\text{-}Si(OH)_3$) the structure of which were taken from the geometry optimized with the periodic model.

The periodic calculations were performed at DFT level using the projector augmented wave approximation (PAW) [69, 70] and the plane wave basis set with a 400 eV kinetic energy cut-off. Brillouin-zone sampling was restricted to the Γ point. Calculations were performed with the VASP program package (version 5.3.3) [71, 72]. The structure optimizations were carried out with relaxed ions and a frozen unit cell. Calculations on cluster models were performed at DFT level with cc-pVTZ basis set using the G09 program.

Chapter 5

Results and Discussion

The main advantage of 2D zeolites with respect to 3D ones is the increased accessibility of active sites. Diffusion of reactants towards the active site (and diffusion of products towards the external surface) is significantly improved and even bulkier molecules can reach active sites. Clearly, 2D zeolites can be used even for the catalysis of large reactants, *e.g.*, in biomass conversion. An important question that remains to be answered is whether the active sites in a 2D zeolite are the same as those in the corresponding 3D zeolite.

When comparing catalytic performance of 2D and 3D zeolites three major issues must be addressed: (i) Diffusion is much more facile and therefore, better catalytic performance of 2D zeolite should be observed. (ii) 2D zeolites for catalysis are obtained by pillaring; part of the active sites is unavoidably destroyed during the pillaring. Thus 2D zeolites typically contains lower concentration of active sites than 3D ones and that can result in the decrease of catalytic performance of 2D zeolites. (iii) The activity of corresponding sites (either Lewis or Brønsted) in 3D and 2D is not necessarily the same. The local environment is slightly different in 2D zeolites than in 3D ones and it can result in either increased or decreased catalytic performance. It is the goal of this theoretical investigation to shed light on the differences in activity of sites in 2D and corresponding 3D zeolites.

This section is organized as follows: first the Lewis acidity of 2D and 3D zeolite is discussed followed by the discussion of Brønsted acidity. Finally we present computational results obtained for catalytic activity of hierarchical zeolites. All calculations presented below are compared with relevant experimental data; both results from literature as well as experimental results obtained by collaborating experimental teams (in some cases unpublished yet) are used for the comparison.

5.1. Understanding the Lewis acidity in 3D and 2D zeolites

Lewis acid sites in zeolites are represented by metal cations exposed towards the void space in the zeolite channel system. These can be either defective sites of framework Al^{3+} that is not fully coordinated to the surrounding framework (not considered herein) or they are formed by extra-framework metal cations charge-compensating framework aluminum (see Section 2.2). The Lewis acidity of an extra-framework cation strongly depends on its localization inside the zeolite and its coordination with the zeolite framework oxygen atoms (coordination number, CN, is defined as number of framework oxygen atoms directly interacting with extra-framework cation). In general, the higher is CN the lower is Lewis acidity of the site. It follows that the Lewis acidity of a cation can be roughly estimated from their location and coordination. Two types of extra-framework cation sites can be distinguished in zeolites [42] and they are shown in Figure 14: (i) type I sites where the cation is placed in one of the zeolite channels on top of a ring located on the surface of the channel wall, and (ii) type II sites located at the intersection of two channels (intersection sites), where the cation is placed on the edge formed by the two intersecting channels. Cations located at channel intersection (type II) are typically coordinated to only two framework oxygen atoms and they are well exposed into the void space at the channel intersection. Cations located in the channel wall sites (type I) are placed closer to the channel surface and they interact strongly with as many framework oxygen atoms as possible. It follows that, in general, cations in intersection sites (type II) show higher Lewis acidity that is reflected in their stronger ability to bind molecules from the gas phase (a larger heat of adsorption and larger changes in vibrational dynamics of adsorbed molecules) and in improved catalytic activity. The largest differences in adsorption heat and larger frequency shifts were observed for smaller extra-framework cations such as Li^+ (see *e.g.*, Refs [73, 74]) and Mg^{2+} (see, *e.g.*, Refs [75, 76]). This is why the study presented here has been carried out for 3D and 2D zeolites in their lithium form. It is shown below that, adsorption energies and stretching frequencies of adsorbed CO probe molecule both depend on the Li-zeolite interaction (coordination) and they allow us to understand differences in Lewis acidity of 3D and 2D zeolites.

Note that the localization and coordination of extra-framework cations in zeolites cannot be, except for few special cases, determined experimentally. Since the framework

aluminum is typically randomly distributed, also the charge-balancing cations (always in the vicinity of AlO_4^- tetrahedron) are randomly distributed and cannot be determined by diffraction techniques. Information about the cation localization and coordination presented here is based on computational investigation; it is therefore critical to evaluate relevant experimental observable also computationally with high accuracy. Our investigation is based on accurate calculations of vibrational dynamics of adsorbed probe molecule (using ω/r correlation described in Section 4.5) and adsorption enthalpies. Calculated values are always compared with experimental data (IR and microcalorimetry) obtained for the same zeolite with the same Si/Al ratio.

To understand the similarities and differences between Lewis acidity in 3D and 2D materials we have investigated three sets of 3D/2D zeolites: IPC-1P based, MWW, and MFI zeolites; results for each of these systems are summarized in Subsections 5.1.1. – 5.1.4.

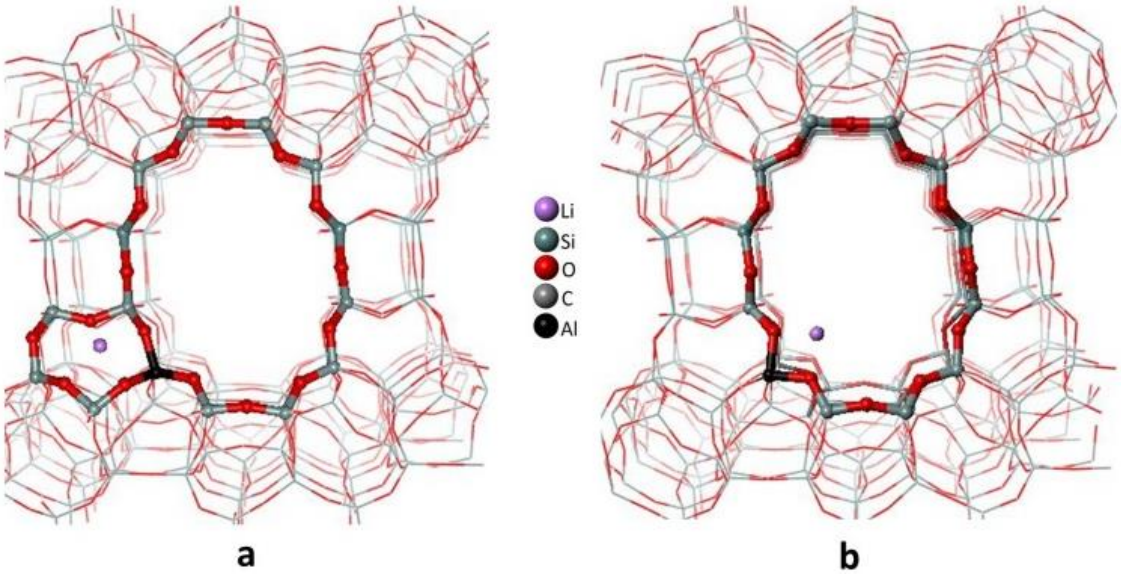

FIGURE 14. Two types of LA sites in zeolite: a) the type I site, b) the type II site.

5.1.1. 3D UTL vs. 2D IPC-1P zeolites

The results obtained for 3D Li-UTL and 2D Li-IPC-1P zeolites are reported first. Note that Figures and Tables presented in this section summarize the data not only for Li-UTL

and Li-IPC-1P but also for Li-OKO and Li-PCR zeolite; the latter results will be discussed in section 5.1.2.

All calculations on CO/Li-zeolite systems were carried out at the DFT/CC level of theory (see Section 4.4) that has been shown to give highly accurate results. Details of these calculations including accuracy assessment can be found in Ref. [77] (Attachment A). The DFT/CC method has been shown to outperform (for this particular set of systems) conventional DFT and DFT-D methods based on GGA functionals as well those based on vdW-DF non-local functionals. CO stretching frequencies were calculated with the ω/r correlation (Section 4.5).

The most stable Li^+ sites in the vicinity of Al in each nonequivalent framework T' site (note that we use the numbering scheme define in section 3.1) are reported in Table 2; both, the site type notation and distances to adjacent framework oxygen atoms are given. Comparing the most stable Li^+ cation positions in UTL and IPC-1P, it is apparent that Li^+ cation positions and coordination number (CN) are the same in both materials when framework Al atom is in T3', T4', T5', T8', T9', and T11' (Figure 9). Since these sites are clearly defined by the 2D layer and they are not affected by the inter-layer linker they will be denoted "layer sites". On the contrary, when framework Al atom is in T6', T7', T10', and T12', a site type and a coordination number change between UTL and IPC-1P. These sites will be denoted "inter-layer sites"; note that such sites are not necessarily located in the inter-layer region, however, their relative stability (and thus populations) are affected by the inter-layer linkers.

To understand the effect of 3D → 2D transition of zeolites on the Lewis acidity, the adsorption complexes with CO (weak base) were investigated for all Li^+ sites described above. Adsorption enthalpies and stretching frequencies of CO are summarized in Figure 15 and examples of adsorption complexes formed on 3D and 2D materials are given in Figure 16; only the C-down adsorption complexes were considered.

TABLE 2. The most stable Li^+ sites found for all possible Al positions in Li-IPC-1P, Li-UTL, Li-OKO, and Li-PCR; Li distances (Å) to framework oxygen atoms (O_f) smaller than 2.4 Å are reported.

Al location	Al site	r(Li^+…O_f)			
		IPC-1P	UTL	OKO	PCR
layer sites	T3’	P8bb 1.98, 2.02, 2.19	M8b 1.86, 1.97, 2.16	M8b 1.87, 2.02, 2.05	M8b 1.88, 2.10, 2.19
	T4’	I2 1.87, 1.88	I2 1.86 ,1.88	I2 1.86 1.87	I2 1.87, 1.89
	T5’	*M8b* *1.93, 1.96, 2.08*	*M8b* *1.94, 1.95, 2.08*	*M8b* *1.91, 1.94, 2.15*	*M8b* *1.92, 1.93, 2.03*
	T8’	*P8bb* *1.92, 1.95, 2.18*	*M8b* *1.91, 1.93, 2.02*	*M8b* *1.93, 1.94, 2.03*	*M8b* *1.94, 1.94, 2.10*
	T9’	*M8b* *1.94, 2.01, 2.02, 2.23*	*M8b* *1.94, 1.99, 2.07, 2.18*	*M8b* *2.00, 2.05, 2.12, 2.13*	*M6b* *1.98, 2.00, 2.12, 2.20*
	T11’	*M6b* *1.93, 1.93, 2.07*	*M6b* *1.97, 2.00, 2.21*	*M6b* *1.95, 2.01, 2.32*	*M6b* *1.97, 1.97, 2.31*
inter-layer sites	T6’	*P5* *1.90, 1.90, 2.04*	*I2* *1.86, 1.87*	*M8b* *1.89, 2.01, 2.04*	*P6* *1.94, 2.06, 2.16, 2.24*
	T7’	*M5’* *1.88, 1.91, 1.99*	*I2* *1.85, 1.88*	*I2* *1.87, 1.91*	*P6’* *1.92, 2.10, 2.17, 2.20*
	T10’	*S8b* *1.93, 2.07, 2.11, 2.11*	*P5’p* *1.90, 1.94, 1.95*	*P5’* *1.83, 2.01, 2.04*	*P6’* *1.97, 1.97, 2.24, 2.24*
	T12’	*P5* *1.92, 1.99, 2.07*	*M8b* *1.89, 1.98, 2.10*	*M8b* *1.89, 2.03, 2.09*	*P6* *1.96, 1.96, 2.16, 2.16*

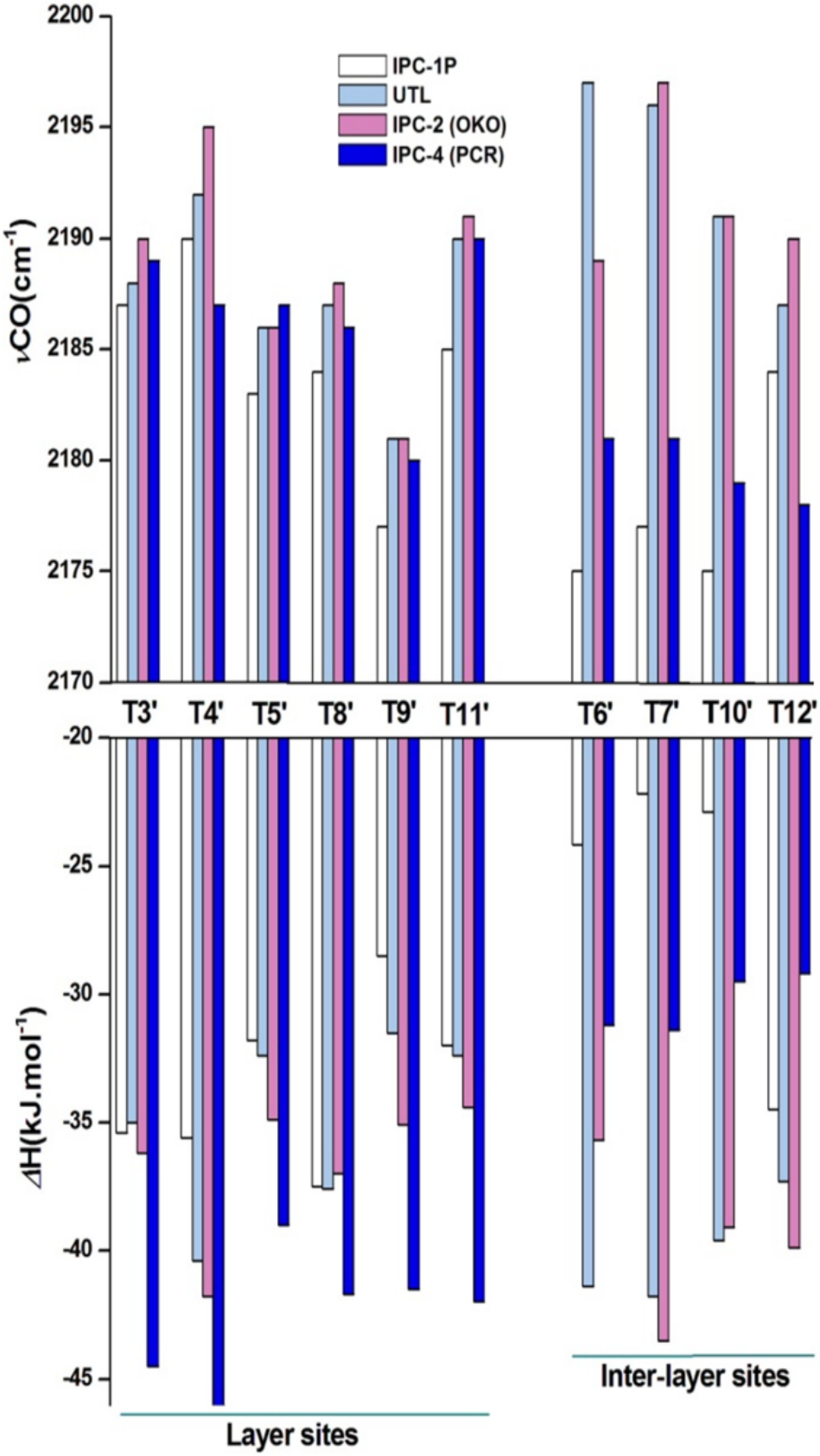

FIGURE 15. CO adsorption energies (lower part) and CO stretching frequencies (upper part) for the most stable Li^+ sites in IPC-1P, UTL, OKO and PCR.

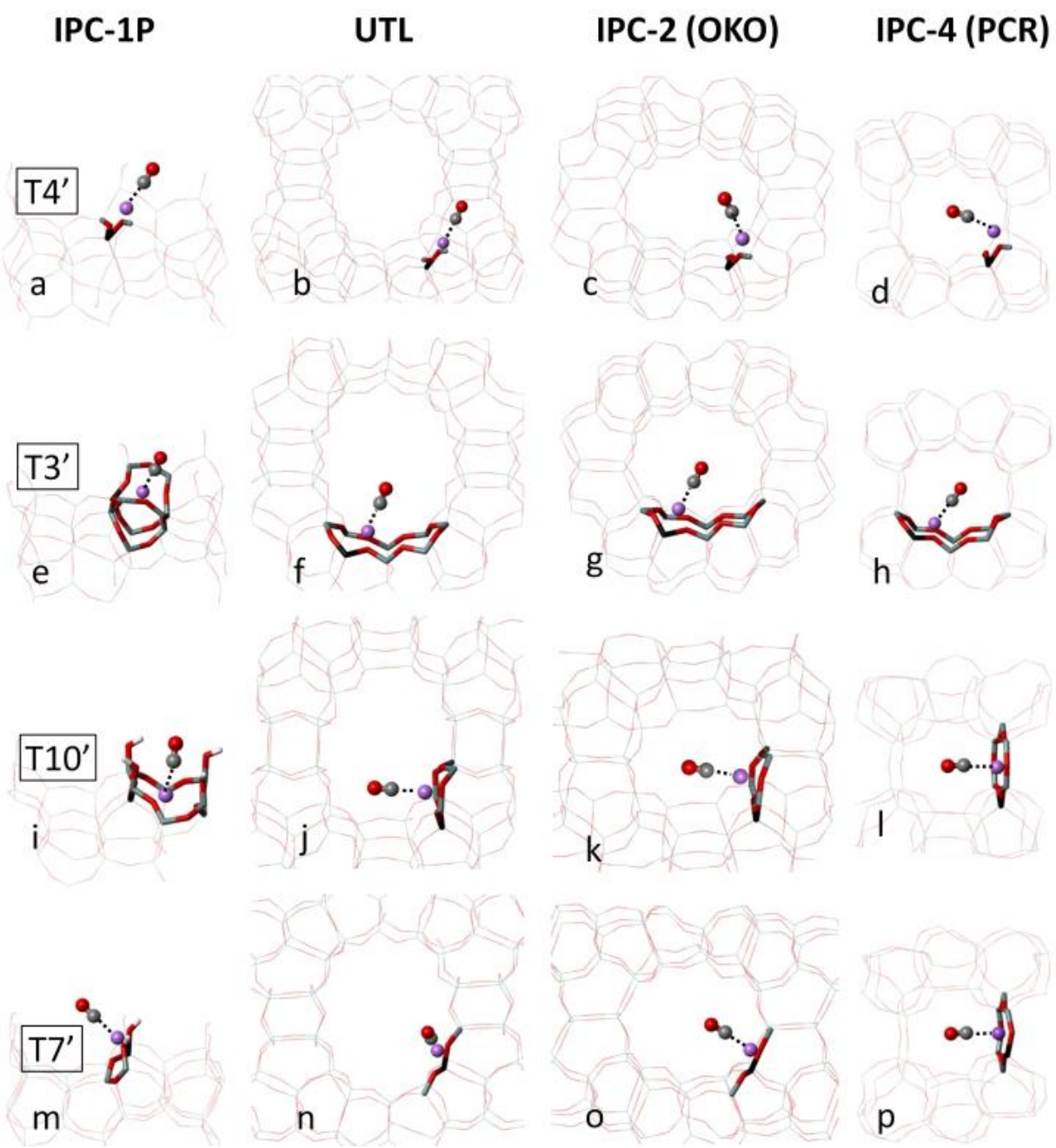

FIGURE 16. The CO adsorption complexes in the most stable position of Li cation in IPC-1P, **UTL**, **OKO** and **PCR** (from left to right); shown for Al in T4' (a-d); T3' (e-h); T10' (i-l) and T7' (m-p). The Al, O, and Si atoms are depicted in black, red and grey color, respectively while Li, C, and O atoms are depicted as purple, grey and red balls, respectively.

It is apparent that the Lewis acidity of Li^+ at inter-layer sites is strongly affected by the 3D → 2D transition as can be quantified by the shifts of CO stretching frequency and the CO adsorption enthalpy (Figure 15). Adsorption enthalpies are almost 20 kJ mol^{-1}

lower and CO stretching frequencies are about 20 cm^{-1} lower in 2D IPC-1P than in 3D UTL. The decrease is mostly due to the loss of channel intersection (channels are not present) and increased coordination of the Li^+ cation with the 2-D framework. Considering the case with Al in T'10 (Figure 16) in detail, ΔH^0 calculated for 3D and 2D systems are -38.3 and -21.8 kJ mol^{-1} (Figure 15), respectively, about 6 kJ mol^{-1} of this 16.5 kJ mol^{-1} difference is due to the smaller contribution of dispersion terms in 2D case, the remaining part must be attributed to the improved coordination of Li^+ with the framework that changes from three to four (P5' and S8b sites, respectively, Table 2). Note that even in this case, where the effect of the changed dispersion is the largest, the difference is mostly determined by the Li^+ coordination with the framework. Situation is rather different for layer sites that show small change of ΔH^0 and ν_{CO}; the difference in adsorption enthalpies does not exceed 3 kJ mol^{-1} and ν_{CO} is not changed by more than 5 cm^{-1}. Note that small changes in the adsorption enthalpy do not correlate with changes of ν_{CO}; the decreased ν_{CO} is thus attributed to the effect from the top – electrostatic interaction between adsorbed CO and the framework oxygen atoms on the opposite site of the zeolite channel (increasing the CO frequency) is missing in 2D IPC-1P.

Calculated results are in good agreement with experimental data reported in Ref. [78] (Attachment B); experimental data will be discussed in Section 5.1.2. together with the results obtained for other zeolites of IPC-1P family. It should be stressed that computational results were confirmed by the experimental investigation and they show that the Lewis acidity of 2D IPC-1P decreases compared to parent 3D UTL zeolite. This decrease is mostly due to the fact that intersection Li^+ sites present in UTL do not exist in IPC-1P; intersection sites (type II) show higher Lewis acidity than channel wall sites (type I). In addition, the presence of surface silanols on IPC-1P results in improved cation coordination with framework oxygen atoms, therefore, even the Lewis acidity of Li^+ at channel wall sites is slightly lower in IPC-1P than in parent UTL zeolite.

5.1.2. 3D and 2D zeolites derived from IPC-1P – effect of zeolite pore size on Lewis acidity

The zeolites of IPC-1P family (see section 2.1.1) – IPC-1PI, **UTL**, **OKO**, and **PCR** – constitute a unique set of adsorbents with the same dense 2D layers separated by different interlayer distances defined by different interlayer linkers. They may give us new insight

on how the pore diameter affects the coordination of extra-framework cations and how that affects their Lewis acid strength. The structures of all four materials discussed here consist of identical 2D dense layers that are interconnected differently into 3D materials (Figure. 3): (i) IPC-1PI pillared material contains 2D IPC-1P layers (containing framework Al and thus extra-framework cations); the void space above the adsorption site is large compared to the size of the adsorbate and adsorption on Li-IPC-1PI can be viewed as an adsorption on thin 2D IPC-1P layer. (ii) IPC-1P layers in **UTL** are connected by D4R units, forming relatively large 14R and 12R interconnected channels. (iii) Connection of IPC-1P layers with S4R, zeolite **OKO**, results in 12R x 10R channel system. (iv) Direct condensation of IPC-1P layers (linked simply by oxygen atoms) gives **PCR** zeolite with 10R x 8R channels. While these four materials differ in the pore size (decreasing in the order IPC-1PI > **UTL** > **OKO** > **PCR**) they have very similar topology – *layer sites* defined above (Al in T3', T4', T5', T8', T9', T11') are not much effected by the inter-layer linking and they are expected to be very similar in all four systems. On the contrary, *inter-layer sites* (T6' and T7' – adjacent T-atoms to inter-layer linker; T10' and T12' – bridging T6' and T7' T-sites) depends on the way how IPC-1P layers are linked together and they are expected to have different properties. Note that this section is not explicitly devoted to the investigation of the differences between 3D and 2D zeolites but the results are interesting and relevant enough to describe them here. We will return to 3D *vs.* 2D problem in next section.

Calculated results for all four zeolites are summarized in Table 2 (Li^+ coordination), Figure 16 (examples of adsorption complexes) and Figure 15 (CO adsorption enthalpies and frequencies) in previous section. More details can be found in Ref. [78] (Attachment B). Computational work has been carried out in close collaboration with experimental investigation carried out by other research groups. Experimental IR spectra in the CO stretching region are presented in Figure 17 and experimental adsorption heats are shown in Figure 18. An excellent agreement between experimental and theoretical data is apparent. Simulated IR spectra presented as insets in Figure 17 show not only perfect match of band maxima but also the band shapes and their dependence on surface coverage agrees remarkably with experimental data. Calculated adsorption heats (Table 2 in Ref. [78]) also agree very well with the data from microcalorimetry Figure 18.

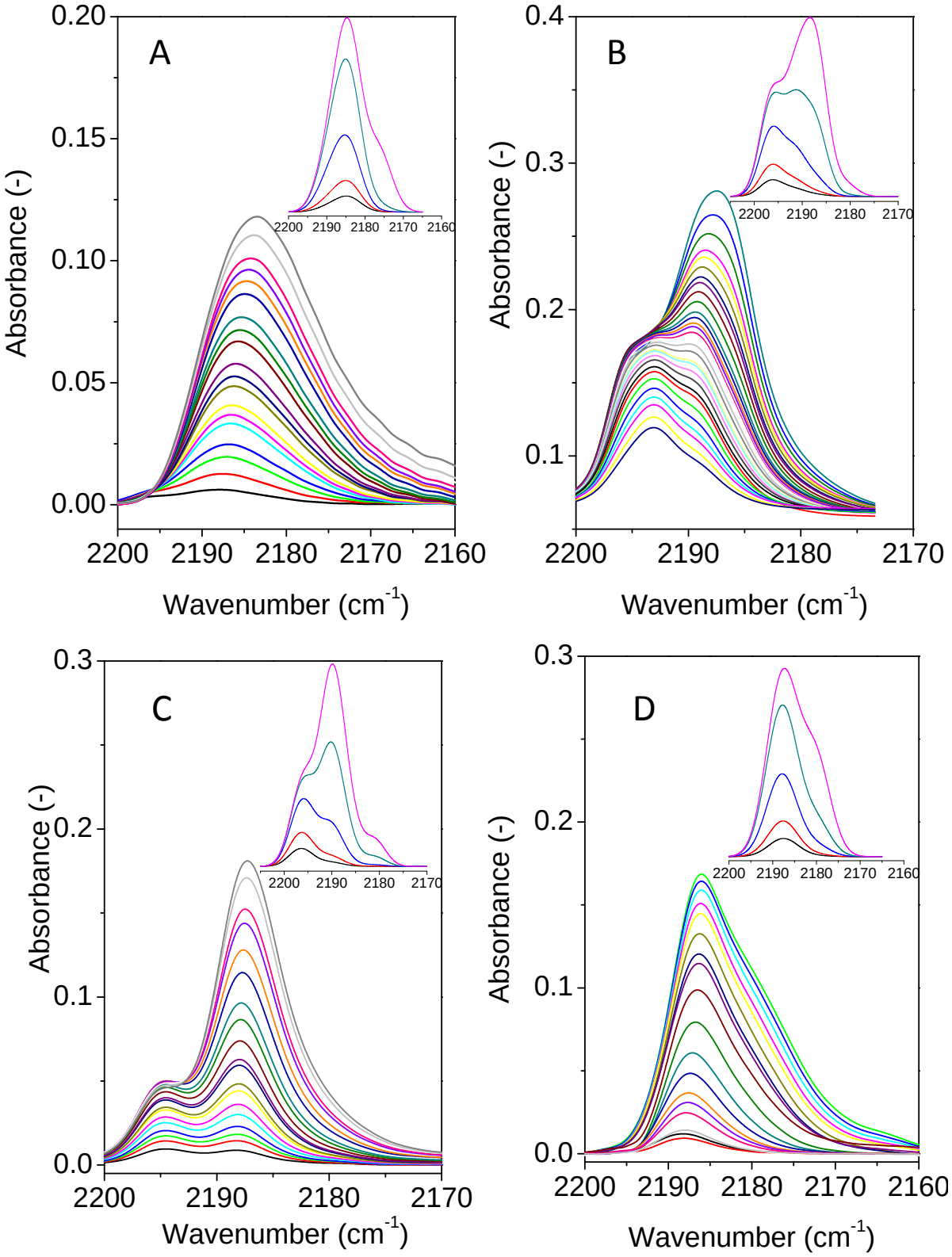

FIGURE 17. FTIR spectra of CO adsorbed at liquid nitrogen temperature on Li-IPC-1P (a), Li-UTL (b), Li-OKO (c), and Li-PCR (d). The intensity of spectra obtained upon CO adsorption decreases with evacuation. Insets in individual panels show theoretical spectra at corresponding Li-zeolites calculated for 0.75, 0.50, 0.25, 0.10, and 0.05 coverages (CO:Li ratio) in cyan, green, blue, red, and black, respectively.

A good agreement between experimental and theoretical results entitles us to draw following conclusions:

(i) The highest Lewis acid strength has been found for Li^+ cation coordinated to only two framework oxygen atoms at the intersection of two channels where Li^+ cation is located at the void space of the intersection. Such sites can only exist on the intersection of channels of the sizes larger than 8R – they only exist in Li-UTL and Li-OKO (having 14Rx12R and 12Rx10R channel systems, respectively). Intersection sites do not exist in Li-PCR (intersection of 10R and 8R channels) and they cannot exist in IPC-1PI. Thus, Li-UTL and Li-OKO have the strongest Lewis acid sites.

(ii) Evaluation of Lewis acid strength based on adsorption heats could be misleading; apart from (mostly electrostatic) interaction with the extra-framework cation there is a significant contribution from dispersion interactions between adsorbate and zeolite framework. Due to a good "fit" of CO into the 10Rx8R channel system of Li-PCR the dispersion component for this system is significantly larger than for other investigated zeolites and the largest adsorption heats were measured (and calculated) for Li-PCR, despite the fact that there are no sites with large Lewis acid strength at the channel intersection.

(iii) A detail analysis of Li^+ sites defined by 2D dense layers shows that Lewis acid strength depends on the channel dimension: Li^+ cations in smaller channels show slightly larger Lewis acid strength.

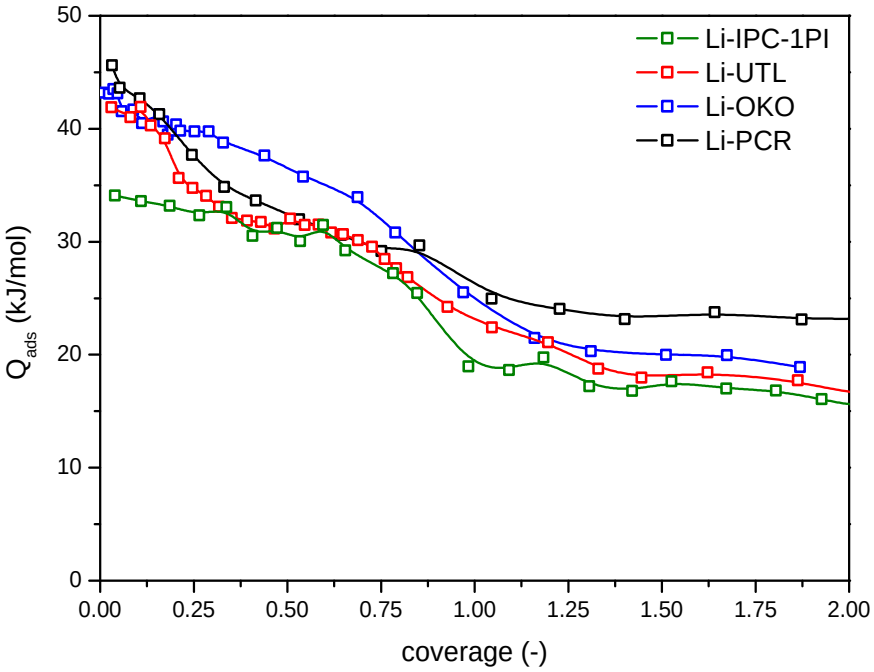

FIGURE 18. Adsorption heats of CO on Li-zeolites and Li-IPC-1PI measured by microcalorimetry at -100°C as a function of coverage.

5.1.3. 3D *vs.* 2D zeolites with MWW topology

Compared to IPC-1P the thickness of MCM-22P layer is larger than the thickness of IPC-1P layer (25 Å and 10 Å, respectively) but the silanol desity is lower in MCM-22P than in IPC-1P (90 $Å^2$ per silanol and 43 $Å^2$ per silanol, respectively). These differences result in a higher flexibility of the IPC-1P layer than the MCM-22P layer. Higher density of surface silanols also lead to large number of possible inter layer arrangements; while there are eight arrangements between IPC-1P layers [79], three are only three arrangements between MCM-22P layers [80] (Attachment C). It is therefore important to understand the effect of layer thickness and surface silanol density on the character of active sites. The Lewis acid properties of Li^+ sites in 3D and 2D materials are discussed herein.

The most stable Li^+ sites in the vicinity of Al in each nonequivalent framework T site are reported in Table 3 including the site type notation and distances to adjacent framework oxygen atoms. Al in T7 is not considered since Al is located in a small cage which is inaccessible for probe molecule.

As can be seen from Table 3 the Li^+ sites and coordination numbers are the same in MCM-22 and MCM-22P, except for the case of Al in T6, where the Li^+ cation is located

in 10-membered ring in MCM-22 but this site does not exist in the MCM-22P; it become intersection site (type II) and coordination number changes from three in MCM-22 to two in MCM-22P (Figure 19 e, f). In both materials Li^+ cation is preferentially located in type I sites. There are only two cases where Li^+ cation is localized in type II site (Al in T1 and T4).

TABLE 3. The Li^+ cation sites and Li-O_f distances (in Å) of the most stable Li^+ sites in the vicinity of Al in seven different framework positions found for MCM-22 and MCM-22P zeolites.

Al position	**MCM-22**		**MCM-22P**	
	Li^+ site[a]	r(Li..O_f)	Li^+ site	r(Li..O_f)
T1	I2	*1.870, 1.871*	I2	*1.869, 1.870*
T2	Sup6	*1.951, 1978, 2.030, 2.303*	Sup6	*1.948, 1.969, 2.041, 2.327*
T3	Bsup6	*1.973, 1.976, 2.210, 2.226*	Bsup6	*1.976, 1.983, 2.244, 2.252*
T4	I2	*1.860, 1.861*	I2	*1.850, 1.852*
T5	Sup6	*1.969, 2.024, 2.114, 2142*	Sup6	*1.976, 2.003,2.125, 2.184*
T6	Cros10	*1.859, 2.031,2.044*	I2	*1.817, 1.843*
T8	Sin5	*1.897, 1.905, 2.029*	Sin5	*1.892, 1.914, 2.044*

[a] Notation of Li^+ sites is shown in Figure 10.

Adsorption of CO was investigated for both 3D and 2D zeolites; adsorption enthalpy and CO stretching frequencies are reported in Table 4 and examples of CO adsorption complexes formed on MCM-22 and MCM-22P are illustrated in Figure 19. Similar to 3D and 2D-UTL systems, only C-down adsorption complexes were considered and CO adsorption energies were calculated at the DFT/CC level (see section 5.1.1).

It is obvious that the CO stretching frequencies are in the same range (2178-2195 cm^{-1}) in both MCM-22 and MCM-22P and also adsorption enthalpies are very similar (in the range from -26 kJ mol^{-1} to -42 kJ mol^{-1}) in both materials. The observed differences of adsorption enthalpies and CO stretching frequencies between particular sites in MCM-22 and MCM-22P do not exceed 2 kJ mol^{-1} and 4 cm^{-1}, respectively. Adsorption

complexes formed in both MCM-22 and MCM-22P zeolite can be classified into two groups: (i) The highest CO frequencies in the range of 2192-2195 cm^{-1} and the highest adsorption enthalpies (from -39.5 to -42.4 kJ mol^{-1}) are observed for complexes formed on Li^+ cations in intersection sites (type II); this corresponds to Al in T1 and T4 (Figure 19 a and b). (ii) The lower CO frequencies (2178-2188 cm^{-1}) associated with the lower adsorption enthalpies (from -26 to -39 kJ mol^{-1}) are observed for CO adsorption on Li^+ cations located in the channel wall sides; this corresponds to framework Al at T2, T3, T5, and T8 (Figure 19).

TABLE 4. Characteristics of CO adsorption complexes formed on the most stable Li^+ sites (the number in parentheses is the coordination numbers of Li^+ cation with framework oxygen) in MCM-22 and MCM-22P. CO frequencies are in cm^{-1}, and adsorption enthalpies are in kJ mol^{-1}.

Al position	**MCM-22**			**MCM-22P**		
	Li^+ site[a]	ν_{CO}	$\Delta H^0(0K)$	Li^+ site	ν_{CO}	$\Delta H^0(0K)$
T1	I2(2)	2195	-42.4	I2(2)	2194	-40.3
T2	Sup6(4)	2178	-26.8	Sup6(4)	2178	-26.9
T3	Bsup6(4)	2181	-31.1	Bsup6(4)	2180	-26.7
T4	I2(2)	2195	-39.5	I2(2)	2192	-38.3
T5	Sup6(4)	2180	-26.4	Sup6(4)	2179	-26.1
T6	Cros10(3)	2188	-36.1	I2(3)	2192	-34.6
T8	Sin5(3)	2186	-39.7	Sin5(3)	2186	-39.3

[a] Notation of Li^+ sites are shown in Figure 6.

The theoretical results are in excellent agreement with experimental IR spectra [81] presented in Figure 20. Peaks at 2195 and 2185 cm^{-1} are evident for both 2D and 3D materials. It can be safely concluded that the Lewis acidity of Li^+ cations is not affected by transformation from 3D MCM-22 to 2D MCM-22P; both the site types and coordination numbers are completely preserved.

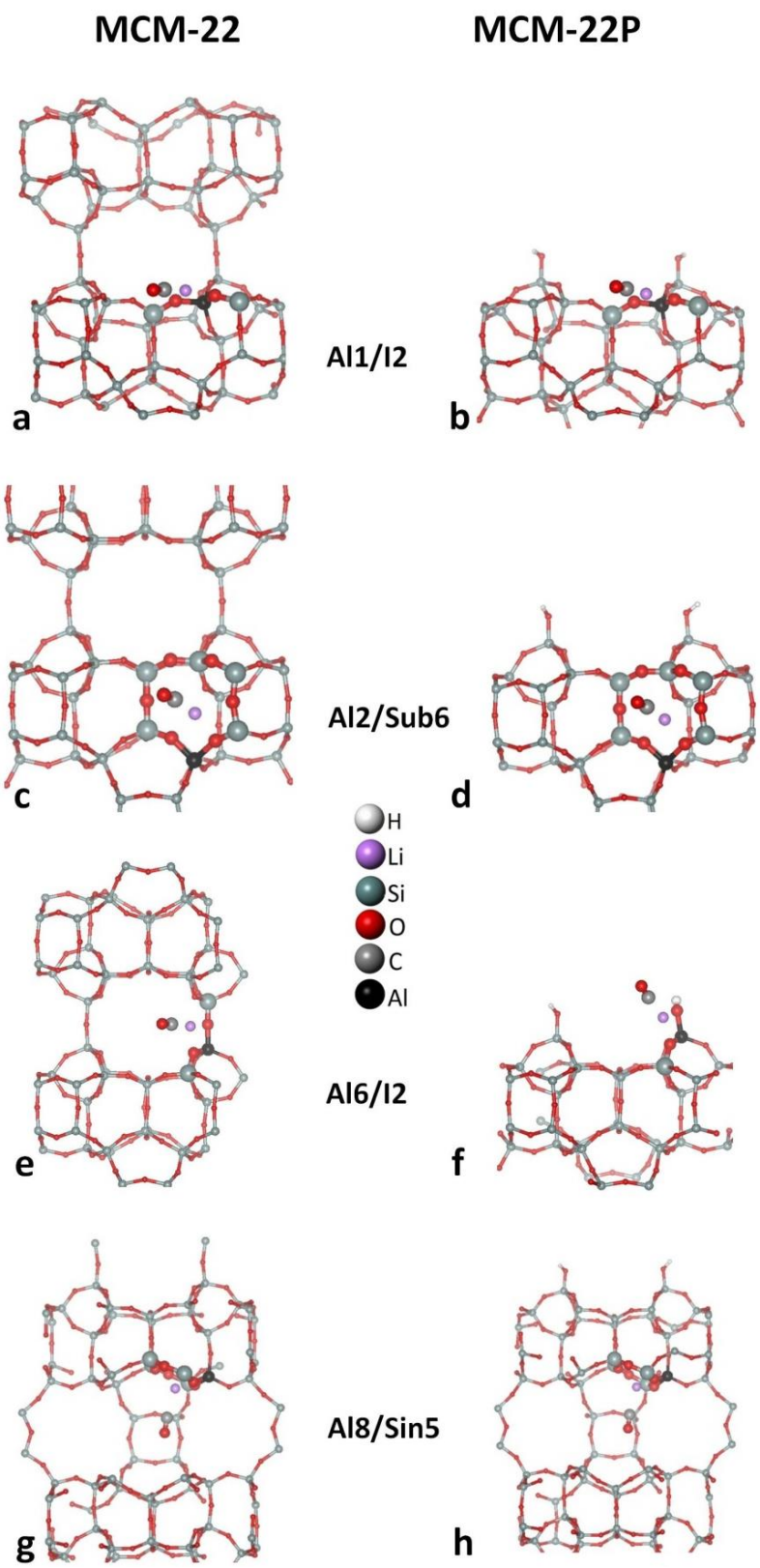

FIGURE 19. CO adsorption complexes of MCM-22 (left column) and MCM-22P (right column), shown for Al in T1 (a,b), T2 (c,d), T6 (e,f) and T8 (g,h).

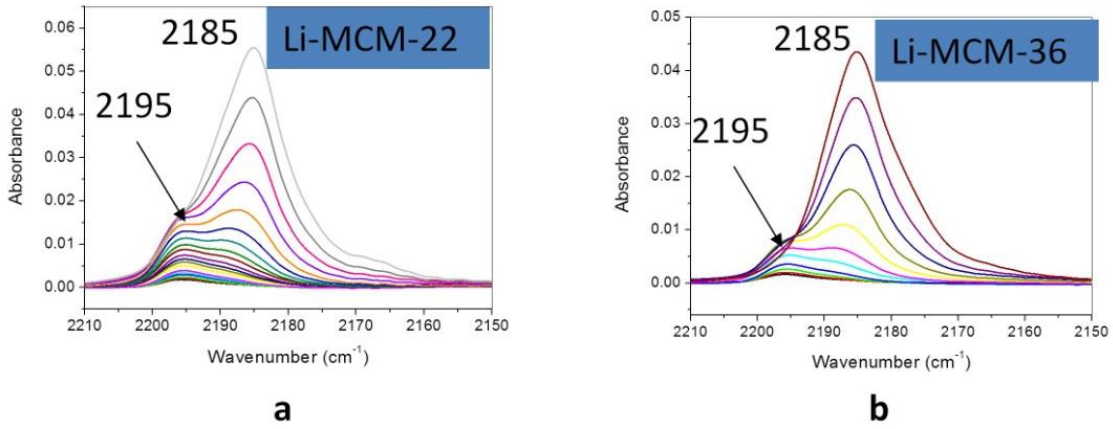

FIGURE 20. The IR spectra of CO adsorption complexes in Li-MCM-22 (a) and Li-MCM-36 (b), adapted from Ref. [81].

5.1.4. 3D *vs.* 2D zeolites with MFI topology

Following the strategy used in previous subsections, the Lewis acidity of Li^+ cations in 3D and 2D ZSM-5 zeolites was investigated. The most stable Li^+ sites in the vicinity of Al in each of 12 different framework T sites of 3D- and 2D-ZSM-5 are reported in Table 5. Li^+ cations are preferably located in type I sites in both materials. Location of Li^+ is changed upon the 3D → 2D transition in many cases, however, coordination numbers are always 3 or 4. Therefore, it is expected that the Lewis acidity of Li^+ sites will be similar in both materials.

The characteristics of CO adsorption complexes for 12 different framework T sites of 3D and 2D ZSM-5 are summarized in Table 6. It is shown that the adsorption enthalpies and CO stretching frequencies are on average higher in 3D ZSM-5 than those in 2D ZSM-5. This is mostly due to the contribution from the effect from the top which is higher in 3D-ZSM-5. The examples of CO adsorption complexes formed on 3D and 2D ZSM-5 are shown in Figure 21 for Al in T4 (Figure 21 a, b) and T9 (Figure 21 c, d). The largest difference in adsorption enthalpy can be observed for Al in T10 and T12 and it results from the change of cation location and change of its coordination. The largest change of adsorption enthalpy is found for Al in T10 (-36 and -22 kJ mol^{-1} for 3D and 2D ZSM-5, respectively); this large difference is due to improved coordination of Li^+ in S6 site and also due to partial loss of dispersion interaction in less dense 2D material. Rather unusual increase of adsorption enthalpy upon the 3D → 2D transformation is observed for Al in T12 (-34 and -45 kJ mol^{-1} in 3D and 2D ZSM-5). This difference is due to

almost 18 kJ mol^{-1} increase of electrostatic interaction in 2D ZSM-5 compared to 3D ZSM-5; this increase is partially cancelled by decreased dispersion interaction. However, the general conclusions can be drawn that the Lewis acidity of Li^+ are on average only slightly decreased due to the transformation from 3D ZSM-5 to 2D ZSM-5.

TABLE 5. The Li^+ cation sites and Li-O_f distances (in Å) of the most stable Li^+ sites in the vicinity of Al in all distinguishable framework positions of 3D and 2D ZSM-5 zeolites.

Al position	**3D-ZSM-5**		**2D-ZSM-5**	
	Li^+ site	r(Li..O_f)	Li^+ site	r(Li..O_f)
T1	M6	1.970, 1.997, 2.146	M6	1.995 2.107 2.185
T2	M6	1.934, 1.950, 2.075	M5	1.912 1.987 2.028
T3	M5	1.907, 1.909, 2.010	M5	1.898 1.926 1.961
T4	Z8	1.901, 1.947, 2.065	S6	1.915 1.954 2.135 2.267
T5	Z10	1.886, 2.005, 2.139	Z10	1.875 1.977 2.075
T6	Z5	1.887, 1.929, 2.040	M5	1.927 1.948 1.971
T7	Z8	1.959, 1.960, 2.212	M4[a]	1.859 1.954 1.993
T8	M6	1.944, 1.992, 2.137, 2.256	S5	1.890 1.995 2.061 2.235
T9	M6	1.893, 2.026, 2.082	I2[a]	1.849 1.994 2.113
T10	Z10	1.914, 2.070, 2.137, 2.163	S6[a]	1.950 1.966 2.106 2.157
T11	M6	1.957, 1.970, 2.186, 2.259	M5	1.900 1.924 1.970
T12	M5	2.023,2.042, 2.063, 20.89	S4[a]	1.856 1.947 1.974

[a] AlOH

TABLE 6. Characteristics of CO adsorption complexes formed on the most stable Li^+ sites (the number in parentheses are CN) in 3D ZSM-5 and 2D ZSM-5. CO frequencies are in cm^{-1}, and adsorption enthalpies are in kJ mol^{-1}.

Al position	**3D-ZSM-5**			**2D-ZSM-5**		
	Li^+ site	ν_{CO}	$\Delta H^0(0K)$	Li^+ site	ν_{CO}	$\Delta H^0(0K)$
T1	M6(3)	2187	-38.51	M6(3)	2183	-34.31
T2	M6(3)	2188	-41.19	M5(3)	2190	-44.07
T3	M5(3)	2189	-41.65	M5(3)	2188	-40.96
T4	Z8(3)	2184	-39.23	S6(4)	2180	-30.61
T5	Z10(3)	2185	-39.56	Z10(3)	2183	-31.67
T6	Z5(3)	2189	-40.23	M5(3)	2188	-41.11
T7	Z8(3)	2189	-40.91	M4(3)	2180	-32.98
T8	M6(4)	2184	-33.58	S5(4)	2181	-33.62
T9	M6(3)	2188	-37.27	I2(3)	2183	-33.88
T10	Z10(4)	2178	-36.23	S6(4)	2176	-21.59
T11	M6(4)	2186	-35.79	M5(3)	2188	-41.46
T12	M5(4)	2188	-34.15	S4(3)	2180	-45.38

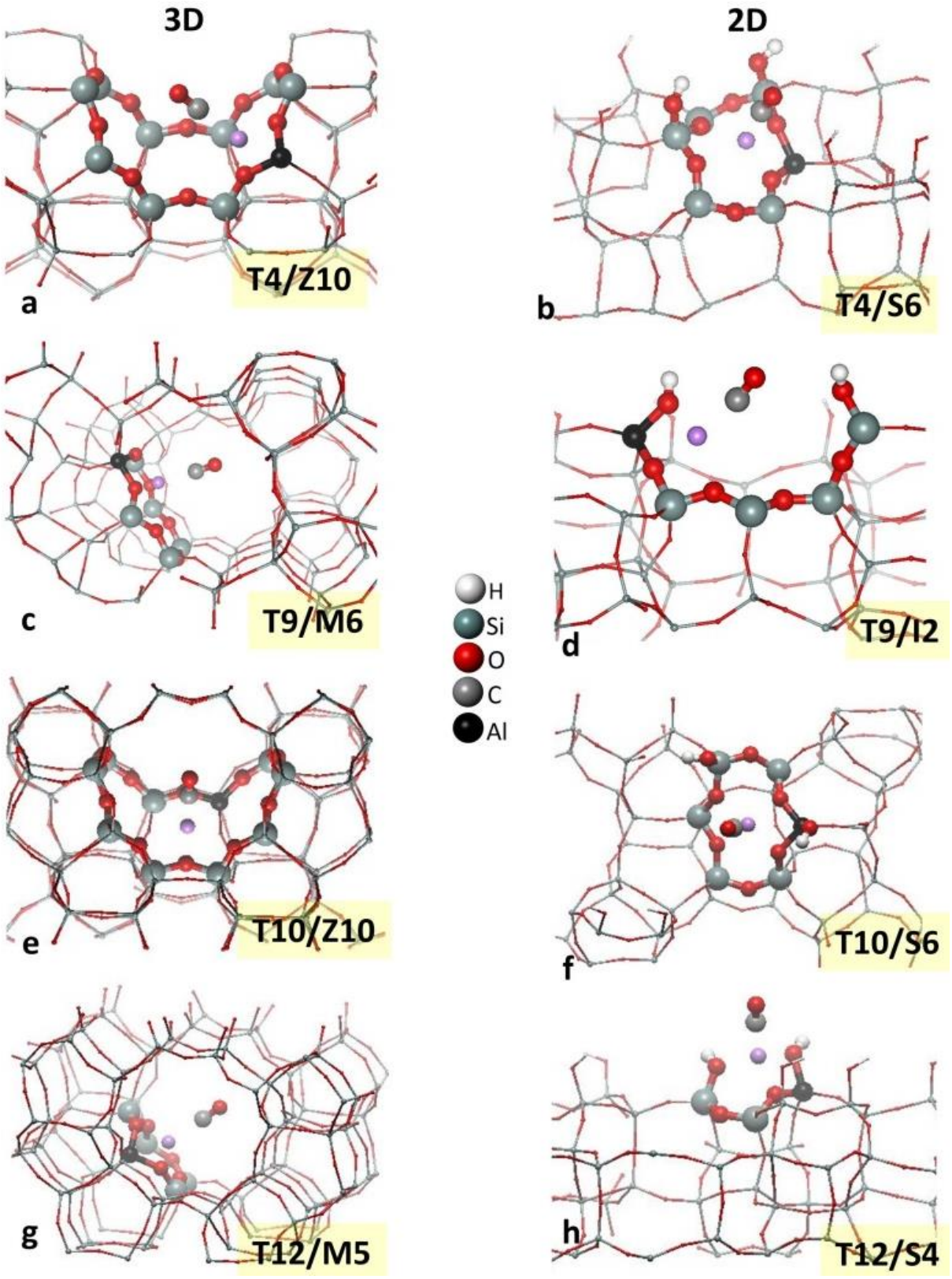

FIGURE 21. CO adsorption complexes of 3D-ZSM-5 (left column) and 2D-ZSM-5 (right column), shown for Al in T4 (a,b), T9 (c,d), T10 (e,f) and T12 (g,h).

5.2. Understanding the Brønsted acidity in 3D and 2D zeolites

The research described in this Section is aimed at understanding the difference between the Brønsted acidity of 3D and 2D zeolites. Compared to alkali-metal exchanged zeolites, that find application mostly based on adsorption properties, the acid zeolites (H-zeolites) are the most important industrial catalysts. The same main factors reported in Section 5.1. must be taken into consideration for evaluation of the catalytic performance of 2D zeolites with respect to corresponding 3D zeolites: (i) increased mobility, (ii) decreased concentration of Brønsted sites, and (iii) a possible change of Brønsted acidity due to the 3D → 2D transition. The latter problem is difficult to be addressed experimentally due to the strong coupling of all three factors described above. Therefore, we have carried out a detail computational investigation of three systems – IPC-1P family zeolites, MWW zeolites, and MFI zeolites – considering always both 3D and 2D forms.

In case of H-zeolite the charge compensating proton is always strongly bound to just a single framework oxygen atom adjacent to the framework aluminum. Two situations can be found in zeolites: (i) H^+ points towards the void space in the channel system (Figure 22 a); these Brønsted sites are characterized by OH stretching frequencies (ν_{OH}) in the range of 3590-3640 cm^{-1}. (ii) H^+ points towards another framework oxygen atom forming thus an intra-zeolite H-bond (Figure 22 b); this situation typically occur in 5- or 6-rings located on the surface of the channel wall. These sites are characterized by a lower ν_{OH}, in the range of 3260- 3515 cm^{-1}.

The IR spectroscopy is the most popular experimental tool for the characterization of the Brønsted acidity in zeolites. The strength of acid sites is often correlated with the OH stretching frequencies υ_{OH}, the shift of these frequencies $\Delta\nu_{OH}$ upon the adsorption of probe molecule or changes in the probe molecule (CO is again the most suitable one) vibrational frequencies ν_{CO} upon adsorption. Also adsorption enthalpy ΔH of suitable probe molecule (CO) can be used for acidity characterization. It has been shown that the larger is $\Delta\nu_{OH}$, ν_{CO}, and ΔH the larger is Brønsted acid site strength. However, it has to be stressed that there are many exception to this simple rule and full understanding of acidity based only on experimental characterization is often impossible. This is why we have carried out this extensive computational investigation of Brønsted acidity of 3D and 2D zeolites presented in this Section.

The CO molecules preferentially form a linear O-H…C-O arrangement in adsorption complexes on Brønsted acid sites. In general, three types of CO adsorption complexes can be distinguished, depending on the localization of the BA site: (i) linear OH…CO complexes with isolated BA sites show the highest $\Delta\nu_{OH}$, ν_{CO}, and ΔH. (ii) Adsorption complexes where CO cannot form the linear adduct with OH due to the smaller pore size of the channel system; smaller values of $\Delta\nu_{OH}$, ν_{CO}, and ΔH can be expected. (iii) For the Brønsted sites with intra-zeolite H-bonding the proton has to move away from channel wall site into the void space to bind efficiently with CO; that results in the lowest $\Delta\nu_{OH}$, ν_{CO}, and ΔH.

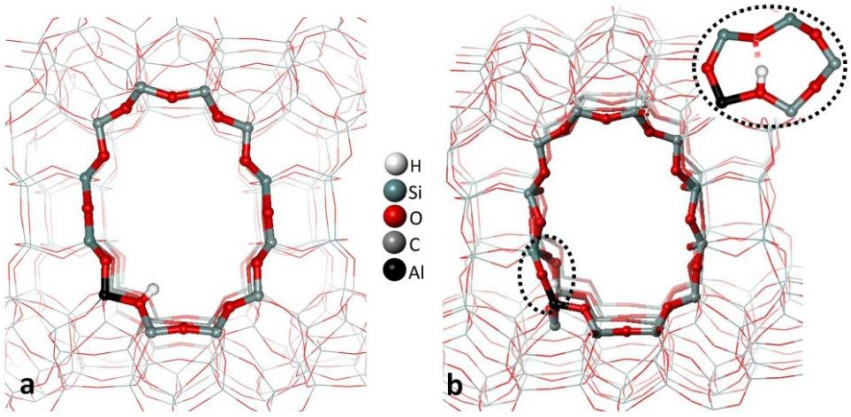

FIGURE 22. Two types of BA sites in zeolite: a) the type of isolated BA site, b) the type of H-bonding BA site

5.2.1. 3D and 2D zeolites derived from IPC-1P – effect of zeolite pore size on Brønsted acidity.

The zeolites of IPC-1P family consist of the same 2D layers of IPC-1P with different interlayer connectivity (Section 5.1.2) and different pore sizes. Therefore, the investigation in this part aims at understanding not only the effect of 3D → 2D transformation but also the effect of the pore size on the BA properties.

The BA properties of these zeolites were investigated for each of 10 different framework T' site (see Table 2 for detail of T' notation); BA sites defined by the 2D layers (Al in T3', T4', T5', T8', T9' and T11') are denoted "*layer sites*" and BA sites affected by the interlayer linker (Al in T6', T7', T10' and T12') are denoted "*inter-layer sites*" . The most stable BA sites in the vicinity of each framework Al site were first

characterized by the OH frequency, ν_{OH}, (Figure 23) followed by the evaluation of characteristics related to the CO adsorption: the shift of OH frequency (Figure 24), the shift of CO stretching frequency and CO adsorption enthalpies (Figure 25). Examples of CO adsorption complexes are given in Figure 26. Our computational results are confirmed by experimental data obtained in collaboration with experimental groups (Figure 27).

The OH frequency of bare BA sites can be grouped into two frequency ranges: (i) The high frequency range (3590-3640 cm^{-1}) is characteristic for isolated BA sites (those not involved in intra-zeolite H-bonding); this is found for majority of BA sites in all four zeolites. (ii) The low frequency range (3326-3513 cm^{-1}) is characteristic for BA sites where proton is involved in intra-zeolite H-bonding; such sites exist in all four zeolites but only in few cases with Al at inter-layer position and only in one case (Al in T8' of UTL) for layer site. Only small differences in ν_{OH} between individual BA sites and the existence of BA sites involved in H-bonding makes the analysis of Brønsted acidity based on ν_{OH} of bare BA sites difficult or even impossible as has been also demonstrated for other zeolites [58].

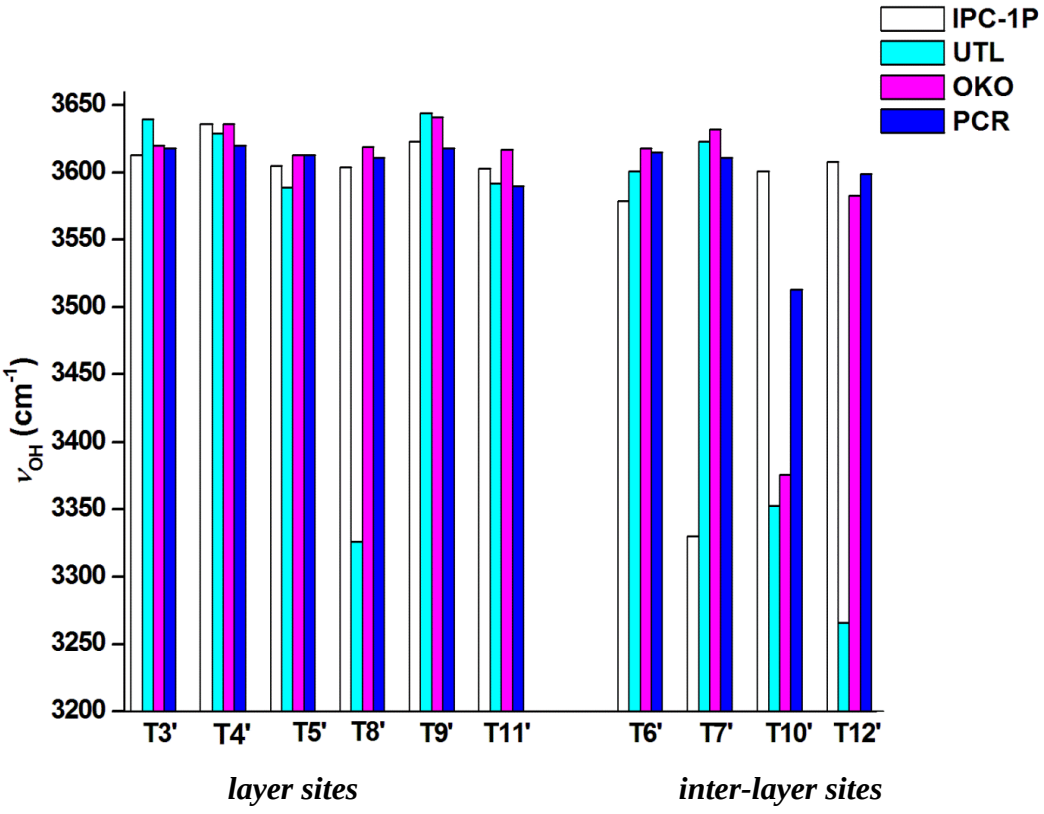

FIGURE 23. OH frequency of bare BA sites for 10 distinguishable framework Al position in IPC-1P, UTL, OKO and PCR

To further investigate the BA properties, the CO adsorption complexes were evaluated at the most stable BA sites. Figure 24 shows that the shift of OH frequencies upon the CO adsorption in zeolites of IPC-1P family is about 300-350 cm^{-1} (note that we do not consider BA sites where proton is involved in intra-zeolite H-bonding). This observation is in good agreement with previous studies for other zeolites [44, 82]. The shifts of OH stretching frequency gradually increases from IPC-1P to UTL to OKO (decreasing pore size) but this trend is not followed in cases of PCR. The CO stretching frequencies exhibit the same trend (upper part in Figure 25) – frequencies increase with decreasing pore size from IPC-1P to OKO and the trend is not followed in case of PCR. A similar trend can be observed for CO interaction energies but only for inter-layer sites: -*E* increases with decreasing channel sizes from IPC-1P to OKO and PCR is off this correlation. Situation is different for CO interaction energies on layer sites where -*E* increases in order IPC-1P < UTL < OKO < PCR. This nice correlation between interaction strength and channel size is due to increasing dispersion interactions with decreasing channel size (and corresponding increase of material density). Dispersion interactions between CO and zeolite framework are about -12 kJ mol^{-1} in case of PCR and they are below -9 kJ mol^{-1} for other zeolites.

Considering the cases of Al in T4' as an example of layer site (Figures 26a-26d), the adsorption enthalpies rise in a series of four zeolites, from IPC-1P (-27 kJ mol^{-1}) to UTL (-31 kJ mol^{-1}) to OKO (-32 kJ mol^{-1}) and to PCR (-34 kJ mol^{-1}). However, interaction energies at the PBE level (neglecting the dispersion contribution) increases in order IPC-1P ~ PCR (-21 kJ mol^{-1}) < UTL ~ OKO (-24 kJ mol^{-1}), showing thus important role of dispersion contributions. The CO stretching frequencies increase in order IPC-1P (2168 cm^{-1}) < PCR (2177 cm^{-1}) < UTL (2180 cm^{-1}) < OKO (2182 cm^{-1}). Lower values of electrostatic interaction energy and ν_{CO} can be attributed to nonlinerar arrangement of O-H…CO adsorption complex in PCR (160º). The lowest values found for IPC-1P zeolite are due to the fact that CO is located in the open space above the zeolite layer (Figure 26a) which leads to lower dispersion interactions and also to lower ν_{CO} due to the missing effect from the top. However, part of the differences between IPC-1P and 3D zeolite is also due to somewhat smaller Brønsted acidity of the site in 2D IPC-1P.

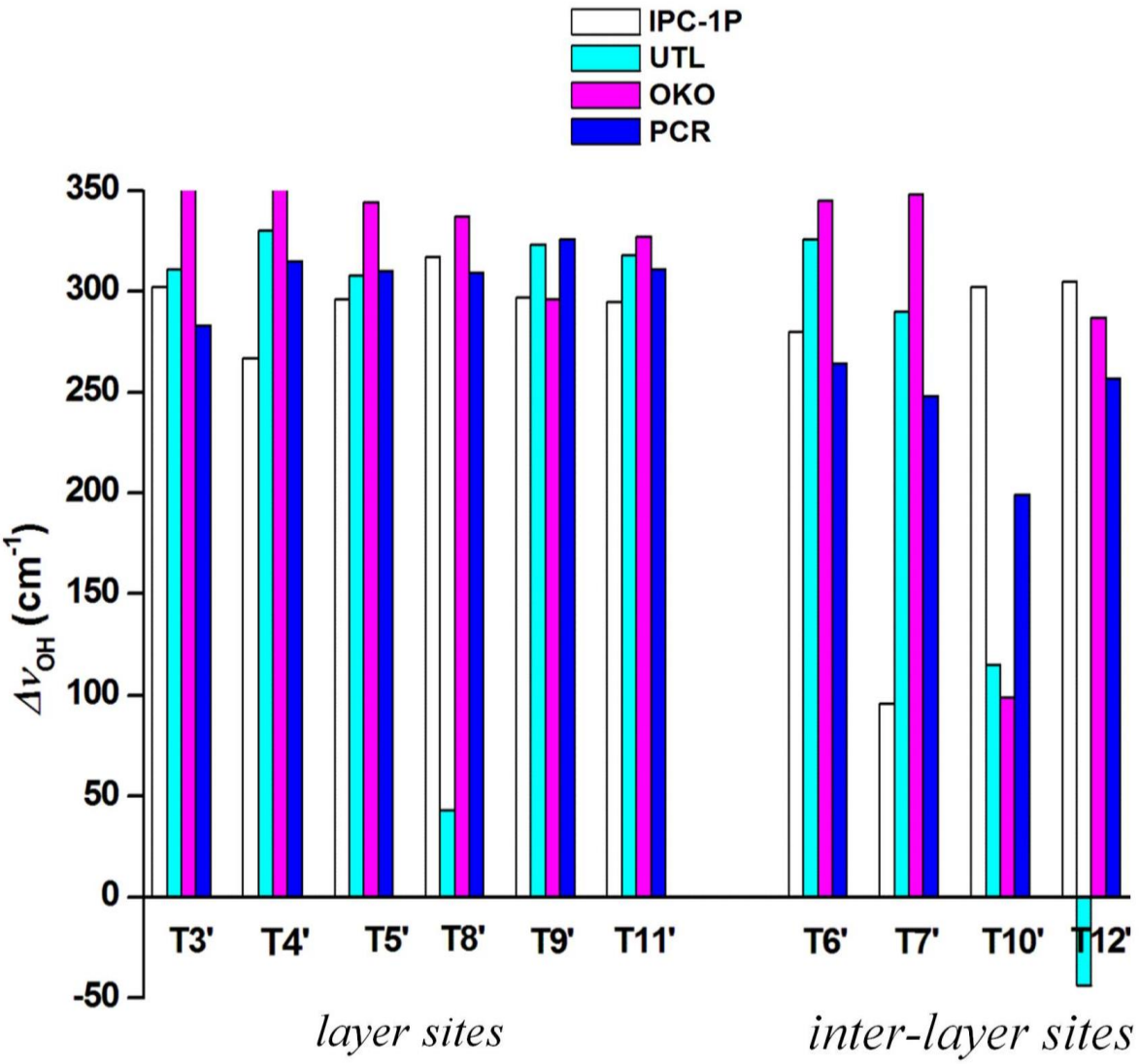

FIGURE 24. The shift of OH frequencies upon CO adsorption in IPC-1P, UTL, OKO, and PCRR

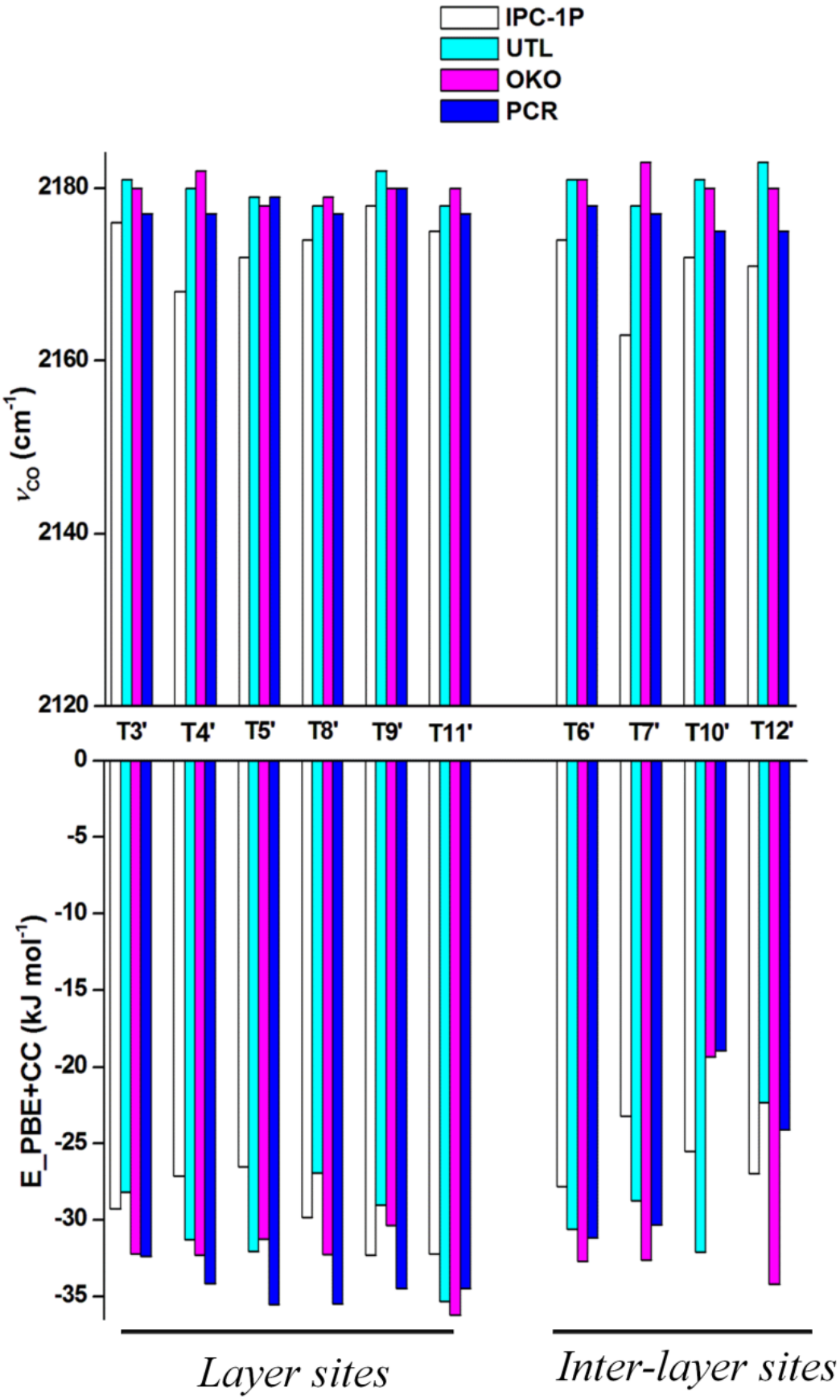

FIGURE 25. Adsorption energies and CO frequencies of CO adsorption complexes in IPC-1P, UTL, OKO and PCR.

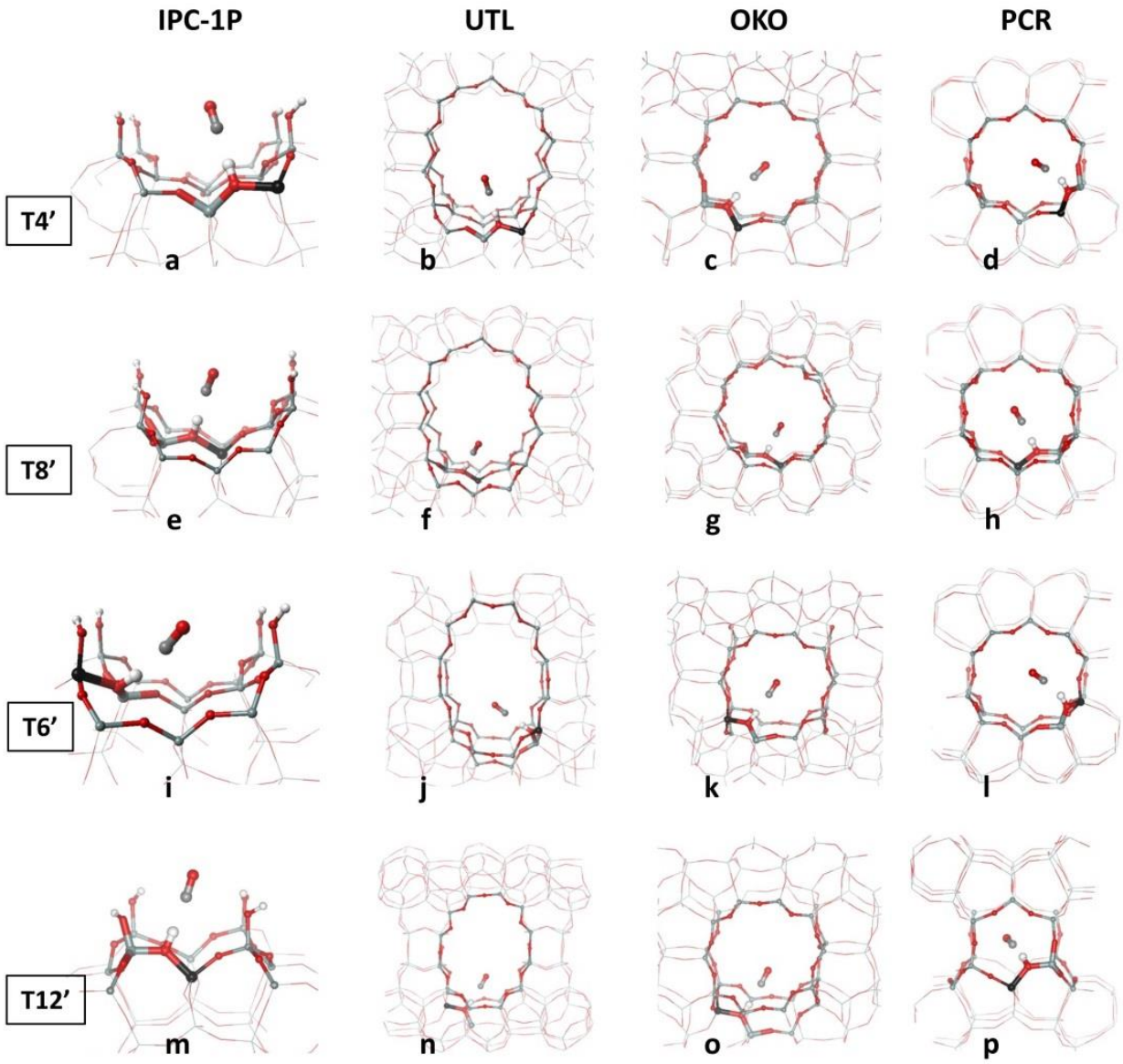

FIGURE 26. The CO adsorption complexes in the most stable BA sites in IPC-1P, UTL, OKO and PCR (from left to right); shown for Al in T4' (a-d); T8' (e-h); T6' (i-l) and T12' (m-p). The H, Al, O, C, and Si atoms are depicted in white, black, red, grey, and light gray color, respectively.

The calculated CO stretching frequencies are well within the range of experimental IR spectra (Figure 27). However, the experimental IR band maxima are about 4 cm^{-1} lower than averaged (for individual zeolites) calculated frequencies, similarly as found previously for other zeolites, *e.g.*, Ref. [83] (Attachment D). The band at 2175 cm^{-1} with a distinct shoulder at 2163 cm^{-1} observed in experimental spectra for IPC-1P compares well with the calculated frequencies for IPC-1P (Figure 25); lower CO frequencies in IPC-1P compared to 3D zeolites were found for many framework Al positions. Zeolites

UTL and OKO have a band centered at 2176 cm^{-1}, slightly higher than 2D IPC-1P; this is again in good agreement with calculated results (Figure 25). This agreement between experimental and computational results entitles us to conclude that the Brønsted acidity of 2D IPC-1P zeolite is just slightly lower than that in 3D UTL and OKO zeolites. Understanding of BA sites in PCR zeolite is more complicated; both experimental and computational data show that CO frequency is lower on BA sites in PCR than on those in OKO and UTL. Lower CO and OH stretching frequencies in PCR cannot be simply attributed to lower acidity. Increased dispersion interaction in PCR together with the smaller size of zeolite channels results in different geometries of CO adsorption complexes on BA sites in PCR – often non-linar O-H…CO complexes characterized by smaller electrostatic contribution than in other zeolites are formed. Consequently, the changes in CO and OH frequencies upon CO adsorption are also smaller and they cannot be correlated with Brønsted acidity.

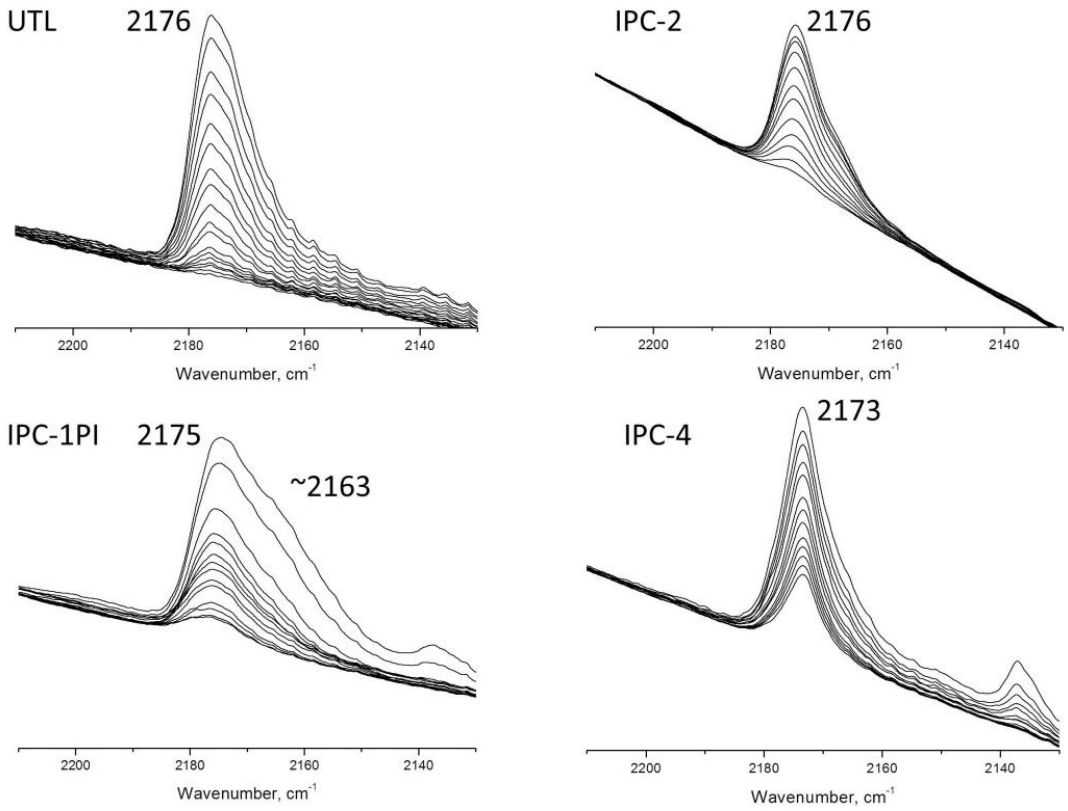

FIGURE 27. IR spectra of CO adsorbed on H-zeolites of IPC-1P family

5.2.2. 3D *vs.* 2D zeolites with MWW topology

As mentioned in section 5.1.3 the Lewis acidity of Li^+ cation is not affected by transformation from 3D to 2D MWW due to the layer thickness and lower silanol density. It remains to be seen whether Brønsted acidity is also the same in both 3D and 2D MWW zeolites. The most energetically stable BA sites along with bond angle of Al-O-Si, OH bond length, and OH stretching frequencies are reported in Table 7. The characteristics of CO adsorption complexes with the most stable BA sites in 3D and 2D MWW are given in Table 8 and the examples of CO adsorptions are shown in Figure 28.

TABLE 7. The Al-O-Si bond angle (deg.), OH bond distance (Å) and OH frequencies (cm^{-1}) of the most stable Brønsted sites in the vicinity each of 8 different framework Al positions in 3D and 2D MWW

BA site	3D			2D		
	Al-O-Si	r_{OH}	ν_{OH}	Al-O-Si	r_{OH}	ν_{OH}
Al1_O3_Si4	128	0.9755	3629	129	0.9757	3627
Al2_O10_Si8	129	0.9756	3628	132	0.9770	3610
Al3_O13_Si3	132	0.9765	3617	131	0.9759	3624
Al4_O3_Si1	129	0.9759	3624	130	0.9760	3623
Al5_O8_Si5[a]	138	0.9919	3414	138	0.9940	3386
Al6_O2_Si1	128	0.9761	3621	134	0.97791	3598
Al7_O4_Si1[a]	128	0.9919	3413	128	0.9919	3414
Al8_O10_Si2	132	0.9753	3633	131	0.9752	3634

[a] BA site involved in intra-zeolite hydrogen bonding

As can be seen from Table 7, the most stable BA sites in 3D MWW are the same (or very similar) as in 2D MWW for all considered framework Al positions – BA hydrogen is bound to the same framework oxygen atom and even other characteristics are similar. The differences in Al-O-Si bond angles and in OH stretching frequency between 3D and 2D MWW does not exceed 6 deg. and 28 cm^{-1}, respectively. It is important to note that the BA proton of Al7_O4_Si1 is localized inside of the small cage and thus it is not accessible to adsorbates.

TABLE 8. Characteristics of CO adsorption complexes with the most stable Brønsted sites in 3D and 2D MWW, adsorption energies and frequencies are reported in kJ mol^{-1} and in cm^{-1}, respectively.

BA site	3D			2D		
	ΔH_{ads}	$\Delta \nu_{OH}$	ν_{CO}	ΔH_{ads}	$\Delta \nu_{OH}$	ν_{CO}
Al1_O3_Si4	-28.1	349	2183	-26.9	325	2180
Al2_O10_Si8	-33.1	314	2181	-32.2	304	2180
Al3_O13_Si3	-32.8	339	2179	-32.8	334	2180
Al4_O3_Si1	-28.7	358	2183	-27.3	334	2179
Al5_O8_Si5[a]	-28.5	100	2178	-27.5	60	2177
Al6_O2_Si1	-27.9	272	2177	-25.5	336	2166
Al7_O4_Si1[a]	-9.5	5	2139	-9.9	0	2139
Al8_O10_Si2	-33.8	306	2180	-32.8	310	2180

[a] BA site involved in intra-zeolite hydrogen bonding

The characteristics including adsorption enthalpies (ΔH_{ads}), the shift of OH stretching frequencies ($\Delta \nu_{OH}$) and CO stretching frequencies (ν_{CO}) of CO adsorption complexes at the most stable BA sites described above are shown in Table 8. It is clearly demonstrated that the adsorption energy, CO frequencies and the shift of OH frequencies are similar in both 3D and 2D MWW. The examples of CO adsorption complexes in 3D and 2D MWW are given in Figure 28.

Characteristics computed for 3D MWW can be compared to experimental ones [83]. Regarding computational results for the CO adsorption on BA sites of MCM-22 system, O–H stretching frequencies are in very good agreement with experimental IR spectra for both, the bare Brønsted-acid sites and those involved in adsorption complexes with CO. Calculated C–O stretching frequencies are about 5 cm^{-1} overestimated with respect to experimentally observed band maxima. The comparisons between theoretical results and experimental data for MCM-22 can be found in Ref. [83] (Attachment D). There are no experimental results relevant to our investigation of properties of 2D MWW so far. Calculated CO stretching frequencies in 2D MWW are only slightly lower compared to those in 3D MWW and this is attributed to the missing effect from the top.

Based on an agreement between experimental and computational results for 3D MWW we can conclude that the Brønsteda acidity of 2D and 3D MWW is the same.

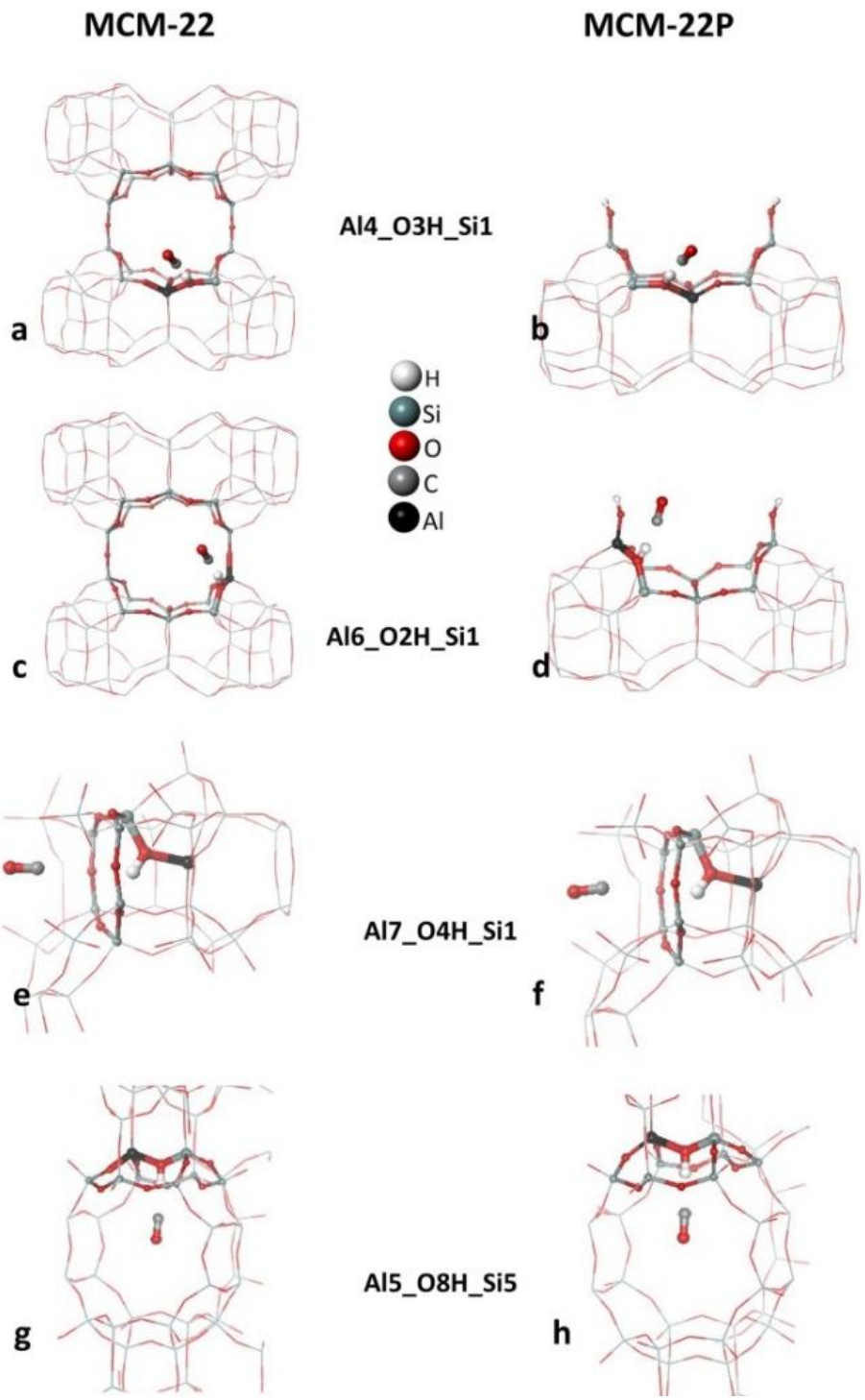

FIGURE 28. CO adsorption complexes at the most stable Brønsted acid sites in MCM-22 (left column) and MCM-22P (right column), shown for Al in T4 (a,b), T6 (c,d) and T7 (e,f) and T5 (g,h)

5.2.3. 3D *vs.* 2D zeolites with MFI topology

Zeolite ZSM-5 (MFI topology) is among the most important industrial catalysts. In addition to 3D conventional ZSM-5 zeolite, hierarchical materials were also successfully synthesized recently, including lamellar 2D MFI (Section 3.3.). The BA properties of 3D and 2D ZSM-5 were investigated herein aiming at understanding of the change of BA properties upon 3D → 2D transformation. Characteristics of the most stable BA sites for each Al position are given in Table 9. The characteristics of CO adsorption complexes formed at these BA sites in 3D and 2D ZSM-5 are presented in Table 10 and examples of CO adsorption complexes are presented in Figure 29.

As can be seen from Table 9, the most stable BA sites in 3D and 2D ZSM-5 are distributed equally into two types, isolated site type with OH frequency in range of 3592-3631 cm^{-1} and H-bonding site type with OH frequency in range of 3161-3432 cm^{-1}. The BA sites can be affected in three different ways upon transformation from 3D to 2D-ZSM-5: (i) There is no change both BA site type and BA location (framework oxygen atom where the BA proton binds to), corresponding to Al in T1, T3, T4, T10, T11, and T12. (ii) The BA sites keep unchanged the site type but proton move to another location of framework oxygen atom, cases of Al in T2, T6, T8, and T9. (iii) The change of BA location and this is associated with the change of BA site type when Al is in T5 and T7. This results in significant difference in OH frequencies.

TABLE 9. The Al-O-Si bond angle (deg.), OH bond distance (Å) and OH frequencies (cm^{-1}) of the most stable Brønsted sites in the vicinity of each of 12 distinguishable Al positions in 3D-ZSM-5 and 2D-ZSM-5 zeolites.

3D-ZSM-5				2D-ZSM-5			
BA site	Al-O-Si	r_{OH}	ν_{OH}	BA site	Al-O-Si	r_{OH}	ν_{OH}
Al1_O2_Si2	129	0.97542	3631	Al1_O2_Si2	130	0.97547	3630
Al2_O7_Si6[a]	139	1.00652	3221	Al2_O6_Si8[a]	138	1.01303	3136
Al3_O9_Si4[a]	136	1.01113	3161	Al3_O9_Si4[a]	135	1.01119	3160
Al4_O9_Si3[a]	139	1.00401	3254	Al4_O9_Si3[a]	138	1.00191	3282
Al5_O1-Si1	134	0.97727	3606	Al5-O14_Si11[a]	139	1.00843	3196
Al6_O7_Si2	138	0.97721	3607	Al6_O15-Si9	136	0.97905	3583
Al7_O17_Si8[a]	130	0.99293	3400	Al7_O16_Si11	134	0.97685	3612
Al8_O17_Si7[a]	131	0.99055	3432	Al8_O20_Si12[a]	133	1.00785	3204
Al9_O15_Si6	131	0.97616	3621	Al9_O19_Si8	142	0.98158	3550
Al10_O22_Si9[a]	142	0.99909	3319	Al10_O22_Si9[a]	128	0.99915	3318
Al11-O16_Si7	135	0.97835	3592	Al11_O16_Si7	133	0.97635	3618
Al12_O8_Si3	132	0.97618	3621	Al12_O8_Si3	138	0.97790	3598

[a] BA sites are involved in intra-zeolite hydrogen bonding

As for the CO adsorption complexes, it is clear that the adsorption energies and shifts of OH and CO frequencies are higher in 3D ZSM-5 than in 2D ZSM-5 for ma T sites. Three situations can be identified depending on the localization and type of BA (how does it change upon the 3D → 2D transformation): (i) The smallest differences in adsorption energy and frequency shifts are observed for the cases of CO adsorption complexes with either isolated BA sites (Al in T1, T6, T9, T11, and T12) or H-bonding BA sites (Al in T2, T3, T4). The differences are within 11 kJ mol^{-1} and 30 cm^{-1} (Figures 29 a-d). (ii) Although the type of BA sites change from 3D to 2D ZSM-5 for the cases of Al in T5 and T7, only the significant difference in OH frequency shift is observed, 183 and 369 cm^{-1}, respectively, however the CO frequency and adsorption enthalpy are similar, within 2 cm^{-1} and 2 kJ mol^{-1} (Figures 29e and 29f). (iii) The largest differences in adsorption enthalpies are presented for cases of Al in T8 and T10, from 15 to18 kJ mol^{-1}, even these BA sites are the same H-bonding site type (Figures 29g and 29h). This is mostly due to dispersion energy. It is apparent that the evaluation of the change of

Brønsted properties of 2D and 3D ZSM-5 is complicated; there are many changes of BA site type induced by the 3D → 2D transformation. The frequency of CO is increased or decreased by the transformation. While the acidity of individual BA sites differs in 3D and 2D ZSM-5, on average acidity remains similar. The distribution of Al among different framework positions appears to have larger influence on Brønsted acidity than the 3D → 2D transformation.

TABLE 10. Characterization of CO adsorption complexes in the most stable BA site in each of 12 distinguishable Al position.

3D-ZSM-5				2D-ZSM-5			
BA site	$\Delta H^o(0K)$	$\Delta\nu_{OH}$	ν_{CO}	BA site	$\Delta H^o(0K)$	$\Delta\nu_{OH}$	ν_{CO}
Al1_O2_Si2	-33.88	303	2180	Al1_O2_Si2	-28.61	315	2180
Al2_O7_Si6[a]	-14.15	-97	2175	Al2_O6_Si8[a]	-16.31	-141	2179
Al3_O9_Si4[a]	-7.40	-97	2175	Al3_O9_Si4[a]	-10.79	-14	2133
Al4_O9_Si3[a]	-9.54	-17	2176	Al4_O9_Si3[a]	-7.05	-21	2171
Al5_O1_Si1	-27.87	301	2177	Al5_O14_Si11[a]	-29.94	-68	2179
Al6_O7_Si2	-39.51	287	2178	Al6_O15-Si9	-28.30	263	2161
Al7_O17_Si8[a]	-31.12	99	2179	Al7_O16_Si11	-30.47	282	2177
Al8_O17_Si7[a]	-32.92	151	2176	Al8_O20_Si12[a]	-16.97	-47	2169
Al9_O15_Si6	-32.20	330	2181	Al9_O19_Si8	-22.54	333	2153
Al10_O22_Si9[a]	-25.96	18	2176	Al10_O22_Si9[a]	-7.18	-5	2123
Al11_O16_Si7	-29.17	319	2178	Al11_O16_Si7	-23.24	289	2173
Al12_O8_Si3	-31.26	322	2179	Al12_O8_Si3	-24.41	316	2168

[a] BA sites are involved in intra-zeolite hydrogen bonding

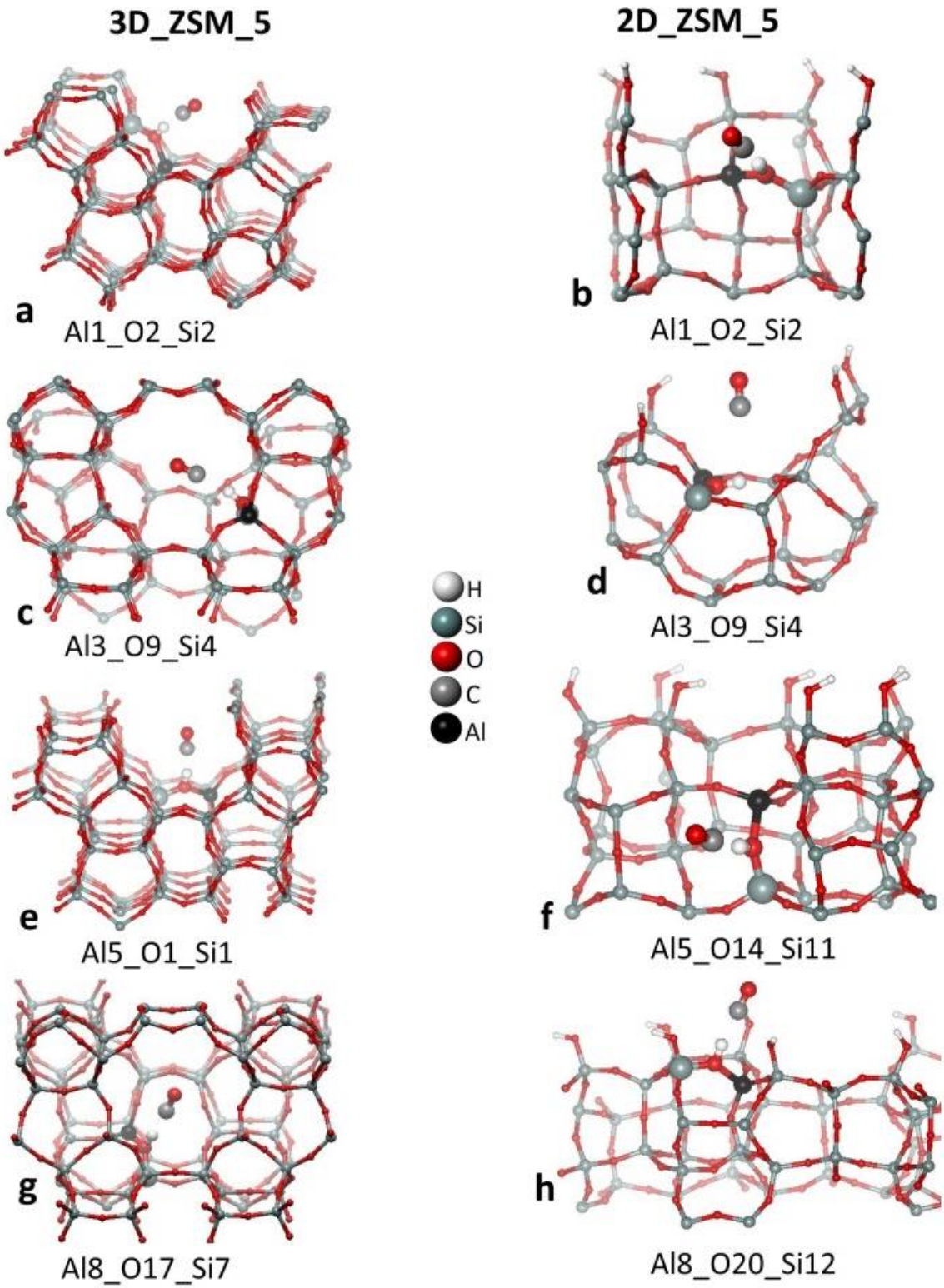

FIGURE 29. CO adsorption complexes at the most stable Brønsted acid sites in 3D ZSM-5 (left column) and 2D ZSM-5 (right column), shown for Al in T1 (a,b), T3 (c,d) and T5 (e,f) and T8 (g,h).

5.2.4. Characterization of 3D and 2D zeolites with MFI topology with the ^{31}P NMR of adsorbed TMPO

As mentioned already in previous Sections, ^{31}P NMR of the adsorbed trialkylphosphine oxide probe molecule has become a suitable tool for the experimental characterization of the zeolite acidity. In particular, this method has been used for the study of Brønsted acidity of MFI zeolites considering both internal (3D zeolite) and external (2D zeolites) surfaces [40, 41, 84, 85]. Results of experimental ^{31}P NMR investigations lead to conclusions that several types of Brønsted sites can be identified and that more acidic sites can be found on the external zeolite surface than inside the channel system. Computational studies based on small cluster model could only bring some qualitative insight [85, 86] while understanding at the molecular level is still missing. The lack of understanding and the fact that MFI characterization with CO probe lead to qualitatively different conclusions motivated us to carry out thorough computational investigation of ^{31}P NMR of adsorbed TMPO presented in this Section. Adsorption complexes were characterized at the PBE-D3 level of theory with the periodic model and chemical shifts were calculated with cluster models (with the geometry taken from periodic calculations); see Section 4.5. for details.

The results for periodic 3D MFI (Table 11) are discussed first followed by the results obtained for 2D MFI (Table 12); calculated characteristics of TMPO adsorption complexes are reported in these Tables for all distinguishable framework Al positions.

Only one type of TMPO adsorption complexes can exist in the case of 3D MFI: TMPO interacts strongly with one Brønsted site that is deprotonated forming thus $TMPOH^+$ (examples of TMPO adsorption complexes are shown for Al in T1 and T6 in Figure 30). Calculated chemical shifts are in the range of 75-86 ppm and there is no correlation between υ_{OH}, E_{ads}, geometry parameters and chemical shifts. For adsorption complexes with shorter O_b-H distance (for Al at T2, T3, T4, and T6) the chemical shift is smaller and adsorption enthalpy is lower.

TABLE 11. Characteristics of TMPO adsorption complexes formed on the most stable Bronsted-acid sites in the vicinity of each of 12 distinguishable framework Al positions in 3D MFI; structural parameters, stretching frequencies, adsorption energy, and chemical shift values are given in Å, cm^{-1}, kJ mol^{-1}, and ppm, respectively.

BA site	E_{ads} (PBE)[a]	E_{ads} (PBE-D3)[b]	$\nu(O_b\text{-}H)$	$r(O_b\text{-}H)$[c]	$r(O_p\text{-}H)$[d]	$(H\text{-}O_p\text{-}P)$[e]	$\Delta(Al\text{-}O_b\text{-}Si)$[f]	Chemical shift
$T9_{Al}$_$O15$_$T6_{Si}$	-118.9	-210.8	3621	1.403	1.072	120	2	86
$T1_{Al}$_$O2$_$T2_{Si}$	-138.2	-222.0	3631	1.426	1.070	118	-2	85
$T8_{Al}$_$O17$_$T7_{Si}$[g]	-137.9	-218.3	3432	1.454	1.062	121	-1	85
$T10_{Al}$_$O3$_$T1_{Si}$	-157.6	-239.5	3603	1.460	1.059	120	-1	85
$T12_{Al}$_$O8$_$T3_{Si}$	-139	-220.0	3621	1.452	1.063	121	-7	84
$T5_{Al}$_$O1$-$T1_{Si}$	-127.5	-208.6	3606	1.443	1.068	121	-4	83
$T7_{Al}$_$O17$_$T8_{Si}$[g]	-132.7	-208.6	3400	1.438	1.066	121	1	83
$T11_{Al}$-$O16$_$T7_{Si}$	-128.3	-216.3	3592	1.526	1.044	125	0	82
$T4_{Al}$_$O9$_$T3_{Si}$[g]	-80.6	-184.1	3254	1.399	1.073	122	9	81
$T3_{Al}$_$O9$_$T4_{Si}$[g]	-72.4	-172.3	3161	1.381	1.080	123	9	80
$T2_{Al}$_$O7$_$T6_{Si}$	-58.5	-154.5	3221	1.387	1.079	124	7	79
$T6_{Al}$_$O7$_$T2_{Si}$	-90.3	-192.0	3607	1.373	1.081	128	1	75

[a] adsorption energy at PBE level. [b] adsorption energy at PBE-D3 level (including dispersion contribution). [c] bond length of zeolite framework oxygen (O_b) and proton H^+(in Å). [d] bond length of oxygen atom of TMPO molecule (O_p) and of Bronsted H^+. [e] H-O_p-P angle of Bronsted H^+, O_p and P of TMPO molecule(in deg). [f] the difference of Al-O_b-Si angle between after and before TMPO adsorption (in deg). [g] BA sites are involved in intra-zeolite hydrogen bonding.

In the case of 2D MFI, three TMPO adsorption complexes can be observed (i) interaction with Brønsted sites only as in the case of 3D MFI; (ii) interaction with BA site and surface silanol simultaneously; (iii) interaction with silanol groups but not with any BA site. Examples of TMPO adsorption complexes on 2D MFI are shown in Figure 31. The differences between these adsorption complexes can be clearly seen from the O_b-H and of O_p-H bond lengths; $r(O_b\text{-}H) > r(O_p\text{-}H)$ indicates the transfer of BA hydrogen and formation of $TMPOH^+$. Other geometrical parameters reported in Table 12 are relatively similar for all adsorption complexes.

The adsorption of TMPO on silanols in energetically the least convenient (E_{ads} ~ -120 kJ mol^{-1}) and chemical shifts are in the range of 43-48 ppm. These adsorption complexes can only occur when there are no free Brønsted sites on the surface.

Adsorption complexes on BA only and on BA and silanol are energetically comparable (E_{ads} are in the range from -130 to -190 kJ mol^{-1} but they show rather different chemical shifts. While complexes on BA only show $r(O_b\text{-}H) > r(O_p\text{-}H)$ and large chemical shifts from 80 to 89 ppm complexes on BA and silanol show $r(O_b\text{-}H) < r(O_p\text{-}H)$ and chemical shifts from 64 to 72 ppm.

Calculated TMPO chemical shifts can be classified into several groups. Complexes formed in 3D MFI (interaction with BA site only) splits into two groups: (i) majority of adsorption complexes is characterized by chemical shift in the range of 80-86 ppm; (ii) for Al in T2 and T6 chemical shifts of 75 and 79 ppm, respectively, are observed. Three groups can be identified for TMPO adsorption complexes in 2D MFI material: (i) adsorption complexes on silanols (43-49 ppm); adsorption complexes with TMPO interacting simultaneously with BA and silanol (64-72 ppm); (iii) adsorption complexes on BA site (80-89 ppm).

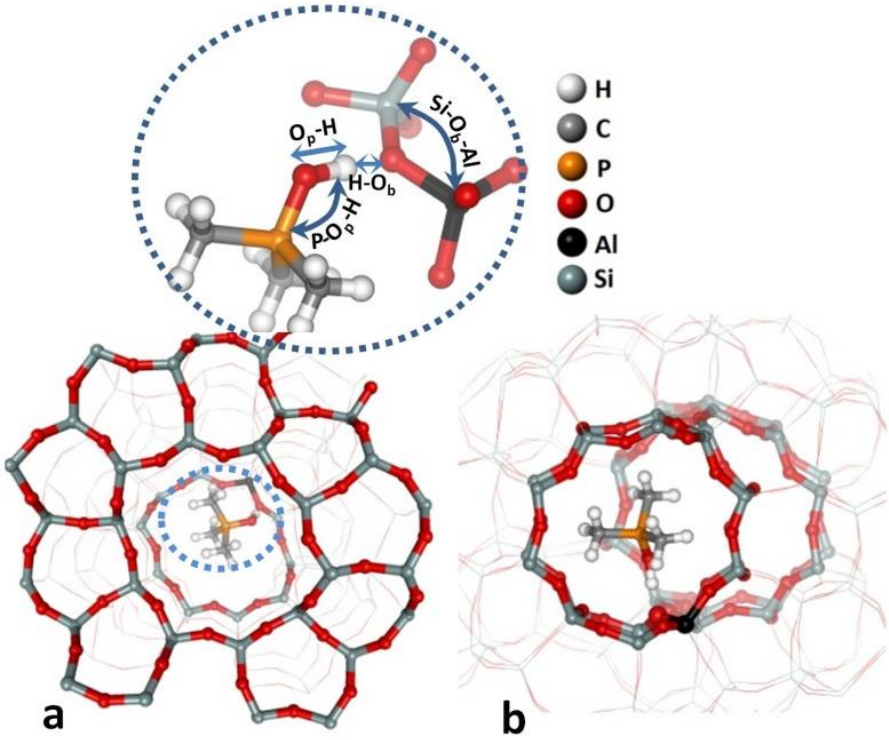

FIGURE 30. TMPO adsorption complexes with BA sites in 3D MFI, shown for Al in T1 (a) and Al in T6 (b).

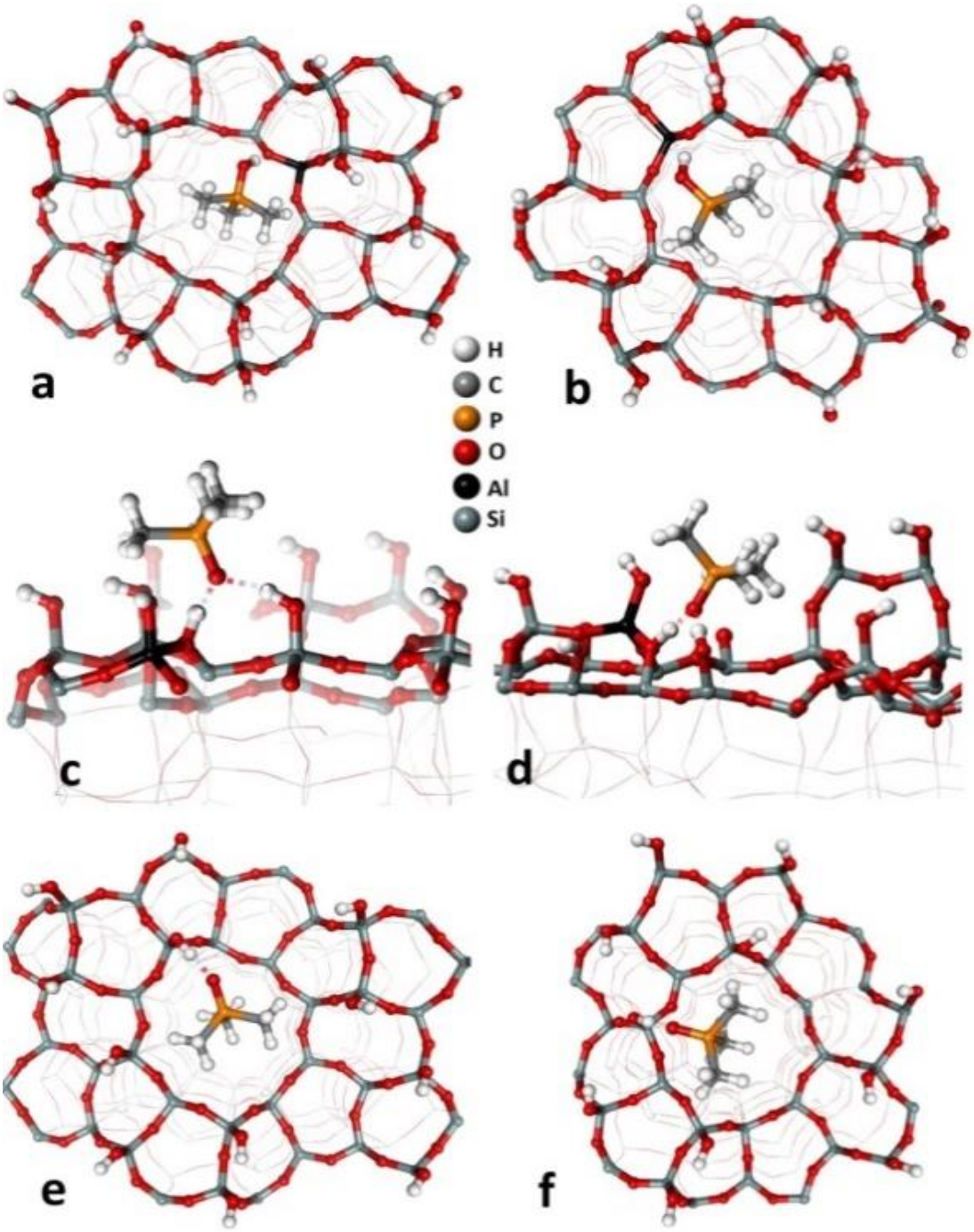

FIGURE 31. TMPO complexes with BA sites in 2D MFI, shown for Al in T1 (a) and Al in T6 (b); a complex with both BA site and silanol, shown for Al in T12 (c) and in T9 (d); complexes only with silanol, shown for T12 (e) and T7 (f).

In order to characterize the BA sites on the external surfaces of MFI, the TBPO was experimentally used instead of a TMPO, due to its large dynamic diameter which prevent the enterance into the microporous channel systems of MFI. For comparison with experimental data taken from Ref. [40], the TBPO was also investigated by us on representative BA sites of 2D MFI and on silanol groups. The results show that the

chemical shifts of TBPO are 6 ppm larger than those of TMPO at the same BA site, in good agreement with experimental data [40, 87]. Taking this into account, three groups of resonance value can be observed for TBPO complexes on 2D MFI materials: 49-55 ppm TBPO complexes with silanol group, 70-78 ppm are due to TBPO complexes with both BA sites and silanol groups, and 86-95 ppm correspond to TBPO complexes with BA sites only. The good agreement between theoretical and experimental results of ^{31}P chemical shifts of adsorbed TMPO in the micropore and TBPO on the external surface sites is shown in Figure 32.

Note that our results differ significantly from previous theoretical investigations employing just a cluster model and not accounting for dispersion contribution [39, 88]. The discrepancy can be easily understood from Tables 11 and 12 where adsorption energies obtained with both PBE and PBE-D3 methods are reported. No relationship between chemical shifts and adsorption energies can be observed; neither in 3D nor in 2D MFI zeolite. This indicates that adsorption energies of TMPO complexes cannot be used to evaluate acid strength in zeolites as used in previous cluster model calculations.

Based on a good agreement between computational results and experimental data, the following conclusions can be drawn: The ^{31}P chemical shifts of adsorbed trialkyphosphine oxide is mainly controlled by the type of adsorption complex formed: (i) the highest ^{31}P NMR chemical shifts (80-89 ppm for TMPO complexes), are due to the interaction of phosphine oxides with only the Brønsted acid sites, where $TMPOH^+$ is formed. Somewhat lower chamical shifts (73-79 ppm) were found for the cases of Al in T2 and T6 in 3D MFI. (ii) The ^{31}P NMR chemical shifts in the range of 64-72 ppm are due to complexes where TMPO simultaneously interacts with both BA sites and silanols group. (iii) The least shifted ^{31}P NMR peak (43-49 ppm) is due to TMPO complexes with silanol groups. The last two types of adsorption complexes can only be formed on the external surface and no H transfer from silanol or BA site to phosphine oxide is observed.

TABLE 12. Characteristics of TMPO adsorption complexes formed on the most stable Bronsted-acid sites in the vicinity of each of 12 distinguishable framework Al positions in 2D MFI; structural parameters, stretching frequencies, adsorption energy, and chemical shift values are given in Å, cm^{-1}, kJ mol^{-1}, and ppm, respectively.

BA site	E_{ads} (PBE)[a]	E_{ads} (PBE-D3)[b]	$\nu(O_b\text{-}H)$	$r(O_b\text{-}H)$[c]	$r(O_p\text{-}H)$[d]	$(H\text{-}O_p\text{-}P)$[e]	$\Delta(Al\text{-}O_b\text{-}Si)$[f]	Chemical shift
TMPO complexes with BA sites								
$T5_{Al}$-O14_$T11_{Si}$	-120.1	-175.0	3619	1.354	1.102	123	-5	89
$T2_{Al}$_O6_$T8_{Si}$[g]	-77.4	-184.9	3136	1.499	1.047	119	3	86
$T10_{Al}$_O22_$T9_{Si}$[g]	-93.2	-126.4	3318	1.342	1.113	126	13	85
$T9_{Al}$_O19_$T8_{Si}$	-130.7	-188.9	3550	1.393	1.085	120	-5	85
$T7_{Al}$_O16_$T11_{Si}$	-125.3	-169.3	3612	1.463	1.062	123	4	84
$T1_{Al}$_O2_$T2_{Si}$	-130.6	-192.0	3630	1.383	1.087	120	-2	83
$T3_{Al}$_O9_$T4_{Si}$[g]	-107.8	-165.7	3160	1.443	1.068	126	3	83
$T12_{Al}$_O8_$T3_{Si}$	-124.0	-177.3	3598	1.417	1.076	123	-4	83
$T6_{Al}$_O15-$T9_{Si}$	-112.6	-167.5	3583	1.373	1.081	120	-4	83
$T11_{Al}$-O16_$T7_{Si}$	-106.1	-157.3	3618	1.422	1.076	124	-1	80
TMPO complexes with both BA sites and silanol groups								
$T9_{Al}$_O19_$T8_{Si}$	-142.0	-194.2	3550	1.089	1.392 (1.827)	129	-11	72
$T10_{Al}$_O22_$T9_{Si}$[g]	-97.0	-128.8	3318	1.092	1.378 (2.039)	125	14	71
$T12_{Al}$_O20_$T8_{Si}$	-139.2	-184.6	3530	1.082	1.391 (1.772)	129	-6	68
$T4_{Al}$_O11_$T7_{Si}$	-120.9	-173.3	3618	1.092	1.374 (2.019)	129	-1	67
$T8_{Al}$_O20_$T12_{Si}$[g]	-104.8	-137.3	3204	1.113	1.335 (1.964)	125	2	67
$T11_{Al}$_O16_$T7_{Si}$[g]	-124.9	-167.8	3618	1.086	1.387 (1.999)	131	-1	67
$T6_{Al}$_O15_$T9_{Si}$	-104.5	-154.8	3583	1.059	1.475 (2.002)	128	-2	64
TMPO complexes with silanol group								
T7	-83.5	-123.8			1.579			48
T9	-69.0	-105.1			1.630			49
T12	-79.6	-120.9			1.624			47
T10	-75.3	-117.7			1.627			43

[a]adsorption energy at PBE level. [b] adsorption energy at PBE-D3 level (including dispersion contribution). [c] bond length of zeolite framework oxygen (O_b) and proton H^+(in Å). [d] bond length of oxygen atom of TMPO molecule (O_p) and of Bronsted H^+, the value in parentheses are the distance between O_p and H atom of silanol group. [e] H-O_p-P angle of Bronsted H^+, O_p and P of TMPO molecule(in deg). [f] difference Al-O_b-Si angle between after and before TMPO adsorption (in deg). [g] BA sites involved in intra-zeolite hydrogen bonding. Italic sites are TMPO simultaneous interaction with BA and silanol group.

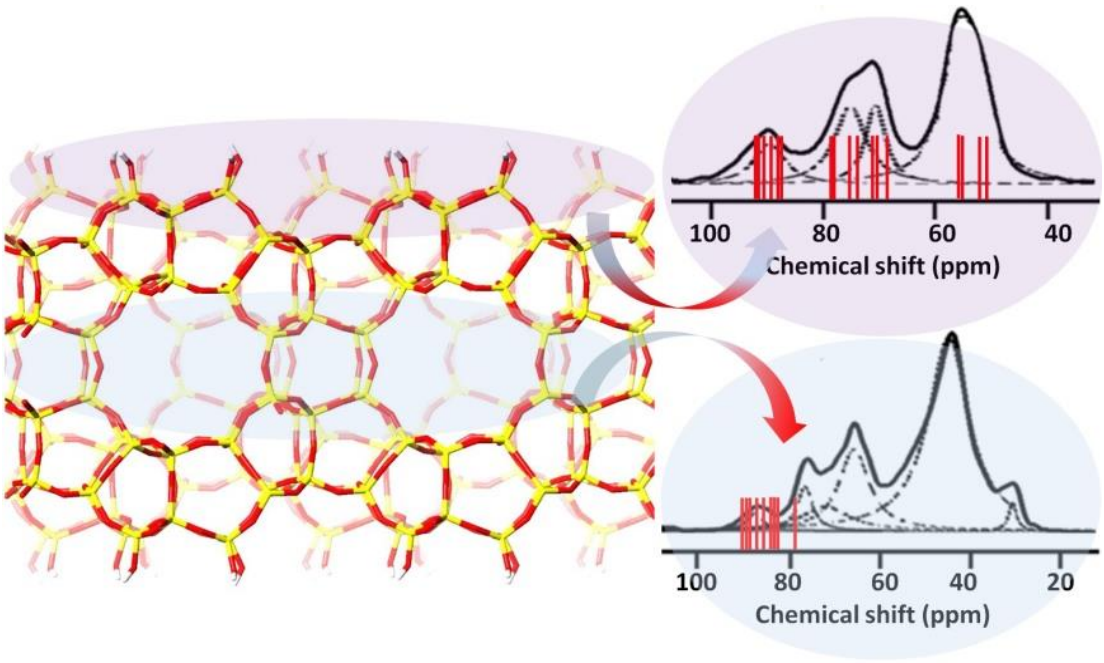

FIGURE 32. ^{31}P NMR chemical shifts of adsorbed TBPO on the surface sites (top) and TMPO on sites inside the channel system (bottom) of the lamellar MFI zeolite; experimental data taken from Ref. [40] (depicted in black) are compared with the DFT results (red bars).

5.3. Hierarchical Na-USY zeolite

Along with lamellar zeolites, other types of hierarchical zeolites combining microporororosity and mesopororisity have been successfully synthesized by various post-synthesis modifications including desilication or dealumination. The hierarchical USY (hUSY) material has very high Si/Al ratio. Therefore, extra-framework cations important for catalytic applications cannot be simply ion-exchanged there since the amount of framework Al is negligible. However, alkali-metal cations can be introduce by special techniques and they probably replace part of the H atoms of numerous silanols [89, 90]. Thus formed Si-O$^-$-Na$^+$ defect sites along with hierarchical structure of the material provide attractive materials for catalytic application in petroleum industry or fine chemical processes. A verification of the hUSY model is described in this Section together with the investigation of its adsorption and catalytic properties. Results are confronted with experimental data obtained in a parallel experimental investigation of these system at the laboratory of our collaborators. Results were summarized in one paper [91] that is also part of this thesis (Attachment E).

5.3.1. Nature of active sites in hierarchical Na-USY

The defects capable of binding alkali metal atoms are known from several siliceous zeolites, such as FAU, MFI, BEA, and they were found to have a moderate basic character [90]. While the type of alkali metal sites in hUSY zeolite plays a crucial role in its catalytic applications, the nature of these basic sites remains somewhat unclear. They have been characterized by a number of experimental techniques, including ^{23}Na MAS NMR, IR, electron microscopy, and temperature-programmed desorption of CO_2; it has been proposed that Na^+ cations replace part of H atoms in surface (external or internal) silanols. Therefore, we have proposed a suitable model (see Section 3.4) and carried out an extensive DFT investigation of CO adsorption on these sites. Such theoretical investigation in combination with experimental study has already been proved for various materials [43, 60, 63, 77] and it has been also applied for the characterization of 2D and 3D zeolites described in previous Sections.

The geometry of various alkali metal sites in hUSY (Na and K) was computationally investigated by adsorption of CO and compared to experimental data based on IR measurement. A structural model of hUSY zeolite was created by introduction of large pore in FAU primitive cell by removal of one fourth of silicon atoms. This model contains several types of different surface silanol nests or defects as a model of mesoporous zeolite surface. The possible positions of grafted alkali metal ions in hUSY are shown in Figure 33. It is shown that CO frequencies nicely fall within experimental range of 2180-2160 cm^{-1} and 2170-2145 cm^{-1} for Na^+ and K^+ cations, respectively (Table 13). While the higher CO frequencies are controlled by interaction of CO with the alkali metal cation only (“effect from bottom”), the lower CO frequencies are strongly affected by the interaction with silanol groups in the nearest vicinity of grafted cations (“effect from the top”). Based on these results, it is realistic to expect that alkali metal grafting in high-silica FAU indeed happens by the deprotonation of silanol groups to silanolates that are charge-compensated by exchanged alkali cations. The details of this investigation are described in Ref. [91] (Attachment E).

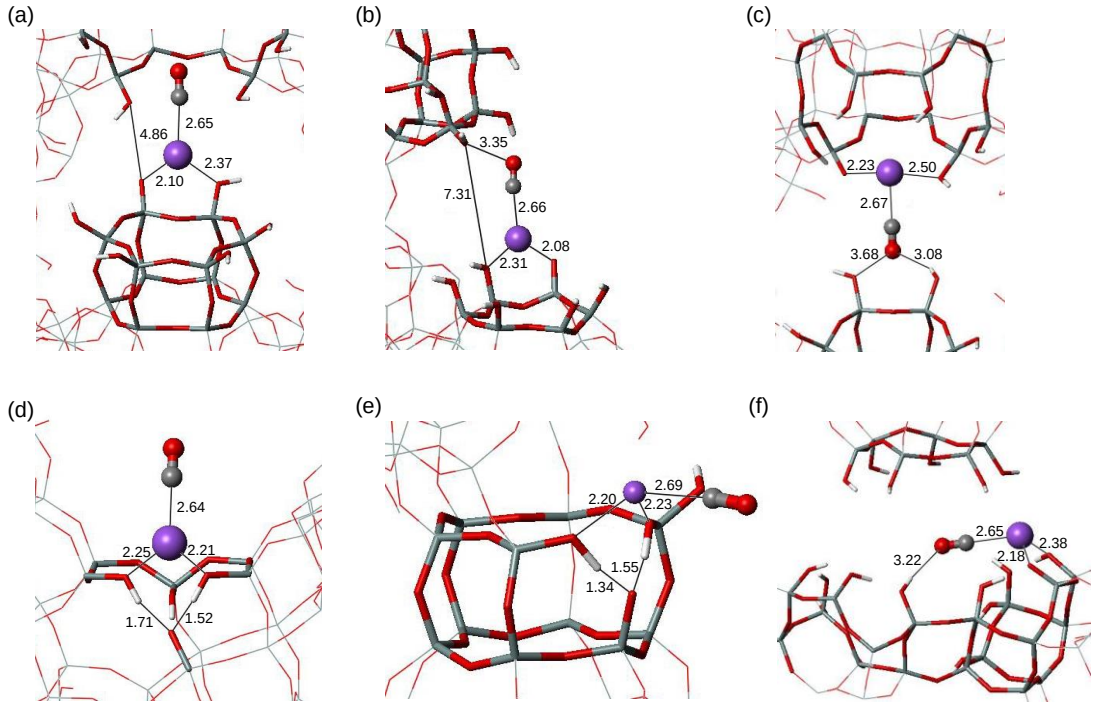

FIGURE 33. CO adsorption complexes formed on (a) S_{D6R}, (b) S_{S6R}, (c) S_{06R}, (d) B_{-1T}, (e) S_{-1T}, and (f) S_{-2T} Na^+ sites in Na-hUSY. Si, O, H, and Na atoms are depicted in gray, red, white, and purple, respectively. All distances are in Å. The notations details can be found in Attachment E.

TABLE 13. Relative exchange energies, CO interaction energies, and stretching frequencies calculated at the PBE level for various alkali metal sites in M-hUSY zeolites.

Site	Na-hUSY			K-hUSY		
	$E_{ex}^{rel}(Na^+)^{a,b}$	$E_{int}(CO)^b$	$\nu_{\omega/r}(CO)^c$	$E_{ex}^{rel}(K^+)^{a,b}$	$E_{int}(CO)^b$	$\nu_{\omega/r}(CO)^c$
S_{06R}	27.4	-11.9	2167	30.2	-14.3	2163
S_{D6R}	61.5	-25.9	2176	57.5	-12.9	2160
S_{S6R}	76.2	-22.7	2178	82.8	-12.4	2162
B_{-1T}	0.0	-25.3	2180	6.2	-14.1	2165
S_{-1T}	11.0	-21.1	2174	9.3	-15.0	2163
S_{-2T}	11.7	-22.1	2162	0.0	-15.6	2142

[a] Relative H/Na(K) exchange energy compared to the lowest-energy lying Na- (K-)containing structure; [b] Energies in kJ mol^{-1}; [c] Frequencies in cm^{-1}

5.3.2. Theoretical investigation of reaction mechanisms of aldol condensation catalyzed by the hierarchical USY zeolite

For further understanding of basic properties of Na-hUSY, the catalytic application of Na-grafted hUSY zeolite for aldol condensation has been investigated experimentally and results show that this catalyst performs better than traditional Al-rich zeolite catalysts [90]. The aldol condensation reactions in acetone and furfural mixture were studied by a joint experimental and theoretical study. Experimental evidence shows that aceton self-condensation is the preferred reaction in acetone and furfural mixture; it is the goal of present theoretical investigation to explain and understand these experimental results. Therefore, acetone-acetone and acetone-furfural condensations catalyzed by Na-hUSY zeolite (Figure 34) were computationally investigated by DFT methods. Cluster models of all sites considered in the hierarchical FAU model have been developed and utilized as potential catalytic sites in Na-hUSY for the acetone-furfural condensation at B3LYP level (results not reported herein). A single six-membered ring site (denoted as Na-S_{S6R}-hUSY) was found to have superior activity to all other sites and was thus used for further investigation.

Investigation of acetone-acetone and acetone-furfural condensation mechanisms was performed using newly developed layered FAU model (see Section 3.4) containing surface S_{S6R} sites to obtain all minima on relevant reaction paths using PBE-D3 method. The reaction barriers were subsequently corrected; corrections were calculated with cluster models as a difference between B3LYP and PBE barriers. The final reaction profiles of reactions in acetone and furfural mixture are shown in Table 14 and Figure 35.

As can be seen from Figure 35, both reactions in acetone and furfural mixture proceed in two steps: i) the tautomerization of acetone to enol or deprotonation to enolate (jointly denoted as $\mathbf{R^{act}}$) followed by condensation to form intermediates; either DAA or FAA (jointly denoted **Int**, see Figure 34 for notation); ii) thus formed intermediates are then tautomerized to form enol/ate and then reactions are finished by water elimination and products formation. Barriers of individual reaction steps are quite similar for aceton-aceton and aceton-furfural condensation; a major difference between two reactions is in the stability of intermediates. The results in Table 14 show that DAA is by 18 kJ mol^{-1} more thermodynamically stable than reactants; however, FAA is by 15 kJ mol^{-1} less stable than reactants. This can be compared with gas phase, where both FAA and DAA

are by 12 kJ mol^{-1} more stable than reactants. The Na-S_{S6R}-USY thus significantly decreases the reaction barriers of aldol condensation; however, for some reactants it strongly destabilizes formation of the product and thus it blocks the reaction. This nicely explains the experimentally results showing formation of DAA and mesityl oxide and only very small amount of FAA and FAc.

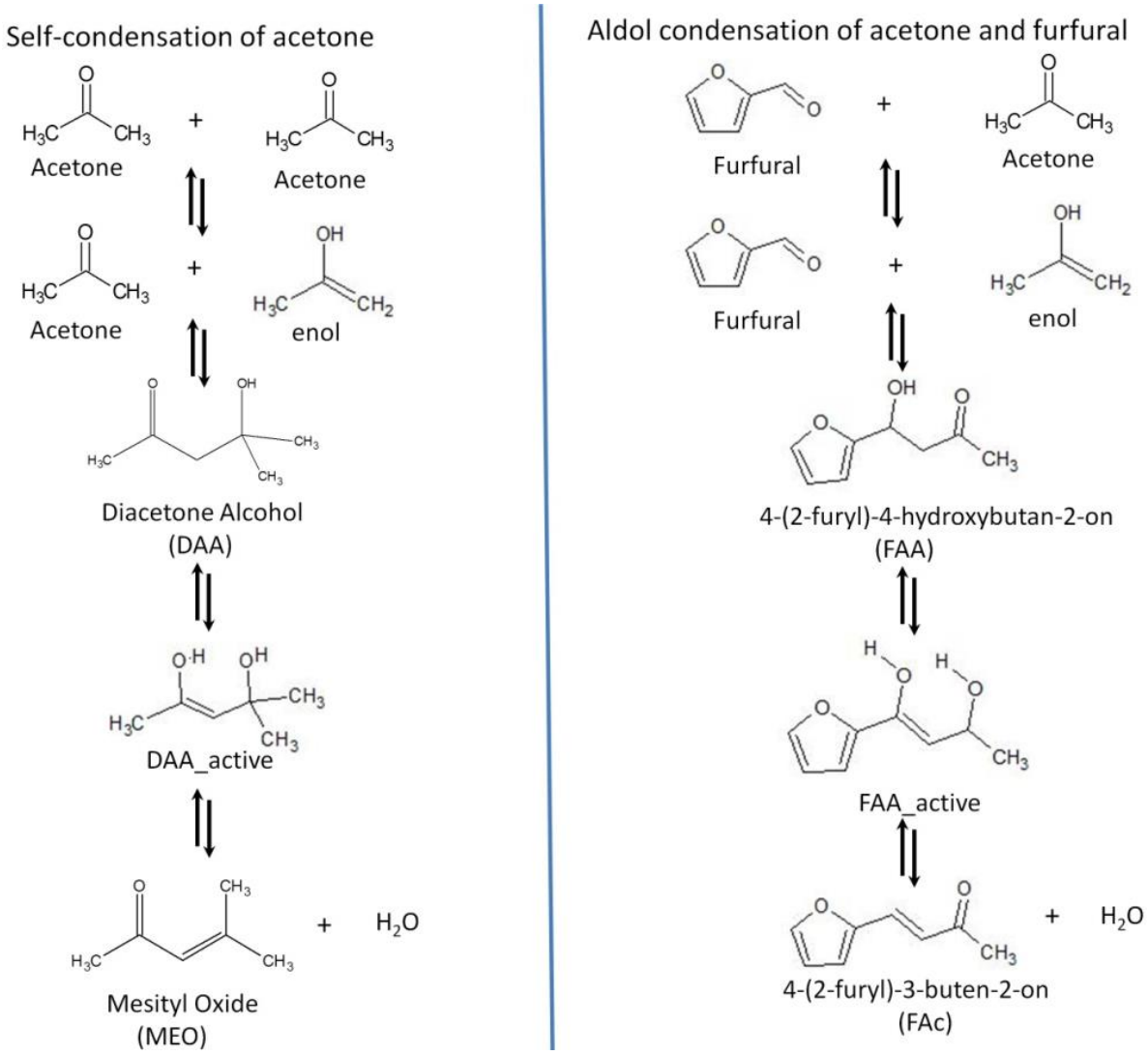

FIGURE 34. Schemes of aldol condensation; acetone-acetone (left column), acetone-furfural (right column).

TABLE 14. Reaction profile of aldol condensation of acetone and furfural with minima obtained in periodic Na-S_{S6R}-hUSY model and PBE+D3 functional and elementary barriers with S_{S6R} cluster model. B3LYP corrections were added as obtained from the S_{S6R} cluster model (as difference between B3LYP/TZVP and PBE/TVZP reaction energies). All energies in kJ mol^{-1}.

	structure	E_{rel}	$E^{\neq}$		structure	E_{rel}	$E^{\neq}$
Acetone+Acetone	acetone+acetone	-154.7		Acetone + Furfural	furfural+acetone	-187.6	
	acetone+enol	-128.0	56.2		furfural+enol(ate)	-159.5	51.4
	TS1	-71.8			TS1	-108.1	
	DAA	-166.3			FAA	-172.0	
	DAA_enol	-111.0	37.7		FAA-enolate	-138.0	37.6
	TS2	-71.8			TS2	-100.4	
	MEO+h2o	-73.4			FAc+h2o	-204.6	

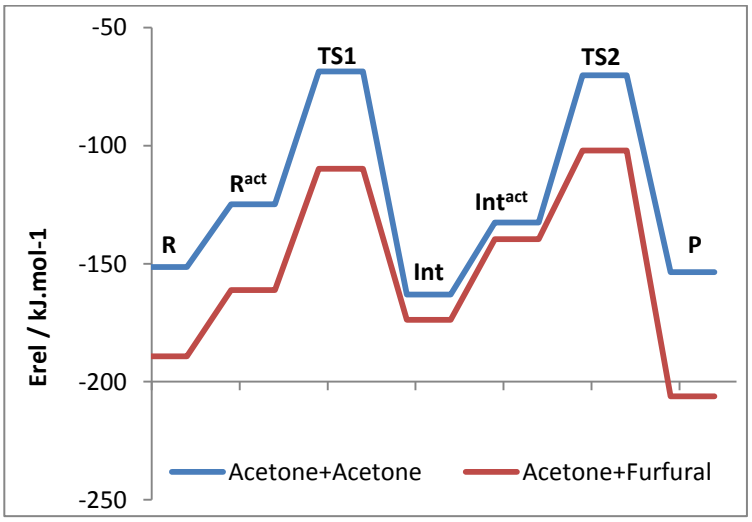

FIGURE 35. Reaction profiles of condensation reactions in acetone and furfural mixture catalyzed by Na- hUSY represented by a S_{S6R} site. All minima were obtained using periodic model and PBE+D3 method and corrected for B3LYP based on cluster model results; the reaction barriers were obtained from cluster model using B3LYP functional.

Chapter 6

Conclusions

Two-dimensional zeolites recently explored experimentally have several advantages with respect to conventional 3D zeolites, in particular in catalysis. Hierarchical zeolites prepared from 2D zeolites by pillaring contains crystalline zeolite layers separated by amorphous pillars; presence of mesoporous channels helps to overcome diffusion limitation while the crystalline character of the zeolite layer guarantee the presence of catalytically active sites similar to those found in conventional 3D zeolite. The goal of this thesis was to systematically investigate the difference between 3D and 2D zeolites by means of computational chemistry tools. And a motivation for the computational work presented here was to improve our understanding of properties of 2D zeolites based on combination of computational results with available experimental ones. The strategy adopted was following – computational investigate the properties of active sites formed at equivalent crystallographic positions in 2D and 3D zeolites and identify the similarities and differences.

The most important properties of zeolites, *i.e.*, the presence of Brønsted and Lewis acid sites, were investigated. A number of different characteristics of acid sites were considered, focusing on those that could be also obtained experimentally. Results obtained computationally were compared with experimental data available in literature and with those newly obtained by collaborating experimental research groups. Several zeolite topologies were investigated, including, UTL, MFI, MWW, and FAU; properties of traditional 3D zeolite as well as of corresponding 2D one were considered in all cases.

The Lewis acidity of 3D and 2D zeolites was investigated for Li-form of zeolites. First the structure of the Lewis site was determined followed by investigation of adsorption complexes with CO probe molecule. This approach was used previously for characterization of 3D zeolites and we have shown that it can be extended for the description of the 2D zeolites. Not only that, our results indicate that the sensitivity of CO probe molecule (in terms of the changes of its vibrational frequency and adsorption heats)

is sufficient to distinguish between the Lewis sites in 3D and 2D zeolites. Following observation can be drawn: (i) Adsorption heats of CO on Lewis acid sites in 2D zeolites are smaller than those on 3D zeolites mostly due to the decrease of the dispersion interactions. (ii) CO stretching frequencies are also lower on Lewis sites in 2D zeolites due to missing effect of the microporous channel. The main conclusions of this part of the thesis include: (i) The acidity of Lewis sites in 2D zeolite is similar as in corresponding (having the same topology) 3D zeolite; this is in particular true for 2D zeolites with thick layers and with lower concentration of surface silanols (MWW). (ii) The Lewis acidity of 2D zeolites with thin layers (about 1 nm) is somewhat lower than acidity of corresponding 3D zeolites; this is due to increase flexibility of 2D layers and due to the loss of intersection sites.

The Brønsted acidity of 3D and 2D zeolites was investigated also with the CO probe molecule; adsorption heats and changes in CO and OH stretching frequencies were evaluated. The same observations as described above for Lewis sites were found also for Brønsted sites (*i.e.*, lower adsorption heats and smaller frequency changes in 2D zeolties). And the same conclusions can be drawn for Brønsted sites, however, the differences between 3D and corresponding 2D zeolite are smaller: (i) There is hardly and change in Brønsted site characteristics for 2D zeolites with thick layers and low concentration of surface silanols. (ii) Brønsted acidity of 2D zeolites with thin layers is slightly lower than that in corresponding 3D zeolite. Investigation of Brønsted acidity was extended to the ^{31}P NMR characterization of 2D and 3D MFI using ^{31}P chemical shifts of adsorbed trialkyphosphine oxide. A consistent interpretation of available experimental data was offered.

Our investigation of acidity of zeolites with similar topology but different size of the microporous channel have revealed an interesting (and not yet discovered) observation that the acidity of channel wall sites increases for zeolites with smaller channels; of course this only holds for the zeolites with similar topology (as was demonstrated on UTL, OKO, and PCR zeolites).

Finally, the catalytic activity of hierarchical zeolites (represented by 2D FAU) was investigated. The nature of active sites in this catalysts were investigated first and from a comparison of experimental and calculated characteristics (IR of adsorbed CO) the structure of these active sites was proposed. In a follow up investigation we have

searched the reaction path for aldol condensation, considering condensation products between aceton and furfural and the reaction mechanism has been proposed.

All computational results reported in this thesis were compared with available experimental data and a good agreement was found in all cases. It is therefore believed that the study presented herein brought new inside on the character and properties of active sites and 2D zeolites and on the differences and similarities between 3D and 2D zeolites. It can be concluded that 2D zeolites hold all important properties of corresponding zeolites and small decrease of acidity can be only expected for 2D zeolites with thin layers.

References

[1] B. Xu, C. Sievers, S.B. Hong, R. Prins, J.A. van Bokhoven, Catalytic activity of Bronsted acid sites in zeolites: Intrinsic activity, rate-limiting step, and influence of the local structure of the acid sites, Journal of Catalysis 244 (2006) 163-168.

[2] D.P. Serrano, R.A. Garcia, G. Vicente, M. Linares, D. Prochazkova, J. Cejka, Acidic and catalytic properties of hierarchical zeolites and hybrid ordered mesoporous materials assembled from MFI protozeolitic units, Journal of Catalysis 279 (2011) 366-380.

[3] M. Niwa, K. Suzuki, N. Morishita, G. Sastre, K. Okumura, N. Katada, Dependence of cracking activity on the Bronsted acidity of Y zeolite: DFT study and experimental confirmation, Catalysis Science & Technology 3 (2013) 1919-1927.

[4] A. Corma, Inorganic solid acids and their use in acid-catalyzed hydrocarbon reactions, Chemical Reviews 95 (1995) 559-614.

[5] R. Rinaldi, F. Schuth, Design of solid catalysts for the conversion of biomass, Energy & Environmental Science 2 (2009) 610-626.

[6] A. Taguchi, F. Schuth, Ordered mesoporous materials in catalysis, Microporous and Mesoporous Materials 77 (2005) 1-45.

[7] R.M. Martin-Aranda, J. Cejka, Recent Advances in Catalysis Over Mesoporous Molecular Sieves, Topics in Catalysis 53 (2010) 141-153.

[8] W.J. Roth, O.V. Shvets, M. Shamzhy, P. Chlubna, M. Kubu, P. Nachtigall, J. Čejka, Postsynthesis Transformation of Three-Dimensional Framework into a Lamellar Zeolite with Modifiable Architecture, Journal of the American Chemical Society 133 (2011) 6130-6133.

[9] P. Chlubna, W.J. Roth, H.F. Greer, W.Z. Zhou, O. Shvets, A. Zukal, J. Cejka, R.E. Morris, 3D to 2D Routes to Ultrathin and Expanded Zeolitic Materials, Chemistry of Materials 25 (2013) 542-547.

[10] M. Choi, K. Na, J. Kim, Y. Sakamoto, O. Terasaki, R. Ryoo, Stable single-unit-cell nanosheets of zeolite MFI as active and long-lived catalysts, Nature 461 (2009) 246-U120.

[11] Y.J. He, G.S. Nivarthy, F. Eder, K. Seshan, J.A. Lercher, Synthesis, characterization and catalytic activity of the pillared molecular sieve MCM-36, Microporous and Mesoporous Materials 25 (1998) 207-224.

[12] A. Corma, V. Fornes, S.B. Pergher, T.L.M. Maesen, J.G. Buglass, Delaminated zeolite precursors as selective acidic catalysts, Nature 396 (1998) 353-356.

[13] A. Corma, V. Fornes, J. Martinez-Triguero, S.B. Pergher, Delaminated zeolites: Combining the benefits of zeolites and mesoporous materials for catalytic uses, Journal of Catalysis 186 (1999) 57-63.

[14] A. Corma, U. Diaz, M.E. Domine, V. Fornes, New aluminosilicate and titanosilicate delaminated materials active for acid catalysis, and oxidation reactions using H2O2, Journal of the American Chemical Society 122 (2000) 2804-2809.

[15] K. Kim, R. Ryoo, H.D. Jang, M. Choi, Spatial distribution, strength, and dealumination behavior of acid sites in nanocrystalline MFI zeolites and their catalytic consequences (vol 288, pg 115, 2012), Journal of Catalysis 327 (2015) 96-96.

[16] H.W. Lee, S.H. Park, J.K. Jeon, R. Ryoo, W. Kim, D.J. Suh, Y.K. Park, Upgrading of bio-oil derived from biomass constituents over hierarchical unilamellar mesoporous MFI nanosheets, Catalysis Today 232 (2014) 119-126.

[17] I. Rodriguez, M.J. Climent, S. Iborra, V. Fornes, A. Corma, Use of delaminated zeolites (ITQ-2) and mesoporous molecular sieves in the production of fine chemicals: Preparation of dimethylacetals and tetrahydropyranylation of alcohols and phenols, Journal of Catalysis 192 (2000) 441-447.

[18] M.V. Rodrigues, C. Vignatti, T. Garetto, S.H. Pulcinelli, C.V. Santilli, L. Martins, Glycerol dehydration catalyzed by MWW zeolites and the changes in the catalyst deactivation caused by porosity modification, Applied Catalysis a-General 495 (2015) 84-91.

[19] D.D. Xu, G.R. Swindlehurst, H.H. Wu, D.H. Olson, X.Y. Zhang, M. Tsapatsis, On the Synthesis and Adsorption Properties of Single-Unit-Cell Hierarchical Zeolites Made by Rotational Intergrowths, Advanced Functional Materials 24 (2014) 201-208.

[20] http://www.iza-structure.org/databases/.

[21] P. Chlubna, W.J. Roth, A. Zukal, M. Kubu, J. Pavlatova, Pillared MWW zeolites MCM-36 prepared by swelling MCM-22P in concentrated surfactant solutions, Catalysis Today 179 (2012) 35-42.

[22] W.J. Roth, P. Chlubna, M. Kubu, D. Vitvarova, Swelling of MCM-56 and MCM-22P with a new medium - surfactant-tetramethylammonium hydroxide mixtures, Catalysis Today 204 (2013) 8-14.

[23] K. Na, C. Jo, J. Kim, K. Cho, J. Jung, Y. Seo, R.J. Messinger, B.F. Chmelka, R. Ryoo, Directing Zeolite Structures into Hierarchically Nanoporous Architectures, Science 333 (2011) 328-332.

[24] W.J. Roth, P. Nachtigall, R.E. Morris, P.S. Wheatley, V.R. Seymour, S.E. Ashbrook, P. Chlubna, L. Grajciar, M. Polozij, A. Zukal, O. Shvets, J. Cejka, A family of zeolites with controlled pore size prepared using a top-down method, Nature Chemistry 5 (2013) 628-633.

[25] P. Eliasova, M. Opanasenko, P.S. Wheatley, M. Shamzhy, M. Mazur, P. Nachtigall, W.J. Roth, R.E. Morris, J. Cejka, The ADOR mechanism for the synthesis of new zeolites, Chemical Society Reviews 44 (2015) 7177-7206.

[26] M. Mazur, P.S. Wheatley, M. Navarro, W.J. Roth, M. Položij, A. Mayoral, P. Eliášová, P. Nachtigall, J. Čejka, R.E. Morris, Synthesis of ‘unfeasible’ zeolites, Nat Chem 8 (2016) 58-62.

[27] E. Verheyen, L. Joos, K. Van Havenbergh, E. Breynaert, N. Kasian, E. Gobechiya, K. Houthoofd, C. Martineau, M. Hinterstein, F. Taulelle, V. Van Speybroeck, M. Waroquier, S. Bals, G. Van Tendeloo, C.E.A. Kirschhock, J.A. Martens, Design of zeolite by inverse sigma transformation, Nature Materials 11 (2012) 1059-1064.

[28] J.-L. Paillaud, B. Harbuzaru, J. Patarin, N. Bats, Extra-Large: Pore Zeolites with Two-Dimensional Channels Formed by 14 and 12 Rings, Science 304 (2004) 990-992.

[29] O. Bludsky, M. Silhan, P. Nachtigall, Theoretical investigation of the effect of the rare gas matrices on the vibrational spectra of solvated molecular ions: Cu+CO, Journal of Chemical Physics 117 (2002) 9298-9305.

[30] D. Verboekend, J. Perez-Ramirez, Desilication Mechanism Revisited: Highly Mesoporous All-Silica Zeolites Enabled Through Pore-Directing Agents, Chemistry-a European Journal 17 (2011) 1137-1147.

[31] A. Inayat, I. Knoke, E. Spiecker, W. Schwieger, Assemblies of Mesoporous FAU-Type Zeolite Nanosheets, Angewandte Chemie-International Edition 51 (2012) 1962-1965.

[32] B.Y. Liu, F. Chen, L.M. Zheng, J.H. Ge, H.X. Xi, Y. Qian, Synthesis and structural properties of hierarchically structured aluminosilicates with zeolite Y (FAU) frameworks, Rsc Advances 3 (2013) 15075-15084.

[33] A. Inayat, C. Schneider, W. Schwieger, Organic-free synthesis of layer-like FAU-type zeolites, Chemical Communications 51 (2015) 279-281.

[34] O. Terasaki, Fine-Structures of Zeolites, Journal of Electron Microscopy 43 (1994) 337-346.

[35] P. Li, Y. Xiang, V.H. Grassian, S.C. Larsen, CO adsorption as a probe of acid sites and the electric field in alkaline earth exchanged zeolite beta using FT-IR and ab initio quantum calculations, Journal of Physical Chemistry B 103 (1999) 5058-5062.

[36] P. Nachtigall, O. Bludsky, L. Grajciar, D. Nachtigallova, M.R. Delgado, C.O. Arean, Computational and FTIR spectroscopic studies on carbon monoxide and dinitrogen adsorption on a high-silica H-FER zeolite, Phys Chem Chem Phys 11 (2009) 791-802.

[37] A. Pulido, P. Nachtigall, M. Rodriguez Delgado, C. Otero Arean, Computational and variable-temperature infrared spectroscopic studies on carbon monoxide adsorption on zeolite Ca-A, Chemphyschem 10 (2009) 1058-1065.

[38] S. Savitz, A.L. Myers, R.J. Gorte, Calorimetric investigation of CO and N-2 for characterization of acidity in zeolite H-MFI, Journal of Physical Chemistry B 103 (1999) 3687-3690.

[39] A. Zheng, H. Zhang, X. Lu, S.B. Liu, F. Deng, Theoretical predictions of P-31 NMR chemical shift threshold of trimethylphosphine oxide absorbed on solid acid catalysts, Journal of Physical Chemistry B 112 (2008) 4496-4505.

[40] Y. Seo, K. Cho, Y. Jung, R. Ryoo, Characterization of the Surface Acidity of MFI Zeolite Nanosheets by P-31 NMR of Adsorbed Phosphine Oxides and Catalytic Cracking of Decalin, Acs Catalysis 3 (2013) 713-720.

[41] S. Hayashi, K. Jimura, N. Kojima, Acid property of MFI-type zeolites probed by trimethylphosphine oxide studied by solid-state NMR, Microporous and Mesoporous Materials 186 (2014) 101-105.

[42] D. Nachtigallova, P. Nachtigall, M. Sierka, J. Sauer, Coordination and siting of Cu+ ions in ZSM-5: A combined quantum mechanics interatomic potential function study, Physical Chemistry Chemical Physics 1 (1999) 2019-2026.

[43] O. Bludsky, M. Silhan, P. Nachtigall, T. Bucko, L. Benco, J. Hafner, Theoretical investigation of CO interaction with copper sites in zeolites: Periodic DFT and hybrid quantum mechanical/interatomic potential function study, Journal of Physical Chemistry B 109 (2005) 9631-9638.

[44] A. Ghorbanpour, J.D. Rimer, L.C. Grabow, Periodic, vdW-corrected density functional theory investigation of the effect of Al siting in H-ZSM-5 on chemisorption properties and site-specific acidity, Catalysis Communications 52 (2014) 98-102.

[45] X.F. Ma, A. Genest, L. Spanu, N. Rosch, Structures and vibrational frequencies of CO adsorbed on transition metals from calculations using the vdW-DF2 functional, Computational and Theoretical Chemistry 1069 (2015) 147-154.

[46] O.V. Ershova, T.C. Lillestolen, E. Bichoutskaia, Study of polycyclic aromatic hydrocarbons adsorbed on graphene using density functional theory with empirical dispersion correction, Physical Chemistry Chemical Physics 12 (2010) 6483-6491.

[47] A. Hmiel, Y. Xue, Water adsorption on hydrogen-passivated silicon nanowires from density functional theory with dispersion correction, Physical Review B 83 (2011).

[48] L. Grajciar, C.O. Arean, A. Pulido, P. Nachtigall, Periodic DFT investigation of the effect of aluminium content on the properties of the acid zeolite H-FER, Physical Chemistry Chemical Physics 12 (2010) 1497-1506.

[49] A. Pulido, M.R. Delgado, O. Bludsky, M. Rubes, P. Nachtigall, C.O. Arean, Combined DFT/CC and IR spectroscopic studies on carbon dioxide adsorption on the zeolite H-FER, Energy & Environmental Science 2 (2009) 1187-1195.

[50] M. Rubes, J. Kysilka, P. Nachtigall, O. Bludsky, DFT/CC investigation of physical adsorption on a graphite (0001) surface, Physical Chemistry Chemical Physics 12 (2010) 6438-6444.

[51] P. Hohenberg, W. Kohn, Inhomogeneous Electron Gas, Physical Review B 136 (1964) B864-+.

[52] W. Kohn, L.J. Sham, Quantum Density Oscillations in an Inhomogeneous Electron Gas, Physical Review 137 (1965) 1697-&.

[53] A.D. Becke, Density-functional exchange-energy approximation with correct asymptotic behavior, Phys Rev A Gen Phys 38 (1988) 3098-3100.

[54] C.T. Lee, W.T. Yang, R.G. Parr, Development of the Colle-Salvetti Correlation-Energy Formula into a Functional of the Electron-Density, Physical Review B 37 (1988) 785-789.

[55] J.P. Perdew, Y. Wang, Accurate and simple analytic representation of the electron-gas correlation energy, Phys Rev B Condens Matter 45 (1992) 13244-13249.

[56] J.P. Perdew, Density-functional approximation for the correlation energy of the inhomogeneous electron gas, Phys Rev B Condens Matter 33 (1986) 8822-8824.

[57] J.P. Perdew, K. Burke, M. Ernzerhof, Generalized Gradient Approximation Made Simple, Phys Rev Lett 77 (1996) 3865-3868.

[58] A.J. Jones, E. Iglesia, The Strength of Bronsted Acid Sites in Microporous Aluminosilicates, Acs Catalysis 5 (2015) 5741-5755.

[59] S. Tosoni, D. Spinnato, G. Pacchioni, DFT Study of CO2 Activation on Doped and Ultrathin MgO Films., Journal of Physical Chemistry C 119 (2015) 27594-27602.

[60] P. Nachtigall, M.R. Delgado, K. Frolich, R. Bulanek, G.T. Palomino, C.L. Bauca, C.O. Arean, Periodic density functional and FTIR spectroscopic studies on CO adsorption on the zeolite Na-FER, Microporous and Mesoporous Materials 106 (2007) 162-173.

[61] K. Lee, E. Murray, L. Kong, B. Lundqvist, D. Langreth, Higher-accuracy van der Waals density functional, Physical Review B 82 (2010) 081101.

[62] O.A. von Lilienfeld, I. Tavernelli, U. Rothlisberger, D. Sebastiani, Optimization of effective atom centered potentials for London dispersion forces in density functional theory, Physical Review Letters 93 (2004).

[63] O. Bludsky, M. Silhan, D. Nachtigallova, P. Nachtigall, Calculations of site-specific CO stretching frequencies for copper carbonyls with the "near spectroscopic accuracy": CO interaction with Cu+/MFI, Journal of Physical Chemistry A 107 (2003) 10381-10388.

[64] S. Grimme, Accurate description of van der Waals complexes by density functional theory including empirical corrections, Journal of Computational Chemistry 25 (2004) 1463-1473.

[65] O. Bludsky, M. Rubes, P. Soldan, P. Nachtigall, Investigation of the benzene-dimer potential energy surface: DFT/CCSD(T) correction scheme., The Journal of Chemical Physics 128 (2008) 114102.

[66] O. Bludsky, M. Silhan, D. Nachtigallova, P. Nachtigall, Calculations of Site-Specific CO Stretching Frequencies for Copper Carbonyls with the “Near Spectroscopic Accuracy”: CO Interaction with Cu+/MFI, The Journal of Physical Chemistry A 107 (2003) 10381-10388.

[67] P. Nachtigall, O. Bludsky, L. Grajciar, D. Nachtigallova, M.R. Delgado, C.O. Arean, Computational and FTIR spectroscopic studies on carbon monoxide and dinitrogen adsorption on a high-silica H-FER zeolite, Physical Chemistry Chemical Physics 11 (2009) 791-802.

[68] K. Wolinski, J.F. Hinton, P. Pulay, Efficient Implementation of the Gauge-Independent Atomic Orbital Method for Nmr Chemical-Shift Calculations, Journal of the American Chemical Society 112 (1990) 8251-8260.

[69] P.E. Blochl, Projector Augmented-Wave Method, Physical Review B 50 (1994) 17953-17979.

[70] G. Kresse, D. Joubert, From ultrasoft pseudopotentials to the projector augmented-wave method, Physical Review B 59 (1999) 1758-1775.

[71] G. Kresse, J. Hafner, Ab initio molecular-dynamics simulation of the liquid-metal-amorphous-semiconductor transition in germanium, Phys Rev B Condens Matter 49 (1994) 14251-14269.

[72] G. Kresse, J. Furthmuller, Efficiency of ab-initio total energy calculations for metals and semiconductors using a plane-wave basis set, Computational Materials Science 6 (1996) 15-50.

[73] C.O. Arean, M.R. Delgado, K. Frolich, R. Bulanek, A. Pulido, G.F. Bibiloni, P. Nachtigall, Computational and Fourier transform infrared spectroscopic studies on carbon monoxide adsorption on the zeolites Na-ZSM-5 and K-ZSM-5: Evidence of dual-cation sites, Journal of Physical Chemistry C 112 (2008) 4658-4666.

[74] P. Nachtigall, K. Frolich, H. Drobna, O. Bludsky, D. Nachtigallova, R. Bulanek, FTIR Study of CO Interactions with Li+ Ions in Micro- and Mesoporous Matrices: Coordination and Localization of Li+ Ions, J. Phys. Chem. C 111 (2007) 11353-11362.

[75] R. Bulanek, I. Voleska, E. Ivanova, K. Hadjiivanov, P. Nachtigall, Localization and Coordination of Mg2+ Cations in Ferrierite: Combined FTIR Spectroscopic and Computation Investigation of CO Adsorption Complexes, Journal of Physical Chemistry C 113 (2009) 11066-11076.

[76] I. Voleska, P. Nachtigall, E. Ivanova, K. Hadjiivanov, R. Bulanek, Theoretical and experimental study of CO adsorption on Ca-FER zeolite, Catalysis Today 243 (2015) 53-61.

[77] H.V. Thang, M. Rubes, O. Bludsky, P. Nachtigall, Computational Investigation of the Lewis Acidity in Three-Dimensional and Corresponding Two-Dimensional Zeolites: UTL vs IPC-1P, Journal of Physical Chemistry A 118 (2014) 7526-7534.

[78] H.V. Thang, K. Frolich, M. Shamzhy, P. Eliasova, M. Rubes, J. Cejka, R. Bulanek, P. Nachtigall, The effect of the zeolite pore size on the Lewis acid strength of extra-framework cations, Phys Chem Chem Phys 18 (2016) 18063-18073.

[79] L. Grajciar, O. Bludsky, W.J. Roth, P. Nachtigall, Theoretical investigation of layered zeolite frameworks: Interaction between IPC-1P layers derived from zeolite UTL, Catalysis Today 204 (2013) 15-21.

[80] M. Polozij, H.V. Thang, M. Rubes, P. Eliasova, J. Cejka, P. Nachtigall, Theoretical investigation of layered zeolites with MWW topology: MCM-22P vs. MCM-56, Dalton Transactions 43 (2014) 10443-10450.

[81] R. Bulanek, M. Kolarova, P. Chlubna, J. Cejka, Coordination of extraframework Li+ cation in the MCM-22 and MCM-36 zeolite: FTIR study of CO adsorbed, Adsorption-Journal of the International Adsorption Society 19 (2013) 455-463.

[82] L. Kubelkova, S. Beran, J.A. Lercher, Determination of Proton Affinity of Zeolites and Zeolite-Like Solids by Low-Temperature Adsorption of Carbon-Monoxide, Zeolites 9 (1989) 539-543.

[83] C.O. Arean, M.R. Delgado, P. Nachtigall, H.V. Thang, M. Rubes, R. Bulanek, P. Chlubna-Eliasova, Measuring the Bronsted acid strength of zeolites - does it correlate with the O-H frequency shift probed by a weak base?, Physical Chemistry Chemical Physics 16 (2014) 10129-10141.

[84] A. Zheng, S.J. Huang, S.B. Liu, F. Deng, Acid properties of solid acid catalysts characterized by solid-state 31P NMR of adsorbed phosphorous probe molecules, Phys Chem Chem Phys 13 (2011) 14889-14901.

[85] A. Zheng, S.J. Huang, W.H. Chen, P.H. Wu, H. Zhang, H.K. Lee, L.C. de Menorval, F. Deng, S.B. Liu, 31P chemical shift of adsorbed trialkylphosphine oxides for acidity characterization of solid acids catalysts, J Phys Chem A 112 (2008) 7349-7356.

[86] A. Zheng, H. Zhang, X. Lu, S.B. Liu, F. Deng, Theoretical predictions of 31p NMR chemical shift threshold of trimethylphosphine oxide absorbed on solid acid catalysts, J Phys Chem B 112 (2008) 4496-4505.

[87] Q. Zhao, W.H. Chen, S.J. Huang, Y.C. Wu, H.K. Lee, S.B. Liu, Discernment and quantification of internal and external acid sites on zeolites, Journal of Physical Chemistry B 106 (2002) 4462-4469.

[88] A.M. Zheng, S.J. Huang, W.H. Chen, P.H. Wu, H.L. Zhang, H.K. Lee, L.C. de Menorval, F. Deng, S.B. Liu, P-31 chemical shift of adsorbed trialkylphosphine oxides for acidity characterization of solid acids catalysts, Journal of Physical Chemistry A 112 (2008) 7349-7356.

[89] T.C. Keller, K. Desai, S. Mitchell, J. Perez-Ramirez, Design of Base Zeolite Catalysts by Alkali-Metal Grafting in Alcoholic Media, Acs Catalysis 5 (2015) 5388-5396.

[90] T.C. Keller, E.G. Rodrigues, J. Perez-Ramirez, Generation of Basic Centers in High-Silica Zeolites and their Application in Gas-Phase Upgrading of Bio-Oil, Chemsuschem 7 (2014) 1729-1738.

[91] T.C. Keller, M. Polozij, B. Puertolas, H.V. Thang, P. Nachtigall, J. Perez-Ramirez, Understanding the Structure of Cationic Sites in Alkali Metal-Grafted USY Zeolites, Journal of Physical Chemistry C 120 (2016) 4954-4960.

List of Attached Publications

This Thesis is based on the following articles

Attachment A:

Ho Viet Thang, Miroslav Rubeš, Ota Bludský, and Petr Nachtigall. (2014): Computational Investigation of the Lewis Acidity in Three- and Corresponding Two-Dimensional Zeolites: UTL *vs.* IPC-1P. In: *Journal of Physical Chemistry A*, 118 7526-7534.

Attachment B:

HoViet Thang, Karel Frolich, Mariya Shamzhy, Pavla Eliášová, Miroslav Rubeš, Jiří Čejka, Roman Bulánek, Petr Nachtigall. (2016): The effect of the zeolite pore size on the Lewis acid strength of extra-framework cations. In: *Physical Chemistry Chemical Physics*, 18, 18063-18073.

Attachment C:

M. Položij, **H. V. Thang**, M. Rubeš, P. Eliášová, J. Čejka, P. Nachtigall. (2014): Theoretical investigation of layered zeolites with MWW topology: MCM-22P vs. MCM-56. In: *Dalton Transaction*, 43, 10443-10450.

Attachment D:

Carlos O. Arean, Montserrat R. Delgado, Petr Nachtigall, **Ho Viet Thang**, Miroslav Rubeš, Roman Bulánek, Pavla Chlubná-Eliášová. (2014): Measuring the Brønsted acid strength of zeolites ─ does it correlate with the O−H frequency shift probed by a weak base?. In: *Physical Chemistry Chemical Physics*, 16, 10129-10141.

Attachment E:

T. C. Keller, M. Položij, B. Puértolas, **H. V. Thang**, P. Nachtigall, J. Pérez-Ramírez. (2016): Understanding the nature of basic sites in alkali metal-grafted USY zeolites. In: *Journal of Physical Chemistry C*, 120, 4954-4960.

Attached Publications

Attachment A

THE JOURNAL OF PHYSICAL CHEMISTRY A

Article

pubs.acs.org/JPCA

Computational Investigation of the Lewis Acidity in Three-Dimensional and Corresponding Two-Dimensional Zeolites: UTL vs IPC-1P

Ho Viet Thang,[†] Miroslav Rubeš,[†] Ota Bludský,[‡] and Petr Nachtigall*,[†]

[†]Department of Physical and Macromolecular Chemistry, Faculty of Sciences, Charles University, Hlavova 8, 128 40 Prague 2, Czech Republic

[‡]Institute of Organic Chemistry and Biochemistry, Academy of Sciences of the Czech Republic, Flemingovo nam. 2, 166 10 Praha 6, Czech Republic

Supporting Information

ABSTRACT: The adsorption and catalytic properties of three-dimensional zeolite UTL were investigated computationally along with properties of its two-dimensional analogue IPC-1P that can be obtained from UTL by a removal of D4R units. Adsorption properties and Lewis acidity of extra-framework Li^+ sites were investigated for both two- and three-dimensional forms of UTL using the carbon monoxide as a probe molecule. The CO adsorption enthalpies, calculated with various dispersion-corrected DFT methods, including DFT/CC, DFT-D2, and vdW-DF2, and the CO stretching frequencies obtained with the ν_{CO}/r_{CO} correlation method are compared for corresponding Li^+ sites in 3D and 2D UTL zeolite. For the majority of framework Al positions the Li^+ cation is preferably located in one of the channel wall sites and such sites remains unchanged upon the 3D → 2D UTL transformation; consequently, the adsorption enthalpies become only slightly smaller in 2D UTL (less than 3 kJ mol^{-1}) due to the missing part of dispersion interactions and ν_{CO} becomes also only up to 5 cm^{-1} smaller in 2D UTL due to the missing repulsion with framework oxygen atoms from the opposite site of the zeolite channel (effect from the top). However, when Li^+ is located in the intersection site in 3D UTL (about 20% probability), its coordination with the framework is significantly increased in 2D UTL and that is accompanied by significant decrease of both ν_{CO} (about 20 cm^{-1}) and adsorption enthalpy (about 20 kJ mol^{-1}). Because the intersection sites in 3D UTL are the most active adsorption and catalytic Lewis sites, the results reported herein suggest that the 3D → 2D transformation of UTL zeolite is connected with partial decrease of zeolite activity in processes driven by Lewis acid sites.

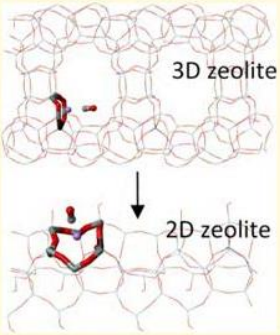

1. INTRODUCTION

Zeolites are well-known for their exceptional catalytic and sorption properties.[1,2] The size of microporous channels is among the most important factors for zeolite applications; however, it can also limit the accessibility of active sites. The concept of hierarchical zeolites combining the microporosity and the mesoporosity has attracted a great deal of attention in the past decade.[3] The presence of mesopores enhances the diffusion in and out of the zeolite crystal and even bulkier molecules can diffuse through mesopores toward catalytic active sites in the pore-mouth of microporous channels.[4] Experimental routes leading toward hierarchical zeolites include post synthesis modification of regular three-dimensional (3D) zeolites leading to the formation of mesoporous channels and cavities (e.g., dealumination and desilication procedures),[3] formation of mesopores between synthesized 2D layered zeolite precursors (e.g., swelling and stabilization of MCM-22P layered precursor),[5] and/or conversion of 3D zeolite into 2D zeolite layers by mild-acid treatment followed by swelling and pillaring (e.g., transformation of UTL into 2D IPC-1P layers).[6−8] Although the first strategy (dealumination and/or desilication) appears to be the most general and experimentally relatively easy, the structure of resulting mesoporous materials is the least understood at the atomistic level. The latter two strategies (based on 2D zeolites) were so far exercised on only a few types of zeolites; however, it is believed that the structure of 2D zeolite layers remains intact.[9]

The presence of mesoporous channels and cavities in hierarchical zeolites has been shown to increase the catalytic activity with respect to the corresponding regular 3D zeolite.[3,10,11] A decrease of diffusion limitations invoked by the presence of mesopores has certainly a positive effect on the catalytic activity of the material, whereas the catalytic activity of individual active sites (either Brønsted or Lewis acid sites) can be influenced in either way upon the transformation from regular 3D zeolite to a hierarchical material, and it has not been well understood so far. It is the goal of the theoretical investigation presented herein to investigate the differences in catalytic activity of individual active sites in regular and

Special Issue: Kenneth D. Jordan Festschrift

Received: January 30, 2014
Revised: April 3, 2014
Published: April 3, 2014

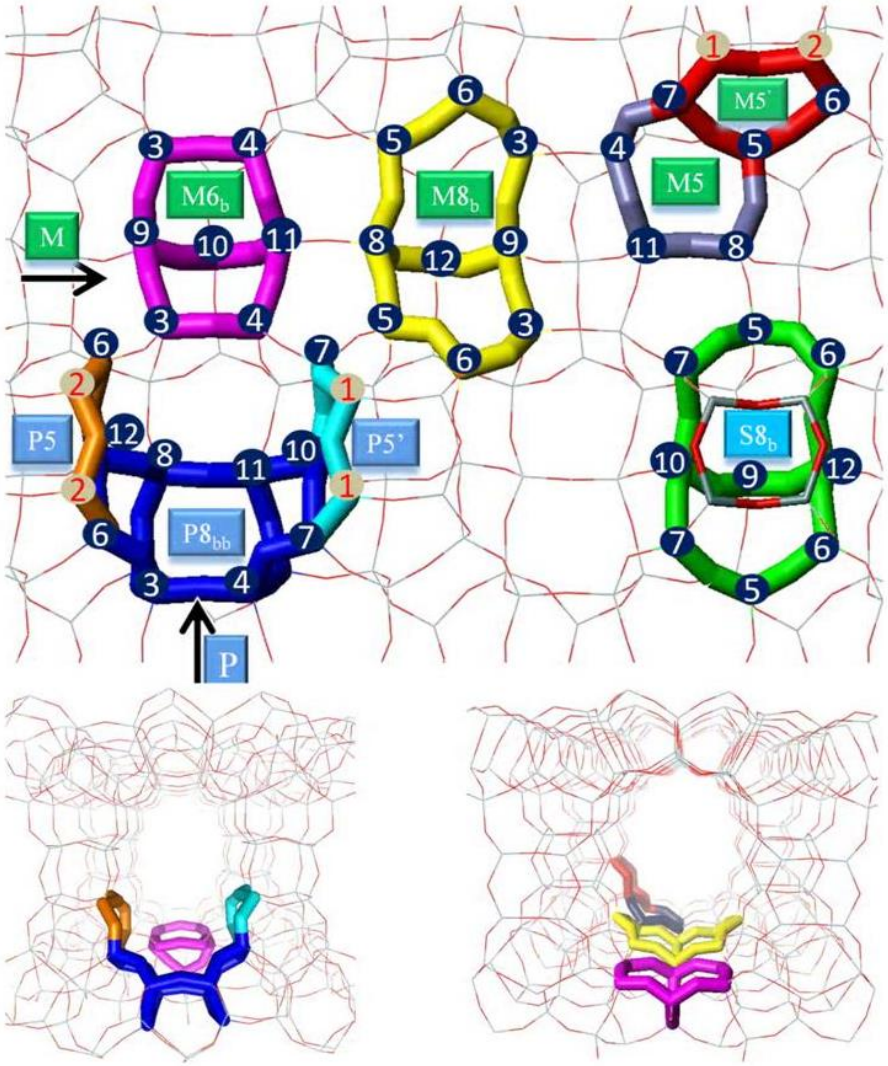

Figure 1. Notation adopted for extra-framework cation sites in UTL and in corresponding 2D-UTL (IPC-1P material). Sites in the main and perpendicular channels are denoted as M*x* and P*x*, respectively, where *x* stands for the size of the ring where the cation is located. A new surface site created by the D4R removal is denoted $S8_b$. The framework atom numbering scheme is also shown. The localization of sites in 12R and 14R channels of UTL are shown in the left and right bottom parts, respectively, keeping the color scheme defined in the upper part of the figure.

hierarchical zeolites. The regular 3D UTL zeolite and the corresponding 2D IPC-1P layered material are chosen for computational investigation of Lewis acidity of extra-framework cation sites in 3D and 2D materials. The small Li^+ cation is used as extra-framework cation because it is expected to be more sensitive to the effects of zeolite dimensionality on its Lewis acidity than larger monovalent cations.[12,13]

The catalytic properties of 2D zeolites have been computationally investigated in only few cases. The most relevant investigation presented so far is the study of Brønsted acid sites formed on the upper surface of aluminosilicate bilayer formed on the Ru(0001) surface.[14] The acidity and the adsorption of probe molecules (CO, C_2H_4, C_5H_5N, and NH_3) on Brønsted sites of such 2D aluminosilicate bilayer were investigated at the DFT level of theory and infrared reflection absorption spectroscopy and compared with those obtained for H−CHA zeolite.[15] Calculations performed at periodic DFT level employing the ν/r correlation method[16] showed, in agreement with experimental observation, the following trends: (i) the interaction of strong bases with bilayer results in the proton transfer from the Brønsted site to the base; (ii) the interaction of weak bases with Brønsted acid site in bilayer leads to a larger red shift in OH stretching frequencies than found for H−CHA, indicating a higher acidity; (iii) larger adsorption enthalpies were calculated for weak bases adsorbed on H−CHA than on bilayer. These results brought new understanding of the differences in Brønsted acidity in 3D and 2D materials.

We are not aware of any such investigation of Lewis acidity; therefore, the coordination of extra-framework Li^+ cations in the vicinity of framework Al atoms is investigated in regular 3D UTL zeolite and its 2D analogue IPC-1P first. The Lewis acidity of Li^+ sites in 3D and 2D materials is investigated as well, modeling the properties of carbon monoxide adsorption complexes.

2. COMPUTATIONAL DETAILS

2.1. Periodic Calculations. The UTL zeolite has a monoclinic unit cell with $C2/m$ space group ($T_{64}Ge_{12}O_{152}$, where T is either Si or Al atom) in which 12 Ge and 4 Si atoms are located in the double-four ring (D4R) units.[17,18] The UTL structure shows a two-dimensional channel system with main channel (approximately) along the c vector defined by a 14-ring (9.5 × 7.1 Å) and the perpendicular channel along b defined by a 12-ring (8.5 × 5.5 Å). The unit cell parameters (a = 29.8004 Å, b = 13.9926 Å, c = 12.3926 Å, and $\alpha = \gamma = 90°$, β = 105.185°) were taken from the ref 17. Following a recent experimental discovery, that D4R units can be selectively hydrolyzed[6,19] leading to a two-dimensional layered zeolite IPC-1P, the model of IPC-1P was simply obtained by removal of D4R units and saturation of broken Si−O−Si surface bonds with hydrogens (forming surface silanols). Two layers of IPC-1P in a unit cell are thus obtained; only one of these layers was kept in subsequent calculations on two-dimensional material IPC-1P and the distance between layers was adjusted to 20 Å along the a direction. A parent (3D) UTL zeolite and its 2D IPC-1P analogue are denoted 3D-UTL and 2D-UTL, respectively.

All calculations were carried out with the periodic model using the Vienna ab initio simulation package (VASP).[20] The Perdew−Burke−Ernzerhof[21] (PBE) exchange−correlation functional, the projector augmented wave approximation (PAW),[22,23] and the plane wave basis set with a kinetic energy cutoff of 400 eV were used for the description of CO adsorption; the Brillouin-zone sampling was restricted to the Γ-point. Geometry optimizations were performed with frozen unit cell parameters while relaxing positions of all ions. The DFT/CC interaction energies were calculated at PBE optimized geometries by employing the correction functions described below in section 2.2. For comparison, the DFT-D2[24] and vdW-DF2[25] values are also included. The zero-point energies (ZPE) were calculated within the harmonic approximation considering six degrees of freedom for the CO molecule (two displacements in each direction with a step size of 0.005 Å were used to calculate the corresponding second derivatives numerically). Following the strategy used previously for CO interaction with H-FER the standard adsorption enthalpy ΔH^0 is reported at 0 K only. The stretching frequencies of all adsorbed CO molecules were evaluated using the ν_{CO}/r_{CO} correlation scheme (see ref 26 for more details). For the selected Li^+ sites the adsorption of carbon monoxide, ammonia, acetonitrile, and pyridine was investigated at the vdW-DF2 level.

The numbering scheme (following the Database of Zeolite Structures[27]) for 2D-UTL and 3D-UTL frameworks is shown in Figure 1. Substitution of Al in 10 distinguishable T sites and all possible Li^+ cation positions in the vicinity of Al atoms to counterbalance the negative charge were considered. The CO adsorption was investigated for the most stable Li^+ sites in the vicinity of each framework Al. The extra-framework cation site notations are also shown in Figure 1; following the notation introduced previously for high-silica MFI and FER[28,29] the sites in main and perpendicular channels (type I sites) are denoted Mx and Px, respectively, x standing for the size of the ring on the channel wall surface where the cation is located. The site formed upon the removal of D4R in 2D-UTL is denoted $S8_b$. Intersection sites where extra-framework cations are located on the intersection, and they interact only with two framework oxygen O_f atoms, are denoted I2.

2.2. Cluster Calculations. The cluster model calculations have been carried out with standard augmented Dunning's correlation-consistent valence-X-ζ basis set with polarization functions.[30] The basis sets will be collectively denoted as AVXZ, where X stands for double, triple and quadruple basis sets, respectively. The complete basis set limit (CBS) has been obtained from simple dependence on basis set cardinal number, as proposed in ref 31. For the calculation on large clusters with up to 53 $TO_{4/2}$ tetrahedra, the triple ζ basis set with polarization functions (def2-TZVPP)[32] was employed. All interaction energies are counterpoise corrected by means of standard Boys and Bernardi procedure.[33]

The DFT/CC method has been employed to correct PBE interaction energies.[34] The DFT/CC correction scheme is based on the pairwise representability of the DFT error given as

$$\Delta E = E_{CCSD(T)} - E_{DFT}$$

where $E_{CCSD(T)}$ and E_{DFT} are interaction energies calculated at the CCSD(T)/CBS and the DFT/AVQZ levels of theory, respectively. The DFT error, ΔE, is then expressed as a sum of pairwise atom−atom correction functions $\varepsilon_{ij}(R_{ij})$:

$$\Delta E = \sum_{ij} \varepsilon_{ij}(R_{ij})$$

where R_{ij} is the distance between atoms i and j. There is no assumption about the functional form of ε_{ij}; instead the reciprocal-power reproducing kernel Hilbert space[35] (RP-RKHS) interpolation is used. The correction functions, ε_{ij}, are calculated from the reference set of molecules; for the purpose of this work H_2···CO, $Si(OH)_4$···CO, $Si_2O(OH)_6$···CO, and $Al(OH)_4Li$···CO complexes were used. All cluster calculations have been carried out in G09, Molpro, and Turbomole quantum chemistry packages.[36−38] More details about the cluster calculations and DFT/CC can be found in the Supporting Information.

3. RESULTS AND DISCUSSION

3.1. Interaction of CO with Zeolites: Accuracy of the DFT/CC Method. The CO interaction with Li exchanged UTL is inadequately described at the PBE level of theory due to the missing dispersion interactions of CO with the UTL framework. Even though this DFT deficiency is well described in the literature, the performance of different dispersion corrected (DC) schemes significantly differs.[39,40] The accuracy of the presented DFT/CC model can be at least partially established against available experimental results. Because the experimental results for CO interaction with UTL are not yet available, the computational results obtained for CO interaction with the purely siliceous MFI material (silicalite-1) and with the Li-exchanged FAU zeolite are presented first and compared with available experimental data. On the basis of the recent investigation of CO_2 adsorption in Na- and Li-FAU zeolites, the calculations on Li-FAU were carried out for Li^+ cations in type II sites formed inside the 6R with 2 framework Al atoms separated by two SiO_4 tetrahedra (site denoted II-2Al(s), see ref 41 for details).

The interaction energies of CO with silicalite-1 and Li-exchanged FAU zeolites are summarized in Table 1. The adsorption enthalpies calculated at the PBE level (not accounting for dispersion interactions) are severely under-

dx.doi.org/10.1021/jp501089n | J. Phys. Chem. A 2014, 118, 7526−7534

Table 1. Comparison of Adsorption Enthalpies (kJ mol^{-1}) Calculated at Various Levels of Theory with Experimental Data; CO Adsorption in Silicalite-1 and in Li-Exchanged FAU[a]

method	silicalite-1	Li−Y[b]
PBE	−1.7[c]	−20.2
DFT-D2	−16.4	−34.6
vdW-DF2	−27.1	−35.2
DFT/CC	−16.0	−26.3
experiment	−16 ± 1[c]	−27.5[d]

[a]All DFT calculations carried out with plane-wave cutoff 400 eV and vdW-DF2 calculations with 400 and 800 eV cutoffs give interaction energies within 0.5 kJ mol^{-1}. PBE exchange−correlation functional employed in DFT-D2 and DFT/CC models. [b]The results obtained for Li^+ in the site II (6R accessible from supercage) with 2 Al atoms are reported (see ref 41 for details on the SII−Al(s) site). [c]Reference 42. [d]Reference 43. [e]Without ZPVE correction.

estimated, as expected. A large overestimation reported in Table 1 for the vdW-DF2 functional is rather unexpected; it follows that this nonlocal functional cannot be used for the description of CO adsorption in zeolites. The results obtained with both PBE-D2 and DFT/CC methods agree well with the experimentally determined CO adsorption enthalpy for Silicalite-1 (−16 ± 1 kJ mol^{-1}).[42] Considering the almost negligible interaction energy obtained at the PBE level of theory, it can be concluded that CO interaction with silicalite-1 can be almost entirely attributed to dispersion interactions.

The calculated adsorption enthalpy of CO on Li-FAU agrees with experimental data[43] only for DFT/CC level of theory. Note that the sum of DFT/CC correction function obtained for Li^+−C and Li^+−O is positive, reflecting the fact that CO interaction with Li^+ cation is overestimated at the PBE level (Figure 2a). The adsorption enthalpy calculated at the DFT-D2 level is overestimated by 7 kJ mol^{-1}; this overestimation comes mainly from PBE deficiency to correctly describe Li^+−CO interaction. Thus, changing the D2 dispersion correction for Li to DFT/CC yields an adsorption enthalpy of −25.3 kJ mol^{-1} in very good agreement with DFT/CC adsorption enthalpy.

To verify the suitability of DFT/CC method for the description of CO adsorption in alkali-metal exchanged zeolites, two additional tests were performed: (i) dependence of DFT error on Li^+ coordination (transferability of Li−C and Li−O correction functions) and (ii) the effect of CO polarization (by Li^+) on the dispersion interaction between the polarized CO and the zeolite framework. Interaction energies of CO with LiF (linear $F^-Li^+\cdots$CO complex) were calculated for different Li−F distances (2.0, 1.8, and 1.6 Å), a model that mimics the increasing Li^+ coordination in zeolites. Calculations were carried out for nine different commonly used exchange−correlation functionals and compared with the results obtained at reference CCSD(T)/CBS level (Table SI-1, Supporting Information). The following conclusions can be drawn: (i) The BP86 functional gives the results within 1 kJ mol^{-1} of CCSD(T)/CBS values. The B3LYP, PBE0, and M06L functionals give results comparable to those at the MP2 level of theory, still about 3 kJ mol^{-1} overestimated with respect to the reference level of theory. Other functionals perform comparably to PBE; they overestimate the interaction by 5−7 kJ mol^{-1}. As for the transferability of the DFT/CC correction function, the corresponding error due to transferability issue is smaller than 1 kJ mol^{-1}. Figure 2b clearly shows that the effect

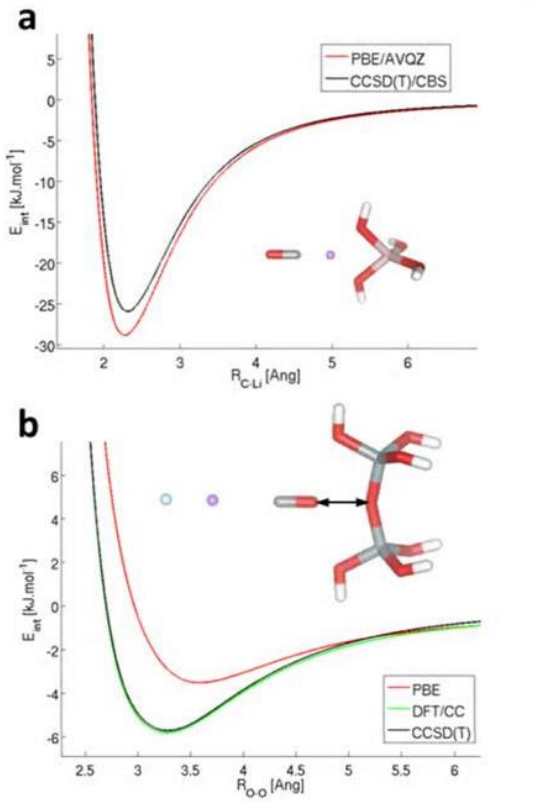

Figure 2. Potential energy functions of CO interacting with the $Li^+\cdots$1T model of the adsorption site (a) and polarized CO interacting with the 2T model of the zeolite channel wall (b) calculated at DFT, DFT/CC, and CCSD(T) levels of theory.

of CO polarization on the transferability of DFT/CC correction functions is negligible. To summarize this part, the DFT/CC method appears to be accurate for the systems investigated herein because this method is designed to correct any deficiency of DFT functionals for intermolecular interactions, not only missing dispersion interactions.

3.2. Li^+ Sites in 3D and 2D UTL Zeolites. The Al atom can be substituted in place of Si in 10 different tetrahedral T positions of 3D and 2D UTL zeolite (T3-T12). The two remaining T positions (T1,T2) are located inside the D4R building units. The negative charge introduced by AlO_4 tetrahedra is compensated by the Li^+ ions placed in the vicinity of T positions occupied by Al atoms. The most stable Li^+ sites for each Al position in 3D-UTL and 2D-UTL zeolites are reported in Table 2. Two types of extra-framework cation positions can be distinguished: (i) type I sites,[44] where the Li^+ cation is placed in the main or perpendicular channel on top of a ring located on the surface of the channel wall (M5, P5, M6b, M8b, P8bb sites), and (ii) type II sites located at the intersection, where Li^+ is placed on the edge formed by the two intersecting channels. As can be seen from Table 2, Li^+ can be coordinated with two, three, and four framework oxygen atoms. Compared with intersection sites, Li^+ located in the channel wall sites are placed closer to the channel surface, interacting thus strongly with the nearest framework oxygen atoms, and as a result the channel wall Li^+ sites have typically a lower ability to bind the CO molecule. The distances between Li^+ and framework oxygen atoms ($r(Li^+\cdots O_f)$) shorter than 2.3

Table 2. Li−O_f Distances (Å) of the Most Stable Li^+ Sites in the Vicinity of Al in Ten Different Framework Positions Found for 3D-UTL and 2D-UTL Zeolites

	3D-UTL		2D-UTL	
Al position	Li^+ site	$r(Li\cdots O_f)$	Li^+ site	$r(Li\cdots O_f)$
T3	M8b	1.86, 1.97, 2.16	P8bb	1.98, 2.02, 2.19
T4	P8bb	1.86, 1.88	P8bb	1.87, 1.88
T5	M8b	1.94, 1.95, 2.08	M8b	1.93, 1.96, 2.08
T6	I2	1.86, 1.87	P5[a]	1.90, 1.90, 2.04
T6(Ge)	M5′	2.03, 2.04, 2.07, 2.08		
T7	I2	1.85, 1.88	M5′[a]	1.88, 1.91, 1.99
T7(Ge)	I2	1.85, 1.86		
T8	M8b	1.91, 1.93, 2.02	P8bb	1.92, 1.95, 2.18
T9	M8b	1.94, 1.99, 2.07, 2.18	M8b	1.94, 2.01, 2.02, 2.23
T10	P5′	1.90, 1.94, 1.95	S8b	1.93, 2.07, 2.11, 2.11
T11	M6b	1.97, 2.00, 2.21	M6b	1.93, 1.93, 2.07
T12	M8b	1.89, 1.98, 2.10	P5	1.92, 1.99, 2.07

[a]AlOH.

Å along with the relative energies with respect to the most stable Li^+ site for each T position are reported in Table SI-2 (Supporting Information); total energies of the most stable Li^+ sites are also included.

In agreement with previous investigation of Li^+ coordination in high-silica zeolites ZSM-5 and FER,[13,29] the Li^+ cation is preferably located in site I types on the channel wall surface. The only exceptions are the cases when framework Al is in T6 and T7 sites in 3D UTL zeolite when the Li^+ cation is located in type II sites I2. Results reported in Table 2 for 3D-UTL and 2D-UTL show that the coordination of Li^+ upon 3D to 2D transformation can be affected in three different ways: (i) There is no change in coordination and location of Li^+ upon transition to 2D material (case when framework Al is in T4, T5, T9, and T11); note that neither the number of O_f coordination to Li^+ nor $r(Li-O_f)$ is affected. (ii) The Li^+ is located in type I sites (channel wall) in both 3D and 2D cases; however, the location of the cation is changed (framework Al in T3, T8, T10, and T12). Apparently, the transformation of 3D UTL into layered material results in changes in relative energies of Li^+ in available cation sites in the vicinity of particular framework aluminum. (iii) Li^+ located in the intersection site in 3D UTL (type II) moves to a type I site and the number of O_f atoms interacting with Li^+ increases. This change, however, is accompanied by only small displacement of the Li^+ position. One of two O_f atoms coordinated to Li^+ in the type II site becomes a surface silanol oxygen atom; due to increased flexibility of such an oxygen atom, both Li^+ and this oxygen atom move closer to different O_f atoms and, consequently, the coordination of Li^+ with the framework increases (see Figure 3e,f for the case with Al in T6 position). Note, however, that in this case the framework Al has one silanol group; thus, such a site would be susceptible to dealumination.

Note also the difference in Li^+ sites when Al is in the T6 position adjacent to either the Si or Ge atom in the T2 position (Table 2). The difference in interaction energy of the Li^+ cation with the negatively charged framework for 3D and 2D zeolite was calculated for Al in the T7 position (I2 and M5 sites, respectively) using cluster models consisting of 53 and 43 $TO_{4/2}$ tetrahedra and the PBE/TZVPP level of theory. The interaction of Li^+ with 3D UTL was found to be stronger than with the 2D UTL; however, the difference was only 7 kJ mol^{-1}.

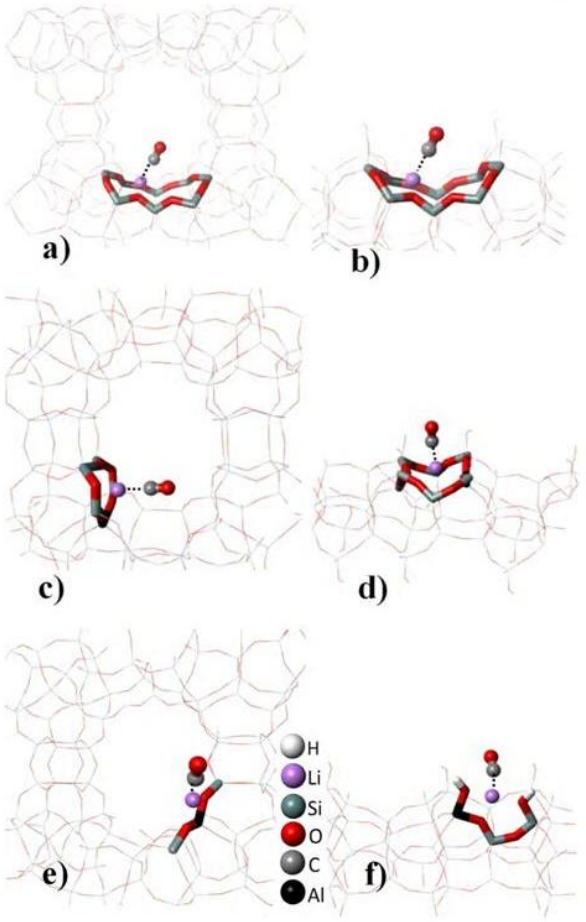

Figure 3. CO adsorption complexes at the most stable Li^+ site in 3D-UTL (left column) and 2D-UTL (right column), shown for Al in T5 (a,b), T10(c,d), and T6 (e,f) positions.

3.3. CO Adsorption in 3D and 2D Li-UTL. To understand the effect of 3D → 2D transformation of zeolites on the Lewis acidity, the adsorption complexes with CO (weak base) were investigated for all Li^+ sites described above. Adsorption enthalpies and CO stretching frequencies are summarized in Table 3 and examples of adsorption complexes formed on 3D and 2D materials are given in Figure 3; only the C-down adsorption complexes were considered. Structures of all adsorption complexes are given in the Supporting Information. Dispersion terms contribute significantly to the total CO binding, ranging from 6 to 14 kJ mol^{-1} for both 3D- and 2D-UTL (Table SI-3 in Supporting Information). The smallest contribution is observed for the intersection sites of 3D-UTL. The 3D → 2D transition is accompanied by a small change of a dispersion contribution; the difference of only about 1 kJ mol^{-1} is observed for majority of sites whereas in some cases (Al in T4, T7, T10, and T12) the dispersion contribution in the 2D material is reduced by 2−6 kJ mol^{-1} with respect to the 3D-UTL.

Compared to those for 3D-UTL, the adsorption enthalpies calculated for corresponding Li^+ sites (the same Al position) in 2D-UTL are lower. Two types of sites can be identified: (i) Sites showing small relative change of ΔH^0 and ν_{CO} (Al in T3, T5, T8, T9, T11, and T12). The difference in adsorption

dx.doi.org/10.1021/jp501089n | J. Phys. Chem. A 2014, 118, 7526−7534

Table 3. Characteristics of CO Adsorption Complexes Formed on Li^+ Sites in 3D- and 2D-UTL: Li−C Distances, CO Frequencies, and Adsorption Enthalpies

zeolite	Al position	Li^+ site	R_{Li-C} [b]	ν_{CO} [a]	$\Delta H^0(0K)$ [c]
3D-UTL	T3	M8b	2.27	2188	−33.7
	T4	P8bb	2.25	2192	−38.9
	T5	M8b	2.29	2186	−31.2
	T6	I2	2.25	2197	−41.6
	T6(Ge)	M5′	2.27	2186	−29.4
	T7	I2	2.25	2196	−40.3
	T7(Ge)	I2	2.26	2196	−36.4
	T8	M8b	2.26	2187	−36.3
	T9	M8b	2.30	2182	−30.4
	T10	P5′	2.26	2191	−38.3
	T11	M6b	2.27	2190	−31.1
	T12	M8b	2.27	2187	−36.0
2D- UTL	T3	P8bb	2.27	2187	−34.1
	T4	P8bb	2.25	2190	−34.2
	T5	M8b	2.29	2183	−30.6
	T6	P5	2.36	2175	−23.5
	T7	M5′	2.31	2177	−21.2
	T8	P8bb	2.27	2184	−36.2
	T9	M8b	2.32	2177	−27.6
	T10	S8b	2.30	2175	−21.8
	T11	M6b	2.29	2185	−30.8
	T12	P5	2.28	2184	−33.3

[a]CO stretching frequencies (cm^{-1}) have been obtained from PBE optimized geometries by means of the ν_{CO}/r_{CO} correlation scheme. [b]In Å. [c]In kJ mol^{-1}.

enthalpies does not exceed 3 kJ mol^{-1} and ν_{CO} is not changed by more than 5 cm^{-1} (Table 3). Note that small changes in the adsorption enthalpy do not correlate with small changes of ν_{CO}; the decreased ν_{CO} is thus attributed to the effect from the top−electrostatic interaction between adsorbed CO, and the framework oxygen atoms on the opposite site of the zeolite channel (increasing the CO frequency) are missing in 2D-UTL.[45,46] (ii) Sites showing significant decrease of both adsorption enthalpy and CO stretching frequency (Al in T6, T7, and T10). Adsorption enthalpies are almost 20 kJ mol^{-1} lower, and CO stretching frequencies are about 20 cm^{-1} lower in 2D- than in 3D-UTL. The decrease is mostly due to the increased coordination of the Li^+ cation with the 2-D framework that results in decreased Lewis acidity of these sites. Considering the case with Al in T10 in detail, ΔH^0 calculated for 3D and 2D systems are −38.3 and −21.8 kJ mol^{-1} (Table 3), respectively; about 6 kJ mol^{-1} (Table SI-3, Supporting Information) of this 16.5 kJ mol^{-1} difference is due to the smaller contribution of dispersion terms in the 2D case, and the remaining part must be attributed to the improved coordination of Li^+ with the framework that changes from three to four (P5′ and S8b sites, respectively, Table 2). Note that even in this case, where the effect of the changed dispersion is the largest (Table SI-3, Supporting Information), the difference between 3D- and 2D-UTL is mostly determined by the Li^+ coordination with the framework.

3.4. Adsorption of Ammonia, Acetonitrile, and Pyridine in 3D- and 2D-UTL. To verify that conclusions drawn above based on the CO adsorption hold also for other adsorbates, the adsorption of NH_3, C_2H_3N, and C_5H_5N was investigated. Results obtained at the vdW-DF2 level are reported in Table 4 together with those obtained for CO at

Table 4. Interaction Energies of Carbon Monoxide, Ammonia, Acetonitrile, and Pyridine on Selected Li^+ Sites in 3D- and 2D-UTL[a]

		3D		2D	
probe	Al position	Li^+ site	ΔE_{int}	Li^+ site	ΔE_{int}
CO	T5	M8b	−47.2	M8b	−50.9
	T6	I2	−53.6	P5	−35.9
	T10	P5′	−57.8	S8b	−41.2
NH_3	T5	M8b	−103.7	M8b	−105.8
	T6	I2	−120.2	P5	−88.2
	T10	P5′	−118.6	S8b	−102.9
C_2H_3N	T5	M8b	−104.5	M8b	−112.8
	T6	I2	−133.1	P5	−96.0
	T10	P5′	−110.1	S8b	−96.4
C_5H_5N	T5	M8b	−142.5	M8b	−131.0
	T6	I2	−155.2	P5	−99.1
	T10	P5′	−138.4	S8b	−96.7

[a]Interaction energies (kJ mol^{-1}) calculated at the vdW-DF2 level without ZPVE corrections.

the same level of theory. Adsorption on three representative sites was considered: the case of Al in T5 represents the situation where there is no change in Li^+ coordination between 3D- and 2D-UTL; and cases of Al in T6 and T10 represent the situation where Li^+ coordination is increased upon 3D → 2D transformation. Note that electronic interaction energies (without ZPVE correction) are reported in Table 4 and that the vdW-DF2 overestimates the interaction compared to DFT/CC and experiment; the results in Table 4 bring a qualitative understanding only.

The adsorption of ammonia and acetonitrile shows exactly the same trends as reported above for the CO adsorption: adsorption enthalpies are relatively unchanged upon 3D → 2D transformation in the case of Al in T5 whereas they are significantly decreased in cases of Al in T6 and T10. A small deviation from this observation is observed for acetonitrile adsorbed on 2D-UTL when Al is in T5; about 10 kJ mol^{-1} larger interaction energy is due to the fact that CH_3 group forms two weak H-bonds with surface silanol groups. Even the adsorption of pyridine supports the conclusions drawn above. The increasing role of dispersion interactions results in small decrease of adsorption energy even in the case of Al in T5 and large decrease of adsorption energy in other two cases.

Results reported herein for the Lewis acidity of Li^+ sites in 3D and 2D zeolites can be compared with relevant results reported previously for Brønsted acidity.[15] A combined experimental and theoretical investigation of 2D planar bilayer aluminosilicate sheets of polygonal prisms and 3D zeolite chabasite showed an increased acidity and weaker interaction with probe molecules for 2D system.[15] These results are only in partial agreement with the results reported herein for Lewis acidity. In agreement with ref 15 the decrease of adsorption due to the decrease of dispersion interactions is observed for adsorption on some Li^+ sites. The effect of 3D → 2D transformation on CO vibrational frequency is, however, rather different for Brønsted and Lewis acid sites. Though the 2D zeolite containing Brønsted acid sites shows a higher CO frequency (compared to corresponding 3D material), indicating higher acidity, the 3D → 2D transformation of Li-UTL leads to a small or moderate (up to 20 cm^{-1}) decrease of CO frequency, indicating a lower Lewis acidity. The difference is most likely due to two effects: (i) A 2D polygonal prism does not contain

dx.doi.org/10.1021/jp501089n | J. Phys. Chem. A 2014, 118, 7526−7534

any surface silanol groups whereas there is a large concentration of surface silanol groups in 2D-UTL that can interact with Li^+ cations, resulting in an improved Li^+ coordination with the framework and lower acidity. (ii) A presence of surface silanol groups in 2D-UTL increases the flexibility of the framework, resulting again in the improved interaction of Li^+ cations with the framework. Note that framework flexibility is essential for the Brønsted acidity as well.[47] Apparently, a 2D planar bilayer aluminosilicate sheet of polygonal prisms used in ref 15 is rather different from a 2D IPC-1P zeolite investigated herein. A former 2D model more closely represents a 3D zeolite than a latter one; however, the silanol-containing 2D zeolite layers are more common and they have been prepared for various zeolites.[48] To reconcile the results reported for Brønsted and Lewis acidities (ref 15 and present investigation, respectively), it is necessary to investigate both types of acidities on the same 2D material.

4. CONCLUSIONS

The differences in extra-framework cation coordination and corresponding Lewis acidity in regular 3D-UTL and layered 2D-UTL (IPC-1P) zeolites were investigated computationally. Small Li^+ cations were chosen because they are most sensitive to the changes in coordination with the zeolite framework and their Lewis acidity was probed by the interaction with the weakly basic CO molecule. The Li^+ sites in the vicinity of framework Al atom in 10 positions (ignoring sites T1 and T2 in D4R) were considered. Similarly as in other high-silica zeolites, the extra-framework Li^+ cations can be coordinated either at the channel wall sites (type I sites) or at the channel intersection sites (type II sites). Upon the 3D → 2D transformation of UTL the intersection sites no longer exist and all Li^+ cations in 2D-UTL are located in type I sites and in some of them Li^+ interacts with framework silanol in addition to regular framework oxygen atoms.

In the majority of cases (8 out of 10 framework Al positions) the Li^+ cation is located in type I site in both 3D- and 2D-UTL; either the same cation site is occupied in 3D- and 2D-UTL or the Li^+ site changes in 2D- with respect to 3D-UTL but both being channel wall sites (type I) with similar coordination of the cation with framework oxygens. The adsorption enthalpies and CO stretching frequencies are then only slightly lowered upon the 3D → 2D conversion (by about 3 kJ mol^{-1} and 5 cm^{-1}, respectively). These changes do not represent any significant change in the Lewis acidity of corresponding Li^+ sites and they result from a combination of decreased dispersion interactions in 2D material (part of the framework atoms is simply missing compared to 3D UTL) and small changes in Li^+ coordination in 3D and 2D zeolite. Small changes in ν_{CO} are most likely due to the missing electrostatic repulsion between adsorbed CO and framework oxygen atoms on the opposite site of the channel where CO is located.

The Li^+ sites exhibiting the highest Lewis acid character are those located at the intersection of 3D-UTL (I2 sites found for framework Al in T6 and T7); they are characterized with the largest adsorption enthalpy of −42 kJ mol^{-1} and the highest CO stretching frequencies 2197 cm^{-1}. This finding is consistent with previous results reported for, e.g., Li-MFI and Li-FER.[13,49] Upon the conversion to 2D-UTL the Li^+ cations in the vicinity of framework Al in T6 and T7 exhibit the smallest Lewis acidity ($\Delta H^0 \sim -23$ kJ mol^{-1} and $\nu_{CO} \sim 2176$ cm^{-1}). Consequently, the strongest Lewis acid sites in 3D-UTL are destroyed by the 3D → 2D transformation and the corresponding activity for processes driven by the Lewis acid sites should be lower in 2D-UTL than in 3D-UTL. Thus, the improved diffusion of reactants and products expected for pillared 2D zeolite layers (compared to regular 3D zeolites) are likely to be partially compensated by the decrease of the Lewis acidity of sites in 2D zeolites. The conclusions drawn here for 3D vs 2D UTL zeolites based on adsorption of the CO probe molecule are supported also by the calculations performed for NH_3, C_2H_3N, and C_5H_5N molecules.

■ ASSOCIATED CONTENT

Supporting Information

Details of DFT/CC calculations are provided together with tables reporting reliability of various exchange−correlation functionals with respect to coupled cluster benchmark calculations (Table SI-1), details of Li^+ sites in 3D- and 2D-UTL (Table SI-2), and evaluation of the importance of dispersion interactions for the adsorption in 3D- and 2D-UTL (Table SI-3). Structures of all CO adsorption complexes are provided in cif format.This material is available free of charge via the Internet at http://pubs.acs.org.

■ AUTHOR INFORMATION

Notes

The authors declare no competing financial interest.

■ ACKNOWLEDGMENTS

This work was supported by the Czech Science Foundation Grant No. P106/12/G015 (Center of Excellence) and by European Union Seventh Framework Programme (FP7/2007-2013) under grant agreement no. 604307. Calculations were partially performed at MetaCentrum and CERIT-SC computational facilities (MSM/LM2010005 and OP VaVpI CZ. 1.05/3.2.00/08.0144).

■ REFERENCES

(1) Corma, A. Inorganic solid acids and their use in acid-catalyzed hydrocarbon reactions. *Chem. Rev.* **1995**, *95* (3), 559−614.
(2) Kubicka, D.; Kubickova, I.; Cejka, J. Application of Molecular Sieves in Transformations of Biomass and Biomass-Derived Feedstocks. *Catal. Rev.* **2013**, *55* (1), 1−78.
(3) Valtchev, V.; Majano, G.; Mintova, S.; Perez-Ramirez, J. Tailored crystalline microporous materials by post-synthesis modification. *Chem. Soc. Rev.* **2013**, *42* (1), 263−290.
(4) Perez-Ramirez, J. ZEOLITE NANOSYSTEMS Imagination has no limits. *Nat. Chem.* **2012**, *4* (4), 250−251.
(5) Roth, W. J.; Čejka, J. Two-dimensional zeolites: dream or reality? *Catal. Sci. Technol.* **2011**, *1* (1), 43−53.
(6) Roth, W. J.; Shvets, O. V.; Shamzhy, M.; Chlubna, P.; Kubu, M.; Nachtigall, P. Čejka, J. Postsynthesis Transformation of Three-Dimensional Framework into a Lamellar Zeolite with Modifiable Architecture. *J. Am. Chem. Soc.* **2011**, *133* (16), 6130−6133.
(7) Roth, W. J.; Nachtigall, P.; Morris, R. E.; Wheatley, P. S.; Seymour, V. R.; Ashbrook, S. E.; Chlubna, P.; Grajciar, L.; Polozij, M.; Zukal, A.; Shvets, O.; Cejka, J. A family of zeolites with controlled pore size prepared using a top-down method. *Nat. Chem.* **2013**, *5* (7), 628−633.
(8) Opanasenko, M.; Parker, J. W. O. N.; Shamzhy, M.; Montanari, E.; Bellettato, M.; Mazur, M.; Millini, R.; Cejka, J. Hierarchical hybrid organic-inorganic materials with tunable textural properties obtained using zeolitic layered precursor. *J. Am. Chem. Soc.* **2014**, DOI: 10.1021/ja410844f.

(9) Chlubna, P.; Roth, W. J.; Greer, H. F.; Zhou, W. Z.; Shvets, O.; Zukal, A.; Cejka, J.; Morris, R. E. 3D to 2D Routes to Ultrathin and Expanded Zeolitic Materials. *Chem. Mater.* **2013**, *25* (4), 542−547.
(10) Jo, C.; Ryoo, R.; Zilkova, N.; Vitvarova, D.; Čejka, J. The effect of MFI zeolite lamellar and related mesostructures on toluene disproportionation and alkylation. *Catal. Sci. Technol.* **2013**, *3* (8), 2119−2129.
(11) Koo, J. B.; Jiang, N.; Saravanamurugan, S.; Bejblova, M.; Musilova, Z.; Cejka, J.; Park, S. E. Direct synthesis of carbon-templating mesoporous ZSM-5 using microwave heating. *J. Catal.* **2010**, *276* (2), 327−334.
(12) Nachtigall, P.; Delgado, M. R.; Nachtigallova, D.; Arean, C. O. The nature of cationic adsorption sites in alkaline zeolites-single, dual and multiple cation sites. *Phys. Chem. Chem. Phys.* **2012**, *14* (5), 1552−1569.
(13) Nachtigallova, D.; Nachtigall, P.; Bludsky, O. Calculations of the site specific stretching frequencies of CO adsorbed on Li+/ZSM-5. *Phys. Chem. Chem. Phys.* **2004**, *6* (24), 5580−5587.
(14) Boscoboinik, J. A.; Yu, X.; Yang, B.; Fischer, F. D.; Wlodarczyk, R.; Sierka, M.; Shaikhutdinov, S.; Sauer, J.; Freund, H. J. Modeling Zeolites with Metal-Supported Two-Dimensional Aluminosilicate Films. *Angew. Chem., Int. Ed.* **2012**, *51* (24), 6005−6008.
(15) Boscoboinik, J. A.; Yu, X.; Emmez, E.; Yang, B.; Shaikhutdinov, S.; Fischer, F. D.; Sauer, J.; Freund, H.-J. Interaction of Probe Molecules with Bridging Hydroxyls of Two-Dimensional Zeolites: A Surface Science Approach. *J. Phys. Chem. C* **2013**, *117* (26), 13547−13556.
(16) Nachtigall, P.; Bludsky, O.; Grajciar, L.; Nachtigallova, D.; Delgado, M. R.; Arean, C. O. Computational and FTIR spectroscopic studies on carbon monoxide and dinitrogen adsorption on a high-silica H-FER zeolite. *Phys. Chem. Chem. Phys.* **2009**, *11* (5), 791−802.
(17) Paillaud, J.-L.; Harbuzaru, B.; Patarin, J.; Bats, N. Extra-Large: Pore Zeolites with Two-Dimensional Channels Formed by 14 and 12 Rings. *Science* **2004**, *304* (5673), 990−992.
(18) Corma, A.; Diaz-Cabanas, M. J.; Rey, F.; Nicolopoulus, S.; Boulahya, K. ITQ-15: The first ultralarge pore zeolite with a bi-directional pore system formed by intersecting 14- and 12-ring channels, and its catalytic implications. *Chem. Commun.* **2004**, (12).
(19) Shvets, O. V.; Nachtigall, P.; Roth, W. J.; Cejka, J. UTL zeolite and the way beyond. *Microporous Mesoporous Mater.* **2013**, *182*, 229−238.
(20) Kresse, G.; Hafner, J. Ab initio molecular dynamics for open-shell transition metals. *Phys. Rev. B* **1993**, *48*, 13115.
(21) Perdew, J.; Burke, K.; Ernzerhof, M. Generalized Gradient Approximation Made Simple. *Phys. Rev. Lett.* **1996**, *77*, 3865−3868.
(22) Blochl, P. E. Projector Augmented-Wave Method. *Phys. Rev. B* **1994**, *50* (24), 17953−17979.
(23) Kresse, G.; Joubert, D. From ultrasoft pseudopotentials to the projector augmented-wave method. *Phys. Rev. B* **1999**, *59* (3), 1758−1775.
(24) Grimme, S. Semiempirical GGA- type density functional constructed with a long- range dispersion correction. *J. Comput. Chem.* **2006**, *27*, 1787−1799.
(25) Lee, K.; Murray, E.; Kong, L.; Lundqvist, B.; Langreth, D. Higher-accuracy van der Waals density functional. *Phys. Rev. B* **2010**, *82*, 081101.
(26) Bludsky, O.; Silhan, M.; Nachtigallova, D.; Nachtigall, P. Calculations of Site-Specific CO Stretching Frequencies for Copper Carbonyls with the "Near Spectroscopic Accuracy": CO Interaction with Cu+/MFI. *J. Phys. Chem. A* **2003**, *107*, 10381−10388.
(27) http://www.iza-structure.org/databases/.
(28) Nachtigallova, D.; Nachtigall, P.; Sierka, M.; Sauer, J. Coordination and siting of Cu+ ions in ZSM-5: A combined quantum mechanics interatomic potential function study. *Phys. Chem. Chem. Phys.* **1999**, *1* (8), 2019−2026.
(29) Nachtigall, P.; Bulanek, R. Theoretical investigation of site-specific characteristics of CO adsorption complexes in the Li+-FER zeolite. *Appl. Catal., A* **2006**, *307* (1), 118−127.
(30) Woon, D.; Dunning, T. Gaussian basis sets for use in correlated molecular calculations. III. The atoms aluminum through argon. *J. Chem. Phys.* **1993**, *98*, 1358.
(31) Halkier, A.; Helgaker, T.; Jorgensen, P. Basis-set convergence in correlated calculations on Ne, N2, and H2O. *Chem. Phys. Lett.* **1998**, *286*, 243−252.
(32) Weigend, F.; Ahlrichs, R. Balanced basis sets of split valence, triple zeta valence and quadruple zeta valence quality for H to Rn: Design and assessment of accuracy. *Phys. Chem. Chem. Phys.* **2005**, *7* (18), 3297−3305.
(33) Boys, S.; Bernardi, F. The calculation of small molecular interactions by the differences of separate total energies. Some procedures with reduced errors. *Mol. Phys.* **1970**, *19*, 553−566.
(34) Bludsky, O.; Rubes, M.; Soldan, P.; Nachtigall, P. Investigation of the benzene-dimer potential energy surface: DFT/CCSD(T) correction scheme. *J. Chem. Phys.* **2008**, *128*, 114102.
(35) Ho, T.; Rabitz, H. A general method for constructing multidimensional molecular potential energy surfaces from ab initio calculations. *J. Chem. Phys.* **1996**, *104*, 2584−2597.
(36) Frisch, M. J.; Trucks, G. W.; Schlegel, H. B.; Scuseria, G. E.; Robb, M. A.; Cheeseman, J. R.; Scalmani, G.; Barone, V.; Mennucci, B.; Petersson, G. A.; Nakatsuji, H.; Caricato, M.; Li, X.; Hratchian, H. P.; Izmaylov, A. F.; Bloino, J.; Zheng, G.; Sonnenberg, J. L.; Hada, M.; Ehara, M.; Toyota, K.; Fukuda, R.; Hasegawa, J.; Ishida, M.; Nakajima, T.; Honda, Y.; Kitao, O.; Nakai, H.; Vreven, T.; Montgomery, J. A., Jr.; Peralta, J. E.; Ogliaro, F.; Bearpark, M.; Heyd, J. J.; Brothers, E.; Kudin, K. N.; Staroverov, V. N.; Kobayashi, R.; Normand, J.; Raghavachari, K.; Rendell, A.; Burant, J. C.; Iyengar, S. S.; Tomasi, J.; Cossi, M.; Rega, N.; Millam, J. M.; Klene, M.; Knox, J. E.; Cross, J. B.; Bakken, V.; Adamo, C.; Jaramillo, J.; Gomperts, R.; Stratmann, R. E.; Yazyev, O.; Austin, A. J.; Cammi, R.; Pomelli, C.; Ochterski, J. W.; Martin, R. L.; Morokuma, K.; Zakrzewski, V. G.; Voth, G. A.; Salvador, P.; Dannenberg, J. J.; Dapprich, S.; Daniels, A. D.; Farkas, Ö.; Foresman, J. B.; Ortiz, J. V.; Cioslowski, J.; Fox, D. J. *Gaussian 09*, Revision D.01; Gaussian Inc.: Wallingford, CT, 2009.
(37) Werner, H. J.; Amos, R. D.; Bernhardsson, A.; Berning, A.; Celani, P.; L.Cooper, D.; Deegan, M. J. O.; Dobbyn, A. J.; Eckert, F.; Hampel, C.; Hetzer, G.; Knowles, P. J.; Korona, T.; Lindh, R.; Lloyd, A. W.; McNicholas, S. J.; Manby, F. R.; Meyer, W.; Mura, M. E.; Nicklaß, A.; Palmieri, P.; Pitzer, R.; Rauhut, G.; Schütz, M.; Schumann, U.; Stoll, H.; Stone, A. J.; Tarroni, R.; Thorsteinsson, T. *MOLPRO*, a package of ab initio programs.
(38) *TURBOMOLE* V6.5 2013, a development of University of Karlsruhe and Forschungszentrum Karlsruhe GmbH, 1989−2007, TURBOMOLE GmbH, since 2007; available from http://www.turbomole.com.
(39) Klimes, J.; Michaelides, A. Perspective: Advances and challenges in treating van der Waals dispersion forces in density functional theory. *J. Chem. Phys.* **2012**, *137*, 120901.
(40) Arean, C. O.; Delgado, M. R.; Nachtigall, P.; Thang, H. V.; Rubes, M.; Bulanek, R.; Chlubna-Eliasova, P. Measuring the Bronsted acid strength of zeolites ? does it correlate with the O-H frequency shift probed by a weak base? *Phys. Chem. Chem. Phys.* **2014**, DOI: 10.1039/C3CP54738H.
(41) Thang, H. V.; Grajciar, L.; Nachtigall, P.; Bludský, O.; Areán, C. O.; Frýdová, E.; Bulánek, R. Adsorption of CO2 in FAU zeolites: Effect of zeolite composition. *Catal. Today* **2013**, DOI: 10.1016/j.cattod.2013.10.036.
(42) Savitz, S.; Myers, A. L.; Gorte, R. J. Calorimetric Investigation of CO and N2 for Characterization of Acidity in Zeolite H - MFI. *J. Phys. Chem. B* **1999**, *103*, 3687−3690.
(43) Čičmanec, P.; Bulánek, R.; Frýdová, E.; Kolářová, M. Study of thermodynamic characteristics of CO adsorption on Li exchanged zeolites. *Adsorption* **2013**, *19* (2−4), 381−389.
(44) Kucera, J.; Nachtigall, P. Coordination of alkali metal ions in ZSM-5: A combined quantum mechanics/interatomic potential function study. *Phys. Chem. Chem. Phys.* **2003**, *5* (15), 3311−3317.
(45) Nachtigallova, D.; Bludsky, O.; Arean, C. O.; Bulanek, R.; Nachtigall, P. The vibrational dynamics of carbon monoxide in a

confined space - CO in zeolites. *Phys. Chem. Chem. Phys.* **2006**, *8* (42), 4849−4852.
(46) Arean, C. O.; Delgado, M. R.; Bauca, C. L.; Vrbka, L.; Nachtigall, P. Carbon monoxide adsorption on low-silica zeolites-from single to dual and to multiple cation sites. *Phys. Chem. Chem. Phys.* **2007**, *9* (33), 4657−4661.
(47) Grajciar, L.; Arean, C. O.; Pulido, A.; Nachtigall, P. Periodic DFT investigation of the effect of aluminium content on the properties of the acid zeolite H-FER. *Phys. Chem. Chem. Phys.* **2010**, *12* (7), 1497−1506.
(48) Roth, W. J.; Nachtigall, P.; Morris, R. E.; Čejka, J. Two-Dimensional Zeolites: Current Status and Perspectives. *Chem. Rev.* **2014**, DOI: 10.1021/cr400600f.
(49) Nachtigall, P.; Frolich, K.; Drobna, H.; Bludsky, O.; Nachtigallova, D.; Bulanek, R. FTIR Study of CO Interactions with Li+ Ions in Micro- and Mesoporous Matrices: Coordination and Localization of Li+ Ions. *J. Phys. Chem. C* **2007**, *111* (30), 11353−11362.

Attachment B

PCCP

PAPER

View Article Online
View Journal | View Issue

Cite this: *Phys. Chem. Chem. Phys.*, 2016, **18**, 18063

The effect of the zeolite pore size on the Lewis acid strength of extra-framework cations†

Ho Viet Thang,[a] Karel Frolich,[b] Mariya Shamzhy,[c] Pavla Eliášová,[c] Miroslav Rubeš,[a] Jiří Čejka,[c] Roman Bulánek[b] and Petr Nachtigall*[a]

Received 17th May 2016,
Accepted 7th June 2016

DOI: 10.1039/c6cp03343a

www.rsc.org/pccp

The catalytic activity and the adsorption properties of zeolites depend on their topology and composition. For a better understanding of the structure–activity relationship it is advantageous to focus just on one of these parameters. Zeolites synthesized recently by the ADOR protocol offer a new possibility to investigate the effect of the channel diameter on the adsorption and catalytic properties of zeolites: **UTL**, **OKO**, and **PCR** zeolites consist of the same dense 2D layers (IPC-1P) that are connected with different linkers (D4R, S4R, O-atom, respectively) resulting in the channel systems of different sizes (14R × 12R, 12R × 10R, 10R × 8R, respectively). Consequently, extra-framework cation sites compensating charge of framework Al located in these dense 2D layers (channel-wall sites) are the same in all three zeolites. Therefore, the effect of the zeolite channel size on the Lewis properties of the cationic sites can be investigated independent of other factors determining the quality of Lewis sites. **UTL**, **OKO**, and **PCR** and pillared 2D IPC-1PI materials were prepared in Li-form and their properties were studied by a combination of experimental and theoretical methods. Qualitatively different conclusions are drawn for Li^+ located at the channel-wall sites and at the intersection sites (Li^+ located at the intersection of two zeolite channels): the Lewis acid strength of Li^+ at intersection sites is larger than that at channel-wall sites. The Lewis acid strength of Li^+ at channel-wall sites increases with decreasing channel size. When intersecting channels are small (10R × 8R in **PCR**) the intersection Li^+ sites are no longer stable and Li^+ is preferentially located at the channel-wall sites. Last but not least, the increase in adsorption heats with the decreasing channel size (due to enlarged dispersion contribution) is clearly demonstrated.

1. Introduction

The adsorption and catalytic properties of zeolites depend on the zeolite topology, chemical composition, and distribution of atoms (Si *vs.* Al) among different crystallographic sites.[1–6] Understanding of this seemingly simple dependence at the molecular level is complicated by the fact that individual effects are strongly coupled. For a better understanding of the structure–activity relationship it is advantageous to focus just on a single effect. At the molecular level, adsorption and catalytic properties depend primarily on the coordination and accessibility of charge-balancing extra-framework cations (protons or metal cations).[7–9] Information about the location and coordination of extra-framework cations for most zeolites cannot be directly obtained from experiment, instead it is often deduced from a combination of various experimental techniques[10–12] (see ref. 13 for a recent comprehensive review). A combination of experimental and computational investigations has been shown to be particularly suitable for understanding the extra-framework cation coordination in high-silica zeolites.[14–28]

To understand the effects of the extra-framework cation coordination and the channel size on the adsorption and catalytic properties of zeolites, a probe molecule, such as CO, has been used.[29–31] In high silica zeolites, the adsorption of CO is driven by two factors: by the effect from the bottom and by the effect from the top.[32,33] The effect from the bottom is due to the interaction of the adsorbate with the primary extra-framework cation and it reflects the cation coordination with the framework; the stronger is the interaction of the extra-framework cation with the zeolite framework the weaker is the interaction with CO and lower adsorption heats and lower CO stretching vibrations ν_{CO} can be expected. The effect from the bottom is more pronounced for smaller cations such as Li^+ and Mg^{2+}.[34,35] Thus, the effect from the bottom reflects the Lewis acid strength of the extra-framework metal cation that is

[a] *Department of Physical and Macromolecular Chemistry, Faculty of Sciences, Charles University, Hlavova 8, 128 40 Prague 2, Czech Republic. E-mail: petr.nachtigall@natur.cuni.cz*
[b] *Department of Physical Chemistry, Faculty of Chemical Technology, University of Pardubice, Studentska 573, 532 10 Pardubice, Czech Republic*
[c] *J. Heyrovský Institute of Physical Chemistry, Academy of Sciences of the Czech Republic v.v.i., Dolejškova 3, 182 23 Prague 8, Czech Republic*
† Electronic supplementary information (ESI) available. See DOI: 10.1039/c6cp03343a

demonstrated by its ability to polarize an adsorbate. The effect from the top is due to the "secondary" interaction of the adsorbed molecule with the zeolite framework in its vicinity. This effect is mostly due to the electrostatic and dispersion interactions and it leads to additional changes of CO stretching frequency. Experimentally observed characteristics of adsorbed probe molecules reflect both effects (from the top and from the bottom) simultaneously and individual effects can be demonstrated only computationally, using suitable models. A recent theoretical investigation of CO adsorption on 2D layered IPC-1PI and corresponding 3D **UTL** zeolites has shown that adsorption enthalpies and CO stretching frequencies are lower by 3 kJ mol^{-1} and 5 cm^{-1}, respectively, in the 2D material (IPC-1P).[36]

It has been recently shown that **UTL** zeolite can be converted into a layered two-dimensional (2D) material IPC-1P by selective hydrolysis[37] and this 2D material can be further converted into new zeolites IPC-2 and IPC-4 (having **OKO** and **PCR** topologies, respectively) *via* the ADOR mechanism.[38–40] The **OKO** zeolite was originally prepared *via* inverse sigma transformation;[41] **OKO** and IPC-2 have the same framework connectivity but differ in the symmetry. A layered 2D material obtained upon the hydrolysis of **UTL** is denoted IPC-1P while the corresponding material obtained by pillaring is denoted IPC-1PI; experimental results reported below were obtained on IPC-1PI while calculations were carried out for IPC-1P layers separated by vacuum (Section 2). We will use IPC-1PI to refer to the pillared material (experimental and theoretical) while IPC-1P notation will denote the structure of 2D layers. These four materials (IPC-1PI, **UTL**, **OKO**, and **PCR**) thus constitute a unique set of adsorbents with the same dense 2D layers separated by different interlayer distances defined by different interlayer linkers. Consequently, these materials have different channel systems parallel to the 2D layer (Fig. 1). We denote these zeolites an "IPC-1P group" since they all can be formally obtained from the IPC-1P precursor. While the channel size increases from **PCR** to IPC-1PI, the structure remains relatively similar since parts of the channel defined by 2D layers do not change. Thus, the IPC-1P group represents a unique series where a majority of extra-framework sites (those defined by dense 2D layers) are very similar, if not the same, and the differences in adsorption and catalytic properties must be related to the channel size. It gives us a unique opportunity to investigate the effect of the channel size without an influence of differences in the extra-framework coordination and improve our understanding of adsorption and catalytic processes taking place in zeolites. The results for such a unique series of zeolites with similar structures but increasing channel size are presented herein for the first time.

All four zeolites of the IPC-1P group were prepared in the Li^+ form and the properties of extra-framework Li^+ sites were probed with the CO adsorbate. In addition to standard characterization techniques, the microcalorimetry and FTIR spectra were obtained from a zero coverage up to coverages greater than the monolayer (CO : Li > 1 : 1). Experimental results are compared with computational results obtained for the same set of materials (the results for Li-**PCR** and Li-**OKO** are presented herein while computational results for Li-IPC-1PI and Li-**UTL** are taken from ref. 36). Based on the excellent agreement of theoretical and experimental data, the effects of the zeolite channel size on the Lewis acid strength (and thus the adsorption and catalytic activity) of extra-framework Li^+ sites are discussed.

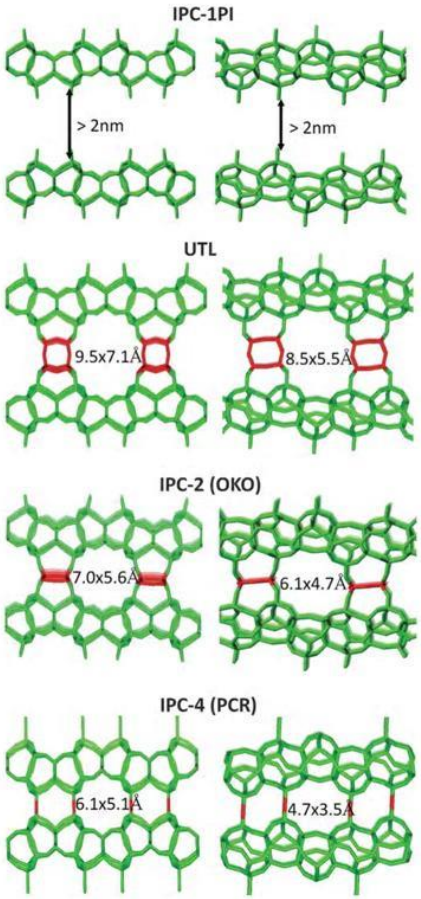

Fig. 1 Structure of IPC-1PI, **UTL**, **OKO** and **PCR** consisting of the same dense 2D layers (in green color) but different linkers (in red color) leading to the different pore sizes in these materials; shown for the main channel (left side) and the perpendicular channel (right side).

2. Experimental and computational methods

2.1. Synthesis and characterization

Aluminogermanosilicate **UTL** and pure germanosilicate **UTL** were prepared according to a procedure described in the literature.[42] For the synthesis of IPC-zeolites, **UTL** was used as the starting material and additional aluminium was incorporated during its hydrolysis as follows: calcined **UTL** (1 g) was hydrolysed in a mixture of solutions 1 M CH_3COOH (150 ml) and 1 M $Al(NO_3)_3$ (100 ml) at 90 °C for 16 hours. The product was isolated by filtration, washed with water and dried at 60 °C. For the synthesis of **OKO**, the hydrolysed sample (1 g) was treated with 1 M HNO_3 solution (10 g) and diethoxydimethylsilane $Si(OCH_2CH_3)_2(CH_3)_2$ (0.2 g). The reaction was performed

in the autoclave under static conditions at 170 °C for 16 hours. The final product was washed with water, dried at 60 °C and finally calcined in the air flow at 750 °C for 6 hours. For the synthesis of **PCR**, the hydrolysed sample was treated with neat octylamine at 80 °C for 16 hours (with w/w ratio 1/13 g). The solid was then isolated by centrifugation and dried at ambient temperature. The product was calcined in the air flow at 750 °C for 8 h. For the synthesis of IPC-1PI, 1 g of hydrolysed sample was first swollen with 20 ml of 20 wt% cetyltrimethylammonium hydroxide solution (C_{16}TMA-OH) by stirring at ambient temperature for 16 hours. The IPC-1SW was then treated with TEOS (for 1 g of zeolite 50 ml TEOS) at 85 °C for 16 hours. The produced solid was hydrolysed in water and then calcined at 550 °C for 6 hours.

The structure and crystallinity of zeolites were determined by X-ray powder diffraction using a Bruker AXS D8 Advance diffractometer equipped with a graphite monochromator and a position sensitive detector Våntec-1 using CuKα radiation in Bragg–Brentano geometry.

Adsorption isotherms of nitrogen (at −196 °C) were measured on a Micromeritics ASAP 2020 static volumetric instrument. The BET area (S_{BET}) was evaluated by the BET method using adsorption data in the p/p_0 range of 0.05–0.20. The adsorbed amount at relative pressure p/p_0 = 0.98 reflects the total adsorption capacity (V_{tot}). For adsorption isotherms of nitrogen, the *t*-plot method was applied to determine the volume of micropores (V_{micro}). Low-pressure adsorption isotherms of argon (at −186 °C) were measured on the same instrument in order to inspect pore-size distribution. Experimental data were treated by the NL DFT model of Ar adsorption in H-zeolite at −186 °C using SAIEUS software (Micromeritics).[43]

The lithium forms of zeolites were obtained by an ion exchange in a 0.5 M aqueous solution of LiCl for two days at 35 °C. After ion exchange, the samples were filtered and thoroughly washed with distilled water several times and finally dried at 120 °C overnight. The crystallinity of Li-zeolites was checked by XRD. No decrease in crystallinity and no additional phase presence were observed in the XRD.

2.2. FT-IR spectroscopy of adsorbed CO

The samples were pressed into self-supporting wafers with a density of 10 mg cm^{-2} and placed into a home-made low temperature IR cell for transmission measurements. The zeolite samples were *in situ* activated (outgassed) in a dynamic vacuum (residual pressure $<10^{-4}$ Pa) for 10 h at 430 °C (with a rate of temperature increase of 1 °C min^{-1} up to 130 °C, then the sample was kept for 30 min at this temperature and subsequently temperature increased with the rate 5 °C min^{-1} up to 430 °C). Infrared spectra (64 scans) were collected at the temperature of liquid nitrogen with a resolution of 2 cm^{-1} on a Nicolet 6700 FTIR spectrometer equipped with an MCT/A cryodetector. Carbon monoxide (99.997 purity) used in the experiments was purified by a freeze–pump–thaw cycle. The CO adsorption on Li-zeolites was performed at an equilibrium pressure of 0.1 Torr; CO pressure was then reduced until vibrational bands of adsorbed CO were detected (approximately 4 h). IR spectra of the surface CO complexes were collected each minute. The spectrum of the dehydrated sample at the temperature of liquid nitrogen recorded before CO adsorption was subtracted from each spectrum shown in this work.

2.3. Adsorption microcalorimetry

Prior to each calorimetric experiment, a sample of weight *ca.* 300 mg was outgassed by slowly increasing temperature with simultaneous careful evacuation up to a residual pressure of 10^{-4} Pa at 450 °C. The microcalorimetric/volumetric experiments were carried out using an isothermal Tian-Calvet type microcalorimeter (BT 2.15, SETARAM) combined with a homemade volumetric/manometric device equipped with capacitance pressure gauges (Pfeiffer Vacuum). The adsorption isotherms and heats of adsorption were measured at −100 °C by the step-by-step introduction of CO (99.997 purity) into the cell. The system was equilibrated for 60 minutes for each dose and the equilibrium was monitored by both the pressure and the heat-flow measurements. The integral area of the peak in the heat flow–time plot provided integral adsorption heat evolved at each adsorptive dose. The dependence of differential adsorption heat *vs.* adsorbed amount was obtained by numeric differentiation.

2.4. Models and computational methods

The numbering scheme of framework atoms in **UTL**, **OKO**, and **PCR** structures is defined in the IZA database;[44] the use of three numbering schemes would make it complicated for a reader to follow the comparison of results for individual structure types. In fact, all three **UTL**, **OKO**, and **PCR** framework types are based on the same dense 2D layer (a material denoted IPC-1P)[37] and they differ only by a linker inter-connecting these 2D layers into 3D zeolites (O atom, S4R, and D4R for **PCR**, **OKO**, and **UTL**, respectively). Therefore, for comparison of all 3 framework types the **UTL** numbering scheme is adopted (Fig. 2) and the mapping with the IZA numbering is shown in the ESI† (Table SI-1). The same numbering is used also for the IPC-1PI layered material. To prevent the confusion with the IZA numbering the T-sites are denoted as T′-sites throughout this manuscript.

The notation of Li^+ cation positions for all structures is shown in Fig. 2. Li^+ positions located on the surface of the channel wall (type I sites) can be classified as M× and P×, where M is the main (larger) channel, P is the perpendicular (smaller) channel, × is the size of the ring on the channel wall that hosts the extra-framework cation and I2 stands for type II sites on the intersection (a similar notation has been introduced previously for other high-silica zeolites[45,46]). The substitution of Al for Si was investigated for all distinguishable T-sites except those located at the interlayer linker (S4R unit in **OKO**). For each investigated location of the framework Al the most energetically stable site of the extra-framework Li^+ cation was found and for these Li^+ sites the adsorption of CO was considered.

Unit cell parameters previously determined for IPC-2 (a = 12.5162 Å, b = 13.8880 Å, c = 13.9682 Å, and α = 118.7520, β = 90.1740°, γ = 107.0870°) and **PCR** (a = 20.3599 Å, b = 14.1746 Å, c = 12.4572 Å, and $\alpha = \gamma = 90°$, β = 114.0905°) were adopted.[38] Since the methods used for the calculations on **OKO** and **PCR** zeolites are exactly the same as described previously for **UTL** and IPC-1PI,[36] they are only briefly summarized below. All calculations

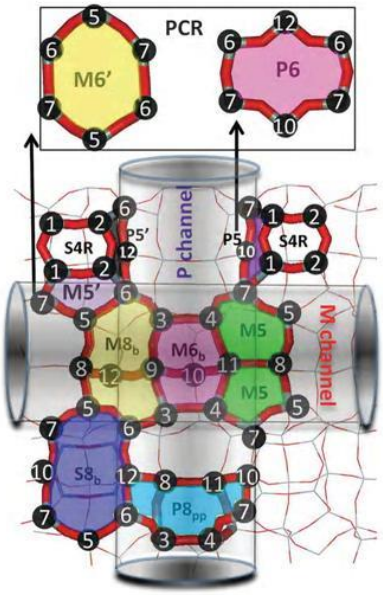

Fig. 2 Notation used for extra-framework Li^+ cation sites in IPC-1PI, **UTL**, **OKO** and **PCR**. Sites in the main and perpendicular channels are denoted as M× and P×, respectively, where × stands for the size of the ring on the channel wall where the Li^+ cation is located. A new surface site in IPC-1PI formed upon the removal of D4R is denoted S8b. Two sites in **PCR** at the location of P5 and M5 in **UTL** are denoted M6 and P6 (insertion on the top). The numbering schemes of T′ atoms following UTL numbering schemes are also shown.

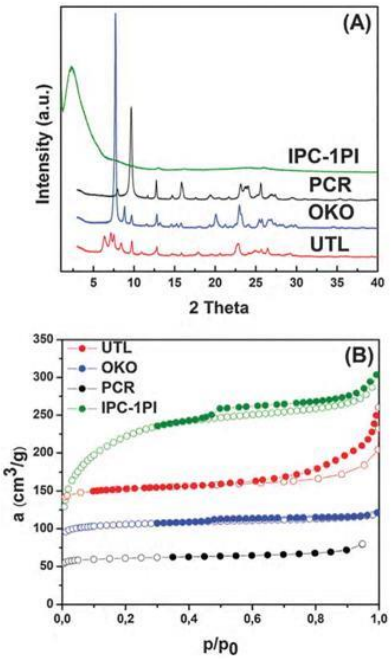

Fig. 3 Powder XRD patterns (A) and adsorption–desorption isotherms of nitrogen measured at −196 °C (B) for **UTL**, **OKO**, and **PCR** zeolites and for the 2D IPC-1PI pillared hierarchical material. The solid points denote the desorption branch.

were performed at the DFT level using the Perdew–Burke–Ernzerhof (PBE) exchange–correlation functional,[47,48] the projector augmented wave approximation (PAW)[49,50] and the plane wave basis set with a 400 eV kinetic energy cut-off. Brillouin-zone sampling was restricted to the Γ point. Calculations were performed using the VASP program package (version 5.3.3).[51,52] The structure optimizations were carried out with relaxed ions and a frozen unit cell. The zero point energies (ZPE) were calculated within the harmonic approximation, considering 6 degrees of freedom of CO. The standard enthalpies were reported at 0 K. CO stretching frequencies were calculated by the ν_{CO}/r_{CO} correlation method described in ref. 53. The CO adsorption energies calculated at the PBE level were corrected for a missing dispersion contribution using the DFT/CC method.[54] The details of the method for Li-zeolites were described in ref. 36. Dispersion and local contributions (denoted Δ_{disp} and Δ_{local}, respectively) to the interaction energy were evaluated as well. The part of DFT/CC correction upon elimination the Li···C and Li···O correction is used for Δ_{disp} and interaction energy calculated at the PBE level is used for Δ_{local}. The IR spectra of adsorbed CO were modelled following the method described previously,[55] assuming statistical distribution of Al inside the dense 2D layers.

3. Experimental results

The X-ray diffraction patterns of **UTL**, **OKO**, **PCR**, and 2D IPC-1PI zeolites reported in Fig. 3A are in good agreement with those reported in the literature.[37,38] No diffraction lines of additional phases were observed in the diffraction patterns. Nitrogen adsorption isotherms (Fig. 3B) are characteristic of a microporous material lacking secondary mesopores, except the isotherm for IPC-1PI that is typical for a mesoporous material. The Si/Al ratios, BET areas, total pore volumes, volumes of micropores, and pore sizes are reported in Table 1. The argon adsorption isotherms and pore-size distributions are shown in the ESI† (Fig. SI-1).

3.1. FTIR spectra of CO adsorbed on OKO and PCR

The IR spectra of CO adsorbed on all four Li-zeolites at liquid nitrogen temperature are shown in Fig. 4 and adsorption characteristics obtained for low coverages are summarized in Table 2. The spectra recorded on individual samples differ in a number and relative intensity of spectral bands. The IR spectra of CO adsorbed on Li-IPC-1PI (see Fig. 4A) are characterized by

Table 1 Textural properties determined by N_2 and Ar adsorption and chemical analysis of **UTL**, **OKO**, **PCR** and IPC-1PI zeolites[a]

		N_2 sorption			Ar sorption
Zeolite	Si/Al	S_{BET}	V_{tot}	V_{micro}	Mean pore width
UTL	45	600	0.195	0.180	0.78
OKO	77	356	0.182	0.144	0.63
PCR	51	206	0.123	0.083	0.51
IPC-1PI	33	788	0.469	0.125	2.29

[a] Surface area, volume and mean pore width are reported in $m^2\,g^{-1}$, $cm^3\,g^{-1}$ and nm, respectively.

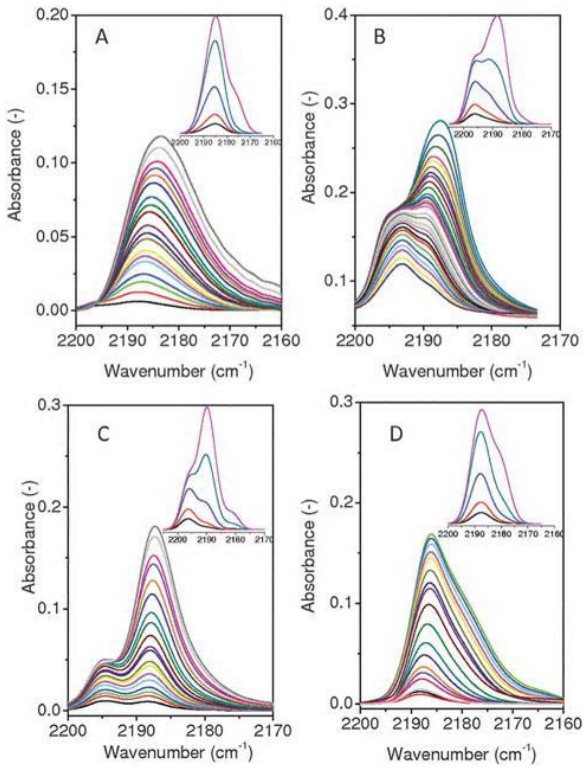

Fig. 4 FTIR spectra of CO adsorbed at liquid nitrogen temperature on Li-IPC-1PI (A), Li-**UTL** (B), Li-**OKO** (C), and Li-**PCR** (D). The intensity of spectra obtained upon CO adsorption decreases with evacuation. The insets in individual panels show theoretical spectra in the corresponding Li-zeolites calculated for 0.75, 0.50, 0.25, 0.10, and 0.05 coverages (CO : Li ratio) in cyan, green, blue, red, and black, respectively.

only one, relatively broad band with the maximum at 2187 cm^{-1}. The band is clearly asymmetric on the low frequency side and its maximum shifts with increasing coverage to 2183 cm^{-1}. The spectra of CO adsorbed on Li-**UTL** (Fig. 4B) reveal two bands at 2194 and 2187 cm^{-1}. The relative intensity of bands changes with coverage. The high-frequency band dominates the spectra at low coverages and there is a shoulder at the low-frequency side at about 2189 cm^{-1}. With increasing coverage, the low-frequency shoulder develops and becomes the dominant band. Simultaneously, the position of the low frequency band slightly shifts from 2189 to 2187 cm^{-1}. IR spectra of the CO adsorbed on Li-**OKO** zeolite (Fig. 4C) resemble spectra obtained for Li-**UTL** zeolite. The spectra obtained for the lowest coverage show two well-distinguished bands at 2195 and 2188 cm^{-1}. The maxima of both bands are rather coverage independent, whereas relative intensities of these bands change. The band at 2188 cm^{-1} dominates the spectra recorded at the high coverage. The relative intensity of the high frequency band with respect to the low frequency one is higher in Li-**UTL** than in Li-**OKO** zeolite. The IR spectra of CO adsorbed on Li-**PCR** (Fig. 4D) are characterized by the single asymmetric absorption band occurring below 2190 cm^{-1}. At low coverage, the band is centered at 2188 cm^{-1} with a half-width around 7.5 cm^{-1}. With increasing coverage, the maximum of the band is shifted to 2186 cm^{-1} and the shoulder at around 2179 cm^{-1} is developed.

Table 2 Experimental and calculated CO adsorption characteristics of Li-IPC-1PI, Li-**UTL**, Li-**OKO** and Li-**PCR**[a]

Zeolite	Q^0_{ads} (exp.)	$-\Delta H$ (calc.)	ν_{CO} (exp.)[b]	ν_{CO} (calc.)[b]
Li-IPC-1PI	34.5	37	2187	2186
Li-**UTL**	41.0	42	2194; 2189	2196; 2188
Li-**OKO**	43.1	43	2195; 2188	2197; 2189
Li-**PCR**	44.0	46	2188	2188

[a] Experimental adsorption heat estimates for zero coverage and a maximum $-\Delta H$ value calculated for a particular system (in kJ mol^{-1}). [b] Frequencies (in cm^{-1}) taken from Fig. 4 for low coverage.

3.2. Adsorption microcalorimetry of CO adsorption on OKO and PCR

Calorimetric curves for the CO adsorption on investigated Li-zeolites and Li-IPC-1PI at −100 °C are depicted in Fig. 5. The differential heat of adsorption is plotted as a function of sample coverage (CO : Li ratio equal to 1 is considered to be 100%). The decrease in the adsorption heat with coverage reflects significant adsorption heterogeneity (in terms of energy) for all studied materials. Li-IPC-1PI exhibits the lowest adsorption heats from all four samples. The calorimetric curve of Li-IPC-1PI starts at 34.5 kJ mol^{-1} and very slowly decreases to approximately 30 kJ mol^{-1} at 60% of coverage. Then the heat falls to 20 kJ mol^{-1} followed again by a slow decrease to 17 kJ mol^{-1}, at which the calorimetric curve levels-off. The adsorption heats on Li-**UTL** zeolite are higher compared to Li-IPC-1PI. The first CO doses (up to 15% of coverage) result in heats of 41 kJ mol^{-1}, followed by a decrease to approximately 32 kJ mol^{-1} where a distinct plateau is clearly visible. The heats start to slowly decrease at coverage higher than 75% and level off at 18 kJ mol^{-1}. The strongest adsorption sites in Li-**OKO** zeolite are characterized by 43 kJ mol^{-1} and the heat higher than 40 kJ mol^{-1} can be detected up to a coverage of 30%. Then the heat monotonically decreases to 20 kJ mol^{-1} at coverages above 100%. Adsorption of

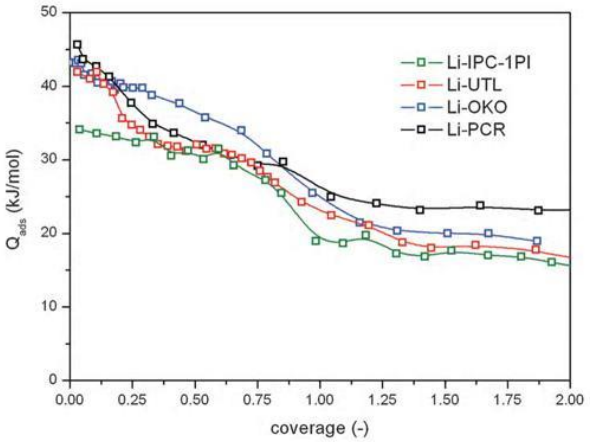

Fig. 5 Adsorption heats of CO on Li-zeolites and Li-IPC-1PI measured by microcalorimetry at −100 °C as a function of coverage.

CO on Li-**PCR** zeolite exhibits the largest initial adsorption heat (44 kJ mol^{-1}) for all investigated materials. A subsequent increase in coverage is reflected by a substantial decrease in the heats to approximately 30 kJ mol^{-1} at near 100% of coverage. It must be noted that heats of CO adsorption on Li-**PCR** are significantly lower compared to heats on Li-**OKO** at intermediate coverage.

4. Computational results

4.1. Li^+ cation sites in OKO and PCR

Following the previous investigation of Li^+ sites in **UTL** and IPC-1PI[36] the energetically preferable Li^+ sites located in the vicinity of each of 10 T-sites in **OKO** and **PCR** were investigated; Li–O_f distances are summarized for all four materials in the ESI† (Table SI-2). Both **OKO** and **PCR** zeolites reflect a strong preference of Li^+ cations in the type I site on the channel wall (Table 3), similar to **FER**[56] and **MFI**.[57] The Li^+ cation is located in the type II site only in one and two cases in **PCR** and **OKO**, respectively (Table 3). Comparing the most stable Li^+ cation position in **OKO** and **PCR**, it is apparent that the Li^+ cation positions and the coordination number (CN) are the same in both materials when the framework Al atom is in T3′, T4′, T5′, T8′, T9′, and T11′ (Fig. 2). Since these sites are clearly defined by the 2D layer and they are not affected by the inter-layer linker they will be denoted "layer sites". In contrast, when the framework Al atom is in T6′, T7′, T10′, and T12′, both the site type and the coordination number change between **OKO** and **PCR**. These sites will be denoted "inter-layer sites"; note that such sites are not necessarily located in the inter-layer region, however, their relative stability (and thus populations) is affected by the inter-layer linkers.

4.2. CO adsorption in OKO and PCR

The adsorption energies and stretching frequencies of CO were calculated to evaluate the Lewis acid strength of the most stable Li^+ cation site found for a particular Al position. Characteristics of CO adsorption complexes on Li^+ sites in **OKO** and **PCR** are reported in Table 3 summarizing Li–O_f distances, adsorption enthalpies ΔH (0 K), and CO stretching frequencies ν_{CO}. The sensitivity of the CO probe molecule to the local environment is reflected in ν_{CO} and ΔH that ranges from 2178 to 2197 cm^{-1} and from −29 to −46 kJ mol^{-1}, respectively. Examples of CO adsorption complexes in **OKO** and **PCR** are shown in Fig. 6 together with corresponding adsorption complexes found previously[36] in **UTL** and IPC-1PI.

Correction of PBE interaction energies evaluated at the DFT/CC level accounts mostly for the lack of dispersion interactions; they are summarized in the ESI,† Table SI-3. They are rather important in **PCR** (−16 kJ mol^{-1} on average) where they represent 30–50% of the overall interaction energy. This is due to a relatively small size of the **PCR** channel system (intersecting 10R and 8R channels) where CO primarily bound to the Li^+ cation is within vdW radii of many framework atoms. Consequently, dispersion interactions do not depend on the cation site. Due to a larger diameter of the **OKO** channel system, dispersion contributions are smaller than in **PCR** (by about 5 kJ mol^{-1} on average) and a larger dependence on a particular Li^+ position in **PCR** can be observed. In the case of **OKO** zeolite, the dispersion corrections account for 20–30% of overall interaction energies. For layer sites (see above), adsorption enthalpies in **PCR** are 4–8 kJ mol^{-1} larger than those in **OKO** that can be attributed mostly to the increased importance of dispersion interaction in **PCR** having a small channel system (effect from the top). Examples of corresponding CO adsorption complexes are shown in Fig. 6 for Al in T4′ (Fig. 6a–d), and T3′ (Fig. 6e–h). In the case of inter-layer sites, the situation is opposite – adsorption enthalpies in **OKO** are up to 12 kJ mol^{-1} larger than those in **PCR** for the corresponding adsorption sites (Table 3). This difference clearly results from the effect from the bottom; coordination of Li^+ is larger in **PCR** (CN = 4) than in **OKO** (CN ≤ 3). For the same reason also ν_{CO} frequencies are larger in **OKO** than in **PCR** by 8–16 cm^{-1}. Examples of CO adsorption complexes are shown for Al located in T10′ and in T7′ sites in Fig. 6k, l and o, p, respectively.

Table 3 The most stable Li^+ cation positions, coordination numbers, distances to framework O_f atoms, adsorption heats and CO vibrational frequencies obtained computationally[a]

		Li^+ cation position[c] (CN)		r(Li···O_f)		ΔH		ν_{CO}	
Al[b] location	Al[b] site	OKO	PCR	OKO	PCR	OKO	PCR	OKO	PCR
Layer sites	T3′	M8b(3)	M8b(3)	*1.87*, *2.02*, *2.05*	*1.88*, *2.10*, *2.19*	−36.2	−44.5	2190	2188
	T4′	I2(2)	I2(2)	*1.86*, *1.87*	*1.87*, *1.89*	−41.8	−46.5	2195	2187
	T5′	M8b(3)	M8b(3)	*1.91*, *1.94*, *2.15*	*1.92*, *1.93*, *2.03*	−34.9	−39.0	2186	2187
	T8′	M8b(3)	M8b(3)	*1.93*, *1.94*, *2.03*	*1.94*, *1.94*, *2.10*	−37.0	−41.7	2188	2186
	T9′	M8b(4)	M8b(4)	*2.00*, *2.05*, *2.12*, *2.13*	*1.98*, *2.00*, *2.12*, *2.20*	−35.1	−41.5	2181	2180
	T11′	M6b(3)	M6b(3)	*1.95*, *2.01*, *2.32*	*1.97*, *1.97*, *2.31*	−34.4	−42.0	2191	2190
Inter-layer sites	T6′	M8b(3)	P6(4)	*1.89*, *2.01*, *2.04*	*1.94*, *2.06*, *2.16*, *2.24*	−35.7	−31.2	2186	2181
	T7′	I2(2)	P6′(4)	1.87, *1.91*	*1.92*, *2.10*, *2.17*, *2.20*	−43.5	−31.4	2197	2181
	T10′	P5′(3)	P6′(4)	1.83, *2.01*, *2.04*	1.97, *1.97*, *2.24*, *2.24*	−39.1	−29.5	2191	2179
	T12′	M8b(3)	P6(4)	*1.89*, *2.03*, *2.09*	*1.96*, *1.96*, *2.16*, *2.16*	−39.9	−29.2	2190	2178

[a] Distances, adsorption enthalpies, and frequencies reported in Å, kJ mol^{-1}, and cm^{-1}, respectively. [b] Al located either at the 2D dense layer (layer sites) or in the proximity of the interlayer linker (inter-layer sites); for T-site numbering see Fig. 2 and Table SI-1 (ESI) [c] See Fig. 2 for site notation; CN stands for the number of O_f atoms at the distance of 2.4 Å or smaller from the Li^+ cation.

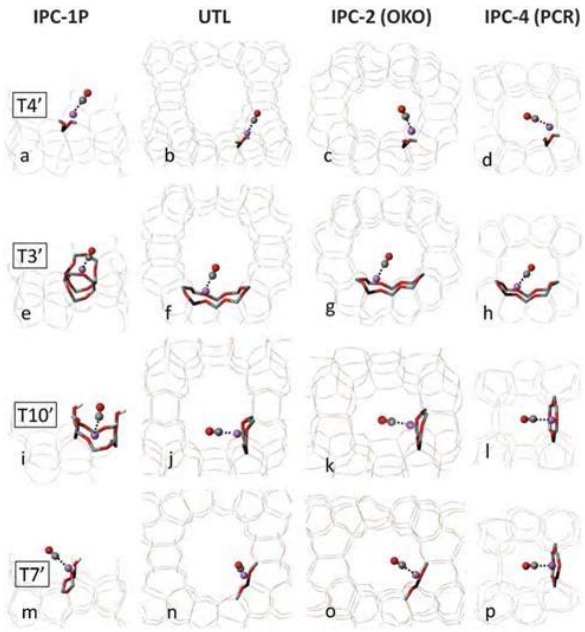

Fig. 6 The CO adsorption complexes in the most stable position of the Li cation in IPC-1PI, **UTL**, **OKO** and **PCR** (from left to right); shown for Al in T4′ (a–d); T3′ (e–h); T10′ (i–l) and T7′ (m–p). The Al, O, and Si atoms are depicted in black, grey, red and grey color, respectively while the Li, C, and O atoms are depicted in purple, grey and red color balls, respectively.

5. Discussion

The experimental and theoretical results reported above for Li-**PCR** and Li-**OKO** zeolites are discussed first, followed by a broader discussion of the results obtained for the series of Li-exchanged IPC-1PI, **UTL**, **OKO**, and **PCR** zeolites.

5.1. CO adsorption on Li^+ sites: experiment *vs.* theory

The calculated CO stretching frequencies are in quantitative agreement with the band maxima obtained experimentally for CO adsorbed on Li-**OKO** (2195 and 2188 cm^{-1}) and on Li-**PCR** (2188 and shoulder at 2176 cm^{-1}), and thus, experimental spectra can be straightforwardly interpreted based on the theoretical investigation. The high-frequency band at 2195 cm^{-1} observed for CO/Li-**OKO** is due to the CO adsorption on two-coordinated I2 sites (Table 2 and Fig. 4). CO adsorption complexes on all other Li^+ sites (with 3- or 4-fold coordination) in Li-**OKO** are characterized by ν_{CO} between 2181 and 2191 cm^{-1}, well within the experimentally observed band centered at 2188 cm^{-1}. Larger values of $-\Delta H$ found for two-coordinated sites explain the relative intensity of two bands reported for CO/Li-**OKO** in Fig. 4C. As for Li-**PCR**, in agreement with experimental data (Fig. 4D) no high-frequency CO adsorption sites (above 2190 cm^{-1}) were found (Table 3). Even the adsorption complex formed on the I2 site is characterized by ν_{CO} = 2187 cm^{-1}, that is 8 cm^{-1} lower than the one found for the corresponding adsorption complex in Li-**OKO**. Note that Li^+ in the I2 site in Li-**PCR** is actually located inside the 8R window of the channel; therefore, the CO adsorption complex is almost perpendicular to the Al–Si direction (Fig. 6d). CO adsorption complexes on layer sites (ν_{CO} between 2186 and 2190 cm^{-1}) are characterized by higher $-\Delta H$ values than complexes on inter-layer sites (ν_{CO} between 2178 and 2181 cm^{-1}); that explains why the band maximum is shifted and a shoulder is formed at higher CO coverage. Experimental and calculated adsorption heats are in good agreement as well: at low CO coverage there are stronger adsorption sites on Li-**PCR** than on Li-**OKO** while at the coverage approaching $CO/Li^+ = 1$ the Li-**OKO** zeolite shows stronger adsorption sites than Li-**PCR** (Table 3). This is in line with experimental data (Fig. 5). Even quantitative agreement is reasonable – estimated experimental adsorption heats at zero coverage (43 and 44 kJ mol^{-1} for Li-**OKO** and Li-**PCR**, respectively) are close to values reported for the low-coordinated Li^+ sites (Table 2). Computational results reported previously for Li-IPC-1PI and Li-**UTL**[36] are compared with experimental results reported above in Table 2. A good qualitative and quantitative agreement between experimental and theoretical results reported above entitles us to discuss the subtle details of extra-framework cation coordination in a series of materials with similar topologies but different pore sizes.

5.2. Li^+ coordination and Lewis acid strength *vs.* pore dimension

The results reported above for Li-IPC-1PI, Li-**UTL**, Li-**OKO**, and Li-**PCR** may give us new insight into how the pore diameter affects the coordination of extra-framework cations and how that affects their Lewis acid strength. The structures of all four materials discussed here consist of identical 2D dense layers that are interconnected differently into 3D materials (Fig. 1): (i) IPC-1PI pillared material contains 2D IPC-1P layers (containing framework Al and thus extra-framework cations); the void space above the adsorption site is large compared to the size of the adsorbate and adsorption on Li-IPC-1PI can be viewed as an adsorption on the thin 2D IPC-1P layer. (ii) IPC-1P layers in **UTL** are connected by D4R units, forming relatively large 14R and 12R interconnected channels. (iii) Connection of IPC-1P layers with S4R, zeolite **OKO**, results in the 12R × 10R channel system. (iv) Direct condensation of IPC-1P layers (linked simply by oxygen atoms) gives **PCR** zeolite with 10R × 8R channels. While these four materials differ in the pore size (decreasing in the order IPC-1PI > **UTL** > **OKO** > **PCR**) they have a very similar topology – layer sites defined above (Al in T3′, T4′, T5′, T8′, T9′, T11′) are not much affected by the inter-layer linking and they are expected to be very similar in all four systems. In contrast, inter-layer sites (T6′ and T7′ – adjacent T-atoms to inter-layer linker; T10′ and T12′ – bridging T6′ and T7′ T-sites) depend on the way how IPC-1P layers are linked together and they are expected to have different properties. Computational results for all four materials are summarized in the ESI;† Li^+ coordination and dispersion contribution to CO interaction with zeolite are reported in Tables SI-2 and SI-3, respectively. Characteristics of CO adsorption complexes are summarized in Table 4.

First, we focus the discussion on layer sites. The coordination of Li^+ cations for the particular layer site (defined by Al position) is the same in all four materials inspected herein and

Table 4 Summary of CO adsorption enthalpies and stretching frequencies for Li^+ sites in Li-IPC-1PI, Li-**UTL**, Li-**OKO**, and Li-**PCR**[a]

		ΔH				ν_{CO}			
Al location	Al site	IPC-1PI	**UTL**	**OKO**	**PCR**	IPC-1PI	**UTL**	**OKO**	**PCR**
Layer sites	T3′	−35.4	−35.0	−36.2	−44.5	2187	2188	2190	2188
	T4′	−35.6	−40.4	−41.8	−46.5	2190	2192	2195	2187
	T5′	−31.8	−32.4	−34.9	−39.0	2183	2186	2186	2187
	T8′	−37.5	−37.6	−37.0	−41.7	2184	2187	2188	2186
	T9′	−28.5	−31.5	−35.1	−41.5	2177	2181	2181	2180
	T11′	−32.0	−32.4	−34.4	−42.0	2185	2190	2191	2190
Inter-layer sites	T6′	−24.2	−41.4	−35.7	−31.2	2175	2197	2189	2181
	T7′	−22.2	−41.8	−43.5	−31.4	2177	2196	2197	2181
	T10′	−22.9	−39.6	−39.1	−29.5	2175	2191	2191	2179
	T12	−34.5	−37.3	−39.9	−29.2	2184	2187	2190	2178

[a] Adsorption enthalpies and frequencies reported in kJ mol^{-1} and cm^{-1}, respectively.

Table 5 Average values of interaction energies (overall and its parts – dispersion and local contributions) and CO stretching frequencies[a]

	ΔH	Δ_{disp}	Δ_{local}	ν_{CO}
Layer sites				
IPC-1PI	−33.5	−11.2	−22.3	2184.3
UTL	−34.9	−11.0	−23.9	2187.4
OKO	−36.6	−11.2	−25.4	2188.5
PCR	−42.5	−16.0	−26.6	2186.5
Inter-layer sites				
IPC-1PI	−25.9	−7.8	−18.1	2177.7
UTL	−40.0	−10.5	−29.5	2192.8
OKO	−39.6	−11.0	−28.6	2191.8
PCR	−30.3	−15.7	−14.6	2179.8

[a] Interaction energies and frequencies in kJ mol^{-1} and cm^{-1}, respectively. Values are averaged for layer sites and for inter-layer sites.

even Li–O distances are very similar (*cf.* Table SI-2, ESI†). Therefore, any differences along the IPC-1PI–**UTL**–**OKO**–**PCR** series found for layer sites must be due to the changes in the channel diameter and its curvature. Averaged values of corresponding adsorption characteristics are reported in Table 5. Adsorption enthalpies increase for layer sites in the order IPC-1PI < **UTL** < **OKO** < **PCR**. Inspection of the dispersion contribution (obtained from the DFT/CC correction) and of the local contribution (PBE part of an overall interaction) reveals that the average dispersion interactions for layer sites are the same for IPC-1PI, **UTL**, and **OKO** (−11 kJ mol^{-1}) while they are larger (−16 kJ mol^{-1}) for **PCR**. It follows that the Lewis acid strength of Li^+ cations which can be roughly quantified by Δ_{local} increases with the decreasing diameter of channels (Table 5). This is also apparent from Fig. 7 that summarizes adsorption enthalpies and ν_{CO} for all four materials.

The CO stretching frequency is determined by a combination of the effect from the bottom and the effect from the top.[32,33] The effect from the bottom is represented by cation Lewis acid strength (its ability to polarize an adsorbate) – ν_{CO} increases with increasing cation Lewis acid strength. The effect from the top also leads to the ν_{CO} increase when the channel becomes smaller and CO vibrates "against" the wall. Following this model, ν_{CO} increases from IPC-1PI to **UTL** to **OKO** (Tables 5); however, ν_{CO} calculated for **PCR** does not increase with respect to

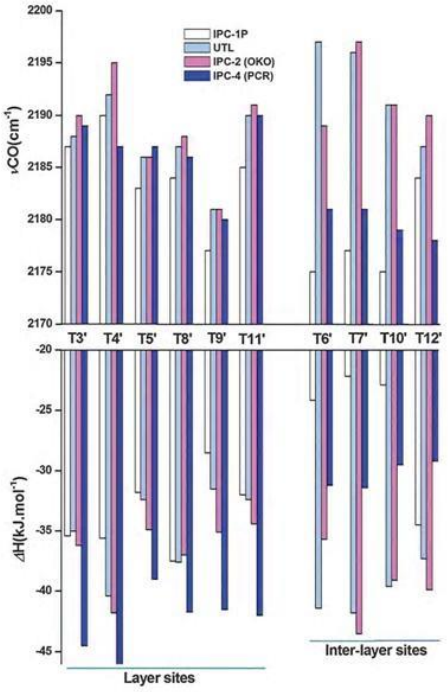

Fig. 7 CO adsorption energies (lower part) and CO stretching frequencies (upper part) for the most stable Li^+ sites in IPC-1PI, **UTL**, **OKO** and **PCR**.

zeolites with larger pores. This unexpected frequency decrease found for layer sites in **PCR** is in agreement with experimental observation (Fig. 4 and Table 2) and it is similar to the situation found previously for Li-**MFI** and Li-**FER** zeolites (having 10R × 10R and 10R × 8R intersecting channel systems, respectively).[34,58,59]

As for the inter-layer sites the coordination of Li^+ changes from system to system (Table SI-2, ESI†). Therefore, there are significantly larger differences between cation characteristics (Table 5). Intersection I2 sites, where Li^+ is coordinated to only 2 framework oxygens, exist only in Li-**UTL** and Li-**OKO**; CO adsorption complexes on these I2 sites show the highest frequency (2196–97 cm^{-1}), in agreement with experiment (Fig. 4). In the case of Li-**PCR**, the Li^+ in inter-layer sites is always coordinated to

four framework oxygen atoms (Table 3) and consequently its Lewis acid strength is rather small (Table 5). It follows that both $-\Delta H$ and ν_{CO} values are significantly lower than those in the case of **UTL** and **OKO**. The inter-layer sites in Li-IPC-1PI have the lowest Lewis acid strength reflected in low $-\Delta H$ and ν_{CO} values. First, there are no channels and intersections in Li-IPC-1PI; second, a smaller rigidity of 2D zeolite (compared to 3D one) results in better accommodation of Li^+ by framework atoms.[36]

The analysis presented above can be summarized on the example of experimental IR spectra of CO on all four materials presented in Fig. 4. The high frequency bands at 2194 cm^{-1} observed only for Li-**UTL** and Li-**OKO** are due to the presence of Li^+ cations in the intersection I2 sites. These sites do not exist in Li-**PCR** where Li^+ preferentially binds at channel wall sites and these sites cannot exist in layered Li-IPC-1PI. The low energy bands experimentally observed at 2183, 2187, 2187, and 2186 cm^{-1} for Li-IPC-1PI, Li-**UTL**, Li-**OKO**, and Li-**PCR**, respectively, correspond to CO adsorbed on channel wall sites where Li^+ is coordinated to at least three framework oxygen atoms. Relatively small differences in band maximum positions are due to the changes in the Lewis acid strength of Li^+ sites. The band shoulders observed for Li-**PCR** and Li-IPC-1PI at about 2176 cm^{-1} are mostly due to Li^+ in inter-layer sites which are formed in place of intersection sites in **OKO** and **UTL**. Thus, the strongest adsorption Li^+ sites in Li-**UTL** and Li-**OKO** become the weakest adsorption sites in Li-**PCR** and Li-IPC-1PI.

The results reported for three Li-zeolites and one structurally related Li-pillared material possessing the same structure of the layers clearly show that the correlation between $-\Delta H$ and ν_{CO} is rather weak.[13] Such correlation can only exist if both $-\Delta H$ and ν_{CO} are determined by the effect from the bottom and the effect from the top is negligible or constant. However, this is not the case as can be nicely demonstrated on the example of Li-**PCR** zeolite: the large adsorption enthalpy is due to a significant dispersion contribution (CO fits well in the 10R × 8R channel system) and it does not correspond to lower values of ν_{CO}.

Adsorption enthalpies were calculated at the DFT/CC level,[54] using correction functions derived previously.[36] Very good agreement between calculated and experimental adsorption heats was found for all four Li-exchanged materials investigated here. This agreement confirms that common DFT functionals overestimate interaction between the CO molecule and the Li (alkali metals in general) cation and good agreement with experiment can only be achieved upon appropriate correction. Adsorption enthalpies calculated at the PBE-D3 level at PBE optimized geometries for Li-**PCR** were as large as −50 kJ mol^{-1}; this overestimation is mostly due to the overestimation of $Li^+ \cdots CO$ interaction.

6. Conclusions

Lewis acidity of alkali-exchanged zeolites is determined by the Lewis acid strength of individual extra-framework cation sites. The Lewis acid strength depends on cation coordination – the weaker is the interaction between the extra-framework cation and the zeolite framework and more accessible is this cation the stronger is its Lewis acid strength. Therefore, cations located at the intersection of two channels are more active in adsorption and catalysis driven by the Lewis acidity than cations located inside the channels at the so-called channel-wall sites. The details of Lewis acid strength of Li-exchanged zeolites have been investigated by a combination of experimental (FTIR and microcalorimetry) and computational (DFT/CC and ω/r) methods using a CO probe molecule.

A unique series of zeolites with the same dense 2D layers with different interlayer linkers (IPC-1PI, **UTL**, **OKO**, and **PCR**) have been investigated. A majority of Li^+ sites defined by framework Al in the 2D layer have an identical local environment in all investigated materials. Therefore, the differences between them can be attributed to the size of the channels parallel to the 2D layers. A very good agreement between calculated and experimental adsorption enthalpies and CO stretching frequencies entitles us to draw following conclusions:

(i) The highest Lewis acid strength has been found for the Li^+ cation coordinated to only two framework oxygen atoms at the intersection of two channels where the Li^+ cation is located at the void space of the intersection. Such sites can only exist on the intersection of channels of the sizes larger than 8R – they only exist in Li-**UTL** and Li-**OKO** (having 14R × 12R and 12R × 10R channel systems, respectively). Intersection sites do not exist in Li-**PCR** (intersection of 10R and 8R channels) and they cannot exist in IPC-1PI. Thus, Li-**UTL** and Li-**OKO** have the strongest Lewis acid sites.

(ii) Evaluation of Lewis acid strength based on adsorption heats could be misleading; apart from (mostly electrostatic) interaction with the extra-framework cation there is a significant contribution from dispersion interactions between the adsorbate and the zeolite framework. Due to the good "fit" of CO into the 10R × 8R channel system of Li-**PCR** the dispersion component for this system is significantly larger than for other investigated zeolites and the largest adsorption heats were measured (and calculated) for Li-**PCR**, despite the fact that there are no sites with large Lewis acid strength at the channel intersection.

(iii) A detail analysis of Li^+ sites defined by 2D dense layers shows that Lewis acid strength depends on the channel dimension: Li^+ cations in smaller channels show slightly larger Lewis acid strength.

Acknowledgements

This work was supported by the Czech Science Foundation Grant No. P106/12/G015 (Centre of Excellence). Computational resources were provided by MetaCentrum under the program LM2010005 and the CERIT-SC under the program Centre CERIT Scientific Cloud, part of the Operational Program Research and Development for Innovations, Reg. No. CZ.1.05/3.2.00/08.0144.

References

1 D. Barthomeuf, *Mater. Chem. Phys.*, 1987, **17**, 49–71.
2 J. D. Rimer, M. Kumar, R. Li, A. I. Lupulescu and M. D. Oleksiak, *Catal. Sci. Technol.*, 2014, **4**, 3762–3771.

3 S. Bordiga, C. Lamberti, F. Geobaldo, A. Zecchina, G. T. Palomino and C. O. Arean, *Langmuir*, 1995, **11**, 527–533.
4 L. Grajciar, J. Cejka, A. Zukal, C. Otero Arean, G. Turnes Palomino and P. Nachtigall, *ChemSusChem*, 2012, **5**, 2011–2022.
5 P. Y. Dapsens, C. Mondelli and J. Perez-Ramirez, *Chem. Soc. Rev.*, 2015, **44**, 7025–7043.
6 T. Mori, A. Itadani, E. Tabuchi, Y. Sogo, R. Kumashiro, M. Nagao and Y. Kuroda, *Phys. Chem. Chem. Phys.*, 2008, **10**, 1203–1212.
7 H. Knozinger and S. Huber, *J. Chem. Soc., Faraday Trans.*, 1998, **94**, 2047–2059.
8 K. Hadjiivanov, in *Adv. Catal.*, ed. F. C. Jentoft, 2014, vol. 57, pp. 99–318.
9 I. Salla, T. Montanari, P. Salagre, Y. Cesteros and G. Busca, *Phys. Chem. Chem. Phys.*, 2005, **7**, 2526–2533.
10 V. V. Terskikh, C. I. Ratcliffe, J. A. Ripmeester, C. J. Reinhold, P. A. Anderson and P. P. Edwards, *J. Am. Chem. Soc.*, 2004, **126**, 11350–11359.
11 T. Yumura, H. Yamashita, H. Torigoe, H. Kobayashi and Y. Kuroda, *Phys. Chem. Chem. Phys.*, 2010, **12**, 2392–2400.
12 H. Yamashita, M. Matsuoka, K. Tsuji, Y. Shioya, M. Anpo and M. Che, *J. Phys. Chem.*, 1996, **100**, 397–402.
13 S. Bordiga, C. Lamberti, F. Bonino, A. Travert and F. Thibault-Starzyk, *Chem. Soc. Rev.*, 2015, **44**, 7262–7341.
14 B. Bonelli, B. Civalleri, B. Fubini, P. Ugliengo, C. O. Arean and E. Garrone, *J. Phys. Chem. B*, 2000, **104**, 10978–10988.
15 B. Civalleri, A. M. Ferrari, M. Llunell, R. Orlando, M. Merawa and P. Ugliengo, *Chem. Mater.*, 2003, **15**, 3996–4004.
16 P. Nachtigall, M. Davidova and D. Nachtigallova, *J. Phys. Chem. B*, 2001, **105**, 3510–3517.
17 C. O. Arean, M. R. Delgado, K. Frolich, R. Bulanek, A. Pulido, G. F. Bibiloni and P. Nachtigall, *J. Phys. Chem. C*, 2008, **112**, 4658–4666.
18 M. Fischer, M. Rodriguez Delgado, C. Otero Arean and C. Oliver Duran, *Theor. Chem. Acc.*, 2015, **134**, 91.
19 G. N. Vayssilov, M. Staufer, T. Belling, K. M. Neyman, H. Knozinger and N. Rosch, *J. Phys. Chem. B*, 1999, **103**, 7920–7928.
20 E. A. Pidko, J. Xu, B. L. Mojet, L. Lefferts, I. R. Subbotina, V. B. Kazansky and R. A. vanSanten, *J. Phys. Chem. B*, 2006, **110**, 22618–22627.
21 A. Itadani, T. Yumura, T. Ohkubo, H. Kobayashi and Y. Kuroda, *Phys. Chem. Chem. Phys.*, 2010, **12**, 6455–6465.
22 P. Rejmak, E. Broclawik, K. Gora-Marek, M. Radon and J. Datka, *J. Phys. Chem. C*, 2008, **112**, 17998–18010.
23 C. Busco, V. Bolis and P. Ugliengo, *J. Phys. Chem. C*, 2007, **111**, 5561–5567.
24 C. Busco, A. Barbaglia, M. Broyer, V. Bolis, G. M. Foddanu and P. Ugliengo, *Thermochim. Acta*, 2004, **418**, 3–9.
25 V. Van Speybroeck, K. Hemelsoet, L. Joos, M. Waroquier, R. G. Bell and C. R. A. Catlow, *Chem. Soc. Rev.*, 2015, **44**, 7044–7111.
26 R. Kumashiro, K. Fujie, A. Kondo, T. Mori, M. Nagao, H. Kobayashi and Y. Kuroda, *Phys. Chem. Chem. Phys.*, 2009, **11**, 5041–5051.
27 P. Y. Storozhev, C. O. Arean, E. Garrone, P. Ugliengo, V. A. Ermoshin and A. A. Tsyganenko, *Chem. Phys. Lett.*, 2003, **374**, 439–445.
28 P. Ugliengo, E. Garrone, A. M. Ferrari, A. Zecchina and C. O. Arean, *J. Phys. Chem. B*, 1999, **103**, 4839–4846.
29 A. Zecchina and C. O. Arean, *Chem. Soc. Rev.*, 1996, **25**, 187–197.
30 K. I. Hadjiivanov and G. N. Vayssilov, in *Adv. Catal.*, ed. B. C. Gates and H. Knozinger, 2002, vol. 47, pp. 307–511.
31 P. Ugliengo, C. Busco, B. Civalleri and C. M. Zicovich-Wilson, *Mol. Phys.*, 2005, **103**, 2559–2571.
32 D. Nachtigallova, O. Bludsky, C. O. Arean, R. Bulanek and P. Nachtigall, *Phys. Chem. Chem. Phys.*, 2006, **8**, 4849–4852.
33 C. O. Arean, M. R. Delgado, C. L. Bauca, L. Vrbka and P. Nachtigall, *Phys. Chem. Chem. Phys.*, 2007, **9**, 4657–4661.
34 P. Nachtigall, K. Frolich, H. Drobna, O. Bludsky, D. Nachtigallova and R. Bulanek, *J. Phys. Chem. C*, 2007, **111**, 11353–11362.
35 R. Bulanek, I. Voleska, E. Ivanova, K. Hadjiivanov and P. Nachtigall, *J. Phys. Chem. C*, 2009, **113**, 11066–11076.
36 H. V. Thang, M. Rubes, O. Bludsky and P. Nachtigall, *J. Phys. Chem. A*, 2014, **118**, 7526–7534.
37 W. J. Roth, O. V. Shvets, M. Shamzhy, P. Chlubna, M. Kubu, P. Nachtigall and J. Cejka, *J. Am. Chem. Soc.*, 2011, **133**, 6130–6133.
38 W. J. Roth, P. Nachtigall, R. E. Morris, P. S. Wheatley, V. R. Seymour, S. E. Ashbrook, P. Chlubna, L. Grajciar, M. Polozij, A. Zukal, O. Shvets and J. Cejka, *Nat. Chem.*, 2013, **5**, 628–633.
39 P. Eliasova, M. Opanasenko, P. S. Wheatley, M. Shamzhy, M. Mazur, P. Nachtigall, W. J. Roth, R. E. Morris and J. Cejka, *Chem. Soc. Rev.*, 2015, **44**, 7177–7206.
40 M. Mazur, P. S. Wheatley, M. Navarro, W. J. Roth, M. Položij, A. Mayoral, P. Eliášová, P. Nachtigall, J. Čejka and R. E. Morris, *Nat. Chem.*, 2016, **8**, 58–62.
41 E. Verheyen, L. Joos, K. Van Havenbergh, E. Breynaert, N. Kasian, E. Gobechiya, K. Houthoofd, C. Martineau, M. Hinterstein, F. Taulelle, V. Van Speybroeck, M. Waroquier, S. Bals, G. Van Tendeloo, C. E. A. Kirschhock and J. A. Martens, *Nat. Mater.*, 2012, **11**, 1059–1064.
42 M. V. Shamzhy, O. V. Shvets, M. V. Opanasenko, P. S. Yaremov, L. G. Sarkisyan, P. Chlubna, A. Zukal, V. R. Marthala, M. Hartmann and J. Cejka, *J. Mater. Chem.*, 2012, **22**, 15793–15803.
43 J. Jagiello, *Langmuir*, 1994, **10**, 2778–2785.
44 C. Baerlocher and L. B. McCusker, http://www.iza-structure.org/databases.
45 D. Nachtigallova, P. Nachtigall, M. Sierka and J. Sauer, *Phys. Chem. Chem. Phys.*, 1999, **1**, 2019–2026.
46 O. Bludsky, M. Silhan, P. Nachtigall, T. Bucko, L. Benco and J. Hafner, *J. Phys. Chem. B*, 2005, **109**, 9631–9638.
47 J. P. Perdew, K. Burke and M. Ernzerhof, *Phys. Rev. Lett.*, 1996, **77**, 3865–3868.
48 J. P. Perdew, K. Burke and M. Ernzerhof, *Phys. Rev. Lett.*, 1997, **78**, 1396.
49 P. E. Blochl, *Phys. Rev. B: Condens. Matter Mater. Phys.*, 1994, **50**, 17953–17979.
50 G. Kresse and D. Joubert, *Phys. Rev. B: Condens. Matter Mater. Phys.*, 1999, **59**, 1758–1775.
51 G. Kresse and J. Hafner, *Phys. Rev. B: Condens. Matter Mater. Phys.*, 1994, **49**, 14251–14269.

52 G. Kresse and J. Furthmuller, *Comput. Mater. Sci.*, 1996, **6**, 15–50.
53 O. Bludsky, M. Silhan, D. Nachtigallova and P. Nachtigall, *J. Phys. Chem. A*, 2003, **107**, 10381–10388.
54 O. Bludsky, M. Rubes, P. Soldan and P. Nachtigall, *J. Chem. Phys.*, 2008, **128**, 114102.
55 D. Nachtigallova, P. Nachtigall and O. Bludsky, *Phys. Chem. Chem. Phys.*, 2004, **6**, 5580–5587.
56 P. Nachtigall and R. Bulanek, *Appl. Catal., A*, 2006, **307**, 118–127.
57 J. Kucera and P. Nachtigall, *Phys. Chem. Chem. Phys.*, 2003, **5**, 3311–3317.
58 C. O. Arean, O. V. Manoilova, M. R. Delgado, A. A. Tsyganenko and E. Garrone, *Phys. Chem. Chem. Phys.*, 2001, **3**, 4187–4188.
59 B. Bonelli, E. Garrone, B. Fubini, B. Onida, M. R. Delgado and C. O. Arean, *Phys. Chem. Chem. Phys.*, 2003, **5**, 2900–2905.

Attachment C

Dalton Transactions

PAPER

View Article Online
View Journal | View Issue

Theoretical investigation of layered zeolites with MWW topology: MCM-22P *vs.* MCM-56

Cite this: *Dalton Trans.*, 2014, **43**, 10443

M. Položij,[a] Ho Viet Thang,[a] M. Rubeš,[b] P. Eliášová,[c] J. Čejka[c] and P. Nachtigall*[a]

Received 8th February 2014,
Accepted 10th March 2014

DOI: 10.1039/c4dt00414k

www.rsc.org/dalton

The inter-layer interactions and the possible arrangements of MWW-type layers were investigated computationally at the non-local density functional theory level. Powder XRD patterns were simulated for structures obtained computationally and compared with experimental data. The MCM-22P material corresponds to the layers bound with relatively strong hydrogen bonds between surface silanol groups that is an energetically preferred structure in the presence of a structure directing agent (hexamethyleneimine). The powder XRD pattern of MCM-56 is best matched for relatively disordered (in the *ab* plane) MWW layers that are partially condensed. The appearance of the powder XRD pattern in the 2θ range of 7.5–10° depends on the extent of interlayer condensation. The combination of density functional investigation of interactions between MWW layers together with simulation of powder XRD patterns brings atomistic insight into the inter-layer arrangement and better understanding of the effects responsible for the differences between various layered materials of the MWW family.

Introduction

Exceptional catalytic and adsorption properties of zeolites are well known.[1,2] The selectivity depending on the size, shape, and connectivity of microporous channel architectures is among the most valued advantages of zeolites; however, the size of pores becomes a major limitation for the use of zeolites for bulky reactants and products. The concept of hierarchical zeolites offers a valuable extension of the zeolite applicability.[3,4] One of the approaches towards hierarchical microporous/mesoporous materials is based on the synthesis of layered zeolite materials.[5]

The family of MWW-type zeolites and related layered materials is undoubtedly the most studied class of layered zeolitic materials and it also has resulted in the largest number of reported materials based on just a single zeolite architecture.[6] The synthesis of 3D zeolites can proceed *via* a layered 2D precursor; since individual layers are held together by weak intermolecular forces only (H-bonding and dispersion interactions, in particular) they can be further manipulated and, consequently, a large variety of related materials has been reported. Three-dimensional (3D) zeolites as well as materials based on two-dimensional (2D) layers with MWW topology reported in the literature include MCM-22, MCM-49, MCM-56, MCM-36, PSH-3, SSZ-25, ERB-1, IEZ-MWW, ITQ-2, EMM-12, and EMM-10.[7–13]

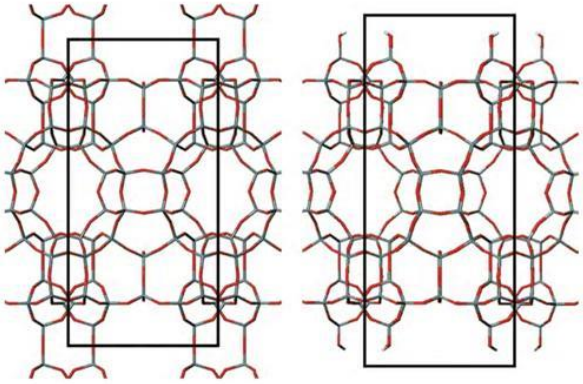

Fig. 1 Structure of the 3D (left) and 2D (right) MWW zeolites. The framework Si and O atoms depicted in grey and red, respectively. UC is shown in black.

The MCM-22 zeolite (MWW topology) contains two independent channel systems: the two-dimensional sinusoidal 10-ring channels and the 12-ring cages (7.1 × 7.1 × 18.2 Å) interconnected *via* 10-ring windows. The corresponding layered material consists of 2D layers with the MWW topology (denoted below as MWW layers) stacked along the *c*-axis (Fig. 1). Those 2D layers can be obtained from 3D MWW

[a]*Faculty of Science, Charles University in Prague, Hlavova 8, 128 43 Prague 2, Czech Republic. E-mail: petr.nachtigall@natur.cuni.cz*
[b]*Institute of Organic Chemistry and Biochemistry, Academy of Sciences of the Czech Republic v.v.i., Flemingovo nám. 2, 166 10 Prague 6, Czech Republic*
[c]*J. Heyrovský Institute of Physical Chemistry, Academy of Sciences of the Czech Republic v.v.i., Dolejškova 3, 182 23 Prague 8, Czech Republic*

crystals by cutting along the plane defined by *a*,*b* lattice vectors (denoted as the *ab* plane) at the middle of the cage, where the density of T–O–T bonds is the lowest. Consequently, 12-ring cups (half-cages) are accessible from the external surface of the MWW layer.[14]

Individual layered materials of the MWW family differ in the distance between the layers, the translation in the *ab* plane, and in the degree of regularity in organization of neighbouring layers. The best known examples of layered materials of this type are MCM-22P and MCM-56. While the structure of the MCM-22P material is relatively well understood the details of the inter-layer interactions of other layered materials of the MWW family are far less clear. The inter-layer interactions and the structure of layered materials are addressed herein in order to improve our understanding of layered zeolites.

The structure of MCM-22P is often related to the inter-layer hydrogen bonds (H-bonds) between surface silanols. The MCM-56 material also consists of MWW layers with significantly smaller stacking repeat than reported for MCM-22P (25 and 27 Å, respectively). The MCM-56 structure is less regular than that of MCM-22P (see, *e.g.*, ref. 15); it is believed that MWW layers in MCM-56 are randomly stacked on top of each other. This explanation was also supported by the powder XRD patterns simulated for just a single MWW layer with experimental crystal sizes, *i.e.* 10 000 × 10 000 × 25 Å; good agreement between experimental and simulated patterns was found. The layered structure has been confirmed for both MCM-22P and MCM-56 materials.[10] MCM-56 can be prepared by direct synthesis[10] or by the conversion of MCM-22P to MCM-56, which was achieved by mild acid treatment that resulted in washing off the structure directing agent (SDA).[11,16] Subsequent addition of SDA (hexamethyleneimine, HMI) resulted in reversible transformation back to MCM-22P.[16]

On the computational side, state-of-the-art methods were used recently for the description of layered zeolites, mostly focusing on the properties of individual layers.[17,18] It should be mentioned, however, that a too large change of the inter-layer distance (2.7 Å) was reported for the MCM-22P/MCM-22 transition based on simple density functional theory (DFT) calculations that does not account for the dispersion interactions.[19] The interactions between adjacent layers of IPC-1P[20,21] were investigated at the dispersion-corrected DFT level. The powder XRD patterns were in good agreement with experimental data and they helped to understand the mechanism of the ADOR protocol leading to the synthesis of new zeolites.[22] The interaction of MCM-22P layers is investigated herein using the similar computational strategy to that used previously for UTL layers (IPC-1P).[21] The role of SDA in the arrangement of MWW layers is also investigated with the goal to improve our understanding of the inter-layer interactions based on a comparison of experimental powder XRD patterns with those simulated for various interlayer arrangements obtained computationally.

Results and discussion

MWW slabs contain two surface silanol groups on each side of the unit cell. The interactions between these silanol groups determine the inter-layer arrangement and, thus, the structure of MWW layered materials. Three possible interaction modes, varying in the type of inter-layer hydrogen bond (H-bond), were identified based on the dispersion-corrected DFT calculations (Fig. 2): (i) the "stack" structure, where silanol groups on adjacent layers are just above each other (Fig. 2a); two weak non-linear H-bonds are formed between each pair of silanols ($R_{O\cdots H}$ = 2.24 Å). (ii) The "hydrogen-bonded" structure (denoted as HB, Fig. 2b) is formed upon a small lateral shift (in the *ab* plane) resulting in the formation of just one strong H-bond between a pair of silanols ($R_{O\cdots H}$ = 1.84 Å). (iii) The

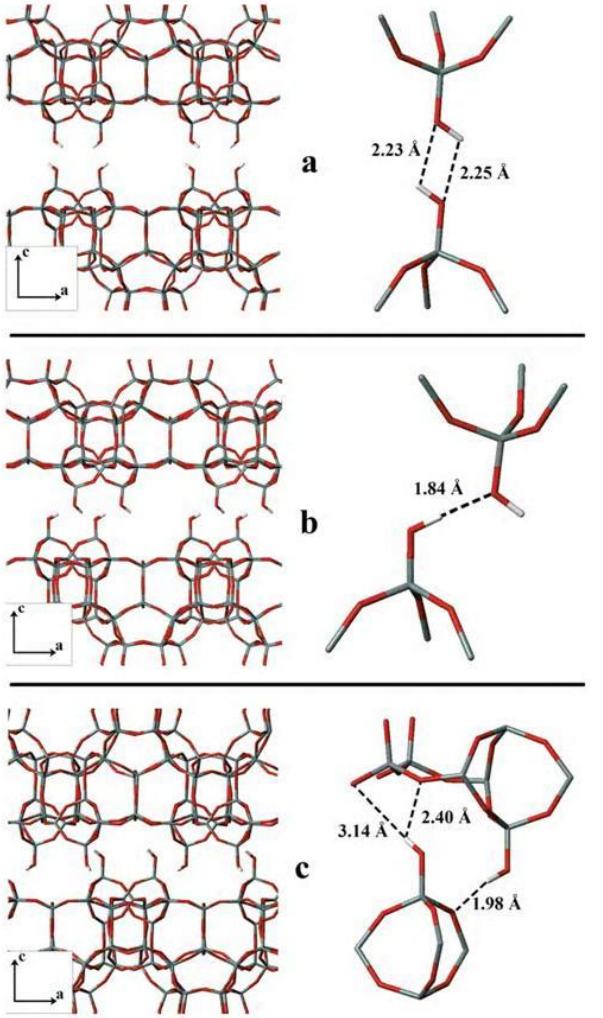

Fig. 2 Three types of inter-layer interactions found at the vdW-DF2 level for MWW layers: stack (a), HB (b) and SM (c); SDA molecules are not shown. The inter-layer interactions and detailed views shown in the left and right part of the figure, respectively; H···O distances are also shown.

"submerged" structure (denoted as SM, Fig. 2c) where the adjacent slabs are shifted by about half of the unit cell in the *ab* plane (Fig. 2c); the surface silanols on the adjacent surface then avoid each other (Fig. 2c) and the layers are submerged closer together. Surface silanol groups form only weak H-bonds with framework O_f atoms of the second slab.

The inter-layer arrangement was investigated without a structure directing agent (Fig. 2) and with one or two molecules of hexamethyleneimine (HMI) in the interlayer area (per UC). The details of SDA interactions with slab surfaces in the stack, HB, and SM arrangement are reported in Fig. 3 for the case with two molecules of HMI between the layers. In all cases the interaction is dominated by H-bonds (1.5–1.8 Å) between the surface silanol and HMI nitrogen. The strongest interaction between the HMI and MWW layer is found for the HB structure (Fig. 3b); only one H-bond is formed between a pair of silanols if no HMI is present (Fig. 2b), thus the second OH group can readily interact with HMI without disruption of inter-layer H-bonds (Fig. 3b). In the case of stack and SM structures, the inter-layer H-bonds are partially replaced by H-bonds with HMI. Note also that the presence of HMI leads to a small increase of the inter-layer distance (Table 1) for the HB structure while the opposite change is found for stack and SM structures.

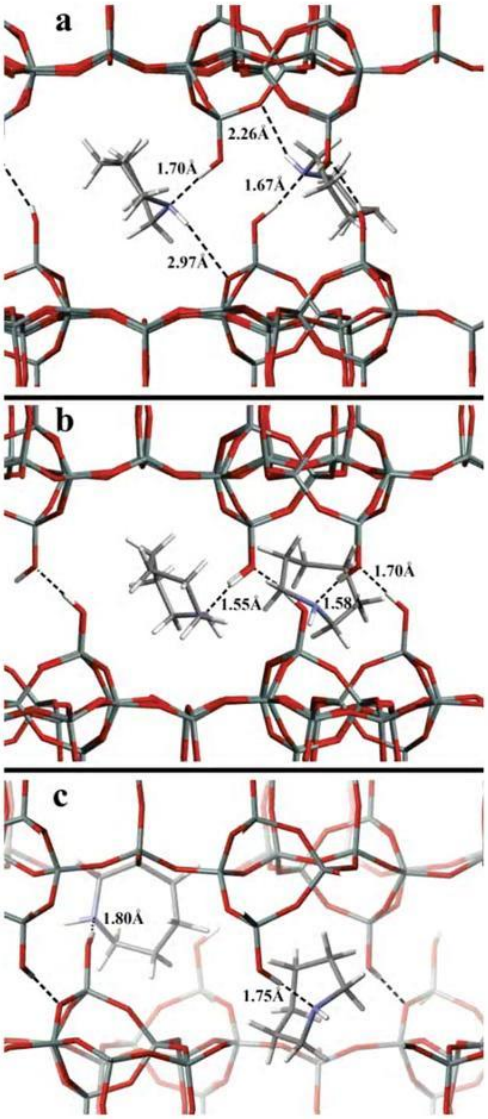

Fig. 3 Location of hexamethyleneimine molecules in the inter-layer region and details of its interaction with MWW layers shown for stack (a), HB (b) and SM (c) structures. N, H, and C atoms of HMI depicted in blue, white, and grey, respectively. H···O distances are also shown.

Table 1 Relative energies and structural parameters of HB, stack, and SM structures without any SDA and with one and two SDA (hexamethyleneimine) molecules

		HB	Stack	SM
No SDA	E_{rel} [a]	—	30.1	0
	c^b	—	28.1	25.6
	d^c	—	28.1	24.8
1 SDA	E_{rel} [a]	14.8	—	0
	c^b	27.1	—	25.6
	d^c	27.0	—	24.7
2 SDA	E_{rel} [a]	0	78.9	5.1
	c^b	27.3	27.8	25.8
	d^c	27.2	27.8	24.7
Exp.[d]	c^b	~27		~25
		MCM-22P		MCM-56

[a] Relative energies in kJ mol^{-1} per UC calculated with vdW-DF2 functional. [b] The length of the unit cell vector *c* in Å. [c] The perpendicular distance between slabs in Å. [d] From ref. 15.

Relative energies of individual structures are reported in Table 1 together with basic structural characteristics (showing the *c* lattice vector and the perpendicular distance *d* between the layers). The relative energies vary greatly depending on the presence of SDA between the layers. Only stack and SM structures were found without HMI, with the SM structure being 30 kJ mol^{-1} more stable. The SM structure remains energetically the most stable also in the case where there is just one HMI molecule between the zeolite layers; the HB structure is about 15 kJ mol^{-1} less stable and the stack structure was not found. After the addition of the second HMI molecule (there are two silanols on each surface), the HB structure becomes energetically the most stable, followed by SM (about 5 kJ mol^{-1}) while the stack structure is almost 80 kJ mol^{-1} higher in energy. The lengths of the *c* lattice vector reported in Table 1 show that our modelled structures could correspond to two experimentally known structures; HB and SM parameters are close to those reported for MCM-22P and MCM-56, respectively.[15] This suggestion is further supported by relative energies showing that in the presence of SDA the HB structure (corresponding to MCM-22P) is energetically preferable while without SDA in the inter-layer space the SM structure (corresponding to MCM-56) becomes energetically preferred. This observation is in good agreement with the experimentally observed reversible transition between MCM-22P and MCM-56 materials.[16] Therefore, the HB structure with SDA

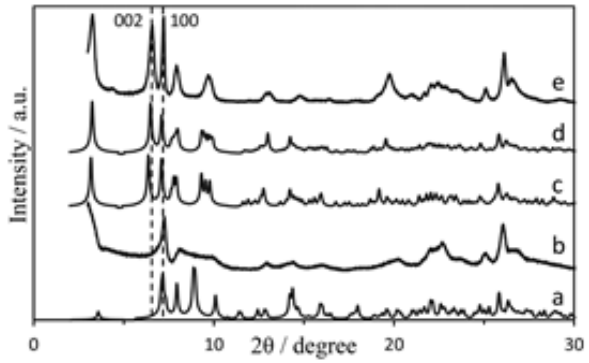

Fig. 4 XRD patterns simulated for regularly stacked layers along the *c* vector obtained at the vdW-DF2 level for SM (a), stack (c) and HB (d) compared with experimental patterns for MCM-56 (b) and MCM-22P (e).

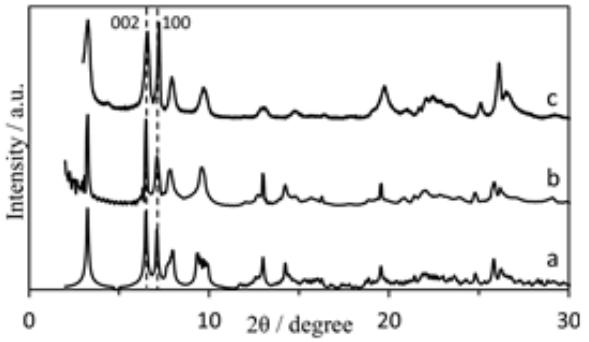

Fig. 5 Simulated XRD patterns for regularly (a) and randomly (b) arranged HB layers (randomness just within the six possible H-bond orientations) and the experimental MCM-22P XRD pattern (c).

molecules is assigned to MCM-22P and the SM structure without SDA is assigned to MCM-56. The stack structure does not match experimental data well; the *c* lattice vector is too long even for MCM-22P and the relative energy is too high with respect to other structures.

For better understanding of the inter-layer interactions and arrangements the experimental XRD powder patterns can be compared with those simulated for calculated structures. In the first, most simplistic, model the MWW layers were arranged regularly along the *c* lattice vector obtained from vdW-DF2 geometry optimization (Fig. 4). The SM structure shows overlapping (100) and (002) peaks (due to the shorter *c* lattice vector) in agreement with the MCM-56 pattern (Fig. 4a and 4b, respectively). However, the broad band in the 2θ region of 7.5–10° does not match the simulated pattern and the overall agreement between simulated and experimental patterns is rather poor. In contrast, the pattern simulated for the HB structure (Fig. 4d) matches the MCM-22P one (Fig. 4e) well; the only differences are in the shape of some peaks, in particular one in the 2θ region of 7.5–10°. The pattern simulated for the stack structure does not even give the right position of the (002) peak and this structure is not further considered.

XRD patterns simulated for regularly ordered layers show more diffraction lines than the corresponding experimental data. Due to the symmetry of MWW layers there are several *c* lattice vectors producing energetically equivalent inter-layer structures; thus, regular ordering along the *c* direction has the highest entropy and the statistical combination of all the possible translation in the *c* direction, producing arrangement with the same interaction energy, is more likely. In the case of the HB structure there are six equivalent arrangements of H-bonds between adjacent layers. The random combination of these six equivalent *c* lattice vectors is considered in the model of 30 layers consisting of 30 × 30 UC's. The corresponding powder pattern is shown in Fig. 5 together with one simulated for regular arrangement and experimental data. It is apparent that randomization of the layer arrangement (within six equivalent

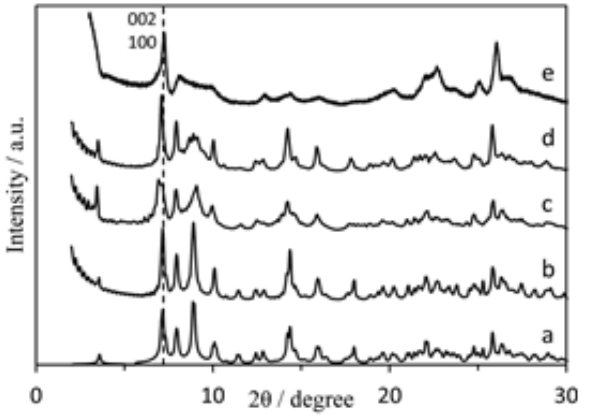

Fig. 6 XRD patterns of regular periodic SM (a); SM with randomly selected shifts (selecting one out of the four possible shifts) between layers (b); the lamellar precursor containing 70% of SM and 30% HB (c) and the calcined crystal containing 70% of SM and 30% MWW (d) compared with MCM-56 (e).

possibilities) brings greatly improved agreement with the experimental data.

The same randomization scheme can be applied for the SM structure as well; there are four symmetrically equivalent shifts (shifted by approximately 0.5 UC along ±[1,1,0] and ±[−1,1,0] directions). Simulated XRD patterns for regular and random arrangements are shown in Fig. 6 (curves a and b, respectively). This randomization does not bring any significant change in the simulated XRD patterns and it cannot explain the differences with respect to experimental data (Fig. 6e), in particular a peak broadening at 2θ 7.5–10°. The origin of this broad feature in the MCM-56 XRD pattern was investigated in detail by Juttu and Lobo;[14] good agreement with experimental XRD patterns was obtained for simulation mixing single and double MWW layers (45 and 55%, respectively). Following their suggestion the XRD patterns were obtained for the system where MWW layers were randomly stacked in the SM and HB arrangement (70 and 30%, respectively, Fig. 6c) and

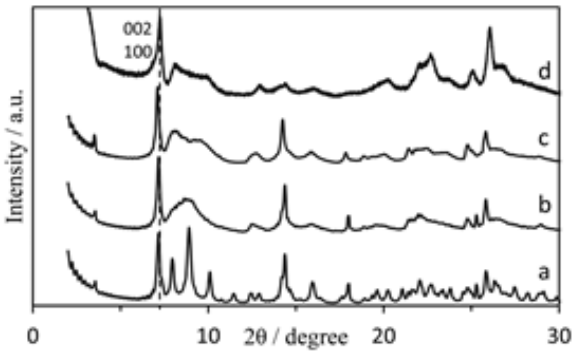

Fig. 7 XRD patterns of SM with regular shifts between layers (a); SM with random translation of adjacent layers (b) and crystals containing 70% of SM (with random translation) and 30% of MWW (c) compared with experimental patterns of MCM-56 (d).

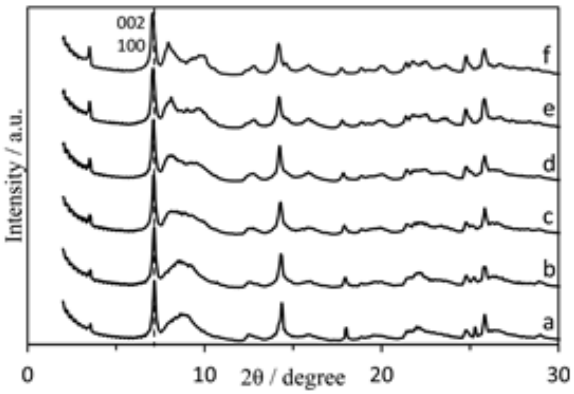

Fig. 8 Simulated XRD patterns of MCM-56 randomly shifted along allowed directions in *ab* (SM structure) and increasing fraction of pairs of condensed layers with the MWW structure; 100% SM structure (a), 90% SM (b), 80% SM (c), 70% SM (d), 60% SM (e), 50% SM (f).

for the system with randomly combined SM and regular MWW stacking obtained upon calcination (70 and 30%, respectively, Fig. 6d). The latter XRD pattern shows a significant broadening of peaks between 7.5 and 10° 2θ; nevertheless, the shape of this broad band is still different from the experimental one.

Another explanation of the broad band in the 2θ range of 7.5–10° was put forward by Roth *et al.*:[15] two distinct peaks in this 2θ range are due to (101) and (102) reflections corresponding to the ordered inter-layer arrangement while a broad band in the range indicates a lack of crystallographic order for the layer arrangement. The analysis of the surface of MWW layers shows that layers cannot be displaced completely randomly; surface silanol groups must avoid each other due to the small distance between the layers. Nevertheless, layers can be shifted in 4 different ways (directions ±[1,0,0], ±[0,1,0], ±[2,1,0] and ±[1,2,0]) with only small energy penalty. Thus, a number of local minima can be formed with different translations in *ab*; different framework O_f atoms take part in the inter-layer H-bonding (Fig. 3c). To simulate this irregularity in the structure, corresponding random translations in the *ab* plane have been imposed (Fig. 7b). In agreement with the suggestion of Roth *et al.* the distinct bands at 7.5–10° 2θ were replaced by a broad band (Fig. 7a). Nevertheless there are still differences between this simulated XRD pattern and the experimental one reported in Fig. 7d.

Inspection of the results reported in Fig. 6 and 7 indicates that the experimental XRD pattern is the result of a combination of both effects: random translation in the *ab* plane and partial condensation of MWW layers. The simulated XRD pattern for 30 MWW layers, where randomly selected 30% are condensed to the MWW structure and remaining 70% are in the SM arrangement with random translation in the *ab* plane (see above), is shown in Fig. 7c, in good agreement with experimental data. Note that the calcined (condensed) MWW has the (002) peak at the same position as the (100) peak of the SM structure. Note that calculations reported herein do not explicitly consider an effect of temperature; nevertheless the effect of temperature is implicitly included when the random translation of adjacent layers (along one of the four directions described above) is taken into consideration.

The results reported above indicate that the shape of XRD patterns in the 2θ range of 7.5–10° depends on the extent of interlayer condensation taking place during the calcination (or synthesis) in agreement with previous analysis.[15] If there is no or negligible inter-layer condensation the XRD pattern of the MCM-56 material should resemble the simulated pattern reported in Fig. 7b. Such XRD patterns were reported in the literature; examples can be found: Wang *et al.*[11] reported XRD patterns of Ti-MCM-56 analogues prepared from the MCM-22P lamellar precursor (the spectrum for the shortest reaction time in Fig. 3 of ref. 11). The condensation of adjacent MWW layers results in the apparent changes in the 2θ range of 7.5–10°; with the increasing degree of condensation the transition of the broad band into two separate bands becomes more pronounced, as indicated in Fig. 8. Similar XRD patterns were also reported by Wang *et al.*[11] for MCM-56 samples after prolonged acid treatments of MCM-22P (Fig. 3 in ref. 11). Similar behaviour has been reported also by Corma *et al.*[23] who compared MCM-56 with ITQ-2 and the reported powder pattern for MCM-56 (Fig. 1b in ref. 23) shows a very well defined gap in the broad band similar to our Fig. 8f reported herein.

XRD patterns of MCM-56 prepared by the direct synthesis with increasing reaction times are shown in Fig. 9. The sample obtained after 30 hours (Fig. 9a) exhibits peaks that are still relatively weakly pronounced and the broad band at 7.5–10° 2θ is clearly apparent. Two peaks at 8 and 10.1° 2θ are clearly visible in the pattern obtained for the sample after 33 hours indicating partial condensation to the MCM-49 zeolite. The pattern due to the structure obtained after 31.4 hours is just intermediate to the former two.

The MCM-22P ↔ MCM-56 transitions in both directions have been reported by Wang *et al.*[16] Upon addition of a strong acid the MCM-22P material "collapses" (along the *c* lattice vector) into the MCM-56 structure. This transition can be

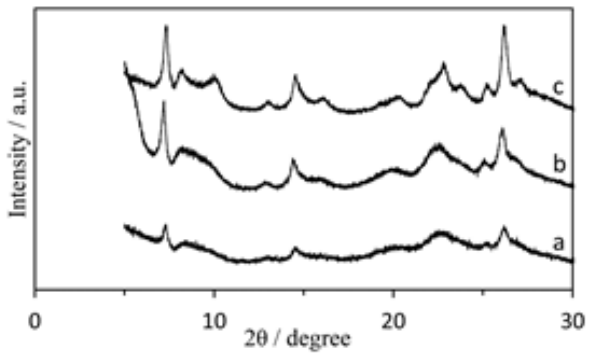

Fig. 9 Experimental XRD patterns for MCM-56 samples obtained from the synthesis after 30 (a), 31.4 (b) and 33 hours (c).

attributed to the loss of strong and stabilizing interaction between HMI (that becomes protonated) and surface silanols that is essential for the stability of the HB structure corresponding to the MCM-22P material (Table 1 and Fig. 2). It is known that the MCM-56 obtained by direct synthesis has a lower Si/Al molar ratio.[10] It is possible that the increased Al concentration in MWW layers consumes substantial part of SDA to compensate for the negative framework charge. Consequently, SDA molecules cannot have the same role in interlayer binding as in the case of the high-silica MCM-22P layered material.

Models and methods

The structure of MWW layers was derived from the parent MCM-22 zeolite[24] simply by cutting the crystal along the plane with the lowest density of T–O–T links and termination of unsaturated surface Si atoms with OH groups (Fig. 2). This leads to MWW layers in which the 12-ring cups are accessible from the surface as proposed by Juttu and Lobo.[14] There are two surface silanol groups on each surface in the unit cell (UC). The resulting UC has a composition $Si_{72}O_{146}H_4$. The interaction between layers was investigated with the periodic model; full geometry optimization (optimizing both the UC size and shape and atomic coordinates) was carried out for various starting geometries. Different mutual displacements (in the *ab* plane) were considered, thus different *c*, α, and β UC parameters were chosen, starting from the experimental UC ($a = b = 14.208$ Å, $c = 25.198$ Å, $\alpha = \beta = 90°$, $\gamma = 120°$).[24] All calculations were performed at the periodic density functional theory (DFT) level using non-local vdW-DF2 exchange-correlation functional[25] and projector augmented wave approximation (PAW).[26] The energy cut-off has been set to 800 eV. The vdW-DF2 functional has been shown to be suitable for the description of layered zeolites.[21] Brillouin-zone sampling was restricted to the Γ-point. All DFT calculations were performed using the VASP 5.3.3 program suite.[27–30]

The theoretical powder XRD patterns were simulated for the structures obtained at the vdW-DF2 level. The majority of the simulated XRD patterns was obtained for the finite size crystals using the UDskip software.[31,32] The wavelength of 1.5418 Å (CuKα) and crystals of the size 30 × 30 × 30 UC were used. Such a crystal has dimensions of about 430 × 430 × 750–820 Å (the *c* dimension depends on the type of inter-layer arrangement). A typical size of crystals measured experimentally is about 10 000 × 10 000 × 1000 Å.[14] A smaller dimension of *a* and *b* used in the simulation (due to the computational limitations) was tested using more than 30 UC in each direction. Simulated powder XRD patterns are not influenced by the size of the crystal except for the relative intensities of peaks corresponding to reflections in *c* and *ab*. Powder XRD patterns of fully periodic (infinite) crystals were also simulated using the Mercury software[33,34] for regular layer arrangements (the same *c* vector used for every pair of adjacent layers). The powder XRD patterns for structures with less regular arrangement of individual layers (see the Results and discussion section) were simulated as follows: *c* vectors defining the position for each pair of neighbouring layers were randomly selected from the pool of allowed *c* vectors and 30 × 30 × 1 UC slabs were combined in this way into the final 30 × 30 × 30 UC crystals. Such a procedure was repeated minimally 12 times and the superposition of the simulated XRD patterns was obtained.

The synthesis of MCM-22P and MCM-56 was carried out in a 1 l Parr autoclave under autogeneous pressure and with inner stirring. For the preparation of both materials hexamethyleneimine (HMI) was used as a structure-directing agent. The synthesis of MCM-22P followed the procedures described in the literature.[7,35,36] The molar composition of the reaction gel was $30SiO_2 : 0.44Al_2O_3 : 9.01Na_2O : 16.82HMI : 1586.34H_2O$. The synthesis proceeded at 143 °C for 96 hours. The solid product was filtered, washed out with distilled water and dried at 65 °C. MCM-56 was prepared by procedures published in ref. 37 and 38. The molar composition of the reaction gel was $30SiO_2 : 1.19Al_2O_3 : 2.9Na_2O : 9.61HMI : 520.26H_2O$. The reaction mixture was heated at 143 °C and the synthesis times were 30, 31.4 and 33 hours. The solid product was filtered, washed out with distilled water and dried at 65 °C. The structure and crystallinity of zeolites were determined by X-ray powder diffraction using a Bruker AXS D8 Advance diffractometer equipped with a graphite monochromator and a position sensitive detector Våntec-1 using CuKα radiation in Bragg–Brentano geometry.

Conclusions

The interactions between MWW layers and the structure of layered materials were investigated computationally using the dispersion-corrected DFT method; the obtained inter-layer arrangements were used in further simulations of powder XRD patterns (using finite size crystal approach) and compared with experimental data to verify the atomistic model derived

from calculations. Based on good agreement between experimental powder XRD patterns and those simulated for the DFT optimized structure the following atomistic model is proposed:

i. The interaction of MWW layers is driven by a balance between the dispersion interactions and inter-layer H-bonding. Stronger dispersion interactions and weaker H-bonding (formed between silanols and framework O_f oxygen atoms) result in a closely packed structure with c = 25.6 Å corresponding to MCM-56. Stronger H-bonding (between silanol groups) and weaker inter-layer dispersion is characteristic for the structure with c = 27.3 Å that corresponds to MCM-22P.

ii. The MCM-22P structure can be only formed in the presence of suitable SDA (HMI) that forms strong H-bonds with surface silanols; a minimum of one HMI molecule per surface silanol in the interlayer region is required. The MCM-22P structure is relatively highly ordered. The most important randomness (that must be respected in the model) is the orientation of inter-layer H-bonds; there are six equivalent c vectors.

iii. The MCM-56 structure is formed by closely packed MWW layers with a larger degree of translational disorder between the neighbouring layers; translations along several vectors in the *ab* plane are possible and they are defined by the repulsion between surface silanol groups on adjacent surfaces. No rotations between the layers are allowed since the layers are too close to avoid repulsion between silanols. The reflection in the 2θ range of 7.5–10° depends on the degree of inter-layer condensation; development of peaks at 8 and 10.1° 2θ is indicative of increased condensation of neighbouring layers.

Results reported herein show that the combination of experimental and theoretical investigation involving the simulation of powder XRD patterns for finite-size crystals is a useful approach for understanding the structure of lamellar zeolites.

Acknowledgements

This work was supported by the Czech Science Foundation grant no. P106/12/G015 (Center of Excellence) and grant no. 14-18521P (MR only). The support from the European Union Seventh Framework Programme (FP7/2007-2013) under grant agreement no. 604307 is also acknowledged. Calculations were partially performed at MetaCentrum and CERIT-SC computational facilities (MSM/LM2010005 and OP VaVpI CZ. 1.05/3.2.00/08.0144).

Notes and references

1 A. Corma, *Chem. Rev.*, 1995, **95**, 559–614.
2 D. Kubicka, I. Kubickova and J. Cejka, *Catal. Rev.*, 2013, **55**, 1–78.
3 J. Perez-Ramirez, *Nat. Chem.*, 2012, **4**, 250–251.
4 V. Valtchev, G. Majano, S. Mintova and J. Perez-Ramirez, *Chem. Soc. Rev.*, 2013, **42**, 263–290.
5 W. J. Roth and J. Cejka, *Catal. Sci. Technol.*, 2011, **1**, 43–53.
6 W. J. Roth, P. Nachtigall, R. E. Morris and J. Cejka, *Chem. Rev.*, 2014, DOI: 10.1021/cr400600f.
7 S. L. Lawton, A. S. Fung, G. J. Kennedy, L. B. Alemany, C. D. Chang, G. H. Hatzikos, D. N. Lissy, M. K. Rubin, H. K. C. Timken, S. Steuernagel and D. E. Woessner, *J. Phys. Chem.*, 1996, **100**, 3788–3798.
8 W. J. Roth, C. T. Kresge, J. C. Vartuli, M. E. Leonowicz, A. S. Fung and S. B. McCullen, *Stud. Surf. Sci. Catal.*, 1995, **94**, 301–308.
9 R. Millini, G. Perego, W. O. Parker Jr., G. Bellussi and L. Carluccio, *Microporous Mater.*, 1995, **4**, 221–230.
10 W. J. Roth, *Stud. Surf. Sci. Catal.*, 2005, **158**, 19–26.
11 L. L. Wang, Y. Wang, Y. M. Liu, L. Chen, S. F. Cheng, G. H. Gao, M. Y. He and P. Wu, *Microporous Mesoporous Mater.*, 2008, **113**, 435–444.
12 W. B. Fan, P. Wu, S. Namba and T. Tatsumi, *Angew. Chem., Int. Ed.*, 2004, **43**, 236–240.
13 A. Corma, V. Fornes, S. B. Pergher, T. L. M. Maesen and J. G. Buglass, *Nature*, 1998, **396**, 353–356.
14 G. G. Juttu and R. F. Lobo, *Microporous Mesoporous Mater.*, 2000, **40**, 9–23.
15 W. J. Roth, D. L. Dorset and G. J. Kennedy, *Microporous Mesoporous Mater.*, 2011, **142**, 168–177.
16 Y. Wang, Y. Liu, L. Wang, H. Wu, X. Li, M. He and P. Wu, *J. Phys. Chem. C*, 2009, **113**, 18753–18760.
17 K. Varoon, X. Zhang, B. Elyassi, D. D. Brewer, M. Gettel, S. Kumar, J. A. Lee, S. Maheshwari, A. Mittal, C.-Y. Sung, M. Cococcioni, L. F. Francis, A. V. McCormick, K. A. Mkhoyan and M. Tsapatsis, *Science*, 2011, **334**, 72–75.
18 W. Park, D. Yu, K. Na, K. E. Jelfs, B. Slater, Y. Sakamoto and R. Ryoo, *Chem. Mater.*, 2011, **23**, 5131–5137.
19 L. Palin, G. Croce, D. Viterbo and M. Milanesio, *Chem. Mater.*, 2011, **23**, 4900–4909.
20 W. J. Roth, O. V. Shvets, M. Shamzhy, P. Chlubna, M. Kubu, P. Nachtigall and J. Cejka, *J. Am. Chem. Soc.*, 2011, **133**, 6130–6133.
21 L. Grajciar, O. Bludsky, W. J. Roth and P. Nachtigall, *Catal. Today*, 2013, **204**, 15–21.
22 W. J. Roth, P. Nachtigall, R. E. Morris, P. S. Wheatley, V. R. Seymour, S. E. Ashbrook, P. Chlubna, L. Grajciar, M. Polozij, A. Zukal, O. Shvets and J. Cejka, *Nat. Chem.*, 2013, **5**, 628–633.
23 A. Corma, U. Diaz, V. Fornés, J. M. Guil, J. Martínez-Triguero and E. J. Creyghton, *J. Catal.*, 2000, **191**, 218–224.
24 M. A. Camblor, A. Corma, M.-J. Díaz-Cabañas and C. Baerlocher, *J. Phys. Chem. B*, 1998, **102**, 44–51.
25 K. Lee, É. D. Murray, L. Kong, B. I. Lundqvist and D. C. Langreth, *Phys. Rev. B: Condens. Matter*, 2010, **82**, 081101.
26 G. Kresse and D. Joubert, *Phys. Rev. B: Condens. Matter*, 1999, **59**, 1758–1775.
27 G. Kresse and J. Furthmüller, *Comput. Mater. Sci.*, 1996, **6**, 15–50.
28 G. Kresse and J. Furthmüller, *Phys. Rev. B: Condens. Matter*, 1996, **54**, 11169–11186.

29 G. Kresse and J. Hafner, *Phys. Rev. B: Condens. Matter*, 1994, **49**, 14251–14269.
30 G. Kresse and J. Hafner, *Phys. Rev. B: Condens. Matter*, 1993, **47**, 558–561.
31 J. Boshoff, *UDSKIP, version 1.0*, University of Delevare, Newark, DE, 2001, http://www.che.udel.edu/research_groups/nanomodeling/resources.html
32 J. L. Schlenker and B. K. Peterson, *J. Appl. Crystallogr.*, 1996, **29**, 178–185.
33 C. F. Macrae, I. J. Bruno, J. A. Chisholm, P. R. Edgington, P. McCabe, E. Pidcock, L. Rodriguez-Monge, R. Taylor, J. van de Streek and P. A. Wood, *J. Appl. Crystallogr.*, 2008, **41**, 466–470.
34 *Mercury 3.1, Cambridge Crystallographic Data Centre*, http://www.ccdc.cam.ac.uk/mercury/
35 M. E. Leonowicz, J. A. Lawton, S. L. Lawton and M. K. Rubin, *Science*, 1994, **264**, 1910–1913.
36 P. Chlubná, W. J. Roth, A. Zukal, M. Kubů and J. Pavlatová, *Catal. Today*, 2012, **179**, 35–42.
37 A. S. Fung, S. L. Lawton and W. J. Roth, *US Pat*, 5,362,697, 1994.
38 W. J. Roth, P. Chlubná, M. Kubů and D. Vitvarová, *Catal. Today*, 2013, **204**, 8–14.

Attachment D

PCCP

PAPER

View Article Online
View Journal | View Issue

Measuring the Brønsted acid strength of zeolites – does it correlate with the O–H frequency shift probed by a weak base?†

Cite this: *Phys. Chem. Chem. Phys.*, 2014, **16**, 10129

Carlos O. Arean,*[a] Montserrat R. Delgado,[a] Petr Nachtigall,[b] Ho Viet Thang,[b] Miroslav Rubeš,[b] Roman Bulánek[c] and Pavla Chlubná-Eliášová[d]

Received 8th November 2013,
Accepted 30th January 2014

DOI: 10.1039/c3cp54738h

www.rsc.org/pccp

Brønsted-acid zeolites are currently being used as catalysts in a wide range of technological processes, spanning from the petrochemical industry to biomass upgrade, methanol to olefin conversion and the production of fine chemicals. For most of the involved chemical processes, acid strength is a key factor determining catalytic performance, and hence there is a need to evaluate it correctly. Based on simplicity, the magnitude of the red shift of the O–H stretching frequency, $\Delta\nu_{(OH)}$, when the Brønsted-acid hydroxyl group of protonic zeolites interacts with an adsorbed weak base (such as carbon monoxide or dinitrogen) is frequently used for ranking acid strength. Nevertheless, the enthalpy change, ΔH^0, involved in that hydrogen-bonding interaction should be a better indicator; and in fact $\Delta\nu_{(OH)}$ and ΔH^0 are often found to correlate among themselves, but, as shown herein, that is not always the case. We report on experimental determination of the interaction (at a low temperature) of carbon monoxide and dinitrogen with the protonic zeolites H-MCM-22 and H-MCM-56 (which have the MWW structure type) showing that the standard enthalpy of formation of OH···CO and OH···NN hydrogen-bonded complexes is distinctively smaller than the corresponding values reported in the literature for H-ZSM-5 and H-FER, and yet the corresponding $\Delta\nu_{(OH)}$ values are significantly larger for the zeolites having the MWW structure type (DFT calculations are also shown for H-MCM-22). These rather unexpected results should alert the reader to the risk of using the O–H frequency shift probed by an adsorbed weak base as a general indicator for ranking zeolite Brønsted acidity.

1. Introduction

By virtue of their relatively strong Brønsted acidity, zeolites containing the structural unit [Si(OH)Al] (where a proton is attached to an oxygen atom that bridges skeletal tetrahedrally coordinated Si and Al atoms) have a wide range of applications as solid acid catalysts in a broad range of chemical processes. Examples can be found, *inter alia*, in the petrochemical industry, methanol to olefin conversion and production of fine chemicals.[1–12] The strength of their (catalytically active) Brønsted acid sites is a main factor determining the catalytic performance (regarding both activity and selectivity) of protonic zeolites, hence the importance of having a reliable method to evaluate relative acidity, which would help to increase the understanding and optimize the performance of these versatile solid acid catalysts; but quantifying the strength of solid acids can be a delicate task to perform.

At variance with aqueous acid solutions for which the corresponding pK_a provides a quantitative measure of acid strength, no clear-cut measurements have yet been found for solid acids. Initial attempts at measuring acid strength of protonic zeolites by using amine-based Hammett indicators did not yield consistent results,[13,14] and indeed some objections to the use of that method were raised.[15,16] Currently, several instrumental techniques are used to gather increasing information on the (relative) Brønsted acidity of protonic zeolites. Among them, calorimetry of an adsorbed base, temperature programmed desorption, IR spectroscopy and solid state NMR[17–28] are sometimes combined with catalytic tests of acid strength.

Due (in part) to the ease of its usage, IR spectroscopy of an adsorbed weak base is (arguably) the most widely used

[a] *Department of Chemistry, University of the Balearic Islands, 07122 Palma de Mallorca, Spain. E-mail: co.arean@uib.es; Fax: +34 971173426; Tel: +34 971173251*
[b] *Department of Physical and Macromolecular Chemistry, Faculty of Science, Charles University of Prague, Hlavova 2030, Prague 2, 128 00, Czech Republic*
[c] *Department of Physical Chemistry, Faculty of Chemical Technology, University of Pardubice, 532 10 Pardubice, Czech Republic*
[d] *J. Heyrovsky Institute of Physical Chemistry, Academy of Sciences of the Czech Republic, 182 23 Prague, Czech Republic*

† Electronic supplementary information (ESI) available. See DOI: 10.1039/c3cp54738h

technique nowadays for measuring Brønsted acid strength of protonic zeolites, carbon monoxide being the preferred base molecule, although dinitrogen could equally well be used.[29–34] In principle, proton transfer between an acid zeolite, ZOH, and a sufficiently strong (adsorbed) base, B, would involve both, hydrogen-bonded and ion-paired intermediates, following eqn (1) below.

$$ZOH + B \leftrightarrows ZOH\cdots B \leftrightarrows ZO^{-}\cdots HB^{+} \leftrightarrows ZO^{-} + BH^{+} \quad (1)$$

However, for weak bases the process stops before the ion pair is formed, yielding only the hydrogen-bonded species, ZOH···B, which can easily be monitored by IR spectroscopy because hydrogen bonding brings about a distinctive bathochromic shift, $\Delta\nu_{(OH)}$, of the O–H stretching mode of the zeolite Brønsted-acid hydroxyl group. Moreover, one would expect that the stronger the Brønsted acid site, the larger should be the value of $\Delta\nu_{(OH)}$ (for any given weak base). Hence, direct measurement of $\Delta\nu_{(OH)}$ in the infrared spectrum of the hydrogen-bonded complex could, in principle, afford ranking of zeolite acidity. This method was pioneered some time ago by Paukshtis and Yurchenko,[35] and more recently reviewed in some detail by Dwyer *et al.*[36] and by Rigby *et al.*,[37] who confirmed the previously proposed logarithmic relationship between $\Delta\nu_{(OH)}$ and zeolite acid strength, as probed by adsorbed CO or dinitrogen. On account of its simplicity, direct correlation of $\Delta\nu_{(OH)}$ with acid strength is broadly invoked to rank zeolite acidity. However, this method is not free from a number of possible pitfalls, as pointed out by several authors.[38–43]

Recently, we found out a notable discrepancy in the apparent Brønsted acidity of H-MCM-22 (a zeolite belonging to the MWW structure type) when results obtained by (i) the $\Delta\nu_{(OH)}$ method and (ii) direct measurement of the enthalpy of hydrogen-bonding formation with adsorbed CO and dinitrogen were compared with those reported in the literature for other protonic zeolites.[44] Herein, we revise those experimental results, and compare them with corresponding calorimetric measurements and DFT calculations. In addition, we report experimental measurements on another H-MCM-22 sample having a different Si : Al ratio, as well as on H-MCM-56, which is another zeolite having the MWW structure type. The whole set of experimental results is discussed in the broader context of corresponding available data for other protonic zeolites having different structure types, with a particular reference to H-FER.

2. Materials and methods

2.1. Samples

Samples of the isostructural zeolites MCM-22 (Si : Al = 24.5 : 1 and 16.4 : 1) and MCM-56 (Si : Al = 16 : 1) were prepared, in their sodium form, following procedures described in detail elsewhere,[45–47] and checked by powder X-ray diffraction, which confirmed good crystallinity and the absence of any diffraction line not assignable to the corresponding MWW structure type. The Si : Al ratio was determined by XRF analysis. These parent samples were ion-exchanged into their corresponding NH_4^+ forms by treating them repeatedly with a 1.0 M aqueous solution of NH_4NO_3 for 4 hours at room temperature, 100 mL of solution per gram of zeolite. From the ammonium form, the corresponding protonic form was obtained by *in situ* thermal treatment inside an IR cell, as described below.

2.2. Variable-temperature IR (VTIR) spectroscopy: determination of the standard adsorption enthalpy and entropy involved in hydrogen bonding

For IR spectroscopy, a thin self-supported wafer of each zeolite sample (in its ammonium form) was prepared and subjected to thermal treatment in a dynamic vacuum (residual pressure smaller than 10^{-4} mbar) for 4 h at 673 K inside an IR cell which allowed *in situ* sample treatment, gas dosage and variable-temperature IR spectroscopy to be carried out.[48] After thermal treatment, 0.2 mbar of helium was admitted into the sample compartment (to improve thermal contact between the cell body and the sample wafer) and cooled with liquid nitrogen before recording the zeolite background spectrum at liquid nitrogen temperature; no bands of ammonium ions were seen in any of the spectra, thus proving complete transformation of the ammonium zeolites into their corresponding protonic forms during thermal treatment. The IR cell was then dosed with a fixed amount of either CO or N_2 and closed, and series of IR spectra were recorded upon gradual warming up of the cell, while simultaneously registering temperature and gas equilibrium pressure. For that purpose, the cell was equipped with a platinum resistance thermometer (Tinsley) and a capacitance pressure gauge (MKS, Baratron). Pressure correction (for helium) was determined from a calibration plot, as described elsewhere.[49] Precision of measurements was better than $\pm 10^{-2}$ mbar and ± 2 K for pressure and temperature, respectively. Transmission FTIR spectra were recorded, at 2 cm^{-1} resolution, on a Bruker IFS66 instrument, accumulating 64 scans for each spectrum.

It is well known that for both carbon monoxide and dinitrogen, adsorption at a low temperature in protonic zeolites results in hydrogen bonding because of localized interaction of the gas molecules with the Brønsted-acid [Si(OH)Al] groups of the zeolite. Such a process results in progressive erosion of the characteristic O–H stretching band, which is red-shifted when forming the corresponding OH···CO or OH···N_2 complex; simultaneously, the characteristic IR absorption band of the hydrogen-bonded molecule builds up. A set of IR spectra obtained over a temperature range while simultaneously recording IR absorbance, temperature and gas equilibrium pressure inside a closed IR cell can be used to determine the standard enthalpy, ΔH^0, and entropy, ΔS^0, of the (localized) gas adsorption process.[50] The method, termed VTIR spectroscopy, was explained in detail elsewhere,[51] and tested not only for hydrogen bonding but also for studying the thermodynamics of gas adsorption on a large number of alkaline zeolites.[52,53] However, in order to facilitate understanding of the results reported here, an abridged account is given below.

Referring to hydrogen bonding, let eqn (2) below represent the adsorption equilibrium of a molecule, M, on the adsorption centre, ZOH, representing a zeolite Brønsted-acid site:

$$ZOH_{(s)} + M_{(g)} \leftrightarrows ZOH\cdots M_{(ads)} \quad (2)$$

For any given temperature, T, the integrated intensity, A, of a characteristic IR absorption band (from either the adsorbent or the adsorbed molecule) should be proportional to surface coverage, θ, of the specific adsorption centres being considered. Hence, that IR absorption band gives information on the activity (in the thermodynamic sense) of both, the adsorbed species and the empty sites $(1 - \theta)$. Simultaneously, the equilibrium pressure, p, monitors the activity of the gas phase. Therefore, the value of the adsorption equilibrium constant, K, at that temperature, can be determined; assuming Langmuir type adsorption, K is given by eqn (3) below:

$$\theta = K(T)p/[1 + K(T)p] \quad (3)$$

The variation of K with temperature is related to standard adsorption enthalpy and entropy through the van't Hoff equation:

$$K(T) = \exp(-\Delta H^0/RT)\exp(\Delta S^0/R) \quad (4)$$

Combination of eqn (3) and (4) leads to eqn (5) below:

$$\ln\{\theta/[(1 - \theta)p]\} = (-\Delta H^0/RT) + (\Delta S^0/R) \quad (5)$$

Eqn (5) can also be written as:

$$\ln\{A/[(A_M - A)p]\} = (-\Delta H^0/RT) + (\Delta S^0/R) \quad (6)$$

where A stands for the actual IR absorbance being measured and A_M is the maximum absorbance (which corresponds to $\theta = 1$). It should be clear that, after determining θ (or relative absorbance) as a function of T and p over a sufficiently large temperature range, eqn (5) or (6) gives direct access to the thermodynamic quantities ΔH^0 and ΔS^0 characterizing the gas adsorption process under study.

2.3. Adsorption calorimetry

As a cross-check of the ΔH^0 values obtained by VTIR spectroscopy, we performed adsorption calorimetry of carbon monoxide on H-MCM-22 (Si : Al = 24.5 : 1), as well as on a H-FER sample (Si : Al = 27.5 : 1) for which VTIR measurements and theoretical (periodic DFT) calculations were already available.[54] Calorimetric measurements were performed at a constant temperature of 303 K using a Tian–Calvet type microcalorimeter (Seratam BT2.15) connected to a volumetric apparatus. The sample cell contained 400 mg of the sample, whereas the reference cell was left empty. Before measurements, the zeolite sample was outgassed by slowly increasing the temperature under a dynamic vacuum up to 700 K, after which it was kept at this temperature and a pressure of 10^{-4} mbar overnight. After this activation of the sample, the cell was placed inside the calorimeter and outgassed to the pressure of 10^{-6} mbar using a turbo-molecular pump. The CO gas used (99.997% Linde) was further purified by means of freeze–pump–thaw cycles before dosing it into the cell. CO dosing was done *via* a computer controlled valve following a designed program. After each dose the system was allowed to equilibrate for 45 min. Data of heat flow and pressure–time dependence were collected throughout the whole measurement run, thus allowing calculation of the differential heat of adsorption as a function of the adsorbed amount for each step.

2.4. Theoretical calculations

The MCM-22 framework has a hexagonal unit cell, space group $P6/mmm$ ($T_{72}O_{144}$, where T is either a Si or Al atom), in which there are eight non-equivalent T sites and thirteen non-equivalent framework oxygen atoms. This structure and the atom numbering scheme (following the Database of Zeolite Structures[55]) are shown in Fig. 1. The channel system including two 10-membered rings (MR) (10-MR sinusoidal and 10-MR crossing windows), as well as the 12-MR supercage are also shown. Calculations were performed with the unit cell (UC) parameters obtained from the Database of Zeolite Structures.[55] All calculations were carried out with one framework Al atom (and charge-compensating H^+) in the UC, which corresponds to a Si : Al ratio of 71 : 1; Al was substituted to each of the eight non-equivalent T sites, and all possible symmetrically non-equivalent Brønsted-acid sites were considered.

All calculations were performed with the periodic model using the VASP program package.[56,57] The Perdew–Burke–Ernzerhof (PBE) exchange–correlation functional,[58,59] the projector augmented wave approximation (PAW)[60,61] and the plane wave basis set with a kinetic energy cut-off of 400 eV were used; the Brillouin-zone sampling was restricted to the Γ-point. Geometry optimizations were performed with fixed UC volume

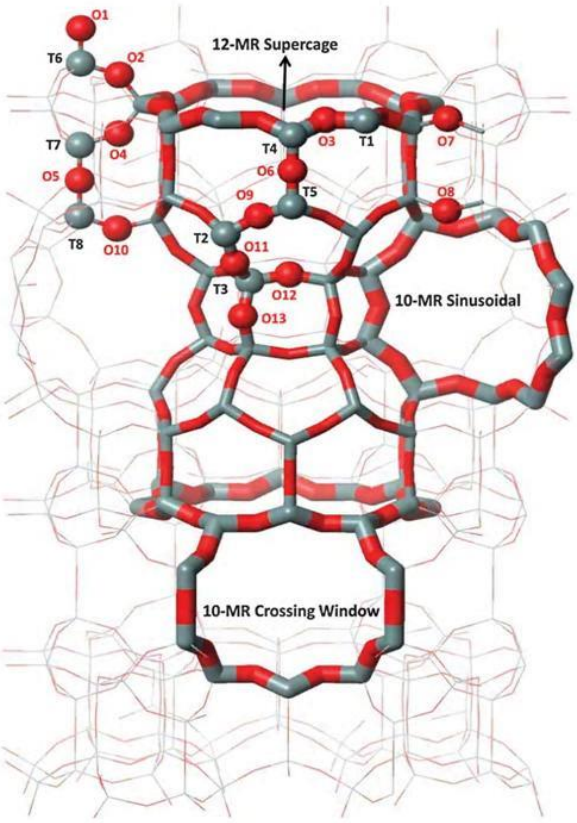

Fig. 1 Structure of the MCM-22 framework and numbering scheme of the eight non-equivalent T sites and thirteen non-equivalent framework oxygen atoms. Framework T sites and framework oxygen atoms are depicted in grey and red, respectively.

and shape, while relaxing the positions of all atoms. At this PBE-optimized geometry the interaction energies were also calculated with dispersion-corrected DFT methods, PBE-D2,[62] PBE-D3,[63] and vdW-DF2,[64] in particular. The C–O stretching frequency of carbon monoxide adsorbed on Brønsted acid sites and the O–H stretching frequencies were evaluated using the ω_{CO}/r_{CO} and ν_{OH}/r_{OH} correlation schemes, respectively, described in detail in ref. 54. Only the PBE exchange–correlation functional was used for calculations of vibrational frequencies within the ω/r correlation scheme, since this correlation is with respect to an accurate coupled cluster, CCSD(T), the level of theory following the method previously established.[65]

Zero-point energies (ZPE) were calculated within the harmonic approximation considering 6 degrees of freedom for CO and 6 degrees of freedom for the Brønsted-acid OH group for the case of Al atoms in the T1 position. Two displacement steps in each direction, with a step size of 0.005 Å, were used to calculate numerically the corresponding second derivatives. Our previous investigation of CO interaction with H-FER[54] justifies the use of this ZPE correction for all of the Brønsted-acid sites investigated herein. Adsorption enthalpies are reported for 0 K only.

The substitution energy, ΔE(Al,H), was evaluated following the same strategy as that used by Li *et al.*[66] Therefore, substitution energies calculated herein within the periodic DFT model can be directly compared with those obtained previously based on cluster models.[66]

To verify the accuracy of various density functional theory-type methods, accurate CCSD(T) calculations were performed on the cluster model shown in Fig. 2. Interaction energies were calculated for CO interacting primarily with the Brønsted-acid site (represented by the 2T cluster model) and simultaneously with a model of zeolite framework represented by a 1T cluster model; C_S symmetry constrain was applied and CO was fixed along the O_B(2T) and Si(1T) axis as indicated in Fig. 2. Interaction energies are plotted as a function of separation, $R_{O(2T)\text{-}Si(1T)}$, between the two cluster models. Reported CCSD(T) interaction potentials are extrapolated to the complete basis set limit, DFT interaction potentials were obtained using the quadruple-ζ basis set with polarization functions.[67,68]

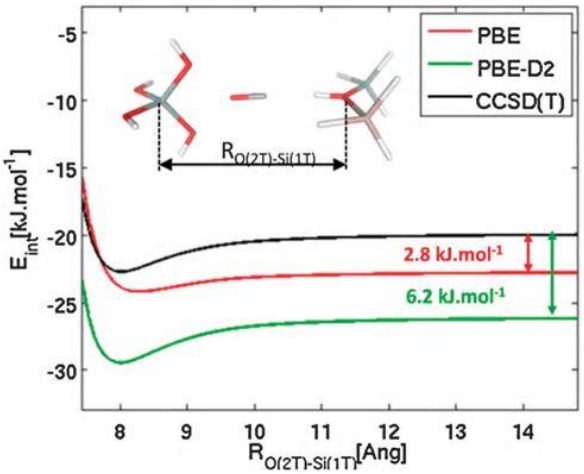

Fig. 2 Interaction energy of CO with the Brønsted-acid site (represented by the 2T cluster model) and the model of the zeolite framework (represented by the 1T cluster model) calculated at CCSD(T), PBE, and PBE-D2 levels, as a function of the $R_{O(2T)\text{-}Si(1T)}$ distance. Framework Si, Al, O, and H atoms are depicted in grey, pink, red, and white colours, respectively, CO atoms are depicted in red and grey (O and C atom, respectively).

3. Results

3.1. Calculations

Interaction energies of CO with Brønsted-acid sites in H-MCM-22 were calculated at PBE-optimized geometries using several exchange correlation functionals, including the GGA-type PBE, semi-empirically dispersion-corrected PBE-D2 and PBE-D3, and the non-local vdW-DF2 functional. Results reported in Table 1 indicate that dispersion interactions are relatively large, ranging from 4 to 15 kJ mol^{-1}. Note also that interaction energies obtained with different dispersion corrected methods for a particular adsorption complex do not agree in some cases (discrepancies as large as 6 kJ mol^{-1} were found).

Results reported in Table 1 are truly disappointing in the light of the experimentally determined CO adsorption enthalpy value of $\Delta H^0 = -22.5$ kJ mol^{-1} (see below). Even when the ZPE correction is accounted for (less than 4 kJ mol^{-1}) adsorption enthalpies calculated with dispersion-corrected methods are about 50% overestimated with respect to reliable experimental data. Even the results obtained at the PBE level (not accounting for dispersion interactions) appear to be overestimated with respect to experiment.

To understand the discrepancy between calculated and experimental results, accurate CCSD(T) calculations were carried out for the cluster model that mimics the simultaneous interaction of CO with a Brønsted-acid site and with the zeolite framework at the opposite side of the channel or cavity (Fig. 2). Results obtained at the PBE level for large $R_{O(2T)\text{-}Si(1T)}$ indicate that the local interaction of CO with just the Brønsted-acid site is overestimated by 2.8 kJ mol^{-1}, and this overestimation becomes significantly smaller (about 1 kJ mol^{-1}) for $R_{O(2T)\text{-}Si(1T)} \approx 8$ Å, which is a typical situation for zeolites. In contrast, results obtained at the PBE-D2 level clearly show that the interaction energy is largely

Table 1 Interaction energies calculated for CO adsorption complexes formed on the most stable Brønsted-acid sites in the vicinity of each of 8 distinguishable framework Al positions calculated at various levels of theory in kJ mol^{-1}

		Interaction energy			
Al position	Brønsted site	PBE	PBE-D2	PBE-D3	vdW-DF2
T1	O3	−28.0	−36.1	−34.9	−31.7
T2	O10	−28.1	−42.1	−43.8	−42.3
T3	O13	−26.8	−41.4	−42.2	−39.0
T4	O3	−28.6	−36.8	−35.5	−32.6
T5	O8	−20.7	−34.2	−38.9	−40.5
T6	O2	−23.2	−35.8	−35.3	−33.5
T7	O4	−3.5	−13.2	−14.3	−18.1
T8	O10	−28.6	−42.6	−44.4	−43.4

overestimated (6.2–6.7 kJ mol^{-1}) for the whole range of $R_{O(2T)-Si(1T)}$ distance investigated. These results show that the PBE functional gives a more accurate description of this system than dispersion-corrected functionals. Although the relatively good performance of PBE should result from fortuitous error cancellations, its use for describing the CO–H-MWW system seems to be justified. Results reported below were all obtained at the PBE level.

Relevant geometrical parameters describing the Brønsted-acid site (BA site) with and without adsorbed CO, O–H and C–O stretching frequencies, and CO adsorption enthalpy are reported in Table 2 for all eight distinguishable framework Al positions. Only the results obtained for the energetically most stable BA sites in the vicinity of each framework Al are reported in this table; the complete set of results obtained for all non-equivalent BA sites in H-MCM-22 is reported in the ESI† (Table S1). A representative set of BA sites with and without adsorbed CO is depicted in Fig. 3.

3.1.1. Structure and stability of Brønsted acid sites. The relative energies of BA sites in the vicinity of a particular Al position are rather small, from 1 to 8 kJ mol^{-1}, when Al is in T1, T2, T3, T4, and T5 sites (Table S1 in the ESI†). Therefore, several different BA sites corresponding to these Al positions can be populated at room temperature. However, large differences, in the range of 25–39 kJ mol^{-1}, were found for Al in T6, T7, and T8. Most of the energetically preferable BA sites show O–H stretching frequencies (ν_{OH}) in the range 3617–3633 cm^{-1}, corresponding to the Brønsted-acid OH group pointing towards the void space in a zeolite channel or cavity (see Fig. 3c and e). However, in two cases the Brønsted acid proton is involved in intra-zeolite hydrogen bonding (see Fig. 3a and g for the case of Al in T7 and T5, respectively) and that results in lower ν_{OH} values (3413 and 3414 cm^{-1}, respectively). For Al in the T5 position there are other BA sites only 2 to 5 kJ mol^{-1} higher in energy that are not involved in H-bonding and they should be considered for possible interaction with an adsorbate. In the case of Al in T7, the proton in the $T7_{Al}$–O4H–$T1_{Si}$ site is hidden inside a small cage, and thus not accessible to adsorbates (Fig. 3a), and the other BA site in the vicinity of Al in T7 is almost 40 kJ mol^{-1} higher in energy. It is therefore impossible for a weak base to induce a proton jump to the energetically less favourable BA site.

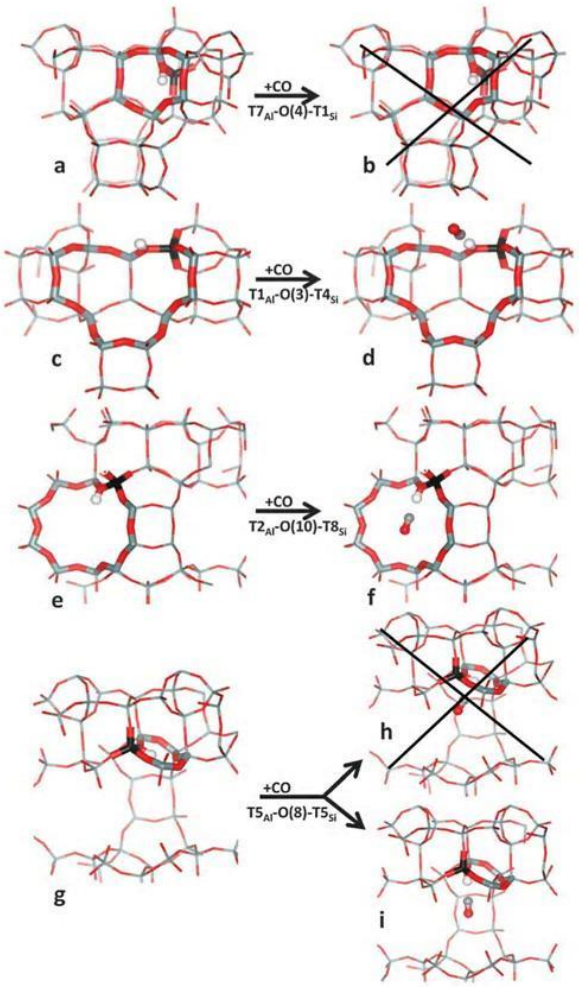

Fig. 3 Brønsted-acid sites without and with an adsorbed CO (left and right parts, respectively) shown for Al in T7 (a, b), T1 (c, d), T2 (e, f), and T5 (g–i). Framework Si, Al, and O atoms are depicted in grey, black, and red colour, respectively, while the H atom of the Brønsted-acid OH group, and C and O atoms of CO are depicted as white, grey, and red balls, respectively.

3.1.2. CO adsorption complexes in H-MCM-22. Adsorption of CO on Brønsted-acid sites was investigated for the most

Table 2 Characteristics of CO adsorption complexes formed on the most stable Brønsted-acid sites in the vicinity of each of 8 distinguishable framework Al positions; structural data, stretching frequencies, and energy (enthalpy) values are given in Å, cm^{-1}, and kJ mol^{-1}, respectively

			Geometrical data				Stretching frequencies			
Al position	Brønsted site	ΔE(Al,H)[a]	Al–O–Si[b]	r(OH)	r(OH) + CO[c]	ΔH^0 (0 K)	ν(OH)	ν(OH) + CO[c]	$\Delta\nu$(OH)	ν(CO)[c]
T1	O3	17	128.1	0.9755	1.0020	−24.4	3629	3280	349	2183
T2	O10	18	129.2	0.9756	0.9994	−24.5	3628	3314	314	2181
T3	O13	21	132.4	0.9765	1.0022	−23.2	3617	3278	339	2179
T4	O3	20	129.0	0.9759	1.0031	−25.0	3624	3266	358	2183
T5[d]	O8	12	138.4	0.9919	0.9994	−17.1	3414	3315	100	2178
T6	O2	13	127.7	0.9761	0.9968	−19.6	3621	3349	272	2177
T7[d]	O4	0	128.2	0.9919	0.9923	−3.5[e]	3413	3408	5	2139
T8	O10	24	131.6	0.9753	0.9985	−25.0	3633	3326	306	2180

[a] Relative energies for framework Si substitution with Al/H with respect to the substitution in the T7 position. [b] Al–O–Si angle (in deg) for the BA site. [c] For the CO adsorption complex on the BA site. [d] BA sites involved in intra-zeolite hydrogen bonding. [e] Not corrected for ZPE.

stable BA site in the vicinity of each framework Al atom. Carbon monoxide forms preferably linear O–H···C–O adsorption complexes (with a deviation from linearity typically not exceeding 3°). Computational investigation of CO adsorption complexes showed that three situations should be considered in H-MCM-22, depending on the localization of the BA site: (i) the BA site is accessible either from 10-MR channel or 12-MR cavity and the OH group points to the void space in the channel or cavity (see *e.g.* Fig. 3d and f). This is the most common case (found for Al in T1, T2, T3, T4, and T8); the corresponding CO adsorption complexes are characterized by the largest adsorption enthalpy (23–25 kJ mol^{-1}), the largest C–O stretching frequency (2179–2183 cm^{-1}) and the largest shift of O–H stretching frequency (306–358 cm^{-1}). Smaller values of adsorption enthalpy, ν_{CO}, and $\Delta\nu_{OH}$ were found for CO adsorbed on $T6_{Al}$–O2H–$T1_{Si}$ BA sites where, due to the framework structure, a linear adsorption complex cannot be formed; thus, the interaction of CO with the BA site is weaker. (ii) The BA site is involved in intra-zeolite H-bonding; the hydrogen atom has to move away from the intrazeolite H-bond in order to bind efficiently to CO, and that results in a lower adsorption enthalpy and smaller C–O stretching frequency. Such a situation was found for Al in the T5 position (Fig. 3g–i); note that $\Delta\nu_{OH}$ is not a meaningful characteristic in this case since ν_{OH} itself is shifted already prior to CO adsorption. (iii) The BA site is non-accessible to the CO molecule (Al in the T7 position) and the proton cannot be moved to another oxygen atom of AlO_4 tetrahedra, since such a process involves an energy penalty larger than the CO adsorption enthalpy itself; no CO adsorption complex on the BA site can be formed in such a case (Fig. 3a and b).

3.2. Variable-temperature IR spectroscopy and calorimetry

The blank IR spectrum, in the O–H stretching region, of H-MCM-22 (Si : Al = 24.5 : 1) is shown in Fig. 4A (inset). The IR absorption band seen at 3750 cm^{-1} arises from silanols, which are of no concern here, whereas that appearing at 3625 cm^{-1} is the characteristic O–H stretching band of the zeolite Brønsted acid sites. The main body of Fig. 4A depicts representative VTIR spectra in the difference mode (*i.e.*, after subtracting the blank zeolite spectrum) of adsorbed CO; they were obtained after dosing a fixed amount of carbon monoxide into the IR cell, small enough to avoid saturation (full monolayer coverage) at the lowest temperature. It is clearly seen how interaction of the zeolite with adsorbed CO results in an intensity decrease of the IR absorption band at 3625 cm^{-1} to an extent that is a function of temperature. Simultaneously, a much broader band corresponding to the hydrogen bonded OH···CO species gradually builds up, showing its maximum at about 3305 cm^{-1}. Therefore, the corresponding bathochromic shift, $\Delta\nu_{(OH)}$, upon hydrogen bonding amounts to −320 cm^{-1}; measured as the peak-to-peak distance in the difference spectra. From the whole set of VTIR spectra, which covered the temperature range 154–214 K, the corresponding van't Hoff plot of eqn (5) shown in Fig. 5 was obtained. Note that, in this case, the integrated intensity of the 3625 cm^{-1} band divided by its maximum gives directly the fraction $(1 - \theta)$ of free OH sites, from which the corresponding

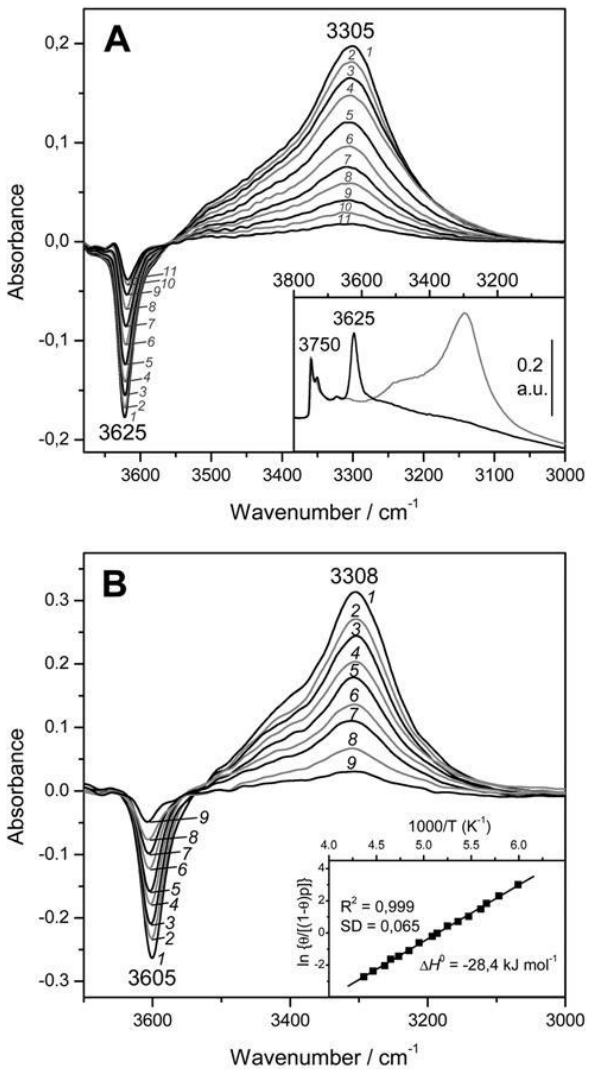

Fig. 4 (A) Representative variable-temperature IR spectra (O–H stretching region) of CO adsorbed on H-MCM-22 (Si : Al = 24.5 : 1). The spectra are shown in the difference mode (zeolite blank subtracted). Temperature (in K) and equilibrium pressure (mbar, in brackets) as follows: 1, 154 (6.52); 2, 160 (6.99); 3, 166 (7.37); 4, 172 (7.72); 5, 178 (8.01); 6, 184 (8.29); 7, 190 (8.55); 8, 196 (8.75); 9, 202 (8.93); 10, 208 (9.11); 11, 214 (9.24). The inset shows the blank zeolite spectrum (black) and the effect of dosing with CO at 77 K (grey). (B) Representative variable-temperature IR spectra (O–H stretching region) of CO adsorbed on H-FER (Si : Al = 27.5 : 1). The spectra are shown in the difference mode (zeolite blank subtracted). From 1 to 9, temperature goes from 167 to 224 K; and the equilibrium pressure from 0.57 to 1.75 mbar. The inset shows the corresponding van't Hoff plot (ref. 52).

value of θ needed for plotting eqn (5) was obtained. From that linear plot, the value of $\Delta H^0 = -22$ kJ mol^{-1} was derived for the standard enthalpy of H-bond formation (OH···CO complexes) in H-MCM-22 (Si : Al = 24.5 : 1). The corresponding value of ΔS^0 was found to be −130 J mol^{-1} K^{-1}. The estimated error limits are ±2 kJ mol^{-1} for enthalpy and ±10 J mol^{-1} K^{-1} for entropy. For comparison, Fig. 4B shows previously reported difference IR spectra of CO adsorbed on H-FER (Si : Al = 27.5 : 1),[54] as well

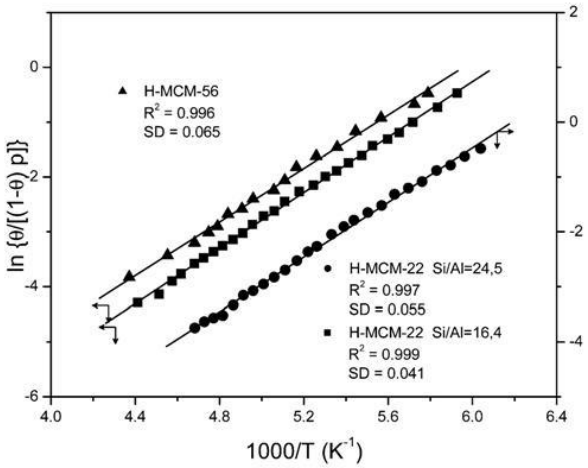

Fig. 5 Plot of the left-hand side of eqn (5) against the reciprocal of the temperature for CO adsorbed on H-MCM-22 (Si : Al = 24.5 : 1 and 16.4 : 1) and H-MCM-56; data obtained from the O–H stretching bands. *R*, linear regression coefficient; SD, standard deviation.

as the corresponding van't Hoff plot (inset). For this zeolite, $\Delta\nu_{(OH)} = -297$ cm^{-1}, a bathochromic shift which is smaller than that shown by H-MCM-22 ($\Delta\nu_{(OH)} = -320$ cm^{-1}), and yet the corresponding enthalpy value for H-FER resulted to be $\Delta H^0 = -28.4$ kJ mol^{-1}, which is significantly larger (in absolute value) than that of $\Delta H^0 = -22$ kJ mol^{-1} shown by H-MCM-22.

A comment on how band intensity was measured seems pertinent here. Several authors have pointed out that the clearly dissymmetric (and rather broad) O–H stretching band assigned to the Brønsted acid hydroxyl groups of H-MCM-22 (IR absorption band at 3625 cm^{-1} in Fig. 4A) can be resolved into two or more components.[69–72] And in fact, Garrone *et al.*[69] used computer procedures to simulate the band envelope by adding up three bands peaking at 3628, 3618 and 3585 cm^{-1}; the first two having nearly the same intensity, and a much weaker third one. However, our attempts at band resolution did not produce quantitatively reliable results (because of inherent uncertainty about how the band should be subdivided) regarding calculation of CO adsorption enthalpy. Therefore, for the corresponding van't Hoff plot we decided to use the integrated intensity of the hydroxyl band (at 3625 cm^{-1}) as it appears in the VTIR spectra of Fig. 4A. As a matter of fact, the rather regular shape of this band across the whole series of VTIR spectra, together with the fact that the derived van't Hoff plot (Fig. 5) fits to a straight line, strongly suggest that the molar absorption coefficients of the main OH species adding up to the overall band profile should not differ much from each other.

Fig. 6 depicts the C–O stretching region of the same VTIR spectra shown in Fig. 4A. The set of IR absorption bands seen at 2174 cm^{-1} corresponds to the C–O stretching mode of carbon monoxide involved in OH···CO complexes. The weaker and broader band at about 2138 cm^{-1}, which comes (mainly) from weakly physisorbed (liquid-like CO),[28,29] is of no concern here. The inset to Fig. 6 shows the van't Hoff plot obtained by applying eqn (6) to the whole set of spectra recorded (band at 2174 cm^{-1}).

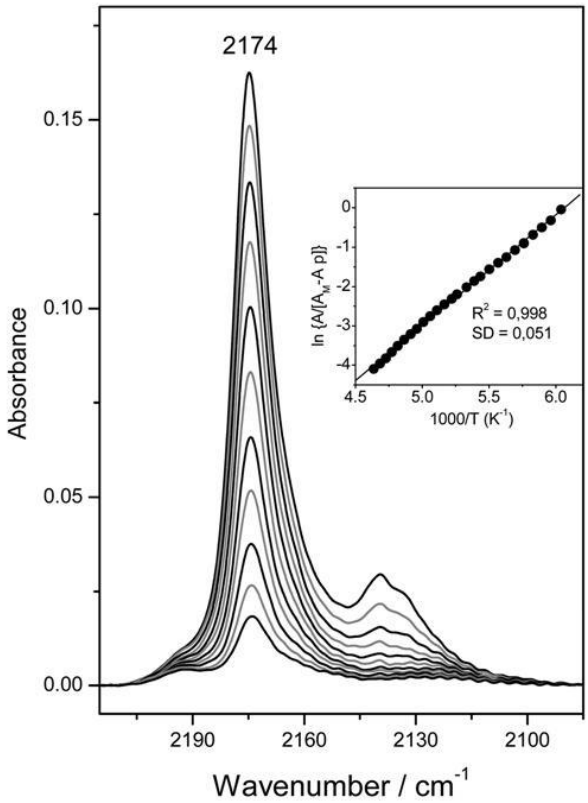

Fig. 6 Representative IR spectra (C–O stretching region) of CO adsorbed on H-MCM-22 (Si : Al = 24.5 : 1). From top to bottom, temperature goes from 154 to 214 K; and equilibrium pressure from 6.52 to 9.24 mbar. The inset shows the corresponding plot of the left-hand side of eqn (6) against the reciprocal of the temperature. *R*, linear regression coefficient; SD, standard deviation.

From this linear plot, the values of $\Delta H^0 = -23(\pm 2)$ kJ mol^{-1} and $\Delta S^0 = -140(\pm 10)$ J mol^{-1} K^{-1} were obtained. As expected, these values practically coincide (within experimental error) with those derived from the O–H stretching band of the same OH···CO hydrogen-bonded species; and such a close agreement between both sets of results provides further reliability on the methods used. The average of both sets of results gives the final values of $\Delta H^0 = -22.5(\pm 2)$ kJ mol^{-1} and $\Delta S^0 = -135(\pm 10)$ J mol^{-1} K^{-1} for the standard enthalpy and entropy of formation of the hydrogen-bonded CO complexes under study.

As stated in the Introduction, adsorption calorimetry was also used to measure the enthalpy change in hydrogen-bonding of CO with the Brønsted-acid hydroxyl groups of both, H-MCM-22 (Si : Al = 24.5 : 1) and H-FER (Si : Al = 27.5 : 1). CO adsorption isotherms, at 303 K, are shown in Fig. 7A and B, respectively, while Fig. 7C shows the corresponding differential heat of adsorption (in the low coverage range). Note that, in order to test reproducibility, two independent sets of measurements were performed for carbon monoxide adsorption on H-MCM-22. The average of the results thus obtained gives the adsorption heat value of 21(±2) kJ mol^{-1}, which agrees (within experimental error) with the value of $\Delta H^0 = -22.5(\pm 2)$ kJ mol^{-1} obtained

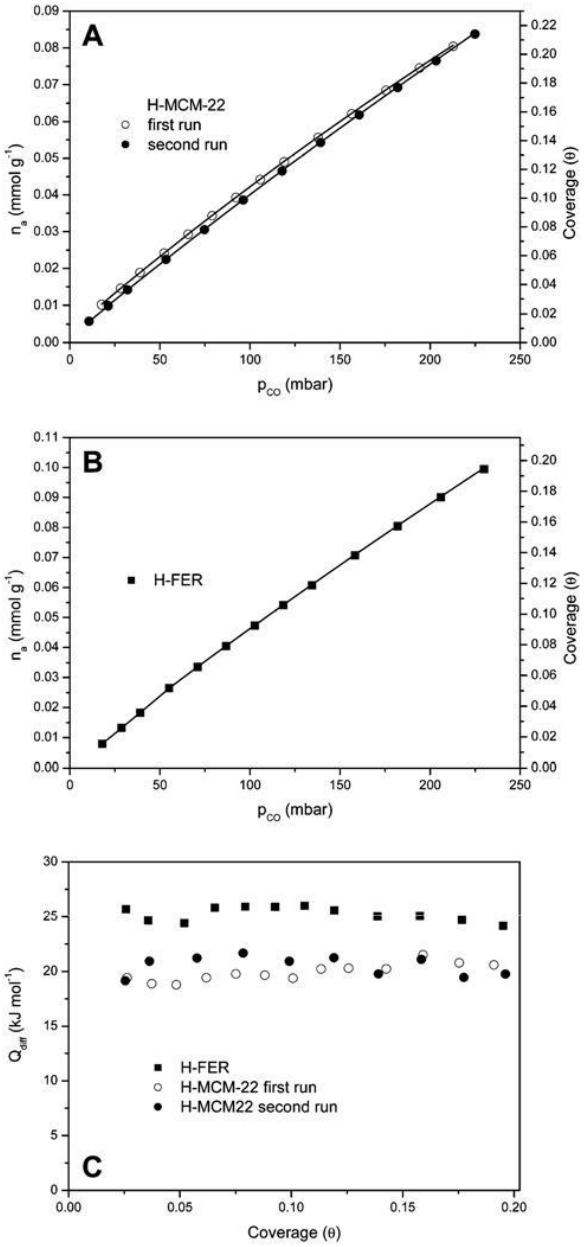

Fig. 7 (A) Adsorption isotherm of CO on H-MCM-22 (Si : Al = 24.5 : 1) at 303 K; (B) adsorption isotherm of CO on H-FER zeolite (Si : Al = 27.5 : 1) at 303 K; (C) adsorption heat of CO on H-FER (squares) and H-MCM-22 (circles) measured by calorimetry at 303 K, as a function of coverage.

by VTIR spectroscopy. Regarding H-FER, Fig. 7C shows an adsorption heat of about 26(±2) kJ mol^{-1}, to be compared with the corresponding value of $\Delta H^0 = -28.4(\pm 2)$ kJ mol^{-1} previously determined by VTIR spectroscopy.[54] It is also noteworthy that (up to the coverage of about 0.2) the CO adsorption heat is (very approximately) independent of coverage for both zeolites.

Fig. 8 (bottom inset) depicts the IR spectrum in the O–H stretching region of the zeolite H-MCM-22 (Si : Al = 16.4 : 1).

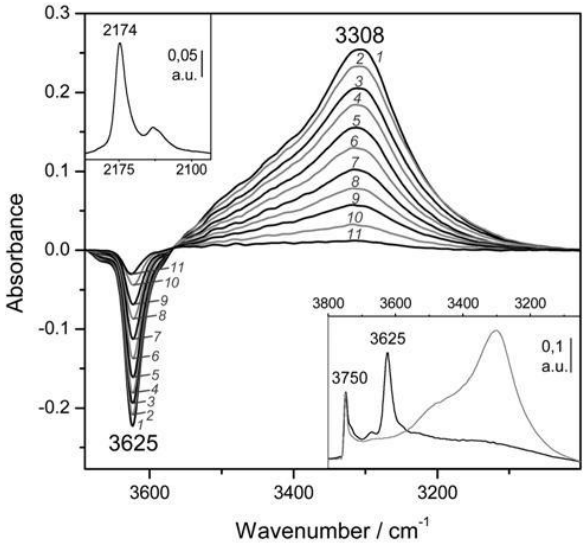

Fig. 8 Representative variable-temperature IR spectra (O–H stretching region) of CO adsorbed on H-MCM-22 (Si : Al = 16.4 : 1). The spectra are shown in the difference mode (zeolite blank subtracted). Temperature (in K) and equilibrium pressure (mbar, in brackets) as follows: 1, 165 (15.13); 2, 171 (15.72); 3, 177 (16.13); 4, 181 (16.41); 5, 187 (16.78); 6, 193 (17.13); 7, 200 (17.47); 8, 206 (17.74); 9, 212 (18.01); 10, 222 (18.35); 11, 235 (18.69). The bottom inset shows the blank zeolite spectrum (black) and the effect of dosing with CO at 77 K (grey). The top inset shows the C–O stretching region of spectrum 1.

The IR absorption bands corresponding to silanols (3750 cm^{-1}) and to Brønsted-acid hydroxyl groups (3625 cm^{-1}) appear at the same wavenumbers as those of the previous H-MCM-22 (Si : Al = 24.5 : 1) sample. Representative VTIR spectra of adsorbed CO are shown (in the difference mode) in the main body of Fig. 8, whereas the top inset depicts the characteristic C–O stretching mode of the OH···CO hydrogen-bonded adsorption complex. From the whole set of the obtained VTIR spectra, the van't Hoff plot shown in Fig. 5 was derived. This linear plot gave the values $\Delta H^0 = -21(\pm 2)$ kJ mol^{-1} and $\Delta S^0 = -128(\pm 10)$ J mol^{-1} K^{-1} for the standard adsorption enthalpy and entropy (respectively) of formation of the hydrogen-bonded OH···CO species. Note that the ΔH^0 value is slightly smaller than that of −22.5 kJ mol^{-1} obtained for H-MCM-22 (Si : Al = 24.5 : 1), which could be correlated with the slightly smaller value of $\Delta\nu_{(OH)}$: −317 cm^{-1} for H-MCM-22 (Si : Al = 16.4 : 1) and −320 cm^{-1} for H-MCM-22 (Si : Al = 24.5 : 1). Although it is true that such a small difference in wavenumber can hardly be assessed experimentally, particularly when dealing with IR absorption bands as broad as those shown by the hydrogen-bonded adsorption complexes.

The IR spectra corresponding to the zeolite H-MCM-56 (Si : Al = 16 : 1) are depicted in Fig. 9. The blank spectrum of the zeolite wafer shows the characteristic silanol and Brønsted-acid hydroxyl group bands at 3749 and 3624 cm^{-1}, respectively (very close to the corresponding values of H-MCM-22). The bathochromic shift of the latter band upon CO adsorption is $\Delta\nu_{(OH)} = -316$ cm^{-1}, as seen in the main body of Fig. 9.

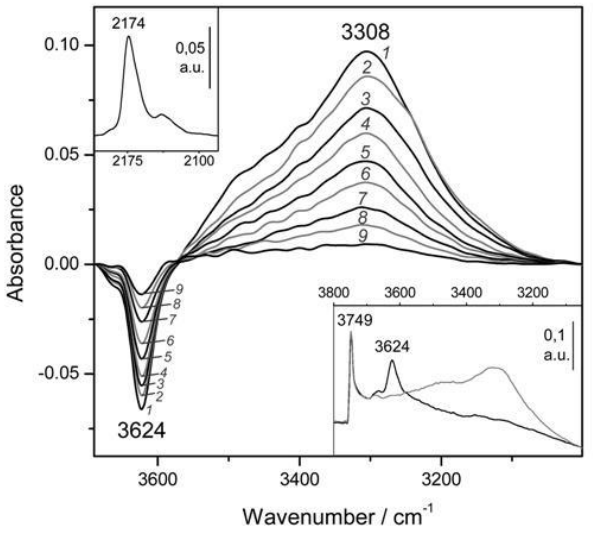

Fig. 9 Representative variable-temperature IR spectra (O–H stretching region) of CO adsorbed on H-MCM-56. The spectra are shown in the difference mode (zeolite blank subtracted). Temperature (in K) and equilibrium pressure (mbar, in brackets) as follows: 1, 165 (10.33); 2, 175 (10.81); 3, 180 (11.01); 4, 184 (11.15); 5, 190 (11.37); 6, 196 (11.54); 7, 204 (11.74); 8, 211 (11.89); 9, 220 (12.07). The bottom inset shows the blank zeolite spectrum (black) and the effect of dosing with CO at 77 K (grey). The top inset shows the C–O stretching region of spectrum 1.

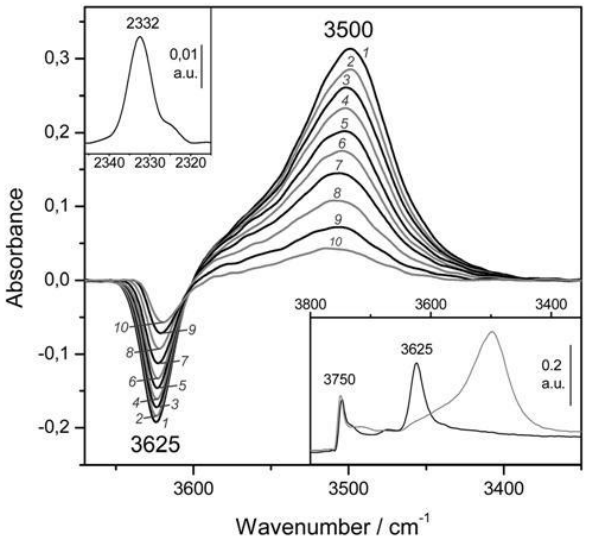

Fig. 10 Representative variable-temperature IR spectra (O–H stretching region) of N_2 adsorbed on H-MCM-22 (Si : Al = 16.4 : 1). The spectra are shown in the difference mode (zeolite blank subtracted). Temperature (in K) and equilibrium pressure (mbar, in brackets) as follows: 1, 117 (4.43); 2, 125 (5.48); 3, 131 (6.27); 4, 137 (6.98); 5, 143 (7.68); 6, 149 (8.22); 7, 155 (8.73); 8, 163 (9.27); 9, 171 (9.70); 10, 179 (10.03). The bottom inset shows the blank zeolite spectrum (black) and the effect of dosing with N_2 at 77 K (grey). The top inset shows the N–N stretching region of spectrum 1.

From the whole series of VTIR spectra of adsorbed CO (some of which are shown in Fig. 9), the corresponding van't Hoff plot (shown in Fig. 5) was obtained, which gave the values of $\Delta H^0 = -20(\pm 2)$ kJ mol^{-1} and $\Delta S^0 = -120(\pm 10)$ J mol^{-1} K^{-1} for the formation of hydrogen-bonded OH···CO species in H-MCM-56.

VTIR spectra of adsorbed dinitrogen, which can also be used for testing Brønsted acidity of protonic zeolites, will now be considered. As examples, we show series of such spectra in Fig. 10 (for H-MCM-22 having a Si : Al ratio of 16.4 : 1) and in Fig. 12 (H-MCM-56, Si : Al = 16 : 1). Corresponding VTIR spectra of dinitrogen adsorbed on H-MCM-22 (Si : Al = 24.5 : 1) and H-FER (Si : Al = 27.5 : 1) were recently reported by Delgado *et al.*,[44] and by Nachtigall *et al.*,[54] respectively.

The bottom inset in Fig. 10 shows the effect of dosing with nitrogen, at 77 K, the H-MCM-22 zeolite wafer. Formation of OH···NN hydrogen bonded species results in a bathochromic shift of the IR absorption band of Brønsted-acid hydroxyl groups from 3625 down to 3500 cm^{-1}, that is, $\Delta\nu_{(OH)} = -125$ cm^{-1}. It should be noted, however, that the exact magnitude of $\Delta\nu_{(OH)}$ depends slightly on the temperature at which the IR spectrum is recorded (as can be seen in the main body of Fig. 10). Formation of the OH···NN adducts results in activation in the IR of the N–N stretching mode, which appears at 2332 cm^{-1} (top inset in Fig. 10). From the whole series of VTIR spectra that were run, some of which are shown in the main body of Fig. 10, the plot of the left-hand side of eqn (5) against the reciprocal of the temperature depicted in Fig. 11 was obtained. From this linear plot the value of $\Delta H^0 = -13.5(\pm 2)$ kJ mol^{-1} was derived for the standard enthalpy of formation of the hydrogen-bonded

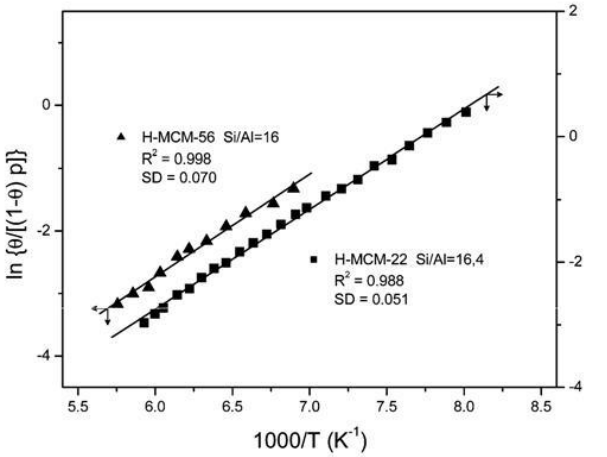

Fig. 11 Plot of the left-hand side of eqn (5) against the reciprocal of the temperature for N_2 adsorbed on H-MCM-22 (Si : Al = 16.4 : 1) and H-MCM-56; data obtained from the corresponding O–H stretching bands. *R*, linear regression coefficient; SD, standard deviation.

OH···NN species. The corresponding entropy change resulted to be $\Delta S^0 = -103(\pm 10)$ J mol^{-1} K^{-1}.

Finally, representative VTIR spectra of dinitrogen adsorbed on H-MCM-56 are shown in Fig. 12. The IR absorption band at 3624 cm^{-1} (Brønsted-acid OH groups) is shifted down to 3500 cm^{-1} upon formation of the hydrogen-bonded species, which results in $\Delta\nu_{(OH)} = -124$ cm^{-1} (bottom inset). From the integral values of absorbance, taken from the band at 3624 cm^{-1} in the

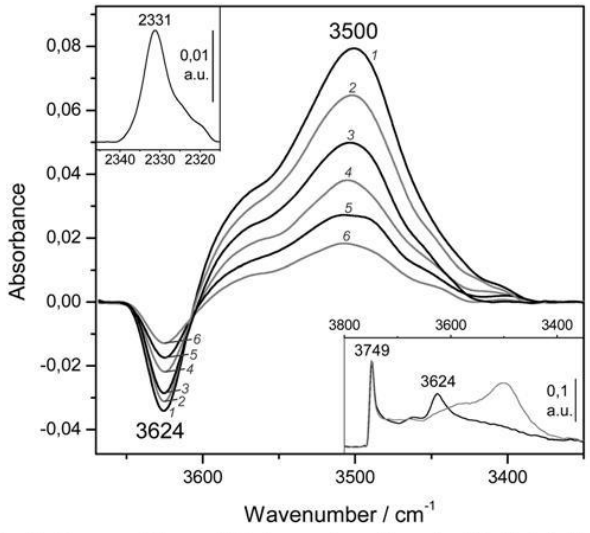

Fig. 12 Representative variable-temperature IR spectra (O–H stretching region) of N_2 adsorbed on H-MCM-56. The spectra are shown in the difference mode (zeolite blank subtracted). From 1 to 6, temperature goes from 145 to 174 K; and equilibrium pressure from 9.55 to 10.95 mbar. The bottom inset shows the blank zeolite spectrum (black) and the effect of dosing with N_2 at 77 K (grey). The top inset shows the N–N stretching region of spectrum 1.

whole series of VTIR spectra, the van't Hoff plot depicted in Fig. 11 was obtained. The corresponding values of ΔH^0 and ΔS^0 (for the formation of the hydrogen-bonded species) resulted to be $-13(\pm 2)$ kJ mol^{-1} and $-104(\pm 10)$ J mol^{-1} K^{-1}, respectively.

4. Discussion

Regarding computational results for the CO–H-MCM-22 system, O–H stretching frequencies calculated with the ω/r correlation method are in very good agreement with experimental IR spectra for both, the bare Brønsted-acid sites and those involved in adsorption complexes with CO. Calculated C–O stretching frequencies (using the ω/r correlation method) are about 5 cm^{-1} overestimated with respect to experimentally observed band maxima. This small overestimation of ν_{CO} is likely connected with overestimated CO interaction energy with Brønsted-acid sites. Adsorption enthalpies calculated at the PBE level are only slightly overestimated with respect to experimental data. However, this seemingly good performance of the PBE functional should not be overrated, it only results from fortuitous cancellation of errors. Interaction energies reported herein should be taken rather qualitatively than quantitatively. Calculations show three effects on the interaction energy between CO and Brønsted-acid OH groups: (i) stronger interaction is found for adsorption complexes where the CO molecule is situated along the O–H bond direction; any deviation from this direction results in a weaker interaction and also a smaller ν_{CO} value. (ii) Stronger interaction is found for Brønsted-acid sites not involved in the intra-zeolite H-bonding prior to the CO adsorption; when the Brønsted-acid OH group is involved in such an H-bond the CO adsorption enthalpy should be lower, since the hydrogen atom must move to a position from where it can efficiently interact with the adsorbate. (iii) Accessibility of the Brønsted-acid site also plays a role; in the case of Al in the T7 position, no adsorption complex with CO can be formed.

For quantitative analysis of the CO adsorption enthalpy a more reliable level of theory would be required. It should be noted that the dispersion corrected functionals tested herein all failed to describe reliably the interaction of CO with Brønsted-acid sites in H-MCM-22. Careful analysis of DFT results obtained for cluster models showed that the problem of dispersion-corrected exchange–correlation functionals stems not so much from the description of dispersion interactions themselves as from just the local (or semi-local) part of the exchange–correlation functional. Results reported in Fig. 2 show that the PBE functional already overestimates the interaction of CO with the Brønsted acid site, mostly due to a too large electrostatic stabilization. It is then not surprising that dispersion-corrected functionals give even a larger discrepancy with respect to the CCSD(T)/CBS level, since the dispersion contribution further stabilizes the adsorption complex. Hence, the problem of the PBE functional cannot be fixed by adding the dispersion interaction (DFT-D2 or DFT-D3). In contrast, the DFT/CC method, which is based on the correction of DFT errors of any kind (and not just dispersion) was used successfully for the description of similar systems, *e.g.*, CO_2 adsorption in zeolites and MOFs;[73–75] and it could possibly be used even for the system dealt with herein. The development of DFT/CC correction functions for the interaction of CO with Brønsted-acid sites in zeolites, which is currently under progress, will be hopefully reported in a future article, together with an in-depth analysis of DFT failure to describe such an interaction.

The substitution energy, ΔE(Al,H), calculated with the periodic model (Table 2) can be compared with corresponding values obtained by Li *et al.*[66] using cluster models. The only agreement between the two models is that the most stable position for framework Al is the T7 site. The relative energies for different positions of framework Al obtained with the periodic model are qualitatively different from those obtained with cluster models. In addition, the relative stability of Brønsted-acid sites in the vicinity of a particular framework Al site is also qualitatively different when using periodic and cluster models. That led us to conclude that the use of cluster models for the description of Brønsted-acid sites in zeolites is questionable.

To facilitate discussion of the experimental results, Table 3 summarizes the relevant numerical data reported herein for MWW type zeolites, as well as corresponding data previously reported for other protonic zeolites.[34,49,54] In all cases, ΔH^0 values were determined by VTIR spectroscopy. $\Delta\nu_{(OH)}$ values were all measured as peak-to-peak distance in the corresponding difference IR spectra for CO (or N_2) doses approaching a coverage of $\theta = 1$. Much larger doses of the adsorbate should be avoided, particularly for carbon monoxide, because at a low temperature that would result in massive formation of a condensed phase and corresponding perturbation of hydroxyl groups and gas adsorption complexes, which can lead to inconsistent $\Delta\nu_{(OH)}$

Table 3 Relevant experimental data for CO and N_2 hydrogen bonding in protonic zeolites

Zeolite	Structure type	Si/Al ratio	ν_{OH} (cm^{-1})	$-\Delta\nu_{(OH)}(CO)^a$ (cm^{-1})	$-\Delta H^0(CO)^b$ (kJ mol^{-1})	$-\Delta\nu_{(OH)}(N_2)^c$ (cm^{-1})	$-\Delta H^0(N_2)^d$ (kJ mol^{-1})	Ref.
H-Y	FAU	5.6	3645	275	25.6	98	15.7	34 and 49
H-ZSM-5	MFI	30	3618	303	29.4	116	19.7	34
H-FER	FER	27.5	3605	297	28.4	110	19.1	54
H-MCM-22	MWW	24.5	3625	320	22.5	125	14.5	This work
H-MCM-22	MWW	16.4	3625	317	21	125	13.5	This work
H-MCM-56	MWW	16	3624	316	20	124	13	This work

[a] Red-shift of the Brønsted-acid OH group upon hydrogen bonding with CO. [b] Standard enthalpy change in the formation of the OH···CO complex. [c] Red-shift of the Brønsted-acid OH group upon hydrogen bonding with N_2. [d] Standard enthalpy change in the formation of the OH···N_2 complex.

values. Besides data reported in Table 3, $\Delta\nu_{(OH)}$ values for some of the same zeolites (but not corresponding ΔH^0 values) were also reported by several authors. Among them, Dwyer *et al.*[36] give the values of $\Delta\nu_{(OH)}(CO) = -308$ cm^{-1} for CO adsorbed (at $\theta \rightarrow 1$) in H-ZSM-5, and $\Delta\nu_{(OH)}(CO) = -273$ cm^{-1} for H-Y; Knözinger *et al.*[27] give, for H-ZSM-5, $\Delta\nu_{(OH)}(CO) = -317$ cm^{-1} and $\Delta\nu_{(OH)}(N_2) = -121$ cm^{-1}; Hadjiivanov *et al.*[76] give, for H-FER, $\Delta\nu_{(OH)}(CO) = -292$ cm^{-1} and $\Delta\nu_{(OH)}(N_2) = -106$ cm^{-1}; and Gil *et al.*[77] give $\Delta\nu_{(OH)}(CO) = -326$ cm^{-1} for carbon monoxide adsorbed (at 173 K) on H-MCM-22. Although some small differences are observed, these values are consistent with those reported in Table 3.

Table 3 shows that the protonic zeolites H-Y, H-ZSM-5 and H-FER display the expected correlation between $\Delta\nu_{(OH)}$ and ΔH^0 for both CO and N_2; that is, increasing (absolute) values of $\Delta\nu_{(OH)}$ correspond to increasing (absolute) values of ΔH^0. However, MWW type zeolites clearly break that trend; they all show a distinctively smaller value of ΔH^0 than (for instance) H-FER and H-ZSM-5, and yet a larger value of $\Delta\nu_{(OH)}$. Regarding H-MCM-22 (Si : Al = 24.5 : 1), the smaller ΔH^0 value, as compared to H-FER, for the formation of hydrogen-bonded OH···CO complexes with the zeolite Brønsted-acid sites was also confirmed by the calorimetric results reported in Section 3.2. Moreover, Li *et al.*[78] and Tsai *et al.*[79] found, by means of temperature programmed desorption of adsorbed ammonia, that (for nearly the same Si : Al ratio) H-MCM-22 has a weaker Brønsted acidity than H-ZSM-5. This is in agreement with the correspondingly smaller values of $\Delta H^0(CO)$ and $\Delta H^0(N_2)$ shown by H-MCM-22 (Table 3), but not so with its distinctively larger values of $\Delta\nu_{(OH)}(CO)$ and $\Delta\nu_{(OH)}(N_2)$ when compared to H-ZSM-5. It should be clear, therefore, that the rather common practice of ranking Brønsted-acid strength of protonic zeolites according to the corresponding O–H frequency shift probed by an adsorbed weak base can be misleading, particularly when dealing with zeolites not having the same structure type. Nevertheless, within the same structural group $\Delta\nu_{(OH)}$ seems to correlate with ΔH^0, as shown by H-MCM-22 and H-MCM-56; both of them belonging to the same (MWW) structural group. Note also that within this group of zeolites the Brønsted acid strength, as tested by the corresponding $\Delta H^0(CO)$ or $\Delta H^0(N_2)$ value, slightly decreases with decreasing Si : Al ratio along the series H-MCM-22 (Si : Al = 24.5 : 1), H-MCM-22 (Si : Al = 16.4 : 1), H-MCM-56 (Si : Al = 16 : 1), as could in principle be expected.

5. Conclusions

The standard enthalpy change, ΔH^0, involved in hydrogen-bonding of Brønsted-acid OH groups of H-MCM-22 and H-MCM-56 zeolites with the probe molecules CO and N_2 was determined by variable-temperature IR spectroscopy, and further checked by adsorption calorimetry. For H-MCM-22 (Si : Al = 24.5 : 1) the obtained values of ΔH^0 resulted to be $-22.5(\pm2)$ and $-14.5(\pm2)$ kJ mol^{-1} for the formation of hydrogen-bonded OH···CO and OH···NN complexes, respectively; corresponding values for H-MCM-56 were $-20(\pm2)$ kJ mol^{-1} [$\Delta H^0(CO)$] and $-13(\pm2)$ kJ mol^{-1} [$\Delta H^0(N_2)$]. Taking the ΔH^0 value as a reliable measure of (relative) Brønsted-acid strength, comparison with the corresponding values for the protonic zeolites H-FER ($\Delta H^0(CO) = -28.4(\pm2)$ kJ mol^{-1}, $\Delta H^0(N_2) = -19.1(\pm2)$ kJ mol^{-1}) and H-ZSM-5 ($-29.4(\pm2)$ and $-19.7(\pm2)$ kJ mol^{-1} for CO and N_2, respectively) clearly shows that the MWW structure type zeolites have a distinctively weaker acidity than H-ZSM-5 and H-FER. Nevertheless, the respective value of $\Delta\nu_{(OH)}$, after hydrogen-bonding with the probe molecule, was found to be significantly larger for H-MCM-22 ($\Delta\nu_{(OH)}(CO) = -320$ cm^{-1}, $\Delta\nu_{(OH)}(N_2) = -125$ cm^{-1}) than for H-FER ($\Delta\nu_{(OH)}(CO) = -297$ cm^{-1}, $\Delta\nu_{(OH)}(N_2) = -110$ cm^{-1}) and H-ZSM-5 ($\Delta\nu_{(OH)}(CO) = -303$ cm^{-1}, $\Delta\nu_{(OH)}(N_2) = -116$ cm^{-1}), and the same applies to H-MCM-56. These results clearly show that the usual practice of ranking acid strength of protonic zeolites by the corresponding O–H frequency shift probed by a weak base adsorbed at a low temperature can be misleading. Determination of the enthalpy change involved in hydrogen bonding was shown to be a more reliable instrumental method. For that, VTIR spectroscopy is a very convenient technique to be used, since it gives simultaneously ΔH^0 and $\Delta\nu_{(OH)}$ values. Alternatively, adsorption calorimetry (at a low temperature) could equally well be used to determine the relevant ΔH^0 value.

Attempts to calculate the interaction energy between H-MCM-22 and adsorbed CO by DFT calculations did not lead to quantitatively accurate results. Accurate calculations at the coupled cluster level of theory performed for cluster models show that dispersion-corrected DFT methods overestimate the interaction energy by about 50%. In contrast, the standard GGA functional (PBE) gives interaction energies in significantly better agreement with the coupled cluster method (for the cluster model) and with experiment (periodic model). The relatively good performance of the PBE functional is however due to fortuitous

error cancellation. O–H and C–O stretching vibrations can be accurately described with the DFT method, only due to the fact that the ω/r correlation scheme used here corrects the DFT results to the coupled cluster accuracy. A highly accurate description of CO adsorption on Brønsted-acid sites remains a challenge for computational chemistry.

Acknowledgements

Financial support from the Czech Science Foundation under the project P106/12/G015 is highly acknowledged. Calculations were partially performed at MetaCentrum and CERIT-SC computational facilities (MSM/LM2010005 and OP VaVpI CZ. 1.05/3.2.00/08.0144).

References

1 S. M. Csicsery, *Pure Appl. Chem.*, 1986, **58**, 841.
2 W. Hölderich, M. Hesse and F. Näumann, *Angew. Chem., Int. Ed.*, 1988, **27**, 226.
3 D. Gubisch and F. Bandermann, *Chem. Eng. Technol.*, 1989, **12**, 155.
4 A. Corma, *Chem. Rev.*, 1995, **95**, 559.
5 K. Tanabe and W. Hölderich, *Appl. Catal., A*, 1999, **181**, 399.
6 M. G. Clerici, *Top. Catal.*, 2000, **13**, 373.
7 A. Raiche, Y. Traa, F. Funder, M. Rupp and J. Weitkamp, *Angew. Chem., Int. Ed.*, 2001, **40**, 1243.
8 B. Xu, C. Sievers, S. B. Hong, R. Prins and J. A. van Bokhoven, *J. Catal.*, 2006, **244**, 163.
9 D. P. Serrano, R. A. Garcia, G. Vicente, M. Linares, D. Prochazkova and J. Cejka, *J. Catal.*, 2011, **279**, 366.
10 J. Li, Y. Wei, G. Liu, Y. Qi, P. Tian, B. Li, Y. He and Z. Liu, *Catal. Today*, 2001, **171**, 221.
11 J. Cejka, G. Centi, J. Perez-Pariente and W. J. Roth, *Catal. Today*, 2012, **179**, 2.
12 M. Niwa, K. Suzuki, N. Morishita, G. Sastre, K. Okumura and N. Katada, *Catal. Sci. Technol.*, 2013, **3**, 1919.
13 D. Atkinson and G. Curthoys, *Chem. Soc. Rev.*, 1979, **8**, 475.
14 H. A. Benesi, *J. Phys. Chem.*, 1957, **61**, 970.
15 X. Rozanska and R. A. van Santen, in *Handbook of Zeolite Science and Technology*, ed. S. M. Auerback, K. A. Karrado and P. K. Dutta, Marcel Dekker, Inc., New York, 2003, ch. 15.
16 D. Farcasiu, *Catal. Lett.*, 2001, **71**, 95.
17 W. E. Farneth and R. J. Gorte, *Chem. Rev.*, 1995, **95**, 615.
18 H. G. Karge, *Stud. Surf. Sci. Catal.*, 1991, **65**, 133.
19 N. Cardona-Martinez and J. A. Dumesic, *Adv. Catal.*, 1992, **38**, 149.
20 D. J. Parrillo and R. G. Gorte, *J. Phys. Chem.*, 1993, **97**, 8786.
21 A. Auroux and J. Vedrine, *Stud. Surf. Sci. Catal.*, 1985, **20**, 311.
22 C. Busco, A. Barbaglia, M. Broyer, V. Bolis, G. M. Foddanu and P. Ugliengo, *Thermochim. Acta*, 2004, **418**, 3.
23 R. Ramos Pinto, P. Borges, M. A. N. D. A. Lemos, F. Lemos, J. C. Vedrine, E. G. Derouane and F. Ramoa Ribeiro, *Appl. Catal., A*, 2005, **284**, 39.
24 M. Hunger, D. Freude, D. Fenzke and H. Pfeifer, *Chem. Phys. Lett.*, 1992, **191**, 391.
25 J. Klinowski, *Chem. Rev.*, 1991, **91**, 1459.
26 A. L. Blumenfeld and J. J. Fripiat, *J. Phys. Chem. B*, 1997, **101**, 6670.
27 S. Kotrel, J. H. L. Lunsford and H. Knözinger, *J. Phys. Chem. B*, 2001, **105**, 3917.
28 A. Zecchina, G. Spoto and S. Bordiga, *Phys. Chem. Chem. Phys.*, 2005, **7**, 1627.
29 A. Zecchina and C. Otero Arean, *Chem. Soc. Rev.*, 1996, **25**, 187.
30 K. Hadjiivanov and G. Vayssilov, *Adv. Catal.*, 2002, **47**, 307.
31 N. S. Nesterenko, F. Thibault-Starzyk, V. Montouillout, V. V. Yushchenko, C. Fernandez, J. P. Gilson, F. Fajula and I. I. Ivanova, *Kinet. Catal.*, 2006, **47**, 40.
32 J. A. Boscoboinik, X. Yu, E. Emmez, B. Yang, S. Shaikhutdinov, F. D. Fischer, J. Sauer and H. J. Freund, *J. Phys. Chem. C*, 2013, **117**, 13547.
33 F. Geobaldo, C. Lamberti, G. Ricchiardi, S. Bordiga, A. Zecchina, G. T. Palomino and C. O. Arean, *J. Phys. Chem.*, 1995, **99**, 11167.
34 C. O. Arean, *J. Mol. Struct.*, 2008, **880**, 31.
35 E. A. Paukshtis and E. N. Yurchenko, *Russ. Chem. Rev.*, 1983, **52**, 242.
36 M. A. Makarova, K. M. Al-Ghefaili and J. Dwyer, *J. Chem. Soc., Faraday Trans.*, 1994, **90**, 383.
37 M. V. Frash, M. A. Makarova and A. M. Rigby, *J. Phys. Chem. B*, 1997, **101**, 2116.
38 A. G. Pelmenshchikov, E. A. Paukshtis, V. G. Stepanov, V. I. Pavlov, E. N. Yurchenko, K. G. Ione, G. M. Zhidomirov and S. Beran, *J. Phys. Chem.*, 1989, **93**, 6725.
39 K. P. Schröder, J. Sauer, M. Leslie, C. R. A. Catlow and J. M. Thomas, *Chem. Phys. Lett.*, 1992, **188**, 320.
40 L. A. M. M. Barbosa, R. A. van Santen and H. Hafner, *J. Am. Chem. Soc.*, 2001, **123**, 4530.
41 L. Yang, K. Trafford, O. Kresnawahjuesa, J. Sepa and R. J. Gorte, *J. Phys. Chem. B*, 2001, **105**, 1935.
42 K. Chakarova and K. Hadjiivanov, *Chem. Commun.*, 2011, **47**, 1878.
43 K. Chakarova and K. Hadjiivanov, *J. Phys. Chem. C*, 2011, **115**, 4806.
44 M. R. Delgado, R. Bulánek, P. Chlubná and C. O. Arean, *Catal. Today*, 2013, DOI: 10.1016/j.cattod.2013.09.013.
45 W. J. Roth, *Stud. Surf. Sci. Catal.*, 2005, **158**, 19.
46 W. J. Roth, P. Chlubna, M. Kubu and D. Vitvarova, *Catal. Today*, 2013, **204**, 8.
47 R. Bulanek, M. Kolarova, P. Chlubna and J. Cejka, *Adsorption*, 2013, **19**, 455.
48 A. A. Tsyganenko, P. Yu. Storozhev and C. Otero Arean, *Kinet. Catal.*, 2004, **45**, 530.
49 C. O. Arean, O. V. Manoilova, A. A. Tsyganenko, G. T. Palomino, M. P. Mentruit, F. Geobaldo and E. Garrone, *Eur. J. Inorg. Chem.*, 2001, 1739.
50 C. Otero Arean, O. V. Manoilova, G. Turnes Palomino, M. Rodriguez Delgado, A. A. Tsyganenko, B. Bonelli and E. Garrone, *Phys. Chem. Chem. Phys.*, 2002, **4**, 5713.

51 E. Garrone and C. Otero Arean, *Chem. Soc. Rev.*, 2005, **34**, 846.
52 P. Nachtigall, M. R. Delgado, D. Nachtigallova and C. O. Arean, *Phys. Chem. Chem. Phys.*, 2012, **14**, 1552.
53 C. O. Arean, M. R. Delgado, C. Lopez Bauca, L. Vrbka and P. Nachtigall, *Phys. Chem. Chem. Phys.*, 2007, **9**, 4657.
54 P. Nachtigall, O. Bludsky, L. Grajciar, D. Nachtigallova, M. R. Delgado and C. O. Arean, *Phys. Chem. Chem. Phys.*, 2009, **11**, 791.
55 http://www.iza-structure.org/databases/.
56 G. Kresse and J. Hafner, *Phys. Rev. B: Condens. Matter Mater. Phys.*, 1994, **49**, 14251.
57 G. Kresse and J. Furthmuller, *Comput. Mater. Sci.*, 1996, **6**, 15.
58 J. P. Perdew, K. Burke and M. Ernzerhof, *Phys. Rev. Lett.*, 1996, **77**, 3865.
59 J. P. Perdew, K. Burke and M. Ernzerhof, *Phys. Rev. Lett.*, 1997, **78**, 1396.
60 P. E. Blochl, *Phys. Rev. B: Condens. Matter Mater. Phys.*, 1994, **50**, 17953.
61 G. Kresse and D. Joubert, *Phys. Rev. B: Condens. Matter Mater. Phys.*, 1999, **59**, 1758.
62 S. J. Grimme, *Comput. Chem.*, 2006, **27**, 1787.
63 S. Grimme, J. Antony, S. Ehrlich and H. J. Krieg, *Chem. Phys.*, 2010, 132.
64 K. Lee, E. D. Murray, L. Z. Kong, B. I. Lundqvist and D. C. Langreth, *Phys. Rev. B: Condens. Matter Mater. Phys.*, 2010, **82**, 081101.
65 L. Grajciar, C. O. Arean, A. Pulido and P. Nachtigall, *Phys. Chem. Chem. Phys.*, 2010, **12**, 1497.
66 Y. Li, W. P. Guo, W. B. Fan, S. P. Yuan, J. F. Li, J. G. Wang, H. J. Jiao and T. Tatsumi, *J. Mol. Catal. A: Chem.*, 2011, **338**, 24.
67 J. B. Nicholas and M. Feyereisen, *J. Chem. Phys.*, 1995, **103**, 8031.
68 T. H. Dunning, *J. Chem. Phys.*, 1989, **90**, 1007.
69 B. Onida, F. Geobaldo, F. Testa, F. Crea and E. Garrone, *Microporous Mesoporous Mater.*, 1999, **30**, 119.
70 D. Meloni, S. Laforge, D. Martin, M. Guisnet, E. Rombi and V. Solinas, *Appl. Catal., A*, 2001, **215**, 55.
71 Z. Sobalik, Z. Tvaruzkova, B. Wichterlova, V. Fila and S. Spatenka, *Appl. Catal., A*, 2003, **253**, 271.
72 P. Ayrault, J. Datka, S. Laforge, D. Martin and M. Guisnet, *J. Phys. Chem. B*, 2004, **108**, 13755.
73 M. Rubes, L. Grajciar, O. Bludsky, A. D. Wiersum, P. L. Llewellyn and P. Nachtigall, *ChemPhysChem*, 2012, **13**, 488.
74 L. Grajciar, A. D. Wiersum, P. L. Llewellyn, J.-S. Chang and P. Nachtigall, *J. Phys. Chem. C*, 2011, **115**, 17925.
75 L. Grajciar, J. Cejka, A. Zukal, C. O. Arean, G. T. Palomino and P. Nachtigall, *ChemSusChem*, 2012, **5**, 2011.
76 K. Chakarova and K. Hadjiivanov, *Microporous Mesoporous Mater.*, 2013, **177**, 59.
77 B. Gil, B. Marszalek, A. Micek-Ilnicka and Z. Olejniczak, *Top. Catal.*, 2010, **53**, 1340.
78 Z. Zhu, Q. Chen, Z. Xie, W. Yang and C. Li, *Microporous Mesoporous Mater.*, 2006, **88**, 16.
79 C. C. Tsai, C. Y. Zhong, I. Wang, S. B. Liu, W. H. Chen and T. C. Tsai, *Appl. Catal., A*, 2004, **267**, 87.

Attachment E

THE JOURNAL OF PHYSICAL CHEMISTRY C

Article

pubs.acs.org/JPCC

Understanding the Structure of Cationic Sites in Alkali Metal-Grafted USY Zeolites

Tobias C. Keller,[†,§] Miroslav Položij,[‡,§] Begoña Puértolas,[†] Ho Viet Thang,[‡] Petr Nachtigall,*[,‡] and Javier Pérez-Ramírez*[,†]

[†]Institute for Chemical and Bioengineering, Department of Chemistry and Applied Biosciences, ETH Zurich, Vladimir-Prelog-Weg 1, CH-8093, Zurich, Switzerland

[‡]Department of Physical and Macromolecular Chemistry, Faculty of Science, Charles University in Prague, Hlavova 2030, 128 43 Prague 2, Czech Republic

Supporting Information

ABSTRACT: This contribution describes the structure of cationic sites in alkali metal-grafted high-silica USY zeolites, a novel class of zeolite base catalysts, through the combination of computational studies and experimental evidence. Based on density functional theory calculations, we investigate the geometry various defects that coordinate sodium or potassium, and their interaction with adsorbed CO. The predicted CO-stretching frequencies are verified experimentally by infrared spectroscopy, which indicates the existence of a distribution of different site geometries rather than a single site type. The corresponding bands lie in the range of 2180−2160 and 2170−2145 cm^{-1} for Na^+ and K^+ cations, respectively. While CO primarily interacts with the grafted metal cation (effect from the bottom), the CO stretching frequency is strongly modulated by neighboring silanol groups (effect from the top). Based on a good agreement of experimental and theoretical results, the deprotonation of silanol groups to silanolates followed by an ion exchange appears to be a realistic mechanism for alkali metal incorporation in silica-rich USY zeolites. The developed insights on the cation site structure represent an important step to understand the catalytic performance of these basic zeolites in aldol-type reactions, and pave the way for future studies investigating transition states to resolve their role in catalysis.

1. INTRODUCTION

The unique combination of a large micropore surface with a tunable mesopore and active site structure renders zeolites one of the most successful industrial solid acid catalysts.[1,2] In contrast, the window of application for their basic counterparts remains very narrow.[3] Basic zeolites are usually obtained by introducing large alkali metals (mainly Cs^+) into cation exchange positions in aluminum-rich zeolites as X or Y, to increase the electron density on the framework oxygen atoms, and consequently their basicity.[4−6] While these zeolites initially found applications mainly in adsorption, their potential in catalysis was discovered soon after. However, despite the excessive loadings (>35 wt %) of costly cesium, the activity of the catalysts was modest and particularly in gas-phase applications, they often suffered from deactivation due to unselective reaction pathways that result in coke formation.[7,8]

Consequently, many new approaches to introduce basic sites into zeolites have been investigated, e.g., nitridation[9−11] or the grafting of organic bases,[12] but the complicated synthesis protocols together with a questionable stability render them industrially unattractive. In contrast, it has been recently demonstrated that via simple alkaline treatments, alkali metal-coordinating defects of supposedly basic nature can be generated in high-silica zeolites.[13−15] The application of appropriate alcoholic solvents prevented framework degradation, and simultaneously offered accurate control over the metalation process, i.e., the amount and environment of the incorporated alkali metals. Based on their atomic or near-atomic dispersion evidenced by ^{23}Na magic angle spinning nuclear magnetic resonance (MAS NMR) spectroscopy, electron microscopy, elemental mapping, and temperature-programmed desorption of CO_2 (CO_2-TPD), it was suggested that the alkali metal cations graft to deprotonated silanol groups. The formed mild basic sites exhibited excellent activity, selectivity, and stability in the gas-phase self-condensation of propanal.[14] However, due to the complexity and heterogeneity of the hierarchically porous zeolites, the suggested active site structure remains difficult to verify experimentally, and further evidence is sought after.

A promising approach capable of answering this issue is the computational investigation by density functional theory (DFT) calculations, which has been extensively used to study the coordination of alkali metal cations exchanged into the cationic positions of various framework topologies.[16−21] For instance, Zecchina et al.[16] outlined the use of diatomic molecular probes such as CO, N_2 and H_2 as a proof of

Received: December 18, 2015
Revised: February 11, 2016
Published: February 11, 2016

DOI: 10.1021/acs.jpcc.5b12413
J. Phys. Chem. C 2016, 120, 4954−4960

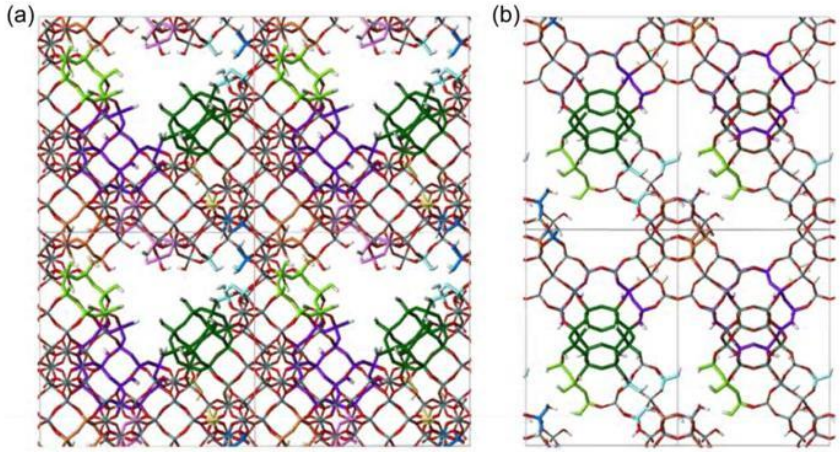

Figure 1. Projections of the investigated hUSY zeolite model along the (a) 100 and (b) 110 vectors. Si, O and H atoms are depicted in gray, red, and white, respectively. Individual sites are shown in dark green (S_{D6R}), light green (S_{S6R}), violet (S_{06R}), blue (S_{-1T}), orange (S_{-2T}), and yellow (B_{-1T}).

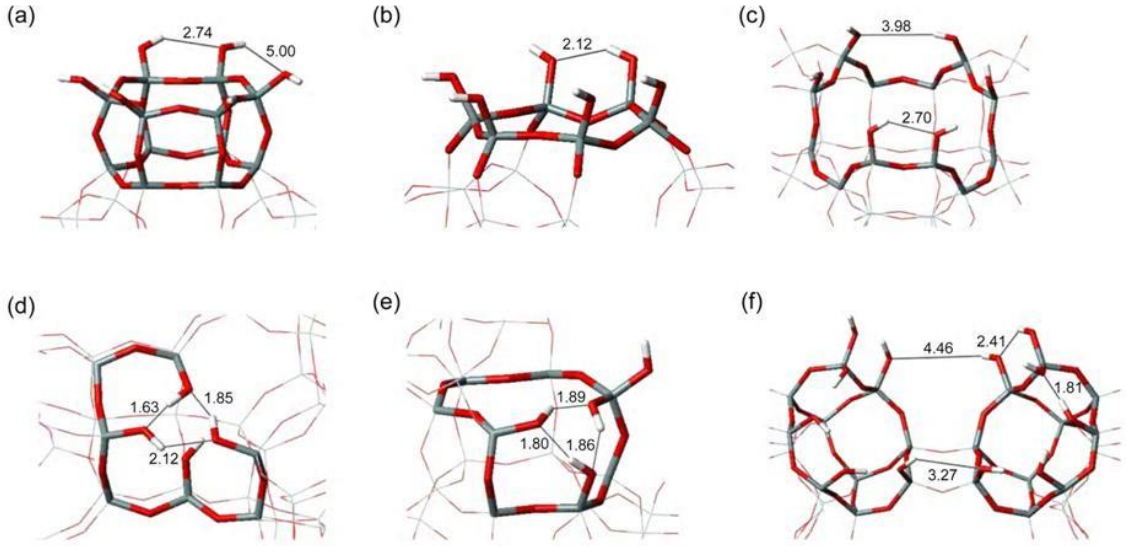

Figure 2. Computationally investigated surface defects for alkali metal grafting. (a) S_{D6R}, (b) S_{S6R}, and (c) S_{06R} sites with 6 silanol groups each; (d) B_{-1T} and (e) S_{-1T} sites with 4 silanol groups each; and (f) two neighboring S_{-2T} sites, each of them containing 6 silanol groups. Si, O, and H atoms are depicted in gray, red, and white, respectively. All distances are indicated in Å.

Brønsted and Lewis acidity, structural defects, internal electric fields, and the siting of extra-framework cations in zeolites with MFI, USY, and MOR topologies. Afterward, Ferrari et al.[19] studied the interaction of CO with alkaline-cation ion exchanged ZSM-5 zeolites and Ugliengo et al.[20] investigated the structure, the binding energy, and the vibrational features of carbon monoxide adsorbed on H^+, Li^+, Na^+ and K^+-exchanged chabazite. Based on a systematic investigation of CO adsorption, a generalized model predicting the vibrational frequency of the CO stretching mode was proposed,[22] enabling an experimental verification of the calculations by variable temperature infrared (VTIR) spectroscopy.[23−25]

In this contribution, we combine the experimental and theoretical evidence to understand the structure of the alkali metal-coordinating defects in high-silica USY zeolites. A novel model of a hierarchical USY zeolite is initially proposed, and the geometries of different postulated alkali metal sites are subsequently computationally investigated at the DFT level. The calculated stretching frequencies for CO adsorption complexes in Na- and K-grafted USY zeolites are then compared with experimental data. A good agreement between experimental and theoretical results entitles us to explain for the first time the nature of the cationic sites in this novel class of basic zeolites.

2. EXPERIMENTAL AND THEORETICAL METHODS

2.1. Experimental Methods. The parent high-silica USY zeolite (USY-P) was obtained in protonic form from Tosoh Corporation (HSZ-390HUA, Si/Al = 405). For the grafting of the alkali metals, the as-received zeolite (2 g) was introduced into a solution (60 cm^3) of the desired concentration (0−0.15 M) of alkali metal hydroxide (NaOH, Sigma-Aldrich, 97%; KOH, Fisher Chemicals, 85%) in methanol (Sigma-Aldrich, 99.8%) at room temperature, stirred at 500 rpm for 10 min, filtered, washed 3 times with ca. 100 cm^3 of methanol, and subsequently dried at 338 K. The samples were coded *x*M-USY,

DOI: 10.1021/acs.jpcc.5b12413
J. Phys. Chem. C 2016, 120, 4954−4960

where x represents the concentration and M the cation of the employed metal salt.

Fourier transform infrared spectroscopy (FTIR) of adsorbed CO (99.998%, Messer) was measured in a Bruker IFS 66 spectrometer (650−4000 cm^{-1}, 2 cm^{-1} optical resolution, coaddition of 32 scans). Self-supporting wafers of the sample (5 tons m^{-2}, 50 mg, 1 cm^2) were evacuated to 10^{-3} mbar for 4 h at 693 K. CO (ca. 2 mbar) was adsorbed on the catalyst at 77 K, followed by evacuation to different pressures, equilibration, and acquisition of the individual spectra. ^{1}H MAS NMR spectra were measured on a Bruker Avance 700 Spectrometer using 2.5 mm ZrO_2 rotors at a spinning speed of 20 kHz. Samples were dried in vacuum prior to the analysis.

2.2. Theoretical Methods. Calculations were performed using a periodic DFT model within the VASP 5.3.3 program suite.[26−28] The PBE functional[29] was used together with the projector augmented wave approximation (PAW)[30] and a plane-wave basis set. The kinetic energy cutoff was set to 400 eV and the Brillouin-zone sampling was restricted to the Γ-point due to the large size of the unit cell (UC, see below). Geometry optimizations were performed with fixed UC volume and shape, while relaxing the positions of all atoms. The CO vibrational frequency was acquired by using the ω_{CO}/r_{CO} correlation[22] adopted for Na^+ and K^+ extra-framework cations.[31,32]

2.3. Models. The following protocol was applied to construct the hierarchical siliceous FAU-type zeolite (hUSY). Starting from the primitive FAU UC ($Si_{192}O_{384}$), 49 Si atoms were removed as detailed in the Supporting Information. Unsaturated oxygen atoms were terminated with H atoms forming surface silanols and the final geometry was optimized. The resulting model of hUSY (Figure 1) has the following composition and UC parameters: $Si_{143}O_{309}H_{46}$, a = 24.545 Å, b = 24.527 Å, c = 24.560 Å, α = 89.97°, β = 90.12°, γ = 90.00°. All structures are provided in cif format in the Supporting Information.

There are several types of potential sites on the internal surface of hUSY that differ in the number and arrangement of surface silanol groups. The sites can be divided into two categories comprising sites formed by the removal of a cluster of framework T atoms that expose some facets of the D6R structural unit (denoted $\mathbf{S}_{N6R}$ sites), and sites formed by the removal of single T atoms (denoted $\mathbf{B}_{-NT}$ sites). Three $\mathbf{S}_{N6R}$-type sites containing six interacting surface silanol groups were considered for further investigation: (i) exposed D6R (denoted $\mathbf{S}_{D6R}$, Figure 2a), (ii) exposed single six-membered ring (S6R) (denoted $\mathbf{S}_{S6R}$, Figure 2b), and (iii) exposed sodalite cage ($\mathbf{S}_{O6R}$, Figure 2c). Additionally, three sites formed by the removal of single T atoms were considered: (i) a silanol nest created by the removal of a regular single T atom (not connected to any silanol) which consists of four surface silanol groups ($\mathbf{B}_{-1T}$, Figure 2d), (ii) a silanol nest formed by deletion of a T atom bearing one silanol group ($\mathbf{S}_{-1T}$, Figure 2e), and (iii) a large silanol nest created by the removal of two out of four OH-bearing T atoms from a partially exposed surface D6R, both containing six surface silanol groups ($\mathbf{S}_{-2T}$, Figure 2f).

Based on an experimentally determined structure of the FAU surface,[33] a periodic slab model consisting of layers of FAU zeolite terminated with D6R structural units on both sides and separated by vacuum was used (Figure 3, composition $Si_{60}O_{126}H_{11}Na$, UC parameters a = c = 17.372 Å, b = 35.000 Å, α = β = γ = 60.00°).

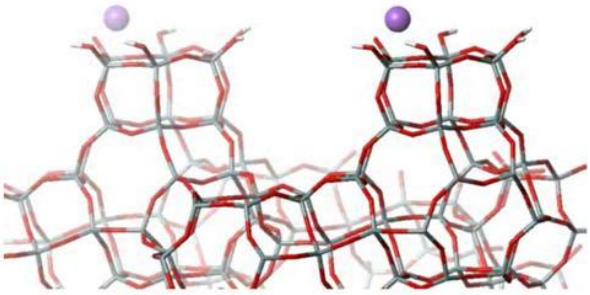

Figure 3. Model of a layered FAU zeolite terminated with D6R structural units exchanged with Na^+ cations. Si, O, H, and Na atoms are depicted in gray, red, white, and purple, respectively.

3. RESULTS

3.1. Characterization of the Catalysts. Na^+ and K^+ were grafted onto high-silica USY zeolites (Si/Al = 405) via treatments in methanolic solutions of the corresponding alkali metal hydroxides. The detailed characterization of the samples by ^{23}Na MAS NMR, CO_2-TPD, electron microscopy, and elemental mapping has been discussed in detail in a previous contribution.[14] The treatment conditions, along with the textural properties and composition of all the catalysts are compiled in Table 1. The crystallinity and microporosity were fully preserved for all sodium-grafted samples, and slightly reduced for the potassium-grafted analogue. The amount of incorporated alkali metal increases with the alkalinity of the treatment solution,[14] as well as with the size of the cation, and is accompanied by an up to 40% decrease in external surface area. Comparison of the IR spectra of the parent zeolite and its NaOH-treated (0.1 M) analogue evidence that all major bands are fully preserved (Figure S1). The only notable difference is a reduced intensity of the band at 3745 cm^{-1}, which could be associated with the ion exchange of terminal silanol groups in basic media, and thus a reduction in the intensity of the signal. These catalysts were also characterized by ^{1}H MAS NMR (Figure S2). The spectra were dominated by two contributions, a band at ca. 3.5 ppm associated with bridging silanol groups and a band at ca. 2 ppm associated with nonbridging silanol groups. While the untreated zeolite (USY-P) mainly evidence bridging silanols, most of the signal intensity is shifted to isolated sites for the treated sample.

3.2. Theoretical Investigation of Grafted Alkali Metal Cations. The alkali metal-grafted hUSY was modeled by deprotonating one silanol group per UC and the resulting negative charge on the silanolate was compensated by an alkali metal cation. The geometry of the system was subsequently optimized. This procedure was applied to various silanols in the hUSY model (vide supra) and the configuration with the lowest energy was selected for further evaluation. The total energies for the following ion exchange reaction were calculated by summing up the energies of the individual reactants multiplied by their stoichiometric coefficient.

$$\mathrm{hUSY(OH)}_n + \mathrm{M}^+ \rightarrow \mathrm{hUSY(OH)}_{n-1}\mathrm{(OM)} + \mathrm{H}^+ \qquad (1)$$

Since the chemical composition is identical among the Na^+ or K^+-grafted systems, their total energies can be directly compared by referencing to the most stable structure (for the corresponding cation), yielding the relative exchange energy (E_{ex}^{rel}) (Table 2). This enables to compare the relative energies among the investigated sites, while the energies of M^+ and H^+

DOI: 10.1021/acs.jpcc.5b12413
J. Phys. Chem. C 2016, 120, 4954−4960

Table 1. Treatment Conditions and Characterization Data of the Catalysts

catalyst	c_{MOH}[a] (M)	cation[b]	V_{pore} ($cm^3\ g^{-1}$)	V_{micro}[c] ($cm^3\ g^{-1}$)	S_{ext}[c] ($m^2\ g^{-1}$)	S_{BET}[d] ($m^2\ g^{-1}$)	crystallinity[e] (%)	M/Si ratio[f] (mol mol^{-1})
USY-P	as-received		0.56	0.30	117	693	100	
0.05Na-USY	0.05	Na^+	0.52	0.29	82	646	98	0.0067
0.1Na-USY	0.1	Na^+	0.51	0.29	70	615	97	0.022
0.15Na-USY	0.15	Na^+	0.51	0.28	69	615	94	0.026
0.1K-USY	0.1	K^+	0.51	0.27	67	590	72	0.075

[a]Metal hydroxide (MOH) concentration. [b]Cation of the hydroxide salt. [c]*t*-plot method. [d]BET method. [e]XRD. [f]Na: ICP-OES; K: XRF.

Table 2. Relative Exchange Energies, CO Interaction Energies, and Stretching Frequencies Calculated at the PBE Level for Various Alkali Metal Sites in M-hUSY Zeolites

	Na-hUSY			K-hUSY		
site	$E_{ex}^{rel}(Na^+)$[a]	$E_{int}(CO)$[a]	$\nu_{\omega/r}(CO)$[b]	$E_{ex}^{rel}(K^+)$[a]	$E_{int}(CO)$[a]	$\nu_{\omega/r}(CO)$[b]
S_{06R}	27.4	−11.9	2167	30.2	−14.3	2163
S_{D6R}	61.5	−25.9	2176	57.5	−12.9	2160
S_{S6R}	76.2	−22.7	2178	82.8	−12.4	2162
$B_{.1T}$	0.0	−25.3	2180	6.2	−14.1	2165
$S_{.1T}$	11.0	−21.1	2174	9.3	−15.0	2163
$S_{.2T}$	11.7	−22.1	2162	0.0	−15.6	2142

[a]Energies in kJ mol^{-1} defined in eq 1. [b]Frequencies in cm^{-1}.

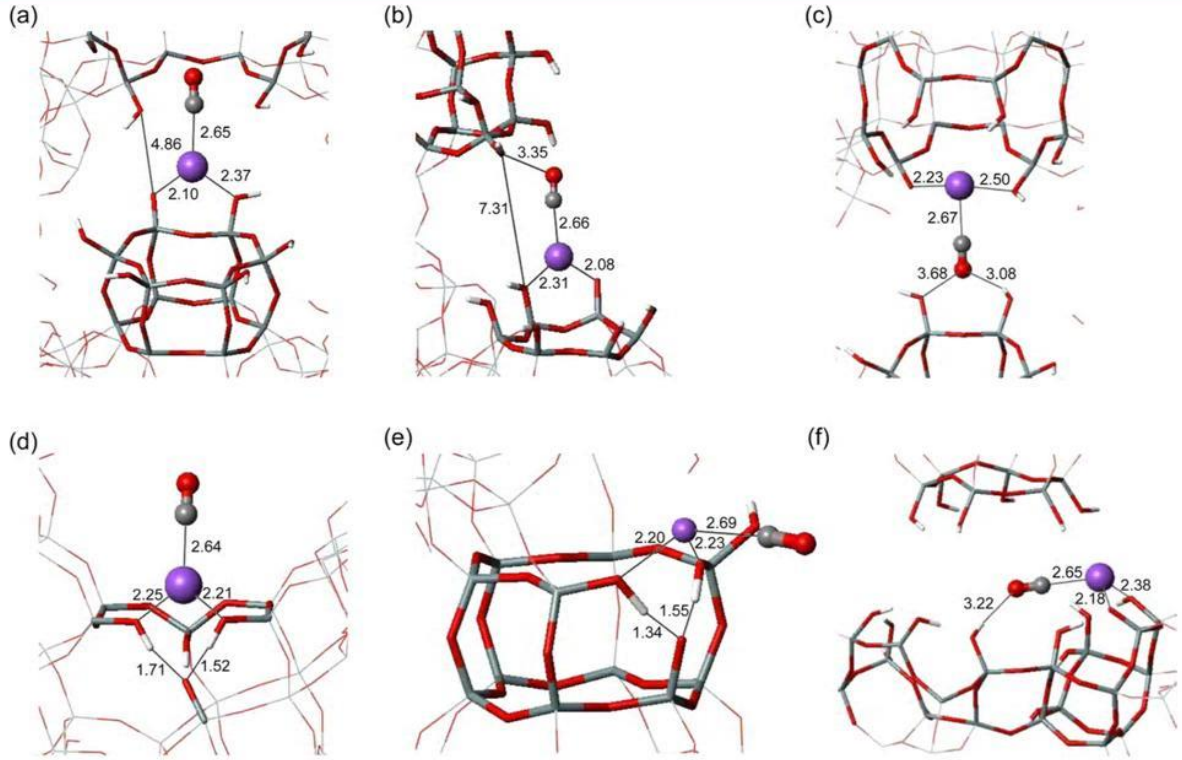

Figure 4. CO adsorption complexes formed on (a) S_{D6R}, (b) S_{S6R}, (c) S_{06R}, (d) $B_{.1T}$, (e) $S_{.1T}$, and (f) $S_{.2T}$ Na^+ sites in Na-hUSY. Si, O, H, and Na atoms are depicted in gray, red, white, and purple, respectively. All distances are indicated in Å.

species cancel out. The thereby attained geometries for sodium-grafted hUSY are reported in Figure 4. In the case of $B_{.1T}$ and $S_{.1T}$ sites, the Na^+ cation is coordinated to oxygen atoms of silanol groups which compensate the charge of the silanolate indirectly via strong hydrogen bonds (the H···O distance is only 1.5 Å) (Figure 4d,e). Similarly, the $S_{.2T}$ site evidences a substantial charge redistribution via hydrogen bonds, resulting in low values of E_{ex}^{rel}. In contrast, for the S_{N6R} sites (S_{D6R}, S_{S6R}, and S_{06R}) the Na^+ cation is bound to the silanolate and one adjacent silanol (Figure 4a–c), but a charge redistribution via hydrogen bonds does not occur, resulting in much higher exchange energies compared to the $B_{.NT}$ sites ($B_{.1T}$, $S_{.1T}$, and $S_{.2T}$). This is particularly evident for the S_{D6R} and S_{S6R} sites, whereas the linear coordination of Na^+ between two oxygen atoms in the S_{06R} site mitigates a part of the effect. Similarly, in the case of the K^+ cation, the ion exchange is energetically more

DOI: 10.1021/acs.jpcc.5b12413
J. Phys. Chem. C 2016, 120, 4954−4960

favorable in sites based on removed single T atoms compared to the S_{N6R} ones (Table 2).

3.3. Theoretical Investigation of CO Adsorption. The interaction energies of CO with the postulated alkali metal sites in hUSY and the corresponding CO stretching frequencies are reported in Table 2. Both the adsorption enthalpy and the vibrational frequency of the adsorbate are determined by two effects, the effect from the bottom and the effect from the top, which affect the experimental observations in opposing ways.[34] The effect from the bottom reflects the coordination of the metal cation within the zeolite framework. Typically, a stronger interaction leads to a weaker adsorption of the CO molecule, and thus a smaller blue-shift of the corresponding stretching frequencies. In contrast, the effect from the top contemplates the interaction of the adsorbate with the adsorbent via its opposite end (O atom in the case of CO). In the case of CO interacting with the positively charged H atom of a silanol (Figure 4f) a red-shift is observed, while CO interacting with a negatively charged framework O atom (Figure 4a) results in a blue-shift of the stretching frequencies that increases with the strength of the interaction. For Na-hUSY, the calculated CO frequencies lie between 2160 and 2180 cm^{-1}, and corresponding interaction energies range from −11.9 to −25.9 kJ mol^{-1}. It is important to note that the reported interaction energies were not corrected for the effect of zero-point vibrational energy, which are 3.3 and 2.5 kJ mol^{-1} for CO adsorption on Na^+ and K^+ sites, respectively. There is no apparent correlation between CO stretching frequencies, the energies of the interaction, and the relative ion exchange energies, which points toward a strong effect from the top:[25] the interaction of CO with two positively charged atoms (Na^+ at the C-end and hydrogen at the O-end) lowers the energy of the system and gives rise to a small prolongation of the C−O bond, which results in a partial cancellation of blue- and red-shifts due to the effects from the bottom and from the top, respectively. This becomes apparent through a comparison of the two-dimensional model of FAU terminated with D6R units (Figure 3) and the S_{D6R} site (Figure 4a), for which the effect from the bottom is identical. For the 2D model, there is no effect from the top and the calculated CO stretching frequency is 2178 cm^{-1}. In comparison, in the S_{D6R} site there are two (relatively distant) silanol groups, and consequently the stretching frequency is red-shifted to 2176 cm^{-1}. The S_{06R} and S_{-2T} sites experience the strongest effect from the top, and accordingly evidence the lowest stretching frequencies. On the other hand, the CO adsorbed on B_{-1T} sites points toward the void space in the FAU supercage, and no interaction with silanol groups occurs on the O-end of CO, resulting in the highest calculated stretching frequency (2180 cm^{-1}). As a side note, the interaction energy of CO with the S_{06R} site (−12 kJ mol^{-1}) is only half of the values found for other sites. This exceptionally low interaction energy can be attributed to the previously discussed linear coordination of the Na^+ cation, since for this geometry the carbon atom of the CO molecule is close to the oxygen atoms of adjacent silanol groups.

The results for CO adsorption complexes formed on K^+ sites in K-hUSY are also reported in Table 2. The calculated interaction energies are very similar for the different sites investigated, and the CO frequencies fall within the narrow range of 2160−2165 cm^{-1}, except for S_{-2T}-type site which exhibits a lower frequency (2142 cm^{-1}). The latter can be explained based on the short distance between the oxygen atom of CO and the next neighboring hydrogen atom, which is much shorter compared to the other sites (2.3 Å instead of ca. 3 Å, Figure S3f), resulting in a very strong effect from the top.

3.4. Experimental Investigation of CO Adsorption. The suitability of the IR-spectroscopic investigation of adsorbed CO to characterize cationic sites in faujasite-type materials has been previously demonstrated for Na−Y zeolites.[25,35] For this material, the chemical shift of the C−O stretching frequency predicted by the DFT model could be accurately verified for low coverage spectra acquired at 195 K and p_{CO} < 3.5 mbar, which could be reproduced in our experimental setup. However, if the parent or alkali metal-grafted USY zeolites are investigated under similar conditions, no adsorption of CO is evidenced (data not shown), which is likely related to the reduced cation concentration and lower adsorption enthalpy of CO, and thus a lower desorption temperature. Accordingly, the experiments were carried out at 77 K using liquid nitrogen as coolant, dosing ca. 2 mbar of CO, followed by a stepwise desorption and equilibration down to ca. $p_{CO} = 10^{-2}$ mbar. Under those conditions, the parent USY zeolite evidence three major bands at 2135, 2158, and 2179 cm^{-1}, of which all except the last one are rapidly desorbed upon evacuation (Figure 5a). These bands are assigned to unspecifically physisorbed CO, CO adsorbed on silanol groups, and CO adsorbed on Brønsted sites, respectively.[36] In contrast, the sodium-grafted samples evidence a broad distribution of adsorption bands in the range of 2180 to 2160 cm^{-1} whose intensity increases with the increasing sodium content (Figures 5b−d). The IR-spectroscopic investigation of adsorbed CO was also carried out over a potassium-grafted USY zeolite (Figure 5e). It also exhibits broad signal pointing toward the coexistence of multiple sites, but compared to its sodium counterpart all bands are red-shifted by ca. 10 cm^{-1}. Despite the higher potassium loading, the CO uptake is lower compared to the sodium-grafted samples.

4. DISCUSSION

Despite actually probing the Lewis acidity of the metal cations, carbon monoxide is arguably the most extensively used probe molecule for the IR-spectroscopic investigation of basic zeolites, mainly because it offers a rare opportunity to directly bridge theoretical and experimental evidence. The C−O bond length, obtained by the DFT model with an affordable computational effort, can be utilized to calculate the corresponding stretching frequency at the coupled cluster level, resulting in a highly accurate prediction with an error not exceeding 2−4 cm^{-1}.[25] The thereby enabled verification of DFT models has substantially contributed to the improved understanding of metal sites, as demonstrated for extra-framework alkali metal cations,[31] alkaline-earth cations,[37] transition metals,[38] and even for Brønsted acid sites.[39]

For the alkali-grafted zeolites investigated herein, a representative model of a hierarchical USY zeolite exhibiting different types of defects was developed, and the alkali cations were subsequently incorporated by the ion exchange of the deprotonated silanol groups. The sodium atoms are coordinated to at least two oxygen atoms, thus preventing the local stabilization by hydrogen bonding between the silanols, which is underlined by ^1H MAS NMR (Figure S2). The calculated stretching frequencies for adsorbed CO ranged from 2180 to 2160 cm^{-1} for Na-hUSY, in agreement with the experimental evidence. For the catalyst with the lowest sodium loading (0.05Na-USY), the appearance of different bands can be clearly detected, indicating that the sodium is incorporated simulta-

DOI: 10.1021/acs.jpcc.5b12413
J. Phys. Chem. C 2016, 120, 4954−4960

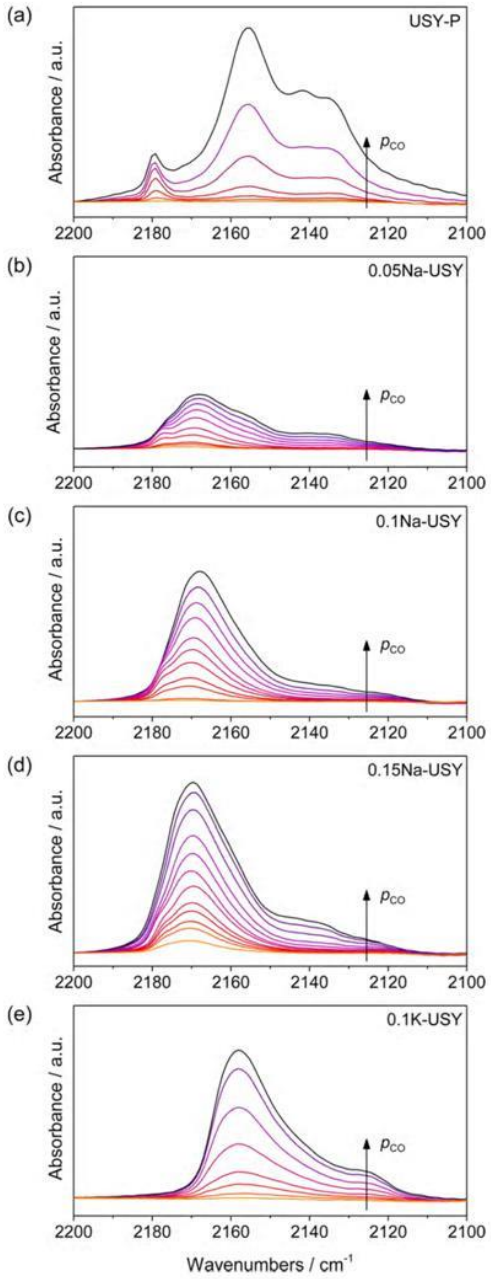

Figure 5. FTIR spectra of (a) USY-P, (b) 0.05Na-USY, (c) 0.1Na-USY, (d) 0.15Na-USY, and (e) 0.1K-USY zeolites after CO adsorption (ca. 2 mbar) at 77 K and subsequent stepwise desorption (until ca. 10^{-2} mbar). The intensity of the spectra was normalized to the wafer thickness.

neously in different types of defects (Figure 5b). With the increasing sodium content in the catalyst, the intensity of the observed bands increases, but the relative proportions are preserved, indicating that only the amount, but not the type of sites, is modified. Our calculations show that the investigated Na^+ sites can be divided into two groups, S_{N6R} and B_{NT} sites, but since the strong effect from the top masks the effects from the bottom and causes the bands to overlap, an experimental distinction between the two groups is not feasible. The potassium-grafted zeolite exhibits a similar distribution of defects compared to its sodium counterpart, but all the bands are red-shifted by ca. 10 cm^{-1} with respect to sodium-grafted one, in agreement with the predictions of DFT (Figure 5e). The broad absorption band observed experimentally (compared to the predictions by DFT) is likely caused by a gradual degradation of the zeolite framework during the alkaline treatment, which is also evident from the reduced crystallinity and micropore volume (Table 1). The CO uptake in potassium-exchanged samples is lower compared to the sodium-grafted ones, despite the higher potassium loading, which can be explained by the ca. 40% lower interaction energies (Table 2). The increased number of silanol groups which can interact with potassium due to its larger size translates into an improved coordination with the surface and, consequently, a weaker interaction with the CO molecules.

5. CONCLUSIONS

In this contribution, we describe for the first time the cationic site structure of alkali metals grafted to USY zeolites, which to date has only been discussed on a speculative basis. The presence of different types of defects in USY zeolites, as a consequence of steaming and acid treatments applied during their synthesis, results in a number of possible environments for grafted alkali cations, for which we have simulated the adsorption of CO at the DFT level and calculated the corresponding CO stretching frequency. Analysis by IR spectroscopy confirmed the coexistence of multiple types of sites for both investigated cations, in agreement with the theoretical predictions. Accordingly, in combination with the previously available characterization, we now have an accurate understanding of the alkali metal site properties on all length scales. In view of the strong effect from the top that neighboring silanols had on adsorbed CO, the latter can be expected to play an important role in catalytic applications. The in-depth understanding of the structure of these alkali metal sites opens the path for further studies of transitions states in C−C coupling reactions, such as aldol condensations to clarify the role of the cationic sites as active centers.

■ ASSOCIATED CONTENT

Supporting Information

The Supporting Information is available free of charge on the ACS Publications website at DOI: 10.1021/acs.jpcc.5b12413.

FTIR and ^{1}H MAS NMR spectra of the zeolites. Details on the modeling of the hierarchical siliceous FAU type zeolite UC. CO adsorption complexes on K-grafted zeolites. (PDF)

Crystallographic information files for all structures. (ZIP)

■ AUTHOR INFORMATION

Corresponding Authors

*Phone: +420 22 195 1289. E mail: nachtig@natur.cuni.cz.

*Phone: +41 44 633 7120. E mail: jpr@chem.ethz.ch.

Author Contributions

[§]The manuscript was written through contributions of all authors. All authors have given approval to the final version of the manuscript. These authors contributed equally.

Notes

The authors declare no competing financial interest.

DOI: 10.1021/acs.jpcc.5b12413
J. Phys. Chem. C 2016, 120, 4954−4960

■ ACKNOWLEDGMENTS

This work was funded by ETH (research grant ETH-31 13-1), the European Union Seventh Framework Programme (FP7/2007-2013) under Grant Agreement No. 604307, the Czech Science Foundation Grant No. P106/12/G015 (Centre of Excellence), and the Charles University in Prague (Project GA UK No. 562214). The calculations were partially performed at MetaCentrum and CERIT-SC computational facilities (MSM/LM2010005 and OP VaVpI CZ. 1.05/3.2.00/08.0144).

■ REFERENCES

(1) Tanabe, K.; Hölderich, W. F. Industrial Application of Solid Acid−Base Catalysts. *Appl. Catal., A* **1999**, *181*, 399−434.
(2) Yilmaz, B.; Mueller, U. Catalytic Applications of Zeolites in Chemical Industry. *Top. Catal.* **2009**, *52*, 888−895.
(3) Davis, R. J. New Perspectives on Basic Zeolites as Catalysts and Catalyst Supports. *J. Catal.* **2003**, *216*, 396−405.
(4) Barthomeuf, D. Basic Zeolites: Characterization and Uses in Adsorption and Catalysis. *Catal. Rev.: Sci. Eng.* **1996**, *38*, 521−612.
(5) Ono, Y.; Hattori, H. *Solid Base Catalysis*; Springer-Verlag: Berlin, 2011; pp 170−187.
(6) Weitkamp, J.; Hunger, M.; Rymsa, U. Base Catalysis on Microporous and Mesoporous Materials: Recent Progress and Perspectives. *Microporous Mesoporous Mater.* **2001**, *48*, 255−270.
(7) Di Cosimo, I.; Apesteguía, C. R. Study of the Catalyst Deactivation in the Base-Catalyzed Oligomerization of Acetone. *J. Mol. Catal. A: Chem.* **1998**, *130*, 177−185.
(8) Keller, T. C.; Isabettini, S.; Verboekend, D.; Rodrigues, E. G.; Pérez-Ramírez, J. Hierarchical High-Silica Zeolites as Superior Base Catalysts. *Chem. Sci.* **2014**, *5*, 677−684.
(9) Srasra, M.; Delsarte, S.; Gaigneaux, E. M. Nitrided Zeolites: A Spectroscopic Approach for the Identification and Quantification of Incorporated Nitrogen Species. *J. Phys. Chem. C* **2010**, *114*, 4527−4535.
(10) Hammond, K. D.; Gharibeh, M.; Tompsett, G. A.; Dogan, F.; Brown, A. V.; Grey, C. P.; Auerbach, S. M.; Conner, Wm. C., Jr. Optimizing the Synthesis of Nitrogen-Substituted Zeolites. *Chem. Mater.* **2010**, *22*, 130−142.
(11) Ernst, S.; Hartmann, M.; Hecht, T.; Jaen, P. C.; Sauerbeck, S. In *Impact of Zeolites and Other Porous Materials on the New Technologies at the Beginning of the New Millennium, Pts A and B*; Aiello, R., Giordano, G., Testa, F., Eds.; Elsevier: Amsterdam, 2002; Vol. *142*, pp 549−556.
(12) Jones, C. W.; Tsuji, K.; Davis, M. E. Organic-Functionalized Molecular Sieves as Shape-Selective Catalysts. *Nature* **1998**, *393*, 52−54.
(13) Keller, T. C.; Rodrigues, E. G.; Pérez-Ramírez, J. Generation of Basic Centers in High-Silica Zeolites and their Application in Gas-Phase Upgrading of Bio-Oil. *ChemSusChem* **2014**, *7*, 1729−1738.
(14) Keller, T. C.; Desai, K.; Mitchell, S.; Pérez-Ramírez, J. Design of Base Zeolite Catalysts by Alkali-Metal Grafting in Alcoholic Media. *ACS Catal.* **2015**, *5*, 5388−5396.
(15) Lari, G. M.; Desai, K.; Mondelli, C.; Pérez-Remírez, J. *Catal. Sci. Technol.* **2016**, DOI: 10.1039/C5CY02020D.
(16) Zecchina, A.; Areán, C. O. Diatomic Molecular Probes for mid-IR Studies of Zeolites. *Chem. Soc. Rev.* **1996**, *25*, 187−197.
(17) Vayssilov, G. N.; Rösch, N. Determination of the Basicity of Alkali-Exchanged Molecular Sieves. *Phys. Chem. Chem. Phys.* **2002**, *4*, 146−148.
(18) Kučera, J.; Nachtigall, P. Coordination of Alkali Metal Ions in ZSM-5: A Combined Quantum Mechanics/Interatomic Potential Function Study. *Phys. Chem. Chem. Phys.* **2003**, *5*, 3311−3317.
(19) Ferrari, A. M.; Ugliengo, P.; Garrone, E. Ab Initio Study of the Adducts of Carbon Monoxide with Alkaline Cations. *J. Chem. Phys.* **1996**, *105*, 4129−4139.
(20) Ugliengo, P.; Busco, C.; Civalleri, B.; Zicovich-Wilson, C. M. Carbon Monoxide Adsorption on Alkali and Proton-Exchanged Chabazite: An Ab-Initio Periodic Study Using the Crystal Code. *Mol. Phys.* **2005**, *103*, 2559−2571.
(21) Wesolowski, T. A.; Goursot, A.; Weber, J. Properties of CO Adsorbed in ZSM5 Zeolite: Density Functional Theory Study Using the Embedding Scheme Based on Electron Density Partitioning. *J. Chem. Phys.* **2001**, *115*, 4791−4797.
(22) Nachtigallová, D.; Bludský, O.; Areán, C. O.; Bulánek, R.; Nachtigall, P. The Vibrational Dynamics of Carbon Monoxide in a Confined Space - CO in Zeolites. *Phys. Chem. Chem. Phys.* **2006**, *8*, 4849−4852.
(23) Garrone, E.; Areán, C. O. Variable Temperature Infrared Spectroscopy: A Convenient Tool for Studying the Thermodynamics of Weak Solid−Gas Interactions. *Chem. Soc. Rev.* **2005**, *34*, 846−857.
(24) Areán, C. O.; Nachtigallová, D.; Nachtigall, P.; Garrone, E.; Delgado, M. R. Thermodynamics of Reversible Gas Adsorption on Alkali-Metal Exchanged Zeolites—the Interplay of Infrared Spectroscopy and Theoretical Calculations. *Phys. Chem. Chem. Phys.* **2007**, *9*, 1421−1436.
(25) Nachtigall, P.; Delgado, M. R.; Nachtigallová, D.; Areán, C. O. The Nature of Cationic Adsorption Sites in Alkaline Zeolites—Single, Dual and Multiple Cation Sites. *Phys. Chem. Chem. Phys.* **2012**, *14*, 1552−1569.
(26) Kresse, G.; Furthmüller, J. Efficient Iterative Schemes for ab Initio Total-Energy Calculations Using a Plane-Wave Basis Set. *Phys. Rev. B: Condens. Matter Mater. Phys.* **1996**, *54*, 11169−11186.
(27) Kresse, G.; Furthmüller, J. Efficiency of ab-Initio Total Energy Calculations for Metals and Semiconductors Using a Plane-Wave Basis Set. *Comput. Mater. Sci.* **1996**, *6*, 15−50.
(28) Kresse, G.; Hafner, J. Ab Initio Molecular-Dynamics Simulation of the Liquid-Metal−Amorphous-Semiconductor Transition in Germanium. *Phys. Rev. B: Condens. Matter Mater. Phys.* **1994**, *49*, 14251−14269.
(29) Perdew, J. P.; Burke, K.; Ernzerhof, M. Generalized Gradient Approximation Made Simple. *Phys. Rev. Lett.* **1996**, *77*, 3865−3868.
(30) Blöchl, P. E. Projector Augmented-Wave Method. *Phys. Rev. B: Condens. Matter Mater. Phys.* **1994**, *50*, 17953−17979.
(31) Areán, C. O.; Delgado, M. R.; Frolich, K.; Bulánek, R.; Pulido, A.; Bibiloni, G. F.; Nachtigall, P. Computational and Fourier Transform Infrared Spectroscopic Studies on Carbon Monoxide Adsorption on the Zeolites Na-ZSM-5 and K-ZSM-5: Evidence of Dual-Cation Sites. *J. Phys. Chem. C* **2008**, *112*, 4658−4666.
(32) Nachtigall, P.; Delgado, M. R.; Frolich, K.; Bulánek, R.; Turnes Palomino, G.; López Bauçà, C.; Areán, C. O. Periodic Density Functional and FTIR Spectroscopic Studies on CO Adsorption on the Zeolite Na-FER. *Microporous Mesoporous Mater.* **2007**, *106*, 162−173.
(33) Terasaki, O. Fine Structures of Zeolites. *J. Electron Microsc.* **1994**, *43*, 337−346.
(34) Grajciar, L.; Čejka, J.; Zukal, A.; Areán, C. O.; Turnes Palomino, G.; Nachtigall, P. Controlling the Adsorption Enthalpy of CO_2 in Zeolites by Framework Topology and Composition. *ChemSusChem* **2012**, *5*, 2011−2022.
(35) Cairon, O.; Guesmi, H. How does CO Capture Process on Microporous NaY Zeolites? A FTIR and DFT Combined Study. *Phys. Chem. Chem. Phys.* **2011**, *13*, 11430−11437.
(36) Daniell, W.; Topsøe, N.-Y.; Knözinger, H. An FTIR Study of the Surface Acidity of USY Zeolites: Comparison of CO, CD_3CN, and C_5H_5N Probe Molecules. *Langmuir* **2001**, *17*, 6233−6239.
(37) Bulánek, R.; Voleská, I.; Ivanova, E.; Hadjiivanov, K.; Nachtigall, P. Localization and Coordination of Mg^{2+} Cations in Ferrierite: Combined FTIR Spectroscopic and Computation Investigation of CO Adsorption Complexes. *J. Phys. Chem. C* **2009**, *113*, 11066−11067.
(38) Bludský, O.; Šilhan, M.; Nachtigallová, D.; Nachtigall, P. Calculations of Site-Specific CO Stretching Frequencies for Copper Carbonyls with the "Near Spectroscopic Accuracy": CO Interaction with Cu^+/MFI. *J. Phys. Chem. A* **2003**, *107*, 10381−10388.
(39) Nachtigall, P.; Bludský, O.; Grajciar, L.; Nachtigallová, D.; Delgado, M. R.; Areán, C. O. Computational and FTIR Spectroscopic Studies on Carbon Monoxide and Dinitrogen Adsorption on a High-Silica H-FER Zeolite. *Phys. Chem. Chem. Phys.* **2009**, *11*, 791−802.

DOI: 10.1021/acs.jpcc.5b12413
J. Phys. Chem. C 2016, 120, 4954−4960